Experimental modelling of a floating wind turbine using a “ software-in-the-loop ” approach

Vincent Arnal

THESE DE DOCTORAT DE

L'ÉCOLE CENTRALE DE NANTES

ECOLE DOCTORALE N° 602
Sciences pour l'Ingénieur
Spécialité : *Mécanique des Milieux Fluides*

Par

Vincent ARNAL

Modélisation expérimentale d'une éolienne flottante par une approche « software-in-the-loop »

Thèse présentée et soutenue à Nantes, le 11 décembre 2020
Unité de recherche : UMR 6598, Laboratoire de recherche en Hydrodynamique, Energétique et Environnement Atmosphérique (LHEEA)

Rapporteurs avant soutenance

Erin Elizabeth BACHYNSKI	Professeure, N.T.N.U (Norvège)
Olivier KIMMOUN	Maître de conférences HDR, Ecole Centrale de Marseille

Composition du Jury

Président :	Franck PLESTAN	Professeur des universités, Ecole Centrale de Nantes
Examinateurs :	Marco BELLOLI	Professeur, Université Polytechnique de Milan (Italie)
	Félicien BONNEFOY	Maître de conférences, Ecole Centrale de Nantes
	Jean-Christophe GILLOTEAUX	Ingénieur de recherche, Ecole Centrale de Nantes
	Alan TASSIN	Ingénieur de recherche, IFREMER, Plouzane
Dir. de thèse :	Sandrine AUBRUN-SANCHES	Professeure des universités, Ecole Centrale de Nantes

Experimental modelling of a floating wind turbine using a « software-in-the-loop » approach

Vincent ARNAL

Centrale Nantes
France

December 2020

Résumé

Cette thèse de doctorat s'inscrit dans le cadre de la recherche appliquée aux éoliennes flottantes. Alors qu'en France et dans le monde les premiers projets de fermes pilotes d'éoliennes flottantes commencent à émerger, leur modélisation dans un environnement complexe et multi-physique reste un défi important. Pour dimensionner ces structures, les outils numériques sont largement utilisés afin de valider le comportement de l'éolienne flottante et son intégrité lorsqu'elle est soumise à un ensemble de sollicitations. Cependant, ces outils numériques issus de l'« état de l'art » se basent sur des hypothèses souvent fortement simplificatrices par rapport à la physique réelle et nécessitent un ajustement de paramètres empiriques pour représenter au mieux la physique. Ces paramètres peuvent être ajustés à partir de simulations numériques haute-fidélité, mais sont principalement recalculés à partir de données expérimentales, que ce soit pour la modélisation de l'hydrodynamique (l'action des efforts dus au courant et aux vagues) du flotteur et du système d'ancrage, ou pour la modélisation de l'aérodynamique agissant sur le rotor et la tour de l'éolienne. En effet, les tests à échelle réduite (facteurs d'échelle typiques entre 1/200 à 1/20) dans des moyens d'essais bien instrumentés et contrôlés permettent de valider les outils de simulation et le dimensionnement de ces structures. Pour les éoliennes flottantes, à la fois l'aérodynamique et l'hydrodynamique sont complexes (de par la présence de phénomènes couplés, transitoires, instationnaires, ...) et encore assez mal maitrisés par manque de retour d'expérience d'éoliennes flottantes installées à l'échelle réelle.

Ce travail concerne la modélisation expérimentale et numérique d'une éolienne flottante lors d'essais en bassin à vagues. Historiquement, des systèmes 100% physiques ont été conçus, avec une soufflerie installée au-dessus d'un bassin à vagues. Cependant, ces systèmes posent plusieurs problèmes, au premier rang duquel une incompatibilité entre les similitudes de Reynolds et de Froude. En effet, les tests à échelle réduite nécessitent une bonne représentation des efforts identifiés comme étant prépondérants. Malheureusement, pour l'hydrodynamique à surface libre, le respect du nombre de Froude est important alors que pour l'aérodynamique sur le rotor, le nombre de Reynolds est important. Cependant, respecter le nombre de Reynolds pour l'aérodynamique du rotor nécessiterait des installations impossibles à réaliser avec des écoulements proches de la frontière compressible. Le défi d'un point de vue de l'expérimentation des éoliennes flottantes en bassin à vagues est donc de représenter les efforts aérodynamiques agissant sur l'éolienne et modifiant significativement le comportement du système. En effet, des couplages et parfois même des instabilités peuvent être causés par les efforts aérodynamiques agissant sur l'éolienne. Face à l'incapacité de respecter une similitude complète, différentes stratégies ont été développées. Récemment, l'utilisation de méthodologies hybrides, mêlant de l'expérimental et du numérique, a ouvert des perspectives intéressantes. Le choix est fait de simuler en temps réel des efforts aérodynamiques agissant sur le rotor pour les essais en bassin, et des efforts hydrodynamiques agissant sur le flotteur pour les essais en soufflerie.

Ces méthodologies sont appelées "Software-In-the-Loop" (SIL), car la modélisation numérique en temps réel est incluse dans le processus expérimental.

Le projet SOFTWIND dans lequel s'inscrit ce travail avait pour but de développer un tel système hybride pour les essais en bassins. Les objectifs du projet étaient :

- Munir le bassin de l'Ecole Centrale de Nantes d'un dispositif fiable permettant le test d'éoliennes flottantes de grande puissance (jusqu'à 15MW) sur des échelles de 1/50 à 1/30 ;
- Tester des lois de contrôle d'éoliennes flottantes lors d'essais en bassin.

Le périmètre de cette thèse concerne donc le dimensionnement et l'identification des performances d'un système hybride SIL pour les essais en bassin à houle de modèles réduits d'éoliennes flottantes. L'accent est mis sur la création d'une méthodologie dédiée à la validation des performances de ces systèmes. Cette thèse s'articule autour des sujets suivants :

- Le contexte général du travail de thèse décrit dans le chapitre 1.
- Le cadre théorique et pratique pour le développement de ces systèmes hybrides, décrit dans les chapitres 2 et 3. Cela concerne les principaux phénomènes physiques d'intérêt ainsi qu'une analyse des efforts agissant sur une éolienne et qu'il convient de reproduire lors d'essais en bassin. Le dimensionnement d'un système d'actionneurs, l'élément central des méthodes SIL, est couvert dans les chapitres 3 et principalement 4.
- Le développement du dispositif expérimental SIL et la quantification des performances de chaque sous-système sont expliqués au chapitre 5.
- L'identification des performances des actionneurs est détaillée en chapitre 6.
- La réalisation et l'analyse d'essais en bassin pour définir l'influence et l'importance relative de la modélisation du rotor sur la réponse de l'éolienne. Egalement, des comparaisons entre des simulations numériques et les essais en bassin renseignent sur la validité des hypothèses pour la modélisation numérique ainsi que sur la qualité des essais. Ces analyses sont présentées dans les chapitres 7 et 8.

Un résumé des principaux questionnements actuels sur ces différents sujets et des différentes contributions dans ce travail est présenté ci-dessous :

Efforts agissant sur le rotor à reproduire lors d'essais en bassin

Les questionnements concernant ces efforts sont multiples. D'une part, on s'intéresse à ce que leur représentation peut apporter à des essais en bassin :

- Pourquoi est-ce important de représenter les efforts agissant sur le rotor lors d'essais en bassin d'éoliennes flottantes ?
- Quels sont les mécanismes qui peuvent expliquer un couplage avec la réponse de l'éolienne ?

Ensuite, pour le dimensionnement du système d'actionneurs de la méthode hybride, il convient de :

- définir précisément quels sont les efforts à reproduire,
- les caractériser finement, en termes de distribution fréquentielle, de valeurs extrêmes et moyennes,
- quantifier en quoi une reproduction partielle des efforts (bande passante, composantes limitées du torseur d'efforts) des actionneurs influencent la réponse des éoliennes.

Dans ce travail, une revue de littérature est réalisée pour chacune de ces questions, pour étudier comment ces problématiques ont déjà été abordées à travers des travaux numériques et des essais en bassin. D'autre part, différentes études numériques ont été réalisées pour répondre à ces questions. Cela inclut notamment une étude numérique paramétrique réalisée sur un grand nombre de cas de chargements et plusieurs types d'éoliennes flottantes. Le cadriciel OpenFAST permettant la modélisation entièrement couplée (aérodynamique, hydrodynamique, ancrage, contrôle, structure) d'une éolienne flottante a été utilisé et modifié pour les objectifs de l'étude.

Les principales contributions par rapport à l'état de l'art sont :

- Quantification dans le domaine fréquentiel des efforts agissant sur les éoliennes flottantes ;

- Application à un grand nombre de cas de chargements définis à partir de conditions de sites et suivant une méthodologie de pré-sélection des cas dimensionnants ;
- Quantification d'une reproduction limitée des efforts, et impacts sur les mouvements de l'éolienne.
- Définition d'un jeu d'indicateurs pour les spécifications des bandes passantes et des retards admissibles du système SIL.

Mise en place d'un système SIL

Ensuite, la mise en place d'un système SIL est détaillée. Les questionnements concernant le choix et l'implémentation des différents sous-systèmes d'un système SIL sont multiples. Les trois principaux sous-systèmes sont :

1. L'outil numérique pour calculer les efforts à représenter agissant sur le rotor,
2. L'environnement temps réel incluant la chaîne de mesure et le système embarqué sur la maquette,
3. Le système de reproduction des efforts, i.e. les actionneurs.

Les questionnements et contributions sont détaillés pour ces trois sous-systèmes :

1. Quel type de modèle aérodynamique est approprié pour réaliser des calculs temps réel ? Quelles différences entre types de modèles sur les caractéristiques de l'effort reproduit ?
2. Quelle architecture pour l'environnement temps réel ?
3. Quels actionneurs sont adaptés et comment les caractériser ? Quelle stratégie d'allocation de la force pour les actionneurs ?

Pour répondre à ces questionnements différents sujets sont abordés.

Tout d'abord, les différentes possibilités pour l'outil numérique sont identifiées. Les impacts sur la représentation des différentes composantes de l'effort agissant sur le rotor (amortissement, excitation …) sont développés via des simulations numériques et des développements analytiques. Pour le développement du système, l'outil numérique existant OpenFAST (NREL, n.d.) implémentant une modélisation Blade Element Momentum Theory (BEMT) est modifié pour pouvoir imposer les mouvements de l'éolienne flottante, mesurés en temps réel dans le bassin.

Ensuite, l'architecture d'un système hybride est introduite. Les différentes options concernant leur mise en pratique sont développées ainsi que la pertinence et la complexité de plusieurs développements possibles (observateur des mouvements, observateur des efforts, …).

Sur cette mise en place du dispositif expérimental, les contributions originales de ce travail concernent principalement les actionneurs. Des actionneurs de types propulseurs à hélices sont sélectionnés. Les principales caractéristiques de ces actionneurs sont présentées ainsi que les stratégies d'allocation de la force pour représenter le plus fidèlement l'effort du rotor.

Un système SIL a été développé et validé par itérations successives au cours de ces travaux. Les objectifs et contributions des différentes campagnes d'essais réalisées sont présentés.

Caractérisation des performances d'un système SIL

La caractérisation des performances de la méthode est au cœur de ce travail. Les questionnements correspondants sont :

- Quelles méthodologies sont adaptées à l'évaluation de ces performances ? Quels sont les indicateurs clefs ?

- Comment calibrer et contrôler les actionneurs pour reproduire au mieux les efforts cibles ?

Ces méthodologies ont été appliquées à différents types d'actionneurs (turbine carénée, propulseur bipales, dispositif multi-actionneurs) et à différentes configurations (banc d'essai, essais en bassin).

La contribution originale concernant l'identification avancée du comportement de ces actionneurs est l'apport de la dynamique inverse pour leurs performances. Des indicateurs basés sur des analyses temporelles et fréquentiels (fonctions de transfert) ont été formalisés et appliqués avec succès aux différents actionneurs. La méthodologie a été principalement développée pour un unique actionneur reproduisant un seule composante du torseur d'effort à reproduire (F_x). Son extension à trois actionneurs et trois composantes du torseur n'a pas posé de problèmes et est très encourageant pour un passage à un système reproduisant le torseur complet.

Sensibilité du comportement des éoliennes à la représentation des efforts du rotor

Les différents questionnements au cours de ces travaux sont traités par des essais en basin à l'échelle 1/40 d'une éolienne flottante de 10MW, dimensionnée spécialement pour ces essais.

Des essais comparatifs permettent de quantifier les impacts des différentes briques du système SIL (outil numérique, performance des actionneurs) sur le comportement de l'éolienne. De même, l'impact de différentes lois de contrôle est exploré au cours de ces essais. Ces comparaisons réalisées au cours d'essais en bassin fournissent de précieuses informations pour le développement ultérieur du dispositif.

Comparaisons entre simulations numériques et essais expérimentaux

Pour conclure ces travaux, un modèle numérique complètement couplé (aérodynamique, hydrodynamique, ancrage, contrôle, structure) est défini à partir des propriétés de l'éolienne flottante dans le bassin. La méthodologie de définition et de validation du modèle est détaillée, ainsi que différentes comparaisons entre essais et simulations numériques.

Les questionnements correspondants sont :

- Quelles sont les stratégies de modélisation numérique adaptées ?
- Comment caler au mieux les paramètres empiriques du modèle hydrodynamique ?
- Quelles sont les différences entre les simulations numériques et les résultats expérimentaux ?
- Quel est l'effet, sur ce dispositif, d'avoir uniquement l'effort du rotor F_x qui est reproduit au lieu du torseur complet ?
- Peut-on confirmer les observations faites lors des essais concernant l'impact des performances des actionneurs sur le comportement de l'éolienne ?

Toutes ces problématiques sont abordées par des états de l'art et des comparaisons entre simulations numériques et données expérimentales. L'influence du comportement des actionneurs a pu être correctement reproduite, confirmant ainsi la pertinence du modèle d'actionneur identifié.

Abstract

Floating wind turbines make possible the use of a vast energy resource in the ocean. However, they are subject to many sources of excitations from their environment, including the waves, the wind, the current, etc…. The numerical modeling of a floating wind turbine with "state-of-the-art" offshore codes still deserves inputs and validation both from high-fidelity numerical models and experiments. Wave tank testing allows testing the hydrodynamic loads and the wave-induced response of a floating structure at a small scale. The goal of the present work is the development and validation of an experimental test bench dedicated to the wave tank testing of floating wind turbines. A hybrid "software-in-the-loop" (SIL) system has been developed for this purpose.

The topics and outcomes of this work cover:

- SIL system requirements based on rotor loads. These requirements are based on a parametrical numerical study for the load specifications and to anticipate the effects of a limited actuation effects on FWT motions.
- Development of the SIL system:
    - Numerical model selection and comparison on the load characteristics (damping, etc…) with simplified models,
    - Actuation system design. This includes the selection and modeling of a single actuator and the force allocation procedure for a multi-actuator system.
    - Real-time environment definition to integrate the numerical model, control the actuators and master the data acquisition,
- Definition of methodologies for the characterization and the identification of the SIL system performance.
- Wave tank testing of FWT:
    - focus on the rotor loads sensitivity,
    - comparison between aero-hydro-servo-elastic simulations and experimental data.

Keywords: Floating Wind Turbines, numerical simulation, experimental modeling, system identification

Acknowledgments

To start, let me thank the reviewers of this manuscript, Olivier Kimmoun and Erin Bachynski. I would like to thank them for their constructive reviews and comments on the manuscript. Thank you Erin for your numerous comments and your detailed review of this manuscript. For most of the topics covered in this word, there was a paper where you have been involved. Many perspectives, conclusions ... of your work constitute the starting point and the guiding principle of this work. Merci Olivier pour avoir accepté de relire ce manuscrit, même si une partie des travaux n'était pas exactement dans tes thématiques de prédilection. J'ai bien conscience d'avoir été « pistonné » par Maïté au détour d'un sentier du Queyras en Août 2020 ! Tes commentaires m'ont permis de chercher à mieux comprendre et expliquer certaines des investigations que nous avions pu faire pour ce manuscrit.

J'aimerais remercier Franck Plestan, à la fois pour avoir présidée cette soutenance de thèse, mais également pour son implication dans le projet SOFTWIND et ses conseils au cours du projet. Thanks to Marco Belloli for its participation to the PhD defense, with its sharp eye on the topic from its experience with real-time hybrid wind tunnel testing of FOWT at Polimi. Merci à Alan Tassin, pour les discussions lors de la soutenance mais aussi, avec Grégory Germain, pour leur accompagnement au cours de ces 3 ans et qui m'ont bien motivé pour finir la thèse. Merci également à Sofien Kerkeni, pour sa participation au Jury et surtout pour les nombreuses implications de D-ICE Engineering dans le projet.

Un très grand merci à Sandrine, Jean-Christophe et Félicien pour leur encadrement, à la fois humain et technique. Merci à tous les 3 pour la confiance, vos disponibilités, votre grande écoute, même les moments où je commençais à en avoir « ras la casquette » face à mon inquiétude de trouver un poste par la suite. Merci Sandrine d'avoir bien voulu encadrer ma thèse, juste après ton arrivée au LHEEA, même si une partie de ce travail ne s'inscrivait pas totalement dans tes thématiques d'expertise. Tu as pris beaucoup de temps pour me transmettre la rigueur scientifique, et tu t'es fortement impliquée dans ce travail pour en faire sortir de la science. Tu m'as fait maintenir le cap, en maintenant un état d'esprit positif ! Merci à Jean-Christophe pour m'avoir accompagné lors de ces 3 ans, d'avoir rendu ce projet SOFTWIND possible qui m'a permis de travailler sur plusieurs thématiques de recherche en éolien flottant, de son encadrement technique et humain sans failles, avec ta porte ouverte pour discuter, avec entrain, de telle ou telle possibilité de modélisation, ... Un immense merci à Félicien, qui s'est très fortement impliqué dans ce travail, avec la spécification, le développement, le débogage du cœur « temps-réel » de l'outil SOFTWIND mais aussi la construction de la SPAR, la définition d'une méthodologie pour ce processus de validation étape par étape de l'outil.... J'ai beaucoup apprécié travailler au bassin avec toi, avec ta dynamique et ta grande pédagogie. Tu travaillais trop pour que je puisse siffloter tranquillement sans remords !! Merci également pour m'avoir permis de faire de l'enseignement sur des thématiques qui m'intéressaient.

Cette thèse a été financée par le West Atlantic Marine Energy Community (WeAMEC) et la région Pays de la Loire, dans le cadre du projet SOFTWIND. Je tiens à remercier toutes les personnes impliquées dans le projet, notamment pour la partie expérimentale. La super équipe du bassin (Anne, Stéphane, Laurent, Mathieu, Bruno, Jérémy et Jérémy), qui avait plaisir à fortement contribuer pour ce projet EMR au bassin, sans qui les essais n'auraient pas été possibles. Natalia et Benjamin de D-ICE, avec qui nous avons passé un grand nombre d'heures au bord du bassin lors des essais, toujours dans la bonne humeur !

Je veux remercier tous les amis et collègues que j'ai pu rencontrer durant ces trois ans de thèse et ces 5 années au LHEEA. Merci à Aurélien Babarit, Thomas Soulard et Christian Berhault pour les

projets avant la thèse, qui m'ont permis de découvrir l'environnement LHEEA et l'éolien flottant en tant que thématique de recherche. Je remercie la première équipe de jeunes chercheurs qui m'ont généreusement accueilli : Marie et Marie, Camille, Francesc, Boris, Maïté, Hélène, Paulo, Catherine… : super content que l'on continue à se voir ! Merci à ceux qui sont arrivés au fur et à mesure, et avec qui j'ai passé aussi de très bons moments : SLucas, Mister Leroy, Louis, Laëtitia, la super « team tup' » (Marco, Nicolas, Marion, Catherine, Ramona, Paul, Gaël, Gaspard, …). Un grand merci également à Anne, Sonia et Elodie (et Blandine sur la fin) mais aussi Adrien et Vincent, pour leur aide précieuse au cours de ces 5 ans au laboratoire.

Je remercie chaleureusement Valentin Chabaud ainsi que Matthew Hall de m'avoir partagé leurs manuscrits de thèses portant sur le même sujet. Un précieux temps a été épargné et les développements guidés par ces premiers retours d'expérience.

Un grand merci à Maïté, sans qui j'aurais probablement arrêté la thèse en cours, pour son soutien, ses conseils et sa grande aide ☺.

Abbreviations

3P	Rotor frequency at which a blade is passing in front of the tower
BEMT	Blade Element Momentum theory
CFD	Computational Fluid Dynamics
CM	Center of Mass
CoB	Center of Buoyancy
DLC	Design Load Case
DoF	Degree of Freedom
ECN	Ecole Centrale de Nantes. The host institute for this work.
ESC	Electronic Speed Controller
FWT	Floating Wind turbine. It includes the floating platform, the wind turbine and all of its components.
GDW	Generalized Dynamic Wake
HAWT	Horizontal Axis Wind Turbine
HDB	Hydrodynamic database. It includes diffraction-radiation coefficients from a potential flow solver.
LF	Low frequency, typically frequencies below the wave frequency range
LHEEA	Laboratoire of Hydrodynamics ; Energetics and Environmental Atmospherics. The academic institution of the author.
MOCAP	Motion Capture system. It consists, in the scope of this PhD thesis, of the different cameras and associated software to capture and process the positions of different markers on the floating wind turbine.
MSL	Mean Sea Level
NF	Natural Frequency of a given mode.
O&G	Oil and Gas
PWM	Pulse Width Modulation
RAO	Response Amplitude Operators.
RNA	Rotor Nacelle Assembly. It includes the different blades and the Hub (= the Rotor) and the Nacelle.
SIL	« Software–in-the-loop » : defines the method we are talking about. It could also be called "Hardware-in-the-loop" ***(HIL),*** Hybrid model testing depending on the application, the point of view and the scientific domain.
SPAR	Single Point Anchor Reservoir. It concerns floating foundations with ballast as the main stabilizing source.
TF	Transfer function. It defines the relation, in the Laplace domain, between an input and an output. A transfer function is characterized by its phase and gain.
TLP	Tension Leg Platform
WF	Wave frequency, the frequencies at which the waves provide most of their energy.

Notations

H_s	Significant wave height [m]
T_p	Peak period [s]
U_w	The incident wind speed [m/s]
X_i	The platform motions. The ordering is 1, 2, 3, 4, 5, 6 for surge, sway, heave, roll, pitch yaw. It is also denoted X, Y, Z, R_X, R_Y and R_Z

Conventions

The important conventions used in this work follow the typical conventions applied both to the hydrodynamics and a wind turbine modeling.

Frames

Different frames are used to express the loads acting on the floating wind turbine or the motions of the platform and tower. Similarly to the conventions used in (Chabaud, 2016, Chapter A), they follow the conventions in both the wind energy and hydrodynamic fields:

- Inertial frame (denoted R_I): x horizontal, directed downwind, z vertical upward and y horizontal, giving a right-hand coordinate system. The inertial frame is earth-fixed. The vertical position of the origin corresponds to the Mean Sea Level (MSL). The horizontal position of the origin is the FWT floater vertical centerline. The platform 6 DoF are defined in the inertial frame.
- Gravity frame (denoted R_{CoG}): Similar to the inertial frame but centered on the center of gravity of the FWT.
- Hub frame (denoted R_{hub}): body-fixed (moves with the FWT, does not rotate with the rotor), origin at the hub center (also called rotor APEX). X is aligned with the shaft (following the rotor tilt angle), directed downwind, z is directed upward and y gives a right-hand coordinate system. Note that in the reference numerical model FAST used in this work, the hub frame rotates with the rotor.
- Tower top frame (denoted R_{twrtop}): similar to the Hub frame but x is aligned with the inertial x-axis when the tower is undeflected. Origin at the tower top centerline.

They are depicted in Figure 1.

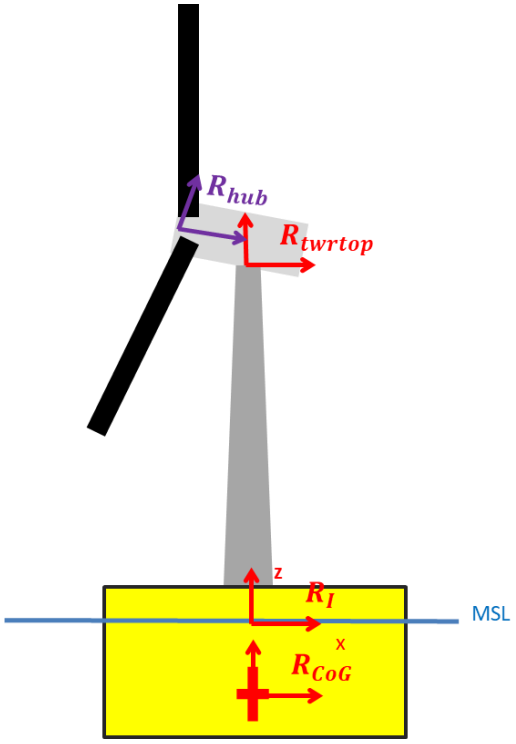

Figure 1: Reference frames

Load case description

In this work, the different notations are used when dealing with a given load case:

- The incident wave field is characterized by H_s, T_p, γ and θ_{wave} , which are respectively the significant wave height, peak period, peak enhancement factor and incident wave direction of a JONSWAP spectrum. By convention, when not specified, $\theta_{wave} = 0°$ and $\gamma = 3.3$
- The incident wind field is characterized by U_w, T_I and $\alpha_{vert\,shear}$, θ_{wind} which are respectively the mean wind speed, the turbulence intensity, the vertical shear power law coefficient and the incident wind direction of a Kaimal spectrum. The coherence model is the one implemented in the TurbSim code (Jonkman, 2009), as specified in IEC standards. By convention, when not specified, $\theta_{wind} = 0°$ and $\alpha_{vert\,shear} = 0.0$

Contents

List of Figures

List of Tables

1 Introduction

Contents

Over the last three decades, moving offshore for harnessing wind energy has become a reality (WindEurope, 2019). Since the first bottom-fixed offshore wind turbine in the Baltic Sea, in 1991 in Denmark, many technological steps have been overcome to enable a significant wind energy extraction offshore. The installed capacity of offshore wind turbines has reached 22 GW for Europe-only in 2019 (WindEurope, 2019), and long-term scenarii envisage a contribution of the wind energy to the total energy mix of up to 1/3 in 2050 (Veers *et al.*, 2019). Floating wind turbine (FWT) technologies unlock the vast wind energy resource far from the coast, where the mean wind speed is higher, the turbulence intensity lower, and where the water depth exceeds the techno-economic limit of bottom-fixed foundations (Joao Cruz, 2016). Several recent projects of full scale prototypes have been successfully commissioned, including the first pilot wind farm (5*6MW) *Hywind Scotland* in summer 2017, the first French offshore wind turbine *FLOATGEN* (*2MW*) in autumn 2018, and *Windfloat Atlantic* pilot wind farm (3*8.4MW) in summer 2020. *FLOATGEN* and *Hywind Scotland* are depicted in Figure 2.

© Statoil/Øyvind Gravås/Woldcam

© Centrale Nantes

Figure 2: Hywind Scotland pilot wind farm (left) and FLOATGEN prototype (right)

1.1 Floating wind turbine design

The wind turbine technology seems to converge, especially for bottom-fixed offshore wind turbines, to 3-bladed upwind horizontal axis wind turbines. However the foundation selection, bottom-fixed or floating, heavily depends on the site conditions. As for Oil and Gas (O&G) platforms' design, each project is unique and requires adapting the platform, the mooring system and many other components to the site conditions. Those re-designs, together with the different environmental conditions, change the FWT behavior. Initial modeling assumptions do not necessarily suit the updated system in its new environment. Different additional reasons could also explain why there are still uncertainties about the

validity of typical modeling assumptions. Without being exhaustive, the following remarks introduce floating wind turbine complexity:

- There are only a few full scale prototypes at sea. Forthcoming wind turbines for floating foundations are expected to be 2 to 3 times bigger than the actual commissioned ones for onshore or offshore bottom-fixed wind turbines. Consequently, the feedbacks from commissioned projects do not necessarily apply to the larger wind turbines;
- The wind and wave conditions could be very harsh, in moderate water depth, with possible strong tidal and wind-induced currents;
- The dimensions and characteristics of the platforms violate typical assumptions concerning the hydrodynamics (e.g between the "small body" and "large body" assumptions), the structural or the mooring modeling;
- Innovative and hybrid concepts – e.g. multi-purpose platforms combining wind turbines and wave energy converters (Pérez-Collazo, Greaves and Iglesias, 2015) as well as other ocean resource uses (Lagasco *et al.*, 2019) -, still at low TRL, are emerging. Their behaviors are expected to differ from the existing concepts.

In the engineering design process of offshore wind turbines, the design certification is quite often the final step. As floating wind turbine maturity is increasing and the number of planned projects is growing, dedicated design practices and guidelines have recently been published (Borisade *et al.*, 2017). Those design guidelines are being continuously updated based on the wind energy community findings but are founded on the feedbacks from Oil & Gas sector (O&G) and offshore bottom-fixed wind turbines industries. Despite continuous progresses of computational resources, using coupled "high-fidelity" methods to represent the multi-physics problem is still computationally too expensive to check that a given FWT design passes through the thousands of design load cases (DLC) imposed by the standards. Consequently, the state-of-the-art numerical tools used by the developers (Robertson *et al.*, 2014) are based on strong assumptions and empirical corrections which need to be evaluated and calibrated by experimental testing at different scales as a project progresses. In the aforementioned guidelines, model testing is a recommended step in the development of a technology to be sure that all important phenomena and associated modeling assumptions have been correctly considered (DNV GL, 2016, 2017).

1.2 Model testing of floating wind turbines

Model testing offers the possibility to evaluate the response of the considered platform in a controlled but representative environment while monitoring many physical quantities of interest. However, evaluation of the fidelity, the uncertainties and the bias is always a concern for the experimenter. The dominating physical phenomena of interest should be evaluated to check if the loads and properties of the setup are correctly scaled.

Due to the complexity of both the unsteady hydrodynamics of moored platforms and the unsteady aerodynamics acting on a wind turbine, separate physical modeling of the floating foundation on one side and the wind turbine on the other side is already a hard task. For the aerodynamics of wind turbines, wind tunnel testing has been used extensively to validate and calibrate "low-fidelity" or "medium-fidelity" numerical models (Schepers, 2012). For the hydrodynamics of floating foundations, wave tank testing has also been extensively used to validate the numerical modeling assumptions for different floater designs in different sea states (e.g. (Faltinsen, 1993)).

Wave tank testing allows to test at a small scale (1:150 to 1:10) the hydrodynamic loads and the wave-induced response of a floating structure. It has been used for decades for O&G platforms. By

controlling and measuring the incident wave field, it is then possible to compare experimental results with numerical results. The ECN wave tank, extensively used in the present work, is illustrated in Figure 3. The importance of some nonlinear loadings (for instance nonlinear slowly varying force, dynamic loads in the moorings lines) had been highlighted thanks to those experimental test campaigns and allowed to reduce the safety factors in the design process.

Figure 3: ECN Ocean Engineering wave tank

Wind tunnel testing allows to test the aerodynamic loads and induced response due to a wind field on a wind turbine structure (i.e. aeroelasticity) at a small scale (1:200 to 1:20).

A floating wind turbine is a "fully-coupled" system, i.e. the floater and the wind turbine influence each other, leading to possible instabilities in the motions of the system or deteriorated energy production. Ideally, the model testing of a floating wind turbine should include both wind and wave reproduction. In a wave tank model testing perspective, the influence of the rotor on the whole structure needs to be represented as closely as possible. However, this requires tackling several challenges:

- The physical phenomena and the forces due to wind and waves are not governed by the same similarity laws. The hydrodynamic phenomena are primarily governed by the Froude number whereas the aerodynamic phenomena are governed by the Reynolds number. This incompatibility requires modeling compromises that often limit the representation fidelity of an operating floating wind turbine (Martin *et al.*, 2012).
- The increasing size of the wind turbines rotors (e.g. 220m for the recent prototypes Haliade-X 12MW and SG 14-222 DD) constrains the scale choice of the tests. The trade-off between a limited scale ratio and an admissible size of the model scale rotor become difficult to combine.
- The wind turbine controller effect needs to be properly modeled. Indeed, floating-specific control strategies are mandatory to avoid possible instabilities and to provide high quality electricity generation (Larsen and Hanson, 2007; Jonkman, 2008).

1.3 Hybrid model testing

Hybrid modeling approaches as developed in different experimental facilities (Azcona *et al.*, 2014; Chabaud, 2016; Hall, 2016; Sauder *et al.*, 2016; Battistella *et al.*, 2018; Bayati *et al.*, 2018; Meseguer and Guanche, 2019) make it possible to significantly improve the quality of the results by avoiding any inconsistency regarding the representation of the aerodynamic forces while keeping a faithful

representation of the hydrodynamic forces. For wave tank testing purpose, the usual approach consists of physically modeling the floating substructure by respecting Froude scaling, while the rotor is modeled with a set of actuators that communicates in real time with an aerodynamic solver. Considering to the measured floater motions, this aerodynamic solver computes, at full scale, the aerodynamic forces and moments to be reproduced. This hybrid methodology, while being used for civil engineering problem for decades (Chabaud, 2016), has recently been applied for floating wind turbine. In a complementary approach, hybrid wind tunnel testing is also under development in different experimental facilities (e.g. (Bayati *et al.*, 2018)).

In terms of terminology, this hybrid model testing methodology could also be called "Software-in-the-loop" (SIL), "Hardware-in-the-loop" (HIL), "Real-time hybrid model testing" depending on the point on view. As our goal is to integrate a numerical tool in experimentations, this methodology will be called *SIL* in this present work.

1.4 Outline and scope of this thesis

This PhD work is part of the SOFTWIND project, funded by the WEst Atlantic Marine Energy Community (WEAMEC) and the Region Pays de la Loire, that aims at developing an innovative experimental test bench dedicated to the wave tank testing of floating wind turbines. The interest in hybrid approaches was motivated by several reasons including (i) the encouraging preliminary results of other research institutes on the topics and (ii) the need to have a test bench dedicated to the ECN wave tank that enables the testing of rotor control laws specifically developed for floating wind turbines. The development of such hybrid systems is however not trivial. (Chabaud, 2016; Hall, 2016; Sauder *et al.*, 2016; Meseguer and Guanche, 2019) demonstrated how challenging the design of the overall SIL system - actuators, sensors, observers and real-time numerical code - is.

The scope of this thesis is about the design of a SIL system and the creation of a dedicated validation methodology to evaluate its performances. This PhD thesis covers the following topics:

- Theoretical background for the development of such a hybrid system. This concerns the main physical phenomena of interest and the load analysis. It is detailed in chapter 2 and 3.
- Design of an actuation system, the central element of SIL methods, explained in part 3 and 4.
- Definition of the validation methodology for a wave tank SIL setup, explained in chapter 5.
- Identification of the actuation system performance is detailed in chapter 6.
- Floating wind turbine experiments and analysis of different wind turbine modeling approaches. This is explained in chapters 7 and 8.

The corresponding topics and questions, chapter per chapter, are detailed in Table 1.

Thesis plan	**Main topics covered and corresponding questions**
Chapter 2	This chapter introduces the related work and identifies the main barriers for the SIL methodology. The main corresponding questions are: • Why is it important to represent the rotor loads during wave tank testing of FWT? What are the coupling mechanisms between the aerodynamic loads and the FWT response? • What has been done so far concerning the rotor loads methodologies in wave tank testing? • How does the hybrid "Software-in-the-loop" methodology work and what are its key components? • What are the main identified barriers for this SIL methodology?

Chapter 3	This chapter covers one of the design objective of the SIL system: the specification of the loads to be reproduced by the actuation system. The main corresponding questions are: • What are those loads? Purely aerodynamics? • What are the detailed specifications? Min, max, and frequency distribution. • What are the effects of a partial reproduction of those loads?
Chapter 4	This chapter presents the different subsystems of a SIL system. This includes the appropriated numerical tool, the real-time environment and the actuation system. The main corresponding questions are: • What kind of numerical model is appropriated for real-time computation? • What is the architecture of the hardware/software? • What kinds of actuators are suitable? How to characterize them? • What is the force allocation procedure to control the actuators from the setpoint load tensor? • How to define a suitable actuators layout?
Chapter 5	This chapter presents the main test campaigns conducted for the validation of the different SIL subsystems. Each setup together with the characterization and identifications performed are described. The main corresponding questions are: • Before running a test campaign in the wave tank, what kind of setups facilitate the understanding and the characterization of the SIL system performances? • What are the characteristics of the platform testing in the wave tank? How to design the FWT and characterize the as-build models?
Chapter 6	This chapter focuses on the most important part of the evaluation of a SIL system: the identification of the actuation system performances. The main corresponding questions are: • Which methodologies have been developed to properly evaluate those performances? What are the key performance indicators? • How to properly calibrate the actuators to get the most accurate generated loads? This methodology is applied to the different actuators (ducted fan, two-bladed aircraft propellers) and setups which have been used in this work. The original contributions are about the dynamic calibration and the advanced identification for those kinds of actuators.
Chapter 7	This chapter focuses on the main wave tank test campaign, looking at the coupling between the aerodynamics and the FWT response. To provide guidelines to the community, the main corresponding question is: What are the impacts of different numerical models, actuators performances and wind turbine controllers on FWT response?
Chapter 8	This chapter deals with the comparison between the test campaign results and state-of-the-art aero-hydro-servo-elastic numerical simulations. The main corresponding questions are: • What are the suitable numerical modeling strategies? • What are the SIL system limitations?

Table 1: Thesis plan and topics covered

The hybrid model testing of FWT addresses several disciplines and requires a good understanding of many topics, both from numerical and experimental sides. Many contributions from the scientific community about existing methodologies or numerical models have been extensively used in the present work. Due to the large scope of involved topics, the existing scientific background is disseminated in the

different chapters. The associated theories are not detailed but the key elements are extracted. The curious reader is invited to look deeper in the given references for additional details.

2 Rotor loads modeling needs for wave tank testing of FWT

Contents

In this chapter, the relevant background about rotor loads modeling for wave tank testing of floating wind turbine is presented. The main underlying issues are:

- Why is it important to represent the rotor loads during wave tank testing of FWT? What are the coupling mechanisms between the aerodynamic loads and the FWT response?
- What has been done so far concerning the rotor loads methodologies in wave tank testing?
- How does the hybrid "Software-in-the-loop" methodology work and what are its key components?
- What are the main identified barriers for this SIL methodology?

The importance of rotor loads on the floating wind turbine responses is first introduced, with the specificities of the different kinds of floating wind turbines. Then, the methodologies that have already been developed to reproduce rotor loads are detailed with their advantages and drawbacks.

2.1 Coupled aero-hydro FWT Physics

Before starting the development of a rotor loads modeling system, it is important to explain how reproducing rotor loads impacts the behavior of a FWT. A load analysis is first performed in part 2.1.2 to emphasize the coupling mechanisms between the rotor loads and the FWT response. Then in part 2.1.3, the coupled physical phenomena that have been observed during wave tank testing campaigns are presented. Those different effects are analyzed in terms of frequencies of interest and are also illustrated with a aero-hydro-servo-elastic simulation of one FWT submitted to irregular waves and turbulent wind.

2.1.1 Floating wind turbines under consideration

In this part, some information about the targeted floating wind turbines are provided. These inputs are important to anticipate the behavior specificities of each type of FWT. A floating wind turbine is composed of different elements. The convention used in this work respects the following breakdown, depicted on the Figure 4:

- The wind turbine:
  - Rotor (hub and blades) (A),
  - Nacelle (B). Together with the rotor, it constitutes the Rotor-Nacelle Assembly (RNA)
  - Tower (C).
- The substructure:
  - Transition piece between the floater and the tower (D)
  - Floater (Hull and Ballast) (E)
- The mooring system:
  - Fairleads (F)
  - Mooring lines (G)
  - Anchors
- Other appendices, such as the dynamic power cable (H)

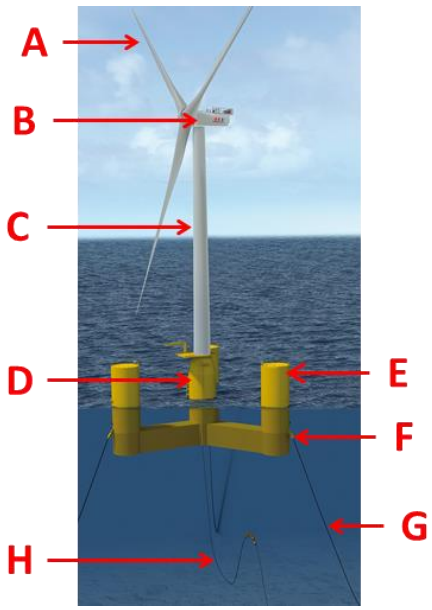

© Naval Energies

Figure 4: Floating wind turbine breakdown

2.1.1.1 Targeted wind turbines properties

Different reference wind turbines (RWT) have been widely used in the literature for offshore wind turbines: the NREL-5MW, published in 2009 (Jonkman *et al.*, 2009), and the DTU-10MW, published in 2013 (Bak *et al.*, 2013). The role of those RWT is to provide ready-to-use open source numerical models to the R&D FWT community, for different kind of studies. It has to be noticed that many other RWT for offshore sites have been published – for instance the LeanWind 8MW(Desmond *et al.*, 2016), the 10 MW one developed in the EU project AVATAR (Sieros, 2017), and the 2 developed in the IEA Wind Task 37, IEA-10-198 (Bortolotti *et al.*, 2019) and IEA-15-240. Some differences - even for the same rated power - in terms of loadings might arise from the different rated wind speed, airfoils characteristics etc…. Consequently, the relative contributions of aerodynamic, inertial and gravitational loads could be slightly different for two wind turbines having the same rated power. However, it has been noticed that orders of magnitude are similar. A short summary of the RWT main characteristics is given in Table 2, inspired from (Bak *et al.*, 2013; Desmond *et al.*, 2016).

Parameter	**NREL 5MW**	**DTU 10MW**	**IEA-10-198**	**IEA-15-240**
Rated power [MW]	5	10	10	15
Rotor Diameter [m]	126	178.3	198	240
Hub height above sea level [m]	90	119	119	150
Shaft tilt angle [deg]	5	5	6	6
Rotor precone angle [deg]	-2.5	-2.5	-4	-4
Rotor Mass [kg]	1.10E+05	2.28E+05	2.25E+05	3.86E+05
[Cut-in, rated, cut-out] wind speed [m/s]	[3, 11.4, 25]	[4 , 11.4, 25]	[3,11,25]	[3, 10.9, 25]
[Minimum - Maximum] rotor speed [rpm]	[6.9 - 12.1]	[6.0 -9.6]	[6.0 - 8.68]	[5.0 - 7.56]
1P frequency range [Hz]	[0,12 - 0,2]	[0,1 - 0,16]	[0,1 - 0,14]	[0,08 - 0,13]
3P frequency range [Hz]	[0,35 - 0,61]	[0,3 - 0,48]	[0,3 - 0,4]	[0,25 - 0,38]

Table 2: Key parameters for the selected reference wind turbines

From the mass parameters in Table 2, a direct upscaling between wind turbines with different rated powers does not seem appropriate. The consequence is that, when possible, sensitivity studies should be conducted on several wind turbines with different rated powers. In the different studies that will be presented along this thesis, two of the RWT have been selected (the NREL 5MW and the DTU 10MW) to give some reference values for their rated power. The reason is that open source models of the wind turbines and of the different associated floaters were available at the beginning of this work. However, those two reference wind turbines have close features; consequently, a similar behavior is expected.

2.1.1.2 Floating foundations

A short presentation of the floaters that are intended to be used with the SIL system is given hereafter. The main goal of the floating foundation with its mooring system is to counterbalance the rotor loads (stability) and to limit the motions of the floater (excursions or offsets). In the perspective of a SIL system development, the interest is the sensitivity of each type of floating foundations to the rotor loads and vice versa.

The floaters are usually classified depending on the main stability mechanism. This classification, while initially defined for O&G platforms, is also applied for the floating foundations of FWTs. The main floater categories are (Joao Cruz, 2016):

- Ballast-stabilized floaters: SPAR (Single Point Anchor Reservoir).
- Waterplane buoyancy stabilized floaters: Semi-submersible, barge.
- Stabilization with the mooring lines: TLP (Tension-Leg-Platform).

The different solutions are depicted in Figure 5.

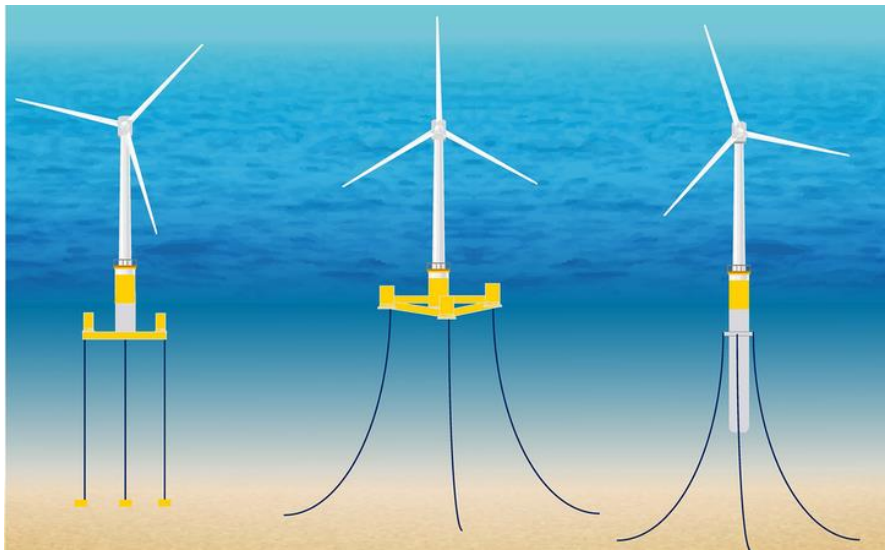

© *Carbon Trust*

Figure 5: Artistic view of different floating foundations
Left: TLP ; middle: semi-submersible; right: SPAR

The moorings system has also a strong influence on the behavior of the floating wind turbine. The main categories of mooring systems, depending on the restoring forces mechanism, are (Faltinsen, 1993):

- Catenary mooring systems, made of chain or wire rope (the main restoring mechanism comes from the weight of the mooring line in the water column).
- Taut leg mooring systems, made of elastic materials such as synthetic materials or steel cables (most of the restoring forces are created by the elasticity of the mooring lines).
- Pretensioned tendons (Bachynski, 2014), for TLP foundations.

The design of such floaters and moorings follows different rules (Faltinsen, 1993; Molin, 2002). The floating wind turbine natural periods are one of the important criteria to avoid failure and large excursions, at a frequency at which there is significant energy in the excitation loads. Some natural frequencies of the 6 DoF of the platform are floater-driven while others are moorings-driven. This is due to the main stiffness mechanism (hydrostatic stiffness contribution compared to the mooring stiffness contribution). Excepted for the TLPs, the natural frequencies of the vertical motions (Z, R_X, R_Y respectively the Heave, Roll and Pitch motions) are floaters-driven while those of horizontal motions (X, Y, R_Z respectively the Surge, Sway and Yaw motions) are moorings-driven. The TLP concepts have very high natural frequencies for vertical motions. Thus, they are impacted by different hydrodynamic and aerodynamic loads (Bachynski, 2014) and could exhibit large structural responses (Gueydon and Jonkman, 2016).

To conclude, the specificities of each floater and mooring systems impact the highest frequencies of interest and also influence the contributions of the different sources of external loadings. Those loadings are explained in the next subsection.

2.1.2 FWT loads and response : background

In this section, a load analysis explores the coupling mechanisms between the rotor loads and the response of a FWT.

A floating wind turbine is a multi-physic mechanical system subjected to different kinds of external loadings. The scope of this load analysis is based on an operating floating wind turbine subjected to any kind of wind fields (in terms of turbulence, wind shear, yaw misalignment, …), and waves. The blades and the tower are flexible, the blade pitch and generator speed controller active. The different loads are (Molin, 2002; Burton *et al.*, 2011):

- Loads acting on the substructure:
  - Gravity and buoyancy loads,
  - Inertia loads,
  - Aerodynamic loads for floaters that have an important emerged part ,
  - Hydrodynamic loads due to waves and current:
    - From potential flow related phenomena (radiation, diffraction, Froude-Krylov)
    - From viscous flow related phenomena (drag)
  - Other environmental loads (Ice loads, …)
- Loads acting on the wind turbine:
  - Aerodynamic loads due to the incident wind field,
  - Inertia loads (centrifugal, gyroscopic, braking),
  - Gravity loads,
  - Controller action on the shaft.
- Loads acting on the mooring system:
  - Gravity and buoyancy loads,
  - Inertia loads,
  - Hydrodynamic loads due to the waves and the current and the induced fluid kinematics:
    - From potential flow related phenomena (radiation, diffraction, Froude-Krylov)
    - From viscous related flow phenomena (drag)

As many other mechanical systems, a floating wind turbine could be simplified, with the relevant assumptions, to a multi-DoF mass-spring-damper system. The nonlinear multiphysic of a FWT is much more complex than just the integral mass, spring and damping terms but using a simplified approximation eases the understanding of the FWT response. The different parameters (mass, stiffness, damping) are frequency-dependent and differ for different operating points of the wind turbine. For each Degree of Freedom (DoF), there are some restoring forces (spring), some damping forces, an equivalent mass (or inertia) and external loadings. The DoF may be coupled (e.g. surge and pitch of a SPAR platform (Haslum, 2000)).

The response of this mass-spring-damper system when subjected to different kind of loads (cyclic, stochastic, transient (Manwell, McGowan and Rogers, 2010)) occurs at different frequencies:

- At the natural frequency of the mass-spring-damper system.
- At the frequencies for which the external loadings have a sufficient energetic content if the damping is not too important.

There are also transient responses for the transient loads, for instance with the blade pitch actuators faults (Uzunoglu and Guedes Soares, 2019).

The main goal in this work is about the relative contribution of the wind turbine loads on the FWT response and its frequency content. The wind turbine loadings are detailed in the next subsection to emphasize which phenomena explain the coupled aero-hydro physic.

2.1.2.1 Wind turbine loadings

The different wind turbine sources of loads that contribute to the load tensor at the tower base are analyzed. Some wind turbine loads are acting on the tower and others on the Rotor-Nacelle Assembly (RNA). The tower and RNA loads are detailed for the different sources of loads in Table 3. A drawing of the RNA with its different elements is depicted in Figure 6, extracted from (Pao and Johnson, 2009). The main assumptions for this load analysis are:

- Rigid hub and nacelle,
-

	Gravity loads	**Inertial loads**	**Aerodynamic loads**
Tower	Mass of the tower elements.	• 6 DoF platform accelerations. • Flexible tower elements accelerations.	• Aerodynamic drag, acting on the tower elements.
RNA	RNA mass, including the mass of the blades, of the hub and of the nacelle.	• RNA mass and the 6 DoF platform accelerations • RNA mass and the flexible tower elements accelerations. • Blades mass and the flexible blade elements accelerations. It is denoted $F_{I\ flex\ bld}$. • Rotating blades mass distributions. The conservation of the blades angular momentum leads to a Coriolis force also called gyroscopic torques (Chabaud, 2016). It is denoted M_{gyro}. • Drivetrain torsional flexibility. It is denoted $F_{I\ flex\ drv}$. • Braking loads acting on the shaft	• Aerodynamic loads (lift and drag) acting on the blade elements. • Blade – tower interaction. • Drag on the hub and on the nacelle.

Table 3: Wind turbine source of loads

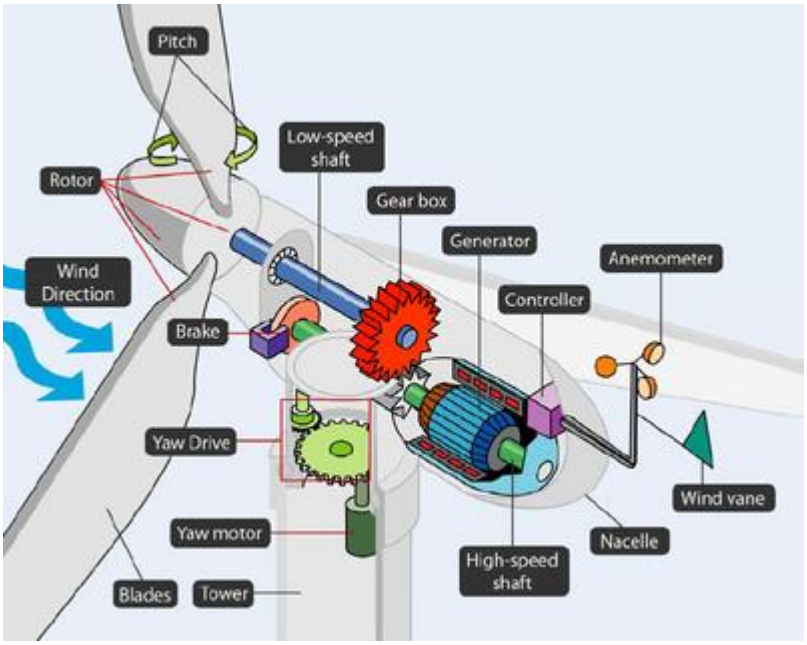

©US DoE

Figure 6: Drawing of a RNA, from (Pao and Johnson, 2009)

The aerodynamic loads on the rotor – part of the RNA loadings – are expected to be the most important contributor to the FWT induced response. To understand the coupling between the aerodynamics and the hydrodynamics of a FWT, it is important to look at the specificities of the rotor loads. Simplified models and experimental investigations in wind tunnel provide insights about the main physical phenomena.

In wind tunnel testing, imposed motions experiments on a 1/75 scale rigid rotor (Bayati *et al.*, 2016) have shown the dependency of the streamwise load component (F_x or $Thrust$) on the wind turbine motions. The corresponding variation of the thrust Δ_{Thrust} due to the varying apparent velocity on the rotor U_{Dyn} is depicted in Figure 7, for different characteristic frequencies of oscillations. From this figure, the dynamic variation of the thrust is relatively in phase with the variation of the apparent velocity, and so out of phase with the rotor velocity. Indeed, U_{Dyn} is related to the FWT motions: if the rotor moves forward/backward, the apparent velocity increases/decreases, as well as the WT thrust, leading to the appearance of a righting moment applied to the floating system. This creates a positive aerodynamic damping term. Depending on environmental conditions and rotor specificities, many phenomena deviate the rotor thrust variations from a pure damping term. These effects include hysteresis effects (unsteady aerodynamics, …), rotor-wake interactions, dynamic inflow, skewed inflow, etc… . Moreover, the damping analysis is valid when the wind turbine controller is not active, but less straightforward with an active generator torque and blade pitch controller, depending on the characteristics frequencies of the oscillations. These effects are detailed in chapter 4, when dealing with the appropriated numerical model for the software-in-the-loop methodology. However, the rotor thrust dependency on the apparent wind velocity and consequently the hub velocities explains different coupled phenomena between the rotor loads and the FWT induced response.

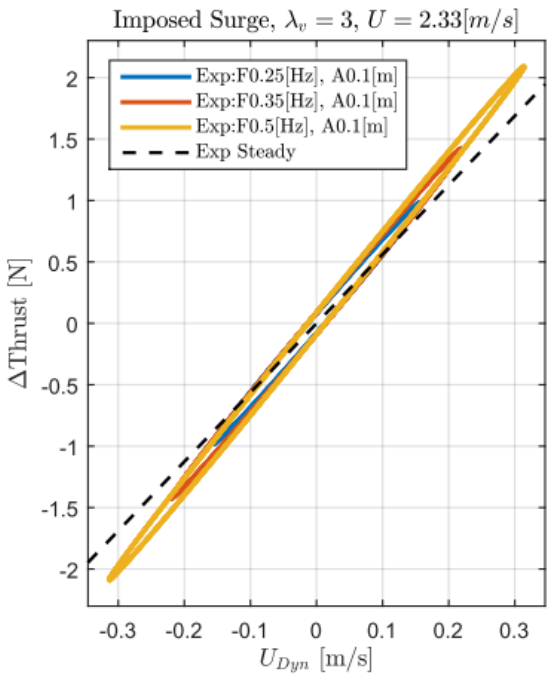

Figure 7: Dynamic variations of the thrust force due to imposed motions of a wind turbine in wind tunnel testing. From (Bayati *et al.*, 2016).

For frequency domain modeling of a FWT (e.g. (Kvittem and Moan, 2014; Pegalajar-Jurado, Borg and Bredmose, 2018)), it is required to linearize the different contributions of the rotor loads and to split them into external frequency-dependent forcing, damping, stiffness and added mass terms. These different contributions could be obtained by linearization capabilities of aero-servo-elastic codes (Jonkman, 2013) or by simplified expressions of the rotor loads (Pegalajar-Jurado, Borg and Bredmose, 2018).

Around a given operating point of the wind turbine, the rotor load forces are often split into different contributions. To simplify, the following developments are introduced for the x-component of the rotor load tensor F_x in the hub frame, i.e. the rotor thrust:

- By assuming a simplified superposition of the FWT induced velocities to the incident wind speed defined by $u_0(t)$
- With velocities of the FWT $\dot{X}_{FWT}$

From the simplified frequency domain modeling and the wind tunnel test, the rotor thrust F_x is approximated by Eq. (2.1).

$$F_x(u = u_0(t) - \dot{X}_{FWT}) \approx F_x(u_0(t)) - B_{aero}\dot{X}_{FWT} \tag{2.1}$$

With :

- $F_x(u_0(t))$ is the varying incident force without the motions of the FWT. It acts as an external loading that can excite the resonant frequencies of the FWT.
- B_{aero} the linear aerodynamic damping

To conclude, from simplified modeling approaches and wind tunnel testing analyses, the main coupling mechanism between the aerodynamics and the FWT response is related to the different components of the aerodynamic loads:

- an external loading that can excite the natural frequencies of the FWT. This could be due to the energetic content of the turbulence in the incident wind.

- a damping that occurs for the different frequency response of the FWT.

2.1.3 Importance of rotor loads on the FWT behavior

The coupling mechanisms between the rotor loads and the FWT response have been briefly explained in part 2.1.2. The aim now is to evaluate the relative contribution of those coupling mechanisms compared to the different sources of loading. To evaluate those contributions, the main phenomena highlighted by the scientific community are first presented. Then, the FWT response is illustrated with the power spectral density (PSD) for a given load case.

2.1.3.1 Highlighted coupled physics in the literature

As the floating wind energy community has already shown and as it will also be illustrated in the present work, there is a strong impact of the aerodynamics loads on the floating wind turbine behavior. For large O&G platforms, the wind loads already provide excitation of the low frequency resonant motions (Molin, 2002). For a FWT, the coupling between aerodynamics and hydrodynamics loads becomes a key point that needs to be addressed in wave tank testing. Some observations about the rotor loads' influence on the different quantities of interest of a FWT include:

- A change in the mean position of the FWT (in particular horizontal offset, tilt and heading) could change the hydrodynamic forces on the floater and on the moorings;
- Aerodynamics loads may dominate the low frequency excitation of a FWT and the induced response, depending on the FWT type and the wind/wave conditions. This has been observed in numerical works (Philippe, 2012; Roald *et al.*, 2013) and experimental works (Courbois, 2013; Azcona, Bouchotrouch and Vittori, 2019).
- The wind turbine controller impacts, via the rotor loads, important properties of the FWT system:
    - Non-adapted controller strategies (initially designed for onshore or bottom-fixed wind turbines) can cause dynamic stability related issues with phenomena like the "negative platform pitch damping" (Larsen and Hanson, 2007; Jonkman, 2008). This phenomenon occurs when the fluctuations of the thrust rotor force are in phase with the FWT velocities (possible when the wind turbine operates in the above-rated region), leading to a negative aerodynamic damping.
    - Natural frequencies of the FWT, especially for the platform pitch DoF (Souza and Bachynski, 2019),
    - Transient motions, i.e. during blade pitch actuators faults (Uzunoglu and Guedes Soares, 2019)(Bachynski *et al.*, 2013),
    - Overall, the dynamics of a FWT could be very sensitive to the controller settings – see results for the Hywind demo (Skaare and Nielsen, 2014) or in wave tank testing in (Goupee, Kimball and Dagher, 2017).
- Total damping, as observed during decay tests in calm water with and without wind in the DeepCWind campaign (Koo *et al.*, 2012) and in regular waves for the TripleSpar platform (Bredmose *et al.*, 2017).
- In case of proper scaling of structural properties of the wind tower, tower base bending moments could be heavily influenced by 3P loadings acting on the rotor. This is correlated to the coupled modes of the FWT, especially between the floater and the tower (DNVGL, 2019). This defines design requirements for the platform, with "stiff-stiff", or "soft-stiff" tower natural configurations design spaces (Hegseth, Bachynski and Martins, 2020).

- 1P loading due to rotor mass imbalance, aerodynamic imbalance and gyroscopic effects can impact the FWT global motions – see for instance the influence of gyroscopic effects on yaw motions of the platforms during wave tanks tests in (Duan *et al.*, 2016; Chen *et al.*, 2018a).

Those different aspects:

- Are diversely important depending on the selected quantities of interest.
- Concern different frequency bandwidths.

The involved frequencies of interest are summarized in the next subsection.

2.1.3.2 Frequency bandwidths of interest

In this work, the different analyses will be based on the different physical effects and their frequency content. This enable specifying refined requirements for the design of the SIL system. This also allows to evaluate the added value of the SIL system compared to other experimental methodologies. Similarly to the methodology adopted (Leroy *et al.*, 2018), different frequency bandwidths are defined to split the energy distribution of the quantities of interest in different parts. The boundaries of each frequency bandwidth will be specified when required to take into account different FWTs considered in this work.

A conceptual frequency map of the important sources of rotor loading is depicted in Figure 8. The frequencies of interest include:

- the natural frequencies of moored FWT rigid-body motion modes (6 DoF, X, Y, Z, R_X, R_Y and R_Z)
- the 1P and 3P rotor frequencies.
- the 1st fore-aft and side-to-side tower bending modes $Twr\ 1^{st}$, and the blade modes (flapwise and edgewise) $Blades$.

The dominating effect in the aerodynamic loads are indicated for each frequency bandwidth: *turbulent wind* for the slowly varying aerodynamic excitation, *wave + tower* for the aerodynamic daming due to the wave frequency motions and tower deflections, *WT rotation* for the tower shadow and *blade aeroelasticity* for the aero-elastic response at the blades modes.

The following frequency bandwidths will be used in this work:

- Low frequency (*LF)* for the $X\ \&\ Y$ natural frequencies. This appelation is based on O&G conventions.
- $R_Y\ NF$ for the R_Y natural frequency which is quite often close to the R_X natural frequency.
- Wave frequency (WF) for the bandwidth corresponding to the significant energetic content of the input wave fields.
- $Twr\ \&\ 3P$ for the bandwidth defined by the tower 1^{st} fore-aft mode which is closed to the 3P rotor frequency for different considered FWTs.
- $> 3P$ is the bandwidth above the 3P rotor frequency. It contains the 6P components and the blade modes natural frequencies.

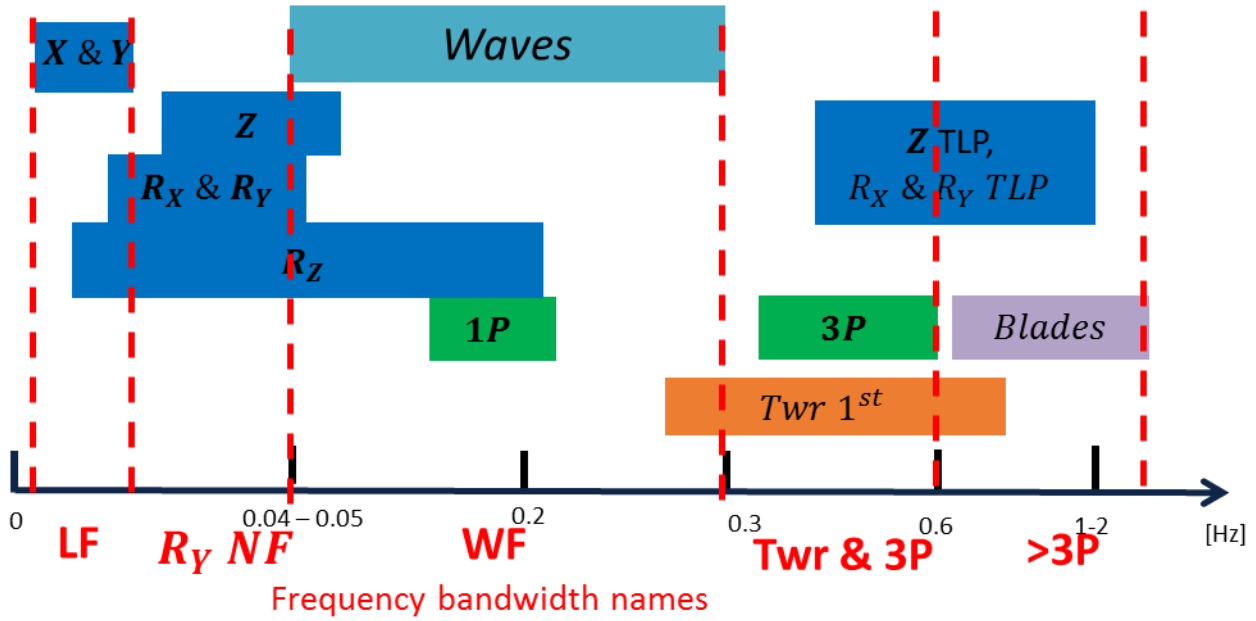

Figure 8: Frequency bandwidths of interest at full scale

2.1.3.3 Frequency content illustration of FWT response and rotor loads

To illustrate the frequency distribution of the rotor loading and the FWT response, one load case is considered for the OC3 Hywind SPAR (Jonkman, 2010). To perform the fully coupled aero-hydro-servo-elastic simulations, the NREL's open source code OpenFAST v2.0 (NREL, no date; Jonkman, 2013) is used, including the hydrodynamic and mooring modules. The aerodynamic module used in the OpenFAST simulations is the AeroDyn v15 module, which includes among others the Blade Element Momentum Theory, correction for skewed-wake, dynamic stall and rotor-tower influence. All the available degrees of freedom within OpenFAST are enabled, including the tower structural modes but except the blades and the drivetrain torsional flexibility. Blades are considered rigid as their elasticity is expected to have a low influence of on the global response (Yu, 2017; Lupton and Langley, 2019). For the mooring restoring forces, the MoorDyn module is used, which can capture the dynamic loading in the mooring lines quite accurately (Hall and Goupee, 2015), based on a lumped-mass approach. For computing the hydrodynamic forces, the HydroDyn module is used which is based on a hybrid Morison drag component and potential flow theories (1st and 2nd order).

The selected load case is one of the most demanding ones in terms of rotor thrust variations, from the different load cases of the parametrical study presented in chapter 3. From chapter 3 simulations, the differences are:

- Duration has been increased to two hours to get a finer resolution for the Power Spectral Density (PSD) functions.
- The blades are considered flexible (2 flapwise modes and 1 edgewise mode)

The different conventions are presented in the *conventions* section before the general introduction. The selected load case has the following characteristics:

- **Waves conditions**: Severe Sea State, $H_s = 8.6m$; $T_p = 13s$; $\gamma = 1.9$; $\theta_{wave} = 0°$
- **Wind conditions:** Normal Turbulence Model ($\alpha_{vert\ shear} = 0.14$; Kaimal Spectrum), $U_w = 18m.s^{-1}$; $T_I = 14.6\%$; $\theta_{wind} = 0°$ at hub height.

The main natural frequencies of this FWT are summarized in Table 4 (Jonkman and Musial, 2010b). For this load case, 1P and 3P frequencies cover the ranges [0.14 – 0.27]Hz and [0.42-0.82]Hz, respectively. Note that these large variations of the 1P and 3P frequencies are due to the high turbulence intensity and to the selected wind turbine controller.

DoF	Natural frequency [Hz]
$[X, Y]$	0.008
$[Z, R_X, R_Y]$	0.033
R_Z	0.12
Twr_{1st}	0.47
$Drivetrain$	0.65
$Blades_{flap\ 1st}$	0.71
$Blades_{edge\ 1st}$	1.09
$Blades_{flap\ 2nd}$	2.0
Twr_{2nd}	3.75

Table 4: Main natural frequencies of the OC3-Hywind (Jonkman and Musial, 2010a)

In Figure 9, spectra of the quantities of interest - computed by Welch method (Welch, 1967) - are plotted. The relevant frequency bandwidths are illustrated by colored polygons. The red polygons correspond to the *Low frequency* bandwidths, associated to the Surge and Sway natural frequencies. The blue polygons correspond to the natural frequency of the Pitch and Roll motions. The green polygons correspond to the wave frequency bandwidths. The purple polygons correspond to the 3P rotor frequency, the 1st tower fore-aft and side-side modes. The light blue polygons correspond to higher frequency content (6P, blades modes, …)

Different observations from these PSD could be made:

- Even if the aerodynamic loads acting on the rotor have quite important components around 3P rotor frequency (Figure 9.f to Figure 9.k), the motions of the platform are not very sensitive to this frequency bandwidth (Figure 9.a to Figure 9.e). They have a coupled response with the 1st tower bending mode, but at least one order of magnitude smaller than the wave frequency response.
- The tower bending moments (Figure 9.m and Figure 9.n), have significant components at the wave frequencies and at the 1st tower bending mode.
- Most of the quantities of interest have a high energetic content in the wave frequency bandwidth.
- The edgewise blade mode has a significant impact on the shaft torque $\boldsymbol{M_x}$ (Figure 9.i)).
- Natural frequencies of the surge, sway, pitch and roll (respectively $\boldsymbol{X, Y, R_Y\ and\ R_X}$) are important components in the mooring line tension and in the $\boldsymbol{X}$ and $\boldsymbol{Y}$ responses.
- For the mooring line tensions (Figure 9.l), a peak between the 3P and the wave frequency bandwidth is not negligible, and is probably linked to an Eigen mode of the mooring lines.

This analysis illustrates the numerous frequencies of interest and the different relative contributions of each frequency bandwidth depending on the quantity of interest considered. Basically, the FWT's dynamics is important for different frequency bandwidths, especially from the low frequency to the wave frequency bandwidths. The 3P rotor frequency bandwidth (close to the 1st tower fore-aft bending mode frequency for this FWT) is less important if the tower deflections and related effects are not of interest.

This analysis provides guidelines and priorities about relevant frequencies of interest for the design of a rotor loads system for wave tank testing.

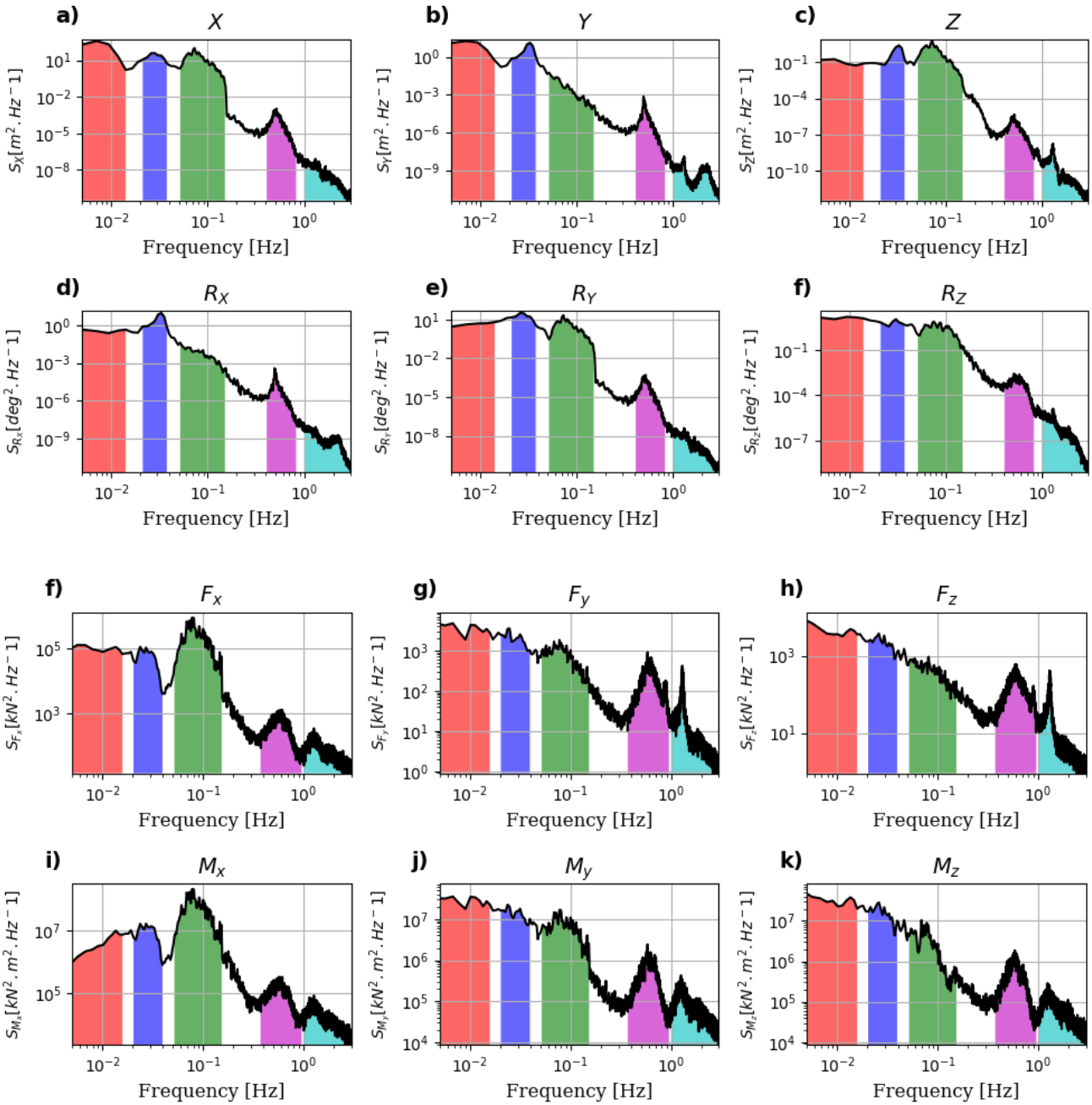

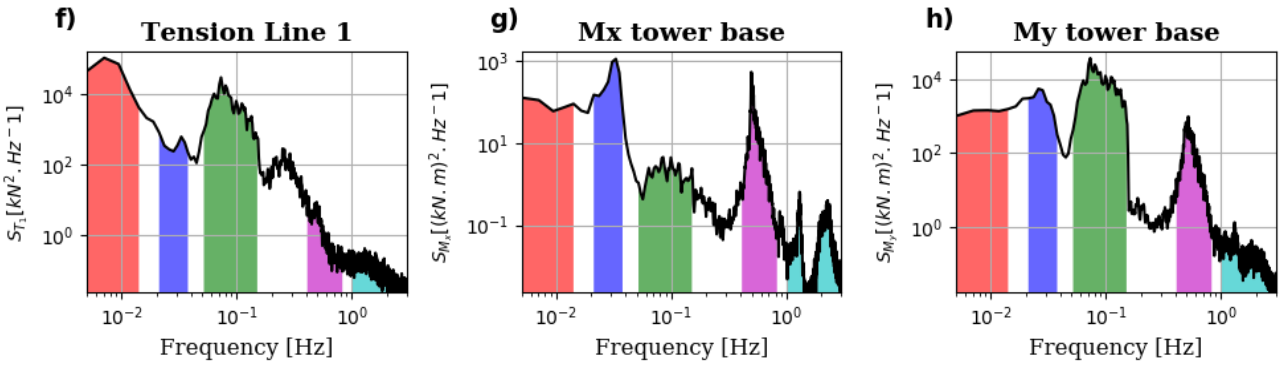

Figure 9: PSD of different quantities of interest for a selected load case.

a) to f) Motions of the platform in the inertial frame. f) to k) Rotor loads. l)tensions in a mooring line. m) and n) Mx and My tower base bending moments

2.2 FWT Wave tank testing: existing rotor loads modeling methodologies

2.2.1 Background about wave tank testing

When looking at the last 15 years, different methodologies have been developed to increase the fidelity of floating wind turbine wave tank testing. Those methodologies concern the hydrodynamics phenomena acting on the platform and on the moorings, the data acquisition system, the testing procedure and many other aspects to get accurate and reproducible model tests. The knowledge summarized in international projects deliverables (Bredmose *et al.*, 2012; J Azcona *et al.*, 2014; Thys *et al.*, 2019) and international committees (such as ITTC (ITTC, 2017)) constitutes a very solid basis. The key FWT wave tank testing methodologies that have been used are summarized in Table 5.

Topic	Existing procedure
Design procedure and scaling factors	Identifications of the most important dimensionless numbers to scale down the FWT parameters (geometry, mass, inertia,…) and the environment (wind and waves conditions). The scaling laws related to the different dimensionless numbers are ranked depending on the quantities of interest of the test campaign.
Moorings system scaling	Different solutions such as aerial mooring systems made of calibrated springs or scaling of catenary chains, with the associated typical assumptions that could be made.
Data acquisition and calibration	Calibration of the data acquisition systems (wave gauges, force sensors,…) with associated procedures to ensure reproducibility.
Verification, Validation and Uncertainty Quantification (VVUQ)	Quantification of the uncertainties have always be a concern for experimenters. Effect of those uncertainties of the different quantities of interest (error propagation) have recently been explored during wave tank testing of floating wind turbines, see (Robertson *et al.*, 2018; Desmond, Hinrichs and Murphy, 2019)
Test matrix design	The different identification tests (e.g. decays, pull-out, regular waves, irregular waves, white/pink noise,…) and their exploitation procedure (fitting of integrated stiffness, damping and mass or RAO) is explicitly defined. The existing procedures also provide the appropriate durations to build converged statistics and to conduct proper frequency analyses.
Analysis procedure	The different analyses required to extrapolate lab-scale results to full scale, to compare with numerical models (*model of the model*,…) and to establish statistics from random wave and wind excitations.

Table 5: Key FWT wave tank testing topics covered by the literature

What needs to be underlined is that the different physical phenomena acting on a FWT need to be sufficiently understood to correctly reproduce them in a wave tank testing campaign. Basically, as it is a moored floating body submitted to ocean waves, the methodologies that have been developed for the stationkeeping analysis need to be followed. However, some of the hydrodynamic phenomena that occur on a moored platform increase in complexity, when focusing on FWT, compared to the understanding built in the last decades for O&G platforms. Some specificities of floating wind turbines are:

- When looking at the dimensions of the floaters, the Keulegan-Carpenters (KC) and the Stokes (β) (Molin, 2002) dimensionless numbers do not clearly indicate which hydrodynamic assumptions should be followed. Indeed, flow conditions around the floater fall between the small body (hydrodynamic loadings dominated by viscous and vortex shedding effects) and large body assumptions (dominated by diffraction-radiation);
- Very harsh wave conditions in shallow to moderate water depth, increasing the nonlinearities of water waves kinematics;
- Strong aerodynamic loads.

Those features, combined with the fact that only scarce full scale data are available for validation, make wave tank testing a required step to validate numerical models. In the selection of a suitable model scale methodology for modeling hydrodynamic or aerodynamic loads, two aspects could be determinant: uncertainties quantification and selection of the quantities of interest. They are detailed above.

Uncertainty quantification

There are many uncertainties and biases that could arise from wave tank model testing. While the rotor loads modeling methodology introduces some uncertainties, comparing these uncertainties to the

other sources of uncertainties is important. In this work, the sources of uncertainty will be discussed for wave tank testing with a focus on the hybrid methodology specific uncertainties, from chapter 5 to 7.

Specifications of quantities of interest for wave tank testing

As explained by Sauder et al. (Sauder *et al.*, 2016), when designing a SIL system, one of the first step is the specification of the main quantities of interest during the wave tank model testing of FWT. Those quantities of interest are required to define indicators about the accuracy of one methodology or another for the rotor loads representation. In the SOFTWIND project, two main scenarii have been defined for an evaluation of those quantities of interest depending on the objectives of the test campaign. These scenarii are:

- Validation of the full design of a floating wind turbine, including the moorings, the hydrodynamic model of the floater, the nacelle acceleration, the wind turbine controller, etc. Basically, this is the most demanding scenario, with all of the quantities of interest being important. By validation, it means providing a reference behavior of the FOWT, for calibration and verification of numerical models.
- Calibration of hydrodynamic models of the floater, for instance in complex sea states and nonlinear waves, with an additional relatively simple aerodynamic loading approach.

For both scenarii, relative significance of the different quantities of interest have been evaluated in Table 6. A low number (1) means a low priority, and a high number (4) is for a high priority. This evaluation objectifies the separation between important frequency content and discarded frequency content. For instance, when calibrating a hydrodynamic model of the floater, the tower base bending moments will not be the main quantity of interest whereas the global motions of the platform will be the most important criteria. However, when checking the design of a FWT, the tower base bending moments are carefully analyzed against admissible designing criteria. This impacts the admissible error level and the maximal frequency relatively well captured.

Quantities of interest	Calibration of hydrodynamic models	Validation of system design
Platform motions (positions)	**4**	**4**
Mooring lines tensions	**2**	**4**
Nacelle acceleration	**2**	**4**
Tower base bending moments	**1**	**4**
RNA forces and moments	**1**	**4**

Table 6 : Assumed quantities of interest for different wave tanks testing scenario

2.2.2 Defining a suitable methodology for reproducing the rotor loads

The most adapted methodology to represent the rotor loads during wave tank experiments of floating wind turbines has been a major research focus for the last decade, with many contributions from the community (e.g. (Gueydon, Bayati and de Ridder, 2020) for a recent review). Basically, in a historical perspective, the increasing complexity of rotor loads methodologies that have been developed worldwide could be illustrated by the different solutions developed at the ECN ocean wave tank during the PhD work of Adrien Courbois (2010 - 2013) (Courbois, 2013; Azcona *et al.*, 2016).

Firstly, wind generation systems made of different fans and honeycombs have been developed to reproduce targeted mean wind speed and turbulence intensity fields (see Figure 10). This introduces one

of the limitations of actual wind-based methodologies as basically, an insufficient quality of the wind flow has been reached by those wind generation systems ex-post added to wave tank facilities. This leads to unwanted vertical/horizontal wind shear, levels of turbulence which are not necessary the same as required and turbulent scales which are not correctly reproduced (Courbois, 2013), compared to referenced atmospheric flows. Also, a full characterization of the generated wind field (Laser Doppler Velocimetry (LDV), hot wire anemometry, pitot tubes …) is usually unaffordable or limited in wave tank facilities. Without a very accurate characterization of the incident wind field, difficulties could arise when trying to calibrate the numerical models.

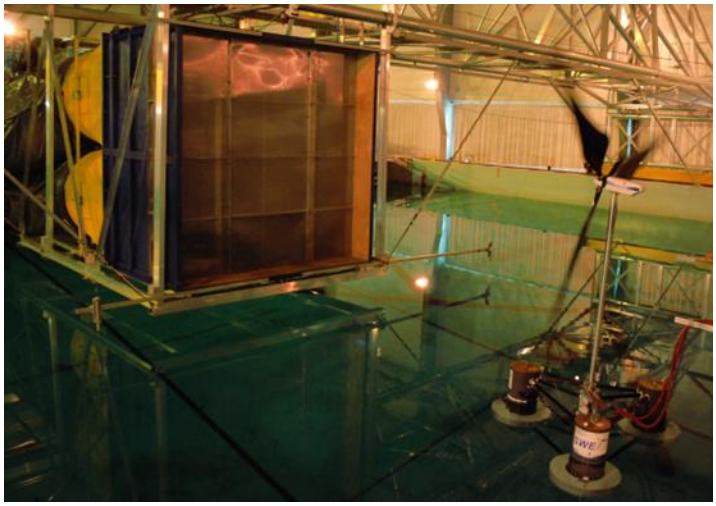

©Centrale Nantes

Figure 10: Wind generation system developed at the ECN (from (Courbois, 2013)*)*

Secondly, once the targeted wind inflow conditions could be reproduced, different ways to reproduce the aerodynamic, inertial and gravitational loading acting of the wind turbine have been tested. However, as mentioned in (Martin *et al.*, 2012; Courbois, 2013; J Azcona *et al.*, 2014; Müller, Sandner and Bredmose, 2014; Chabaud, 2016; Hall, 2016; ITTC, 2017; Chen *et al.*, 2018b) each of these physical approaches has different sources of problems:

- A “drag” or “porous” disc, which gives a constant thrust coefficient. The diameter, the holes in the disc and the wind velocity are adjusted to reach the target mean rotor thrust, for a given operating point. When the incident wind speed varies, the thrust acting on the disc varies proportionally to the square root of the wind speed. When the RNA moves forward or backward, a damping is inherently reproduced. This damping reproduction is detailed in chapter 4 when detailing the simplified aerodynamic model. The main limitations of this approach are:
    - A steady-state operating point, which is not respecting the fluctuations of the blade pitch and rotor speed for slowly varying fluctuations of the wind speed.
    - Concerning the thrust, an aerodynamic damping is reproduced for all the FWT motions without any considerations for the controller effects. Moreover, the fluctuations of the thrust acting on the disc may differ between low frequency and high frequency FWT motions;
    - The other rotor loads components are not reproduced;
- A geometrically scaled rotor, which keeps the shapes of the blades. Consequently, due to the mismatch of the Reynolds number, the thrust is usually smaller than the target model scaled one for the same tip speed ratio (Courbois, 2013). It impacts the steady value of the thrust and also its dynamic variations.

- A "performance matched" rotor, such as the ones defined during the INNWIND project, the WINFLO project (Boulluec *et al.*, 2013) and at the MARIN wave tank (Goupee *et al.*, 2015). Those rotors have been equipped with redesigned blades adapted to the lower Reynolds numbers of the model scale experiments, basically thicker blade sections, which makes the rotor loads to be rather correctly scaled for the thrust component. However, different drawbacks have been identified (Martin *et al.*, 2012):
    - While the thrust is correctly scaled, the aerodynamic torque and the other load components are not correctly scaled due to the change in the blade section. This makes the design of a model scale generator torque and blade pitch controller a hard task (but still possible (Goupee, Kimball and Dagher, 2017))
    - Heavier blades, even using low density and stiff materials, which makes the inertial loads scaling complicated.

The thrust sensitivity to the chosen physical approach has been explored during the DeepCwind test campaigns, as depicted in Figure 11, from (Goupee *et al.*, 2014). This figure shows the differences between the target thrust coefficient (C_t) of the NREL 5MW at different TSRs (Tip Speed Ratio) compared to the C_t values for the geometrically scaled rotor (*2011 DeepCwind Turbine*) and the redesigned performance-matched rotor (*MARIN Stock Turbine*). Finally, the design of performance-matched rotor is a complicated task and has still some limitations to correctly reproduce the rotor loads.

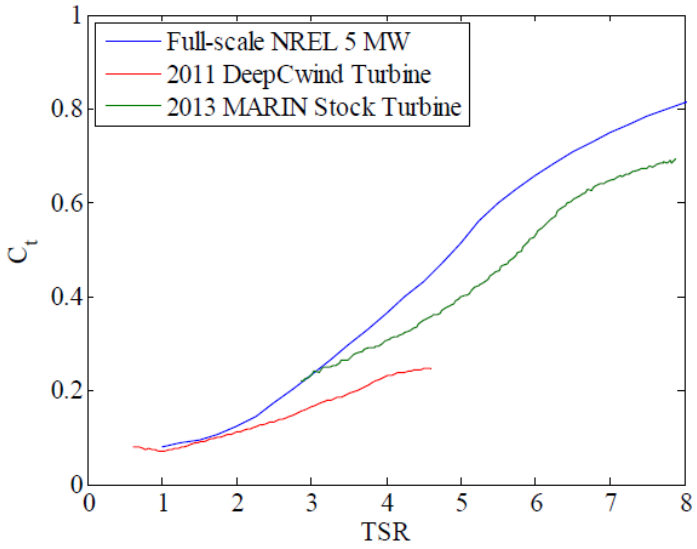

Figure 11: Thrust coefficient at different TSRs for the full scale NREL 5MW rotor and the model scale rotors. From (Goupee *et al.*, 2014)

The three physical methodologies have already been tested at the ECN's Ocean engineering wave tank, at scale 1/50 and 1/60, and are depicted in Figure 12.

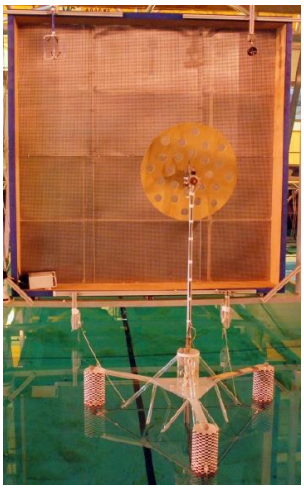

Drag disk

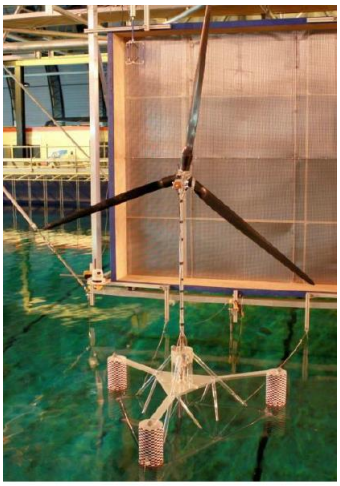

Geometry scaled rotor

Performance matched scaled rotor

Figure 12: Wind turbine loads physical modelling at ECN's Ocean engineering wave tank (from (Courbois, 2013; J Azcona *et al.*, 2014)*)*

As explained above, it is quite challenging and costly to reproduce 100% physical FWT during wave tank experiments. Developing a new experimental tool that could create more representative fluctuating forces acting on the wind turbine, especially due to the wind turbine controller, was the main motivation to the development of a hybrid "SIL" system in the scope of the SOFTWIND project.

2.2.3 Software-in-the-loop methodology: principle and actual limitations

The so-called « software-in-the-loop » methodology is presented in this part, with its subsystems. The different choices done in other experimental facilities and the limitations that have been encountered are detailed.

2.2.3.1 Presentation of the methodology and its key elements

The "software-in-the-loop" approach (SIL) consists here in physically modeling the floating substructure, while the rotor loads are reproduced with a set of actuators that communicates with a floating wind turbine numerical model. The floating substructure could respect Froude scaling while the numerical simulation of the wind turbine is performed at full geometric and Reynolds scales. The aerodynamic and inertial forces and moments to be reproduced are scaled down by using Froude scaling factors. A real-time coupling is performed: those forces and moments depend on the motions of the platform as measured in the wave tank.

An illustrative drawing of this method is depicted in Figure 13.

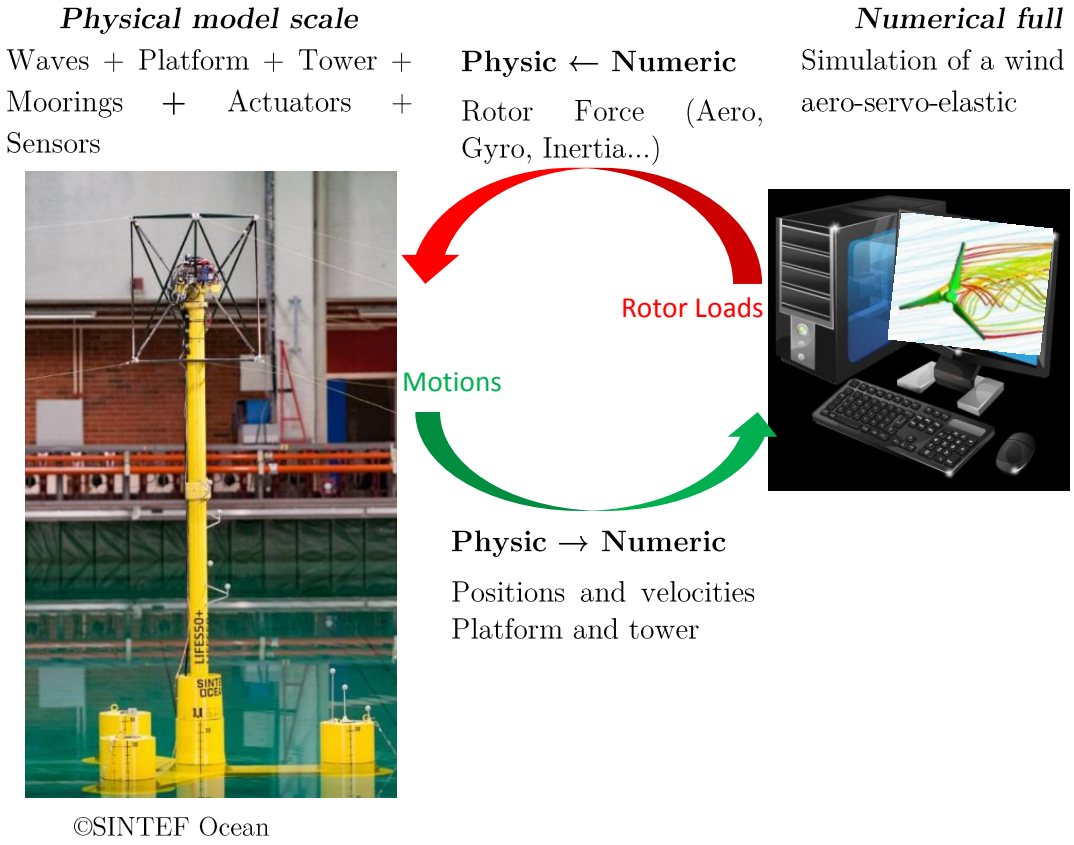

Figure 13: Schematic description of the Software-in-the-loop methodology

Different components compose the SIL system. This software-in-the-loop system could be split into 3 parts:

- The physical part, composed by all the equipment in the wave tank, i.e. the floater, the moorings, the tower, the different sensors – Force transducers, Motion CAPture system (MOCAP),...- and the actuators.
- The real-time DAQ and control environment that acquires measurement signals, control the numerical part and interacts with the physical part.
- The purely numerical part of the setup, which is the real-time computation of the aerodynamic and inertial loads acting on the rotor.

As explained in details in the PhD Thesis of Matthew Hall (Hall, 2016) and published paper (Hall, Goupee and Jonkman, 2017), different alternatives exist for the separation point between the numerical and the physical modeling. Up to now, the solution that has been adopted by all of the SIL system developers is an aero-rotor coupling strategy. In this strategy, most of the system components are physically represented. Only the global rotor aerodynamics, the generator and some inertial loads (gyroscopic, flexible blades) are simulated. The target RNA model scale mass is ideally respected on the physical side, which makes most of the inertial and gravity loads inherently reproduced. This aero-rotor coupling strategy is also selected for the present system. More details about this strategy and the loads setpoints for the actuators are given in Chapter 3.

2.2.3.2 Required developments

From the different parts of the SIL system, different equipment and development are mandatory. To illustrate the requirements, order of magnitudes about real-time characteristics or frequencies of interest are given for each subsystem. The detailed requirements for the system will be detailed in chapter 3 and the implementation of those subsystems will be detailed in chapter 5.

Physical part

On the physical part, a complex data acquisition system is required. It synchronizes and collects signals and data coming from various measurement systems with different dynamics, formats and ranges. A real-time motion capture system (MOCAP) is a key sensor for the method accuracy.

To be able to identify the performances of the SIL methodology, force transducers are required to evaluate the loads produced by the actuators. For closed-loop control of the actuators, those force transducers become even more important.

The actuation system is one of the central parts of the SIL methodology. Different subsystems compose the actuation system. Firstly, the *actuators* themselves, composed by a motor and a mechanical converter which can reproduce a given force on the model. This mechanical piece could be a rotating propeller, or a winch plus a cable. The different possibilities are described in the next part. Secondly, the *frame* which defines the layout of the actuators and acts as the mechanical interface between the tower top and the different actuators. Thirdly, the *power system*, either battery or stabilized electrical supply. Fourthly, the *motor control* from the real-time environment to the different motors. It includes the controller (speed or torque control) and passes through servo signals, basically PWM signals or CAN Bus messages.

The frequencies of interest - depending on the type of floater, moorings, tower and scale factor as seen in part 2.1.3 - are between 0 and 5 Hz. Sensors (respectively actuators) must, as much as possible, properly capture (respectively reproduce) their dynamics.

Real-time environment

A key aspect of the SIL methodology is the real-time environment that controls the actuators, executes the numerical model and masters the data acquisition. A particular attention should be paid to synchronization with other wave tank equipment (MOCAP, wavemakers, additional DAQ systems)

In terms of order of magnitude, the real time control frequency, is expected to be in the range [100 – 600] Hz (Sauder *et al.*, 2016; Meseguer and Guanche, 2019). Consequently, this real-time environment needs to be programmed on a programmable logic controller (PLC), with a hierarchization of operations and small *jitter* characteristics.

To limit the high frequency noise in the hub motion velocities sent to the numerical model, a dedicated *motion observer* needs to be implemented. Indeed, if the velocities are not filtered, high frequency energetic content appears in the setpoint force. While this is not necessarily a problem for the FWT, as its mass and inertia limit its sensitivity to high frequency excitation, this could be problematic for the actuators and for the frame of the actuators:

- A dramatic increase in the frequency bandwidth requirements for the actuators makes its control more difficult. A saturation of the actuator command could reduce its overall predictability and increase its temperature. This might be a concern for the actuator integrity;

- High frequency vibrations of the frame that supports the actuators could be excited by this setpoint.

For closed-loop control of the actuators a real-time *Force observer* that isolates the forces and moments produced by the set of actuators, is mandatory. For open-loop control of the actuators, this force observer is used in post-processing only. In both cases relevant sensors (IMU, accelerometers) are required to make this force observer possible. Particular attention should be paid to the filtering techniques, as the trade-off between the efficacy to remove the high frequency noise and the phase delay induced by the filter.

Numerical model

To be able to emulate, in real-time, realistic rotor loads that depend on the measured platform motions, the numerical model should receive the hub positions and velocities as inputs and should output the relevant loads acting on the RNA. The setpoint loads will be detailed in chapter 3. The main specification for this numerical model is a sufficient accuracy but also an ability to ensure real-time computations. The additional specifications for the numerical model are described in chapter 3.

The different requirements for each subsystem are summarized in Table 7.

Physical part	Real-time environment	Numerical model
• Actuators: frame design, electrical supply, control of motors, calibration • Sensors: Force transducers, MOCAP	• Control of the actuators • Force observer: essential for closed-loop control and for evaluation of the actuators performances • Motion observer: essential for the real-time numerical model	• Aerodynamic loads on the rotor • Ideally, inertial loads • Needs to include a servo module • Robust, sufficiently accurate, real-time

Table 7: Requirements for the different parts of a SIL system

2.2.3.3 Type of actuators

Different approaches regarding the type of actuation have already been used, as explained in the PhD manuscripts of V. Chabaud (Chabaud, 2016) and M. Hall (Hall, 2016). It is important to define what are the setpoints and the disturbances in each case, possible advantages and drawbacks.

Some actuators are earth-fixed which means they are connected both to the moving RNA and also to the wave tank infrastructure. Other actuators are on-board, meaning they are not connected to the fixed infrastructure of the wave tanks. Some information about the different solutions are given hereafter.

Earth-fixed

Typically, this is a set of different controlled wires with winch units, connected to the side of the wave tank and to the RNA Some systems have been developed with several actuators, e.g. (Sauder *et al.*, 2016) at SINTEF Ocean and at the University of Maine (Hall, 2016). This constitutes a *parallel cables robot,* which is a well-known engineering object.

The main expected advantage of this solution is about the dynamics and the control of the actuators. As the heavy part of the actuators (motors, ESC, power cables) could stay next to the wave tank facilities, this enables using highly dynamical motors. Moreover, the power cables of those actuators do not need to connect the *dry side* of the wave tank to the moving body, which could significantly impact the motions of the FWT.

The main expected drawback is about the impact of the FWT motions (disturbances) on the force-controlled winch units. The positions of the wires attachment points on the RNA need to be optimized to reduce the disturbances to the wires tension due to any FWT motions (Chabaud *et al.*, 2018). For waves only cases with or without steady rotor forces, it might be a challenge for such systems. One of the identification tests of such systems is a zero-force test, where the setpoints are zeros and the platform moves (Hall and Goupee, 2018).

On-boards

Typically, a set of fans or propellers fixed atop the mast of the wind turbine is used. Early work was done by CENER at ECN in 2013, using a ducted fan mounted at the top of the wind turbine mast (José Azcona *et al.*, 2014). Similar systems have been used more recently at UCC (Desmond, Hinrichs and Murphy, 2019) and at Oceanide BGO First wave tank. On the same principle, counter rotating fans have also recently been used at the IFREMER wave tank facility to reproduce vertical and horizontal axis wind turbine rotors. With 4 fans, IH Cantabria (Battistella *et al.*, 2018; Meseguer and Guanche, 2019) extended the number of load components reproduced in real-time during the tests. They have also illustrated the calibration process required to make the system working. Similar actuators have been used for a floating bi-rotor vertical axis wind turbine (Kanner, Yeung and Koukina, 2016), using propellers mounted on rotating masts.

The main expected advantage of on-board actuators is about the much smaller disturbances that need to be tackled:

- The motions of the platform introduce very small disturbances, and consequently the need for advanced feedback strategies is less crucial;
- The system is lightweight and could be easily moved to another experimental facility;
- It also offers the possibility to put all the equipment on-board with a very limited quantity of cables connected to the dry side of the facility.

Some expected drawbacks and constraints are:

- Those propellers, widely used for Unmanned Aircraft Vehicles (UAV or *drones*), have their own dynamics that can limit the reproduction of the thrust variations (Pounds, Mahony and Corke, 2010);
- The programmable logic controller (PLC) needs to be onboard, which imposes a trade-off between cost, weight, and computational power.

This is the actuator solution that has been retained in the SOFTWIND project and the advantages and drawbacks will be further detailed in chapter 4.

2.2.3.4 Actual limitations of SIL systems

A characterization of the different limitations of SIL systems to model the rotor loads for different kinds of tests (decays, turbulent wind, …) has been one of the main concerns of all the SIL system development, see e.g. (Chabaud, 2016; Hall, 2016; Sauder *et al.*, 2016; Desmond, Hinrichs and Murphy, 2019). This has also been a guiding principle along the SOFTWIND project. Those limitations could be divided into different parts (i) the actuation system limitations and (ii) the numerical model assumptions for a real-time integration. More details about each of the limitations are given hereafter.

Actuation system limitations

One of the major limitations to the SIL methodology are due to the limitations of the actuators. Those limitations are linked to the characteristics of each actuator and their layout. They are not specific to this actuation problem, but the specificities of this floating wind turbine wave tank testing

problem define the constraints (mass budget) and characteristics for the actuators (disturbances and setpoints):

- Number of rotor load components that have to be modeled. Ideally 6 (3 forces and 3 moments), but limiting the number of components reduces the number of required actuators, reducing the complexity and making the mass constraint smaller;
- Time characteristics of closed-loop force-controlled actuation systems. As explained by Chabaud (Chabaud, 2016), the total time latency of the system could be split into (i) a pure time delay – communication, processing of the motions, filtering techniques, and computational time for the numerical model – and (ii) a phase lag - dynamic response of the actuators. Those two kinds of delay could be problematic and suitable strategies have to be employed in order to limit their effects.
    - Pure time delay drives the choice of the numerical modeling (CPU time requirements of the numerical calculations) and the setup of compensation schemes (delay from optical measurements,…)
    - The dynamic response of open-loop or closed-loop controlled actuators drives the choice of actuators types (layout, size, on-board versus earth-fixed…). It also drives the selection of suitable control strategies and motors. Physically, this dynamic response limits the maximum frequency of the actuated load which can be accurately reproduced (limited phase lag and targeted amplitude), and introduces a bias because of the disturbances.

Numerical model assumptions

Another limitation is due to the assumptions employed in the numerical models. Even if the wind turbine is simulated at full geometric scale - bypassing the Reynolds scaling problems - the strong assumptions of the real-time numerical models limit the fidelity of the computed aerodynamic loads. For a floating wind turbine, especially in the tested design conditions, aerodynamics is far from the strong assumptions of the classical Blade Element Momentum Theory (BEMT), which is the theory used in most of the frameworks. Those approximations on the aerodynamics impact the quantities of interest (motions, …) of the floating wind turbine (Farrugia, Sant and Micallef, 2016; Leroy, 2018). While out of scope of the present work, the sensitivity to the numerical model assumptions needs to be taken into account in the total uncertainty quantification. Details about the assumptions inherent to the selected numerical model and its effects are given in chapter 3 and chapter 7.

In this chapter, two topics have been covered. Firstly, the different reasons why we need to reproduce the rotor loads during wave tank testing. Secondly, the different existing methodologies to reproduce these rotor loads, with a focus on hybrid SIL methodologies. The next two chapters present the work done to design a SIL system. In chapter 3, the setpoint loads for the actuation system are characterized as it is the main design specification.

3 Rotor loads specifications for SIL methodology

Contents

This chapter is about the target rotor loads for the actuators. It constitutes one of the requirements for the actuation system design. The target rotor loads are specified, characterized in terms of frequency content, maximum and mean values, and a sensitivity analysis to a deteriorated actuation is performed. Considerations about numerical modeling assumptions and their effects on the frequency content of the setpoint load tensor are also developed.

3.1 Loads setpoints: background

3.1.1 Loads to reproduce: framework

As explained in chapter 2, in the scope of the SOFTWIND project, the aero-rotor coupling strategy has been selected. The different wind turbine loadings are split between proper design of the model (mass distribution, dimensions) and load setpoints for the actuators. In Table 8, the different contributions to the wind turbine loading are detailed, based on the load analysis presented in chapter 2.

3.1.1.1 Forces inherently reproduced by the experimental set-up

When the contribution could be reproduced by a proper design of the model, its requirements are explained. The requirements and feasibility of two sources of loading are detailed to provide additional explanations.

Inertial loads on the tower due to the flexible tower accelerations

This structural scaling has the following requirements:

- Mode shapes are correctly reproduced;
- Mode frequencies are correctly scaled;
- Structural damping is correctly reproduced.

In terms of feasibility, fulfilling those requirements is challenging for an experimental setup. More details are given in chapters 5 and 6 about the tower scaling, as a trade-off between accuracy and feasibility.

Aerodynamics loads on the tower

The tower aerodynamic forces, mostly drag forces, induce distributed loads on the tower. Most of the actual SIL systems neglect this load source (see Appendix E), as for an operating wind turbine, the relative contribution of the tower drag is relatively small. However, as the wind speed increase, this contribution significantly increases. It is expected to become significant near the cut-out wind speed of the wind turbine. Comparison between rotor thrust steady-state values and approximated drag on the tower are depicted in Figure 17. To take the tower drag into account, different options may be envisaged:

- It could be added into the RNA load setpoint. To reproduce the correct forces and torques due to the integrated tower drag, it is important to locate the actuators below the RNA height, somewhere within the upper half of the tower.
- Alternatively, applying an equivalent point load by one or two actuators located at the representative point of application of the integrated tower drag.

However, for those two solutions, the differences introduced by applying a point load and moment (on the tower or at the RNA) instead of distributed loads on the tower has to be checked and, if possible, mitigated. For a rigid tower, this should be relatively similar but for a flexible tower, this has to be studied. In the scope of the SOFTWIND project, the aerodynamic drag force on the tower has been neglected because it is considered negligible. Order of magnitude from a simplified tower

aerodynamic force model are described in chapter 3. However, the rotor-tower interaction has been taken into account. It is included in the rotor aerodynamics.

Load component	Requirements for model design in the SIL method.	Model design of actuators setpoints
Tower		
Gravity	Tower mass distribution correctly reproduced (CoG, total mass).	Physical setup
Inertial | 6 DOF platform	Tower mass distribution correctly reproduced (CoG, total mass).	Physical setup
Inertial | flexible tower	Tower mass distribution correctly reproduced and flexible deformations of the tower are correctly scaled. This means a proper structural scaling of the tower.	Physical setup, approximated or neglected
Aerodynamics	Included in the setpoints of the actuators (existing actuators or dedicated ones)	Dedicated actuators, approximated in existing actuators or neglected
RNA		
Gravity	RNA mass distribution correctly reproduced (CoG and total mass)	Physical setup
Inertial | platform 6DOF accelerations	RNA mass distribution correctly reproduced (CoG, total mass and inertia).	Physical setup
Inertial | flexible tower acceleration	RNA mass distribution correctly reproduced (CoG and total mass) and structural scaling of the tower respected.	Physical setup or neglected
Inertial | flexible blades	Included in the setpoints of the actuators	Actuators setpoints
Inertial | rotating blades	Gyroscopic torques could be actuated by a separate actuator (spinning masses (Roddier *et al.*, 2010)) or directly included in the setpoints loads of the existing actuators.	Actuators setpoints
Inertial | drivetrain flexibility	Included in the setpoints of the actuators	Actuators setpoints
Aerodynamics	Included in the setpoints of the actuators	Actuators setpoints
Interaction between free rotor velocity and aerodynamic torque	Included in the setpoints of the actuators	Actuators setpoints

Table 8: Requirements for model design and actuators load setpoints from the different wind turbine loadings

3.1.1.2 Rotor loads setpoints for the actuators

From the loads analysis, the setpoints of the actuators need to include:

- Inertial loads acting on the rotor due to the blades, rotating blades and drivetrain flexibility.
- Rotor aerodynamic loads, with a special treatment of the M_x component as explained hereafter.

Details about the frames orientations and origins are given in the *conventions* section at the beginning of this manuscript.

M_x setpoint component

What needs to be reproduced by the SIL system is the reacting torque at the connection between the rotating shaft and the nacelle, $M_{twr\,top\,x}$ .This is equal to the low speed shaft M_{LSS_x}, and is computed by the numerical model. Hereafter is briefly presented the reasoning why this is not the aerodynamic torque $M_{aero\,x}$ that has to be reproduced by the actuator but the low speed shaft torque $M_{LSS\,x}$ which has significantly smaller variations. This low-speed shaft torque is also related to the generator torque.

Simplifications are being made for this reasoning, as presented in (Manwell, McGowan and Rogers, 2010, pp. 161–165).The blades and the drivetrain are considered as rigid. The fundamental principle of the dynamics applied to the rotor leads to Eq. (3.1):

$$\sum \boldsymbol{M_{x\,|\,rotor} = J_r\,\dot{\Omega}_{rot}} \tag{3.1}$$

With:

- J_r the moment of inertia of the rotor (blades and hub)
- The free rotor speed Ω_{rot}.

The torques along the x axis acting on the rotor, are:

- The aerodynamic torque $M_{aero\,x}$
- The opposite of the low-speed shaft torque, -$M_{LSS_{rigid}\,x}$

Reorganizing Eq. (3.1) leads to an expression of the low-speed shaft $M_{LSS_{rigid}\,x}$ depending on the aerodynamic torque $M_{aero\,x}$ in Eq. (3.2)

$$\boldsymbol{M_{LSS_{rigid}\,x} = M_{aero\,x} - J_r\,\dot{\Omega}_{rot}} \tag{3.2}$$

The relation between the generator torque and the low speed shaft torque could be obtained with another fundamental principle of the dynamics to the wind turbine shaft. This leads to Eq.(3.3):

$$\sum \boldsymbol{M_{x\,|\,shft} = J_{shft}\,\dot{\Omega}_{shft}} \tag{3.3}$$

J_{shft} is the equivalent moment of inertia of the high speed shaft (generator, …) taking into account the gearbox ratio $\frac{\Omega_{HSS}}{\Omega_{LSS}}$. ($J_{shft} \sim J_{Gen} * \left(\frac{\Omega_{HSS}}{\Omega_{LSS}}\right)^2$, J_{Gen} the high speed shaft generator inertia)

$M_{x\,|\,shft}$ is composed by:

- The low speed shaft, $M_{LSS_{rigid}\,x}$
- The resistive generator torque transmitted to the low-speed shaft due to the electrical conversion or braking, which is denoted Q_{gen} .

Reorganizing Eq. (3.3) leads to Eq. (3.4) , which establishes the link between the low speed shaft torque and the generator torque.

$$\boldsymbol{M_{LSS_{rigid}\,x} = Q_{gen} - J_{Shft}\,\dot{\Omega}_{rotor}} \tag{3.4}$$

Summary

The different contributions to the setpoint load tensor, expressed in the shaft frame R_{shaft} tilted compared to the tower top frame of reference, could be summed-up by Eq. (3.5):

$$F_{set} = \begin{pmatrix} F_{aero\,x} \\ F_{aero\,y} \\ F_{aero\,z} \\ 0 \\ M_{aero\,y} \\ M_{aero\,z} \end{pmatrix} + \begin{pmatrix} 0 \\ 0 \\ 0 \\ M_{LSS_{rigid}x} \\ 0 \\ 0 \end{pmatrix} + \begin{pmatrix} 0 \\ 0 \\ 0 \\ 0 \\ M_{gyro\,y} \\ M_{gyro\,z} \end{pmatrix} + \begin{pmatrix} F_{I\,flex\,bld\,x} \\ F_{I\,flex\,bld\,y} \\ F_{I\,flex\,bld\,z} \\ M_{I\,flex\,bld\,x} \\ M_{I\,flex\,bld\,y} \\ M_{I\,flex\,bld\,z} \end{pmatrix} + \begin{pmatrix} F_{I\,flex\,drv\,x} \\ F_{I\,flex\,drv\,y} \\ F_{I\,flex\,drv\,z} \\ M_{I\,flex\,drv\,x} \\ M_{I\,flex\,drv\,y} \\ M_{I\,flex\,drv\,z} \end{pmatrix} \quad (3.5)$$

The numerical framework used to compute those loads is presented in part 4.1.

3.1.2 Illustration of load setpoint characteristics

To illustrate the different frequency distribution of the different wind turbine loadings, PSDs of the RNA loads for one particular load case are given in part 3.1.2.1. Then, in part 3.1.2.2, details about the M_x component are given, to explain in details the effect of a freely rotor speed on the M_x setpoint component. In part 3.1.2.3, the illustrating load case is applied for the quantification of the blade, tower and drivetrain flexibilities on the different quantities of interest. Finally, in part 3.1.2.4, the aerodynamic force acting on the tower is compared to the rotor thrust and induced overturning moment.

The illustration case is the same as the one defined in Chapter 2. The main characteristics are:

- Wind and wave conditions defined by $H_s = 8.6m\,;\ T_p = 13s\,;\ U_w = 18m.s^{-1}; T_I = 15\%$,
- OC3 Hywind SPAR FWT (Jonkman, 2010),
- Aero-hydro-servo-elastic simulations performed with OpenFAST. Except for the illustration of the structural flexibility, the active DoF are the 6 platform DoF, the tower fore-aft and side-side modes, and a free rotor speed.

3.1.2.1 Frequency distribution of RNA loads

Figure 14 shows the spectra of the aerodynamic forces (*Aero rotor)*, low speed shaft forces (*Shaft)*, tower top forces *(Nacelle)* and the setpoints loads for the actuators *(SIL setpoint)* as defined in Eq. (3.5).

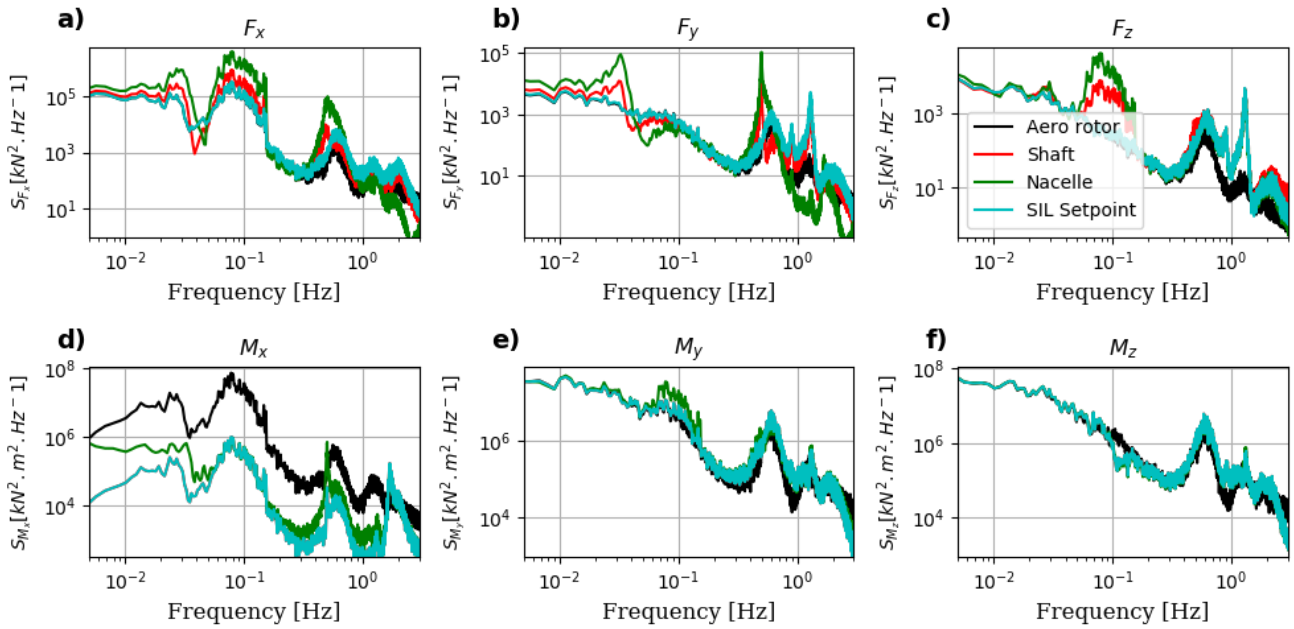

Figure 14: RNA loads decomposition

Different observations from those figures:

- As expected, the inertial loads due to the mass of the RNA significantly increase the resulting loads at the tower top around the 1st fore-aft and side-to-side tower bending mode, at 0.5Hz. This is particularly visible on Figure 14.a, and Figure 14.b for the F_x and F_y load components with the peak at 0.5Hz being significantly higher for the nacelle loads than for the aerodynamic loads. During a wave tank test, a force transducer measuring the total force acting at the tower top will also measure this large inertial contribution. This could make the evaluation of the force only produced by the actuator a hard task if the signal-to-noise ratio (SNR) is not sufficiently high.
- For the wave frequency bandwidth (~0.1Hz), the inertial loads have also a large contribution.
- For the 3P component (~0.6Hz), most of the energetic content is already contained in the aerodynamic loads. This 3P content is a large contributor to the total loading for all the load components
- The setpoint load for the actuators is quite similar to the aerodynamic loads but differs for some load components and frequency bandwidth:
    - The M_x torque setpoint energetic content is much smaller than the aerodynamic torque. This topic is covered in part 3.1.2.2.
    - For the other load components, the differences are particularly important at the blades natural frequencies (0.9Hz and 2.0Hz). There are also some small differences on M_y and

M_z (Figure 14.d and Figure 14.e) especially at the wave frequencies (~0.1Hz) due to the gyroscopic torques.

Those observations are useful to provide insights about the energetic content for the actuators setpoint loads. The aerodynamic loads, for this load case, are by far the main contributor to the setpoint loads. However, taking into account flexible blades can severely increase the energetic content at the blades natural frequencies.

3.1.2.2 Torque setpoint

To better understand how the torque variations on the shaft are smaller compared to the incident aerodynamic torque on the rotor, an illustration for one load case has been performed. For the same illustrating load case as before, the different torque and power are superposed on a short portion of the time series in Figure 15. For this illustration, the tower was considered rigid in the simulation. Being in the above-rated region, the control strategy is based on a constant generator torque and variable blade pitch angle.

To make comparable results between the different quantities, the electrical generator torque has been multiplied by the gearbox ratio, and the moment arm effect of the aerodynamic F_y force on the tower top torque M_x has been withdrawn. $LSShaft$ denotes the low speed shaft, *aero* denotes the aerodynamic component, Twr_{top} denotes the tower top torque and Ω is the rotor speed Ω_{rot}. The rotor speed and blade pitch angle are also plotted at the bottom of the figure to clearly identify the phase between the signals.

The expressions given in part 2.2 superpose well with the OpenFAST output. We observe:

- $M_{aero\,x} - J_r\dot{\Omega}_{rot} \sim M_{LSShaft\,x}$
- $M_{LSShaft\,x} - J_{shft}\dot{\Omega}_{rot} \sim Q_{gen} \sim constant$
- $M_{LSShaft\,x} \sim M_{twr\,top}$

Some small differences in the above mentioned equalities are due to the mesh mapping differences between the aerodynamic module and the structural module. In terms of power generated, this example highlights the large variations in the electrical generator power for floating wind turbines especially at the wave frequencies. The variation of the aerodynamic torque (and power), especially at the wave frequencies, is significantly higher than the variation of the low-speed shaft torque and generator power. This highlights that fixing the rotor speed and the blade pitch angles during the test - as it is sometimes the case for a simplified validation of numerical models – will probably significantly increase the dynamic variations of the M_x setpoint.

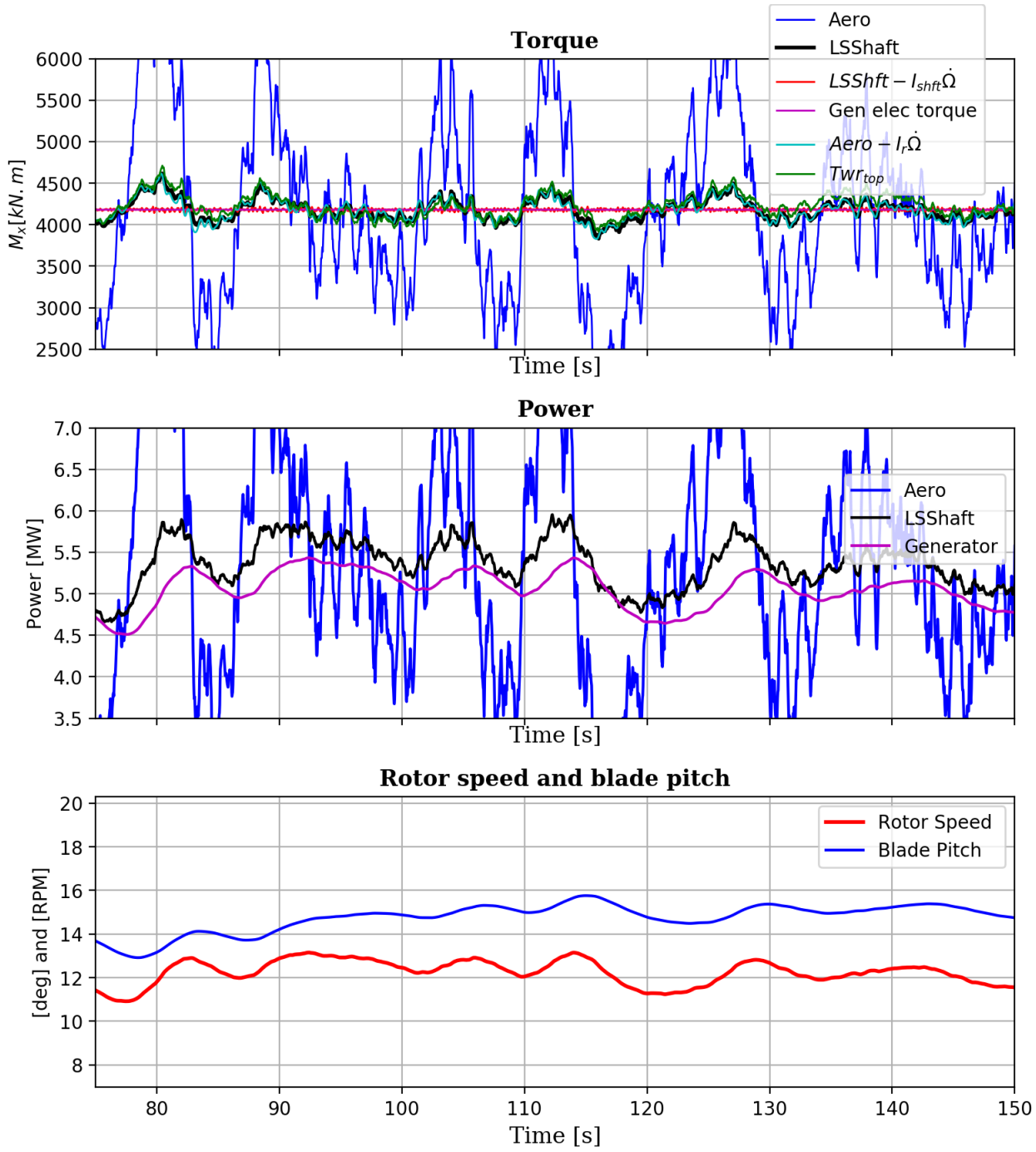

Figure 15: M_x propagation along the shaft and associated power. Top plot: Comparison between aerodynamic, generator torque, low speed shaft torque and simplified formula. Middle plot: Aerodynamic, Mechanical and electrical power. Bottom plot: Rotor speed and blade pitch angle variations

3.1.2.3 Effect of structural flexibility

The effects of the blade, tower and drivetrain flexibilities on the setpoint force and other quantities of interest are now addressed. These flexibilities - aero-elastic modeling of the blades, tower and drivetrain torsion – are taken into account, for the blades and the tower, via modal shapes decomposition in ElastoDyn. The shapes of the modes are computed in BModes (Bir, 2005) considering cantilevered - free beams. For the blades, they are the 1st and 2nd flapwise modes, as well as the 1st edgewise mode. For the tower, they are the 1st and 2nd fore-aft and side-side modes. This approach is limited for large 10 MW rotors and Finite Elements Analysis (FEA) solvers should be preferred. Moreover, for offshore wind turbines, the tower modes are coupled with the foundation modes. The

hydro-elasticity could also impact the frequencies, the shapes and the damping of those modes (Borg, Bredmose and Hansen, 2017; Pegalajar-Jurado *et al.*, 2018). For the drivetrain, an equivalent spring-mass-damper system is considered (Jonkman *et al.*, 2009).

Considering blade or drivetrain flexibility significantly increases the rotor loads setpoint at the natural frequencies of the blade modes (flapwise and edgewise) and drivetrain torsional mode. To a smaller extent, it also changes the rotor loads setpoints at other frequencies. From what has been observed by (Yu, 2017; Lupton and Langley, 2019), the effect is relatively minor on the platform motions.

3.1.2.4 Contribution of the tower aerodynamic drag

As presented in part 3.1.1, the tower aerodynamic drag has been neglected in the actuators setpoints. In this part, we briefly cover the content of this force and its relative contribution.

The tower aerodynamic drag $\overrightarrow{F_{twr\ drag}}$ is due to the wind field acting on the wind turbine tower. The tower is usually a conical steel cylinder. The wind flow impacting the tower is $\overrightarrow{U_{local}}$, a 3D wind field disturbed by the rotating blades and U_∞ is the incident undisturbed wind field.

A simplified expression of the tower drag is given by Eq. (3.6) (Bachynski, 2014):

$$\overrightarrow{F_{twr\ drag}} = \frac{1}{2}\rho_{air}\begin{pmatrix}\sum_z C_{D\ twr}(z)D_{twr}(z)\left|U_{(local\ |x)(z)}\right|U_{(local\ |x)(z)}\delta_z \\ \sum_z C_{D\ twr}(z)D_{twr}(z)\left|U_{(local\ |y)(z)}\right|U_{(local\ |y)(z)}\delta_z \\ 0\end{pmatrix} \tag{3.6}$$

With:

- $U_{local\ |x}(z)$ the x component of the local velocity.
- $U_{local\ |y}(z)$ the y component of the local velocity.
- $C_{D\ twr}(z)$ a drag coefficient for each tower section.
- δ_z an infinitesimal length in the z direction

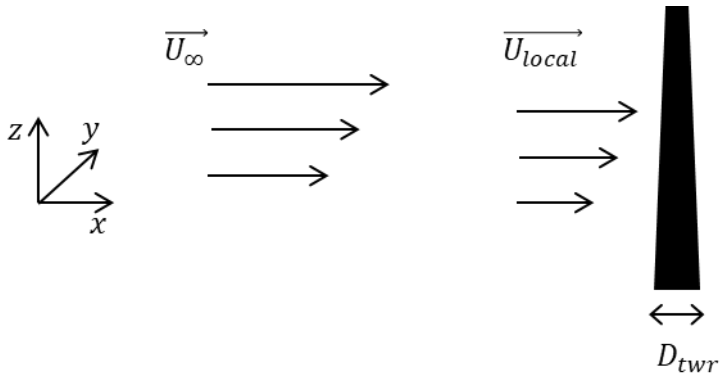

Figure 16: Wind field acting on the tower

In general case, the drag coefficient is Reynolds dependent and Keulegan-Carpenters dependent for oscillatory flows (Molin, 2002). The U_{local} velocity is due to the incident wind field but also due to the velocities of the tower sections. $U_{local} \sim \alpha_{induction}\left(U_\infty - \dot{X_{twr}}\right)$ with $\alpha_{induction}$ a coefficient related to the induction factor of the rotor.

To ease the separation of the different contributions, we do the following assumptions:

- The flow is mostly unidirectional in the x direction and there is no vertical shear.

- The diameter is constant and the drag coefficient does not vary with z.
- The local flow on the tower is close to the undisturbed flow $\alpha_{induction} \sim 1$

Then Eq. (3.6) simplifies to Eq. (3.7)

$$F_{twr\ drag} = \frac{1}{2}\rho_{air} C_{D\ twr} D_{twr} h_{twr} |U_\infty - \dot{X}_{twr}| (U_\infty - \dot{X}_{twr}) \tag{3.7}$$

For the motions and wind speed of interest, $U_\infty > \dot{X_{twr}}$. Eq. (3.7) is equivalent to Eq. (3.8)

$$F_{twr\ drag} = \frac{1}{2}\rho_{air} C_{D\ twr} D_{twr} h_{twr} \left(U_\infty^2 - 2\dot{X}_{twr} U_\infty + \dot{X}_{twr}^{\ 2}\right) \tag{3.8}$$

By doing a Taylor expansion at first order using $\frac{\dot{X_{twr}}}{U_\infty} << 1$, the tower drag force simplifies to Eq. (3.9):

$$F_{twr\ drag} \sim \frac{1}{2}\rho_{air} C_{D\ twr} D_{twr} h_{twr} (U_\infty^2 - 2\dot{X}_{twr} U_\infty) \tag{3.9}$$

This simplified expression of the tower drag defines the different contributions:

- A drag force proportional to the square of the incident freestream velocity, i.e. constant for a given incident wind velocity,
- A damping term.

The steady force is given approximately by Eq. (3.10):

$$F_{twr\ drag\ steady} \sim \frac{1}{2}\rho_{air} C_{D\ twr} D_{twr} h_{twr} U_\infty^2 \tag{3.10}$$

The relative contribution of the steady force is given in Figure 17 with the following parameters for the DTU 10MW(Bak *et al.*, 2013):

$$C_{D\ twr} \sim 0.65\ ;\ h_{twr} = 115.6m;\ D_{twr} = 6.9m;\ \rho_{air} = 1.225\ kg.m^{-3}$$

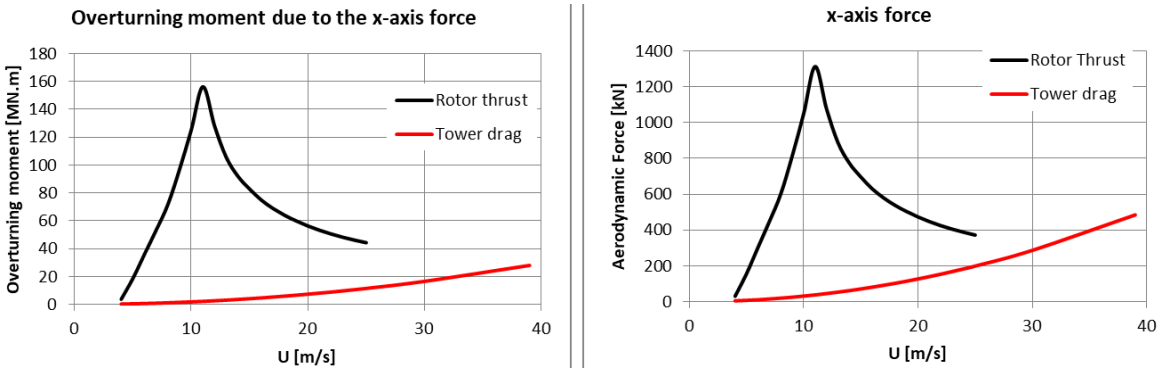

Figure 17: Steady rotor thrust compared to steady drag on the tower and their induced overturning moment for the DTU 10MW RWT

The important outcomes are:

- For wind speed close to the cut-out wind speed (25 m/s) of this wind turbine, the steady contribution of the tower drag is approximately half the steady contribution of the rotor thrust.
- For survival wind conditions (wind speed up to 40 – 50 m/s), the drag on the tower reaches higher values than the rotor thrust near the cut-out wind speed.
- Concerning the induced overturning moment about the tower base, the relative contribution of the tower drag is divided by approximately 2 compared to x-axis force.

The conclusion is that neglecting the tower drag has a certain effect at least on steady values, but only for high wind speeds regions ($> 20m.s^{-1}$). From the induced overturning moment, the tower drag effect is expected to be more important for the platform surge and tower fore-aft than for the platform pitch.

3.2 Loads setpoints: specifications

To select and design the actuators, different characteristics of the setpoints loads are required:

- average and maximum values,
- frequency distribution of these efforts and in particular the maximum frequency to consider.

Thereby, in order to better understand the nature of the forces and moments to model and particularly their frequency content, an analysis based on numerical simulations has been performed.

3.2.1 Scope of the parametrical study

A set of baseline wind and wave conditions are simulated for different FWTs. These baseline simulations provide the specifications for each load component in terms of load ranges and dynamic characteristics. The frequencies of interest for each quantity are highlighted. The considered floating wind turbines along with the numerical model parameters are presented in part 3.2.1.1 and the selection of the wind and wave conditions are detailed in part 3.2.1.2. The outcomes of this parametrical study are detailed in part 3.2.2

The original contributions of this study concern the different types of FWTs and the realistic and large number of load cases.

3.2.1.1 Selected floating wind turbines

Different well-documented models of floating wind turbines are selected from the literature. They consist in SPAR and semi-submersible floaters in order to obtain different requirements depending on the floater type. An overview of the considered floating wind turbines is given in Table 9. For the TripleSpar_10 MW (Lemmer *et al.*, 2016), the hydrodynamic database was recalculated using the Boundary Element Methods code NEMOH (Babarit and Delhommeau, 2015) because excitation forces at different wave directions were not available in the open source model.

The NREL baseline offshore controller as detailed in the OC3 and OC4 project reports (Jonkman, 2010; Robertson *et al.*, 2014) is used for the 5MW floating wind turbines. The modified DTU Baseline controller for the DTU 10 MW as described by (Hansen *et al.*, 2005) and (Lemmer *et al.*, 2016) is used for the 10MW floating wind turbine. They both use collective blade pitch control and generator torque control, with detuned gains in order to avoid negative damping for the platform pitch motions.

Name of FWT	**OC4_Semi**	**OC3_Spar**	**TripleSpar_10MW**
Representative picture	 (Robertson *et al.*, 2014)	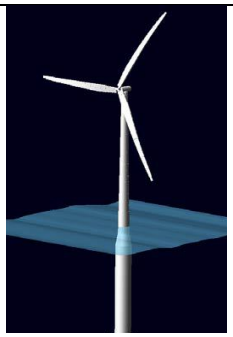 (Jonkman, 2010)	 (Lemmer *et al.*, 2016)
Wind Turbine	NREL-5MW (Jonkman *et al.*, 2009)	NREL-5MW (Jonkman *et al.*, 2009)	DTU-10MW (Bak *et al.*, 2013)

Table 9: Selected Floating wind turbines for numerical simulations

Note that aerodynamic loads are expressed in the hub frame, see the *conventions* section at the beginning of this manuscript.

3.2.1.2 Selection of suitable test cases

To define the relevant wind and waves conditions to simulate, it has been decided to follow the design load cases (DLC) recommended by the standards (IEC, 2009; DNV GL, 2016) for a given floating wind turbine site. These wind and wave conditions are expected to be run by a floater designer in wave tank testing when validating a FWT platform design. The focus here was to select DLCs that may provide a global significant dynamical behavior. They are expected to lead to the highest loads on the rotor due to the combination of high levels of turbulence, severe wave conditions and wind-wave misalignment. For the guidelines, the DNVGL-ST-0437 (DNV GL, 2016) and the IEC 61400-3 (IEC, 2009) have been followed. Among the design load cases (DLCs) associated to an operating rotor, DLC type 1.2, 1.3, 1.4, 1.5 and 1.6 are considered as relevant load cases for wave tank testing purpose. Parked rotor conditions with high wind speed and extreme waves (DLC 6.x) are not treated in this study because the aerodynamic loads are different (drag forces on the feathered blades and on the tower) and could not be necessarily reproduced with the same actuator layout.

In order to define the relevant load cases, environmental data characteristics of harsh environmental conditions are required. It is expected that the most harsh conditions (very severe sea states and high turbulence levels basically) will induce the most important aerodynamic loads. A brief summary of the procedure for load cases choice is given in Figure 18 to facilitate the understanding.

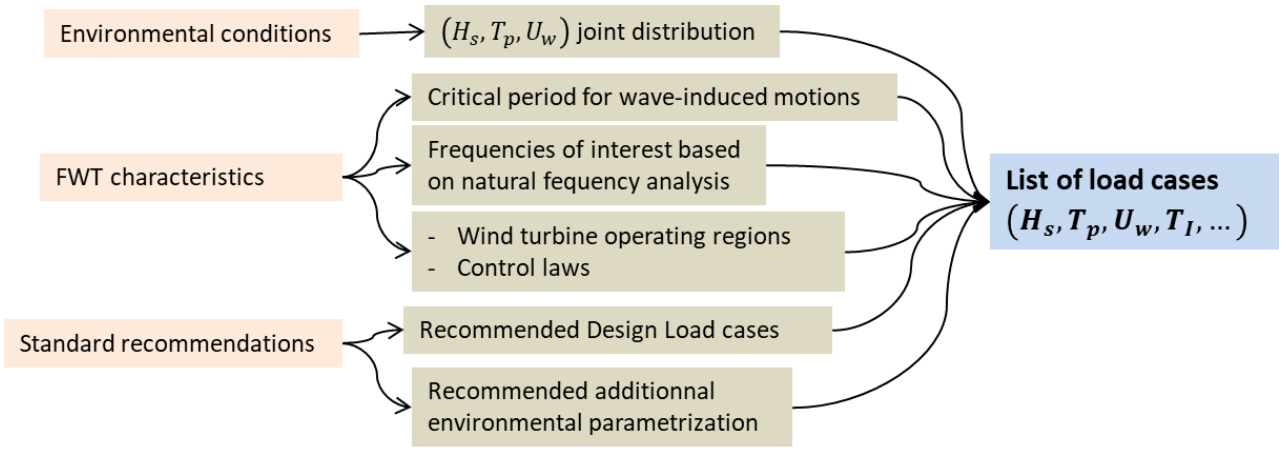

Figure 18: Procedure for load cases choice

The definitions of the required parameters and the choice made concerning the wind and wave conditions are detailed hereafter.

Wind conditions:

From DNVGL-ST-0437, the turbulence intensity levels for the Normal Turbulence Model (NTM) and the Extreme Turbulence Model (ETM) are input to the load cases definition. High levels of turbulence are assumed with class OA (see part 2.2.3 in DNVGL-ST-0437), which lead to the turbulence intensity levels as shown on the right of Figure 21. The turbulent wind fields are defined by Kaimal spectra (Kaimal *et al.*, 1972) using the TurbSim (Jonkman, 2009) pre-processor.

A few wind speeds are considered. Firstly, the rated wind speed, 11.4 m/s for the two reference wind turbines, as it gives the maximal mean thrust. Additionally, one wind speed above rated (18 m/s) and one wind speed below rated (8 m/s) have been considered for different control strategies and resulting forces acting on the rotor.

Wave conditions:

From DNVGL-ST-0437, the wave conditions for the Severe Sea State and the Normal Sea States need to be defined. Both a 50 years contour of (H_s, T_p, U_{hub}) (for the Severe Sea States) and the expected values of H_s depending on the hub velocity $H_s = E[H_s|U_{hub}]$ (for the Normal Sea States) are required. These wave conditions are based on the Norway 5 site (Li, Gao and Moan, 2015), with a suitable parametrization to use an Inverse First Order Reliability Method (I-FORM) methodology. Waves are described by JONSWAP spectra (Hasselmann *et al.*, 1973), with the peak enhancement factor of the spectra computed from the norm recommendation.

- For the Severe Sea States, different correlated (H_s, T_p, U_{hub}) contours have been computed. They are shown on the left part of Figure 21.
- For the Normal Sea States, the range proposed by DNVGL-ST-0437 for the wave peak periods has been considered. This range is expressed in Eq. (3.11).

$$11.1\sqrt{\frac{H_{s,NSS}(U_{hub})}{g}} < T_p < 14.3\sqrt{\frac{H_{s,NSS}(U_{hub})}{g}} \tag{3.11}$$

With $H_{s,NSS}(U_{hub})$ the wave height of the Normal Sea State (NSS) correlated to the hub velocity U_{hub}, and g the gravity.

To help in the selection of the most critical peak periods for the considered FWT, the motions Response Amplitude Operators (RAO) of the floating wind turbines have been computed. These RAOs are expressed in an earth-fixed frame with origin at (0, 0, 0), i.e. intersection of the Mean Sea Level (MSL) and of the platform vertical centerline. In order to compare different motion characteristics for different incident wave directions, the x-axis is defined by the wave direction as illustrated in Figure 19. This is the difference with the inertial frame defined in the conventions section. This makes possible to define consistent out-of-plane and in-place motions for different incident wave directions. These out-of-plane motions are called Y, R_X and R_Z.

As explained in chapter 4, the velocities and accelerations at hub height are important parameters for the thrust variations. The wave-induced hub motions could be expressed by a combination of wave-induced platform surge and pitch motions. Indeed, the wave induced velocity is expressed as Eq.(3.19).

$$U_{hub,\ wave-induced}(t) = \dot{X}(t) + h_{hub} * \dot{R_Y}(t) \tag{3.12}$$

The wave-induced velocity RAO at hub height is then $\dot{X}(\omega) + h_{hub} * \dot{R_Y}(\omega)$ and the wave-induced acceleration RAO at hub height $\ddot{X}(\omega) + h_{hub} * \ddot{R_Y}(\omega)$. The velocity RAO is used for looking at the maximum wave-induced thrust variation Δ_{F_x} and the acceleration RAO is used for the maximal temporal derivative $\frac{\partial F_X}{\partial t}$. The platform yaw velocity is used for the maximal variations of the rotor torque around the Z axis (M_z). In Figure 20, the platform velocities RAO are represented for the 3 floaters, as well as the velocities and accelerations RAO at hub height.

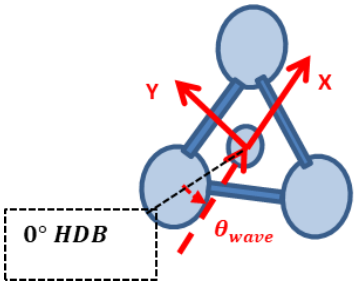

Figure 19: Frame defined by the incident wave direction. $\boldsymbol{\theta_{wave}}$ is the incident wave direction and HDB is the hydrodynamic database for the calculation of the diffraction and radiation forces.

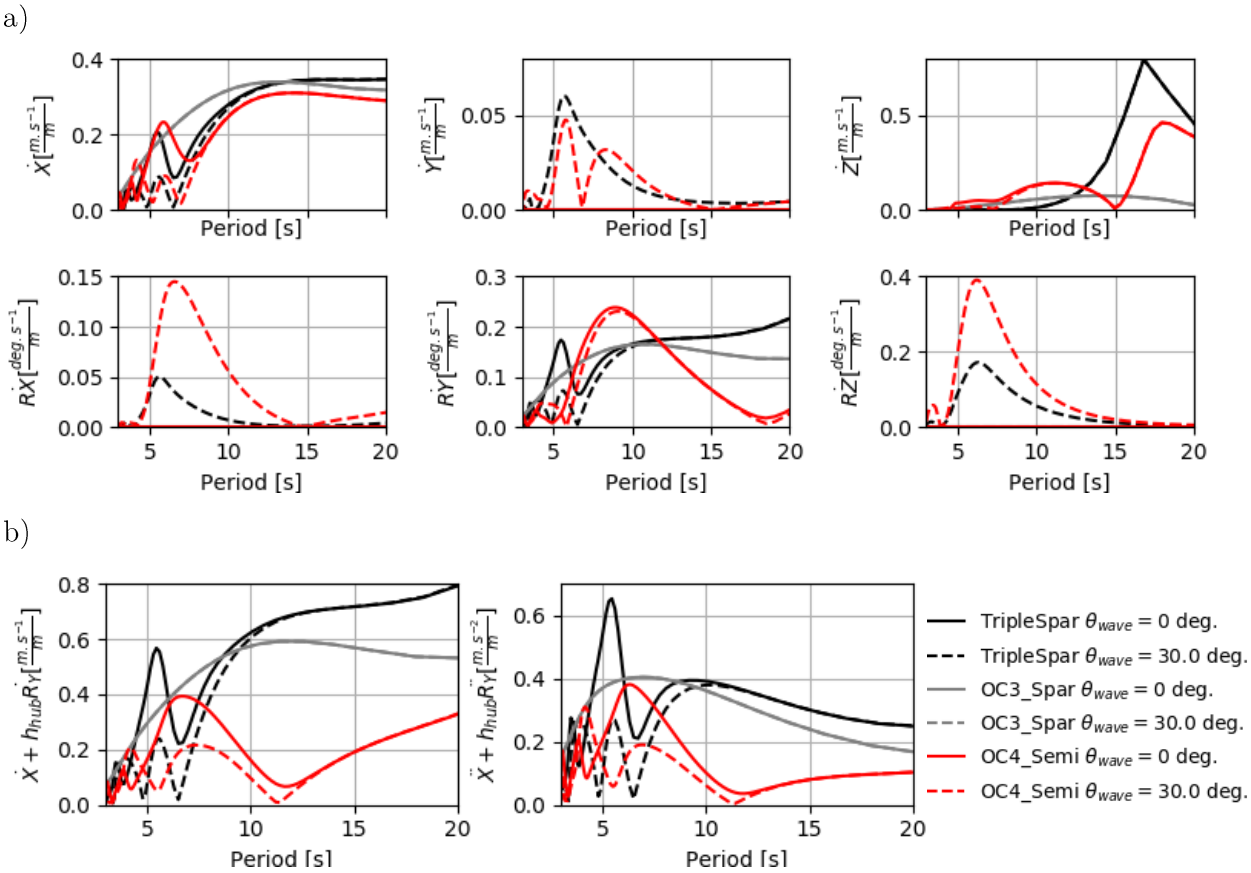

Figure 20: RAO of the 3 floaters, for 2 incident wave directions. (a)Velocity RAO of the different floaters at origin point (b) Velocity and acceleration RAO at hub height for the different floaters

For the three criteria listed in Table 10, different ranges of wave periods are defined for each floater. These ranges are then used in the definition of appropriated load cases. Finally, a total of 31 load cases are considered for each FWT.

Criteria	OC3_Spar	OC4_Semi	TripleSpar_10MW
Max acceleration at Hub (Figure 20.b right)	[5.5-9]s	[5.5-7.5]s	[5-6]s and [8-12]s
Velocity max at hub (Figure 20.b left)	[10-16]s	[6-8]s and [18-20]s	[5-6]s and >10s
Yaw velocity max (Figure 20.a bottom right)	None	[5-8]s	[5-8]s

Table 10: Wave peak periods of interest to get maximum wave-induced hub motions and maximum platform yaw motions.

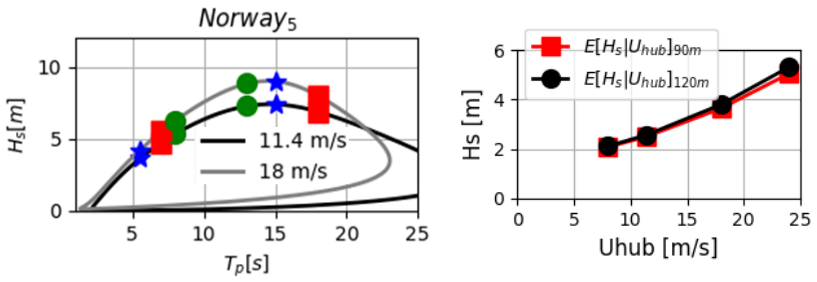

U_{hub} [m/s]	8	11.4	18
E[$H_s|U_{hub}$] [m]	2.1	2.6	3.8
Tp [s]	[5.1-6.6]	[5.7-7.4]	[6.9-8.9]
TI ETM [%]	38.4	31.0	24.6
TI NTM [%]	17.2	15.0	14.6

Figure 21 Left: $(\boldsymbol{H_s, T_p})_{\boldsymbol{50years}}$ *for 3 wind speeds at 90m. Red squares are the values for the OC4_Semi, green circles for the OC3_Spar and blue stars for the TripleSpar. Middle: Expected* $\boldsymbol{H_s}$ *for different mean wind*

speed at 90m. Right: Wind speed, expected significant wave heights, range of peak periods and turbulence intensity levels recommendations for class OA.

To conclude, a parametrical study has been used for the specification of the rotor loads and their effects on the FWT behavior. Different FWTs have been used to get the specificity of each floater, and a list of load cases have been defined based on:

- FWT's specificities
- Realistic environmental conditions
- Design Load Cases (DLC) from the standards

Different limitations of this parametrical study have been identified. These limitations are described in the perspectives section of this manuscript (chapter 9). To take those limitations into account in the design process, some safety factors have been defined for the maximal loads and the frequencies of interest.

3.2.2 Summarized loads specifications

In this part, the load characteristics are summed up for the different load cases in terms of mean, max and frequency content. As explained in Chapter 2, a separation between different frequency bandwidths is used for facilitating the analysis. The frequency bandwidth limits, for this study, are specified in Table 11.

	LF	R_Y **NF**	**WF**	**Twr & 3P**	**> 3P**
f_{low} [Hz]	0.01	0.03	0.04	0.4	0.8
f_{high} [Hz]	0.03	0.05	0.33	0.8	2.0

Table 11: Limits of the frequency bandwidths at full scale

3.2.2.1 Frequency distribution

In Figure 22, the maximum of the standard deviations of $F_{rotor\ setpoint}$ among the three platforms and all the load cases, are represented for each frequency bandwidth. To make comparable results between the 10MW and the 5MW wind turbines, a scale factor of $\lambda_{power} = \frac{10}{5}$ has been defined to scale down DTU 10MW setpoints loads. The assumption that has been made is that forces scale with λ_{power} and moments with $\lambda_{power}^{\frac{4}{3}}$ (Bak *et al.*, 2013).

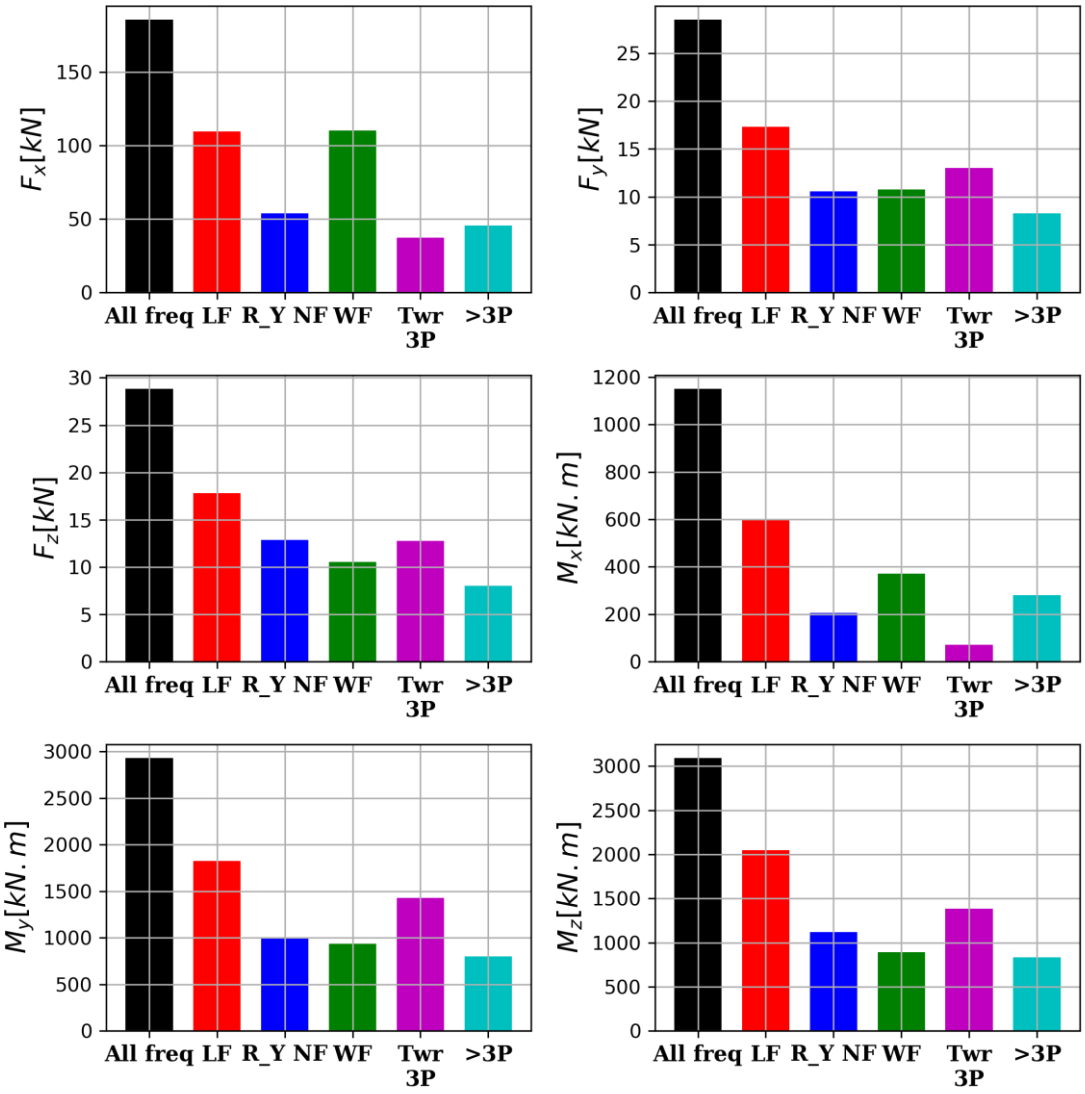

Figure 22: Maximum standard deviations of the aerodynamic load components encountered for all tested platforms and DLCs by frequency bandwidth

As expected, one can notice on Figure 22 that the thrust variation (F_x) is predominant at the wave frequency for all the load cases. For the other load tensor components - which have a smaller influence on the overall motions of the wind turbine (Bachynski, Chabaud and Sauder, 2015) – the energetic content is quite significant around the 3P/Tower bending mode but is smaller in the wave frequency range. As a consequence, actuators in charge of reproducing the F_x component will have large oscillating setpoints at wave frequencies while for the other components the oscillations will be more spread around the different frequencies.

To pursue the frequency distribution of the setpoint loads and the actuators related load setpoints, another indicator identified by previous studies (Azcona *et al.*, 2014; Meseguer and Guanche, 2019) is the maximum temporal derivatives of each aerodynamic load component. Large temporal derivatives may lead to saturations of the actuators thrust variations, as presented in chapter 4. Those derivatives have been computed, in post processing for different perfect low-pass filters (based on Inverse Fast Fourier Transform *IFFT*), with different cut-off frequencies. The maximum derivative value, along the different load cases (DLC types 1.2, 1.3 and 1.6.), has been computed for each cut-off frequency. This is presented in Figure 23 with the main frequencies of interest represented by vertical lines.

While a more or less constant slope between the derivatives and the cut-off frequency appears, this is not due to an identification of the low pass filtering technique. This is due to a large frequency distribution in the load setpoint, each bandwidth contributing more or less to the overall variations of the setpoint load tensor. Different contributions can be highlighted:

- For the F_X component, there is a strong impact of the wave frequency bandwidth on the maximum load derivative.
- There is no jump in the maximum derivative requirement around the tower mode frequency, but there is a steep increase at the 3P frequency.
- Above the 3P rotor frequency, the only modeled physical phenomenon was the blade-tower interaction (creating minor 6P and 9P variations) and the turbulence wind inflow. For high frequency, the energetic content of the Kaimal spectrum has a -3/2 slope in a logarithmic diagram.
- For all the load components, specifying a maximum derivative should be done in accordance to a maximum frequency captured.

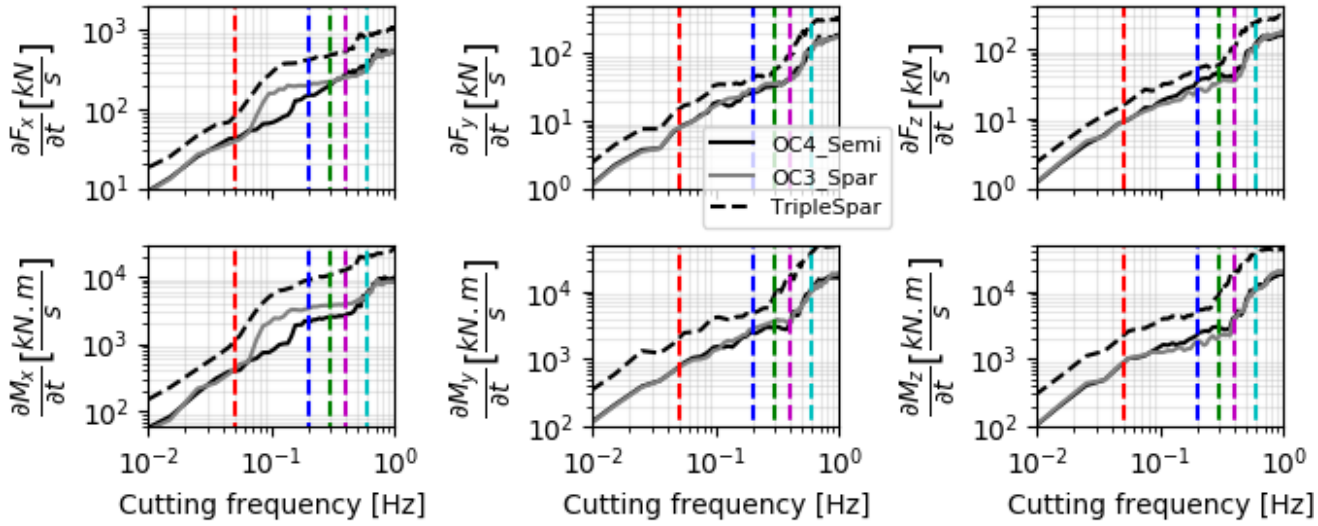

Figure 23: Maximum variation of low pass filtered aerodynamic load components. Red: coarse limit of significant energy of low frequency wind turbulent force, compared to wave excitation force. Blue: 1P frequency of the NREL 5MW above rated. Green: first fore-aft moment of the wind tower mast. Magenta: Rough estimation of maximum wave frequency of interest. Cyan: 3P frequency of the NREL 5MW above rated.

3.2.2.2 Mean loads

A first overview of the influence of the different components of the aerodynamic loading on FWT motions could be given by steady wind cases. Simulations are run in still water with steady wind speeds of 8, 11.4, 18 and 24 m/s. A power law with $\alpha = 0.14$ is used for the vertical wind speed profile and the rotor-tower influence is modeled.

The mean rotor aerodynamic forces in the hub frame are summarized in Table 12 using grayed scales for each load component from low (white) to high (dark grey) values. These are the values for the OC3_SPAR platform. The mean forces and moments increase with the wind speed, except for F_x and M_z. This is due to the increasing blade pitch angle in the above-rated region. This strategy is used to mitigate the aerodynamic performance of the rotor and maintain a rated power production.

	NREL 5 MW				DTU 10MW			
U_w [m/s]	**8**	**11.4**	**18**	**24**	**8**	**11.4**	**18**	**24**
F_x [N]	3.6E+05	7.0E+05	3.6E+05	2.8E+05	7.2E+05	1.5E+06	7.1E+05	5.7E+05
F_y [N]	-4.1E+03	-8.5E+03	-1.9E+04	-2.6E+04	-9.8E+03	-2.0E+04	-3.7E+04	-5.0E+04
F_z [N]	1.2E+03	3.1E+03	1.1E+04	2.3E+04	3.4E+03	7.2E+03	1.9E+04	4.0E+04
M_x [N.m]	1.9E+06	4.1E+06	4.2E+06	4.2E+06	5.6E+06	1.0E+07	1.0E+07	1.0E+07
M_y[N.m]	5.8E+05	1.1E+06	2.1E+06	2.3E+06	1.6E+06	3.4E+06	6.0E+06	7.3E+06
M_z [N.m]	1.6E+05	4.0E+05	-3.5E+05	-9.8E+05	5.3E+05	1.4E+06	-3.8E+05	-2.0E+06

Table 12: Mean aerodynamic forces for the 5MW and 10MW RWT

3.2.2.3 Maximum loads

The transient state being skipped in the analysis, Figure 24 illustrates the maximum setpoint load components. Each FWT is denoted by a symbol (+, o and ☆), and the different load cases are split (DLC 1.2, 1.3 and 1.6). Note that, to facilitate the analysis of the figures, a lateral spreading has been randomly introduced. After preliminary analyses of the time series, DLC 1.4 and 1.5 have been removed from the requirements as leading to very high transcient values. It has been considered that these load cases will not be necessarily reproduced during wave tank testing.

The DLC 1.3 and 1.6 leads to the maximum values for all the load components. Most of the load components (F_y, F_z, M_y and M_z) seem to be turbulence-driven (related to the DLC 1.3 and its extreme turbulence model) while F_x is both wave-driven (related to the DLC 1.6 and its severe sea state) and turbulence-driven.

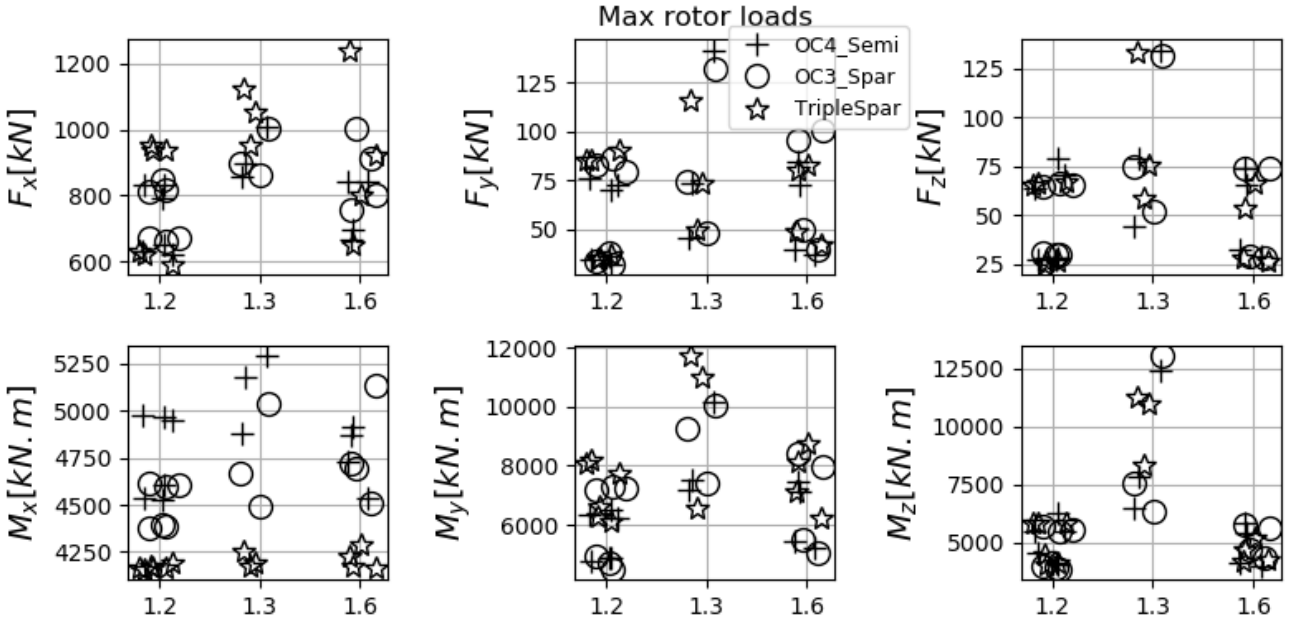

Figure 24: Maximum load component for the 3 platforms and the different DLC.

The maximum values for each load component, considered as inputs to the design of the actuators, are given in Table 13. A safety factors of 1.3 is integrated to take into account limitations of this study. The maximum values of the F_y and F_z components are one order of magnitude below the F_x load component. This makes the requirements for representing F_x much more important than the F_y and F_z requirements. However, this requirement is expressed in the hub frame, which rotates with the nacelle. Applied to a wave tank system, this means either a change of the nacelle angle when the initial

orientation of the nacelle is modified, or requirements being more symmetrical to be able to reproduce the F_x load component in different directions.

F_x [kN]	F_y [kN]	F_z [kN]	M_x [kN.m]	M_y [kN.m]	M_z [kN.m]
1.5 E+3	1.6 E+2	1.6 E+2	6.8 E+3	1.6 E+4	1.6 E+4

Table 13: Maximum SIL setpoint load component for a 5MW FWT

To conclude, depending on the type of physical phenomena that want to be investigated or reproduced in wave tank experiments, the requirements for the dynamic responses significantly change. The mean and maximal values for each load component have been defined, to provide starting points for SIL system design.

3.3 Partial reproduction of the setpoint loads

In this part, the main focus is on anticipating the effect of the SIL system limitations on the FWT global motions during the wave tank tests. Firstly, a simplified analytical model presents how latency and actuator bandwidth impact the actuated force characteristics. Secondly, the parametrical study initiated for a characterization of the loads was extended to mimic the experimental setup limitations. Indeed, the experimental setup, with its selected actuators, will not apply the load setpoint as it is computed. The objectives of this study is to check the effects of the partial reproduction of the actuated loads. This could provide guidelines in the actuators choice, number and layout. A similar methodology has already been used in other works for latency effect and actuator bandwidth effect (Hall, Goupee and Jonkman, 2017) and load component removal effect (Bachynski, Chabaud and Sauder, 2015) on floating wind turbines.

3.3.1 Admissible delay

In this subsection, a simplified analytical model of a harmonic oscillator is introduced to get order of magnitudes about suitable delays of the overall SIL real-time system depending on the natural frequency of the system.

As explained in chapter 2, one of the artifacts introduced by hybrid methodologies is a pure delay $\tau_{puredelay}$. This delay is due to the communication, processing time, and filtering techniques needed in the methodology (see chapter 5). Another source of delay is the phase lag due to the actuator dynamic response (Chabaud, 2016), denoted τ_{dyn}. To anticipate the effect of the SIL system delay on the FWT behavior, a simple one DoF harmonic oscillator is considered. The objective of this simple harmonic oscillator is to provide guidelines about acceptable phase corresponding to the delay in real-time system. The corresponding DoF of the FWT system could be the tower deflection in the fore-aft direction or any platform DoFs. The mechanical system is the {tower + RNA + floater} system. The 2nd law of Newton applied to this one DoF harmonic oscillator leads to Eq. (3.13) (Molin, 2002):

$$\ddot{X} = -2\zeta_1\omega_0\dot{X} - \omega_0^2 X + \frac{F_{ext}}{M} \tag{3.13}$$

With:

- $\omega_0 = \sqrt{\frac{K}{M}}\ [rad.s^{-1}]$. K is the system stiffness and M the system mass.
- $\zeta_1 = \frac{B_1}{B_c}[-]$ the linear damping ratio – due to the hydrodynamics forces (radiation, drag) or due to the structural properties (internal damping). It is expressed as a ratio with the critical damping $B_c = 2 * \sqrt{KM}$.

Oscillations at the natural frequency of this DoF, $\omega_{nat} = \frac{\sqrt{4KM-B^2}}{2M}$ are considered, with B the total damping of the system. The external forces F_{ext} are the actuated forces at the tower top. Denoting F_{set} the setpoint load for the actuator (basically aerodynamic load), the actuator reproduce this force with the delay $\tau_{act} = \tau_{dyn}(\omega_{nat}) + \tau_{puredelay}$ and an attenuation $0 \leq G(\omega_{nat}) \leq 1$ as expressed in Eq. (3.14):

$$F_{ext}(t) = G(\omega_{nat}) F_{set}(t - \tau_{act}) \tag{3.14}$$

To ease the understanding of this development, different assumptions are made:

- the attenuation of the actuated force from the setpoint force due to the actuator dynamics is neglected, i.e. $G(\omega_{nat}) = 1$;
- the other sources of damping are neglected, i.e. $\zeta_1 = 0$;
- the setpoint load F_{set} is made of a slowly varying term F_0 and a damping term ζ_{aero} (aerodynamic damping), as in Eq. (3.15). ζ_{aero} is the aerodynamic damping expressed in percentage of the critical damping $\zeta_{aero} = \frac{B_{aero}}{B_c}[-]$. This decomposition between a damping term and a slowly varying term will be discussed in chapters 4 and 7.

$$\frac{F_{set}(t)}{M} = \frac{F_0(t)}{M} - 2\zeta_{aero}\omega_0 \dot{X}(t) \tag{3.15}$$

This external force $F_{ext}(t)$ can be expressed as in Eq. (3.16):

$$\frac{F_{ext}(t)}{M} = \frac{F_0(t)}{M} - 2\zeta_{aero}\omega_0 \dot{X}(t - \tau_{act}) \tag{3.16}$$

The slowly varying force $F_0(t)$ is not of interest for the oscillations at ω_{nat}. It is neglected hereafter.

The system governing equation Eq. (3.13) becomes Eq. (3.17)

$$\ddot{X} = -2\zeta_{aero}\omega_0 \dot{X}(t - \tau_{act}) - \omega_0^2 X \tag{3.17}$$

To find the solutions of this equation, $\dot{X}(t - \tau_{act})$ needs to be developed. To simplify the problem and to evaluate the effect on the damping (as the resonant response of the system is largely dependent to the damping), simplifications lead to the characteristic equation as in Eq. (3.18).

$$\lambda^2 = -2\omega_0\lambda\left(\zeta_{aero} e^{-\lambda\tau_{act}}\right) - \omega_0^2 \tag{3.18}$$

It is the characteristic equation of the same mechanical system with a resulting damping of $\zeta_{resulting} = \zeta_{aero} e^{-\lambda\tau_{act}}$, λ a root of this characteristic equation.

In Figure 25, the ratio of the resulting damping $\zeta_{resulting}$ divided by the setpoint aerodynamic damping ζ_{aero} is computed for different values of τ_{act} and different values of ζ_{aero}. Two arbitrary thresholds, at 50 % and at 75 % highlight the corresponding admissible phase (delay) of the SIL system to sufficiently reproduce the damping component. With a phase of approximately $\frac{\pi}{4}$, the damping reproduced is 25% smaller than the setpoint one. To achieve an damping component amplitude of 50%, the admissible phase is between $\frac{\pi}{3}$ and $\frac{2\pi}{5}$ depending on the value of ζ_{aero}.

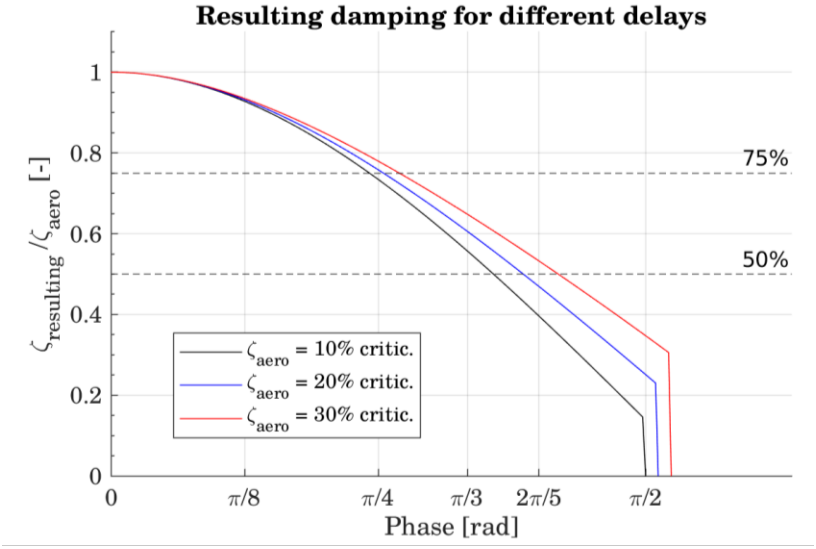

Figure 25: Resulting damping for different delays and aerodynamic damping

To provide guidance about the admissible overall delay of the SIL system for different frequencies of interest, the most severe criterion ($\phi = \frac{\pi}{4}$) has been selected and applied to different scale ratios and full scale characteristic frequencies. This is summarized in Table 14. The selected characteristic frequencies are the tower 1st fore-aft mode natural frequency (target values $f \in [0.3, 0.6, 0.9]$ Hz), a wave peak period ($f \sim 0.12$ Hz) and a platform pitch natural frequency ($f \sim 0.03$ Hz).

	Model scale [-]		
Characteristic frequency at full scale [Hz]	**1/30**	**1/40**	**1/50**
0.03 (platform pitch natural frequency)	760	660	590
0.12 (wave peak period)	190	160	150
0.3 (tower 1st fore-aft mode)	76	66	59
0.6 (tower 1st fore-aft mode)	38	33	29
0.9 (tower 1st fore-aft mode)	25	22	20

Table 14: Admissible delay in [ms] for different model scales and characteristics frequency. The illustrative criterion is $\phi = \frac{\pi}{4}$ (to ensure the reproduction of 75% of the aerodynamic damping)

Consequently, if the highest frequency of interest is the tower 1st fore-aft mode, the admissible overall delay is in the range [20-75]ms. If the highest frequency bandwidth of interest is the wave frequencies bandwidth, this range is [150 - 190]ms. For the SIL system design, this makes the requirements much more severe when targeting the tower 1st fore-aft mode.

3.3.2 Partial reproduction: sensitivity analysis

In the scope of this parametrical study, the selected limitations were of two kinds: load component removal and deteriorated performances of the actuators. Mimicking those limitations in numerical simulations are obtained using different types of modifications within OpenFAST.

3.3.2.1 Effects of the load component removal

The purpose is to check which of the 6 aerodynamic load components have a significant impact on the quantities of interest of the FWT behavior. To do this, a generalized (3 forces and 3 moments) force corresponding to the integrated aerodynamic loads along the 3 blades is modified in the hub frame within the structural module (ElastoDyn). In the scope of this study, the case $M_x = 0$ has not been

simulated for the same reason as the deterioration of the performances (see next subsection): interaction with the servo module was problematic.

Additionally, the F_x load component has not been removed as it was already clear that its effect on the quantities of interest is very important.

This coupled approach methodology has been selected because many physical phenomena act on a FWT. For instance, if the aerodynamic forces change, then the motions of the FWT, the nacelle accelerations will also be different and then the control laws will adapt to this new state of the FWT. Only a coupled approach reproduces instabilities which could occur when a delay becomes too important. Consequently, a coupled approach has been considered much more representative to evaluate precisely the deterioration effect than cancelling *a posteriori* some motions (by frequency bandwidth or by component) which are assumed to be due to the aerodynamic loads.

The objective of calculating relative errors was to impose a certain admissible level of error and to define the admissible performances and required load components to meet this requirement. The same procedure has been adopted by (Bachynski, Chabaud and Sauder, 2015; Chabaud, 2016) with a maximum level of error of 5% on the standard deviation of the quantities of interest. The same value of 5 % has been used here. To avoid high level of relative errors due to very small absolute values, some additional checks have been introduced to ensure consistent comparisons:

- If the standard deviation of the quantity is less than 5 times the sensor accuracy for this quantity, the load case is discarded. The sensors accuracy for this study has been extracted from the OC5 wave tanks experiments (Robertson, 2017).
- Some considerations of both the relative error but also the relative importance are taken into account. The error level on a given bandwidth is neglected in the statistics if the standard deviation for this bandwidth is less than 1/100 of the standard deviation of the unfiltered signals. Indeed, high relative error levels for frequency bandwidth where the quantity is negligible are not of interest.

Results are analyzed in terms of relative error levels on the main quantities of interest. The comparisons are between the baseline cases (perfect actuation) and the deteriorated cases (limited actuation). The selected load cases for this analysis were the DLC 1.2 and 1.6 with normal turbulence model for the wind inflow. The DLCs 1.3 were discarded as leading to a higher sensitivity, higher coupling between aerodynamics and hydrodynamics. This was due to the very high level of turbulence intensity in the Extreme Turbulence Model, which have been considered too severe for the partial reproduction requirements.

Table 15 summarizes the maximum contributions, for different load cases, of a one-by-one load component removal. *neg.* denotes an error level less than the admissible threshold of 5 %. The effects of the different load component removal could be summarized as follow:

- $F_y = 0$ induce large levels of errors on $\ddot{Y}_{Nac}, R_X$ and Y
- $F_z = 0$ induce medium levels of errors on Z for the SPAR platforms
- $M_y = 0$ induce medium levels of errors on $\ddot{X}_{Nac}$ and R_Y
- $M_z = 0$ induce large levels of errors on R_Z, R_X and Y

DoF ⇨ / Load component ⇩	X	Y	Z	R_X	R_Y	R_Z	$\ddot{X}_{Nac}$	$\ddot{Y}_{Nac}$
$F_y = 0$	*neg.*	~60%	*neg.*	~60%	*neg.*	*neg.*	*neg.*	~60%
$F_z = 0$	*neg.*	*neg.*	>20%	*neg.*	*neg.*	*neg.*	*neg.*	*neg.*
$M_y = 0$	*neg.*	*neg.*	*neg.*	*neg.*	>10%	neg.	~20%	~20%
$M_z = 0$	*neg.*	>20%	*neg.*	>30%	*neg.*	>75%	*neg.*	~20%

Table 15: Effect of load components removal

To conclude, each load component has an impact on a certain DoF of the FWT. If the number of actuators and their layout – see chapter 4 - do not allow to reproduce any of the load components, some quantities of interest will not be correctly reproduced in the wave tank. Those results corroborate the load component removal study of (Bachynski, Chabaud and Sauder, 2015). One of the original contributions of the present work is that the F_z component has an influence on the Z (heave) motions of the platform, for SPAR floating foundation. This could be explained by the low hydrostatic stiffness and hydrodynamic excitation force along the Z direction for those platforms.

Those synthetic results have been obtained thanks to the analysis of Figure 26 which represents the details on each quantity of interest with respect to the different load component withdrawal. For this figure, only the load case 1.2 and 1.6 are included. The error level has been computed on the standard deviation of each quantity of interest. In this figure, the average, max, and standard deviation of the error values have been computed for the different load cases. The crosses (+) are the maximum values of the error, the thin bars are the standard deviation summed to the average error level, and the thickest bars are the average error levels.

a)

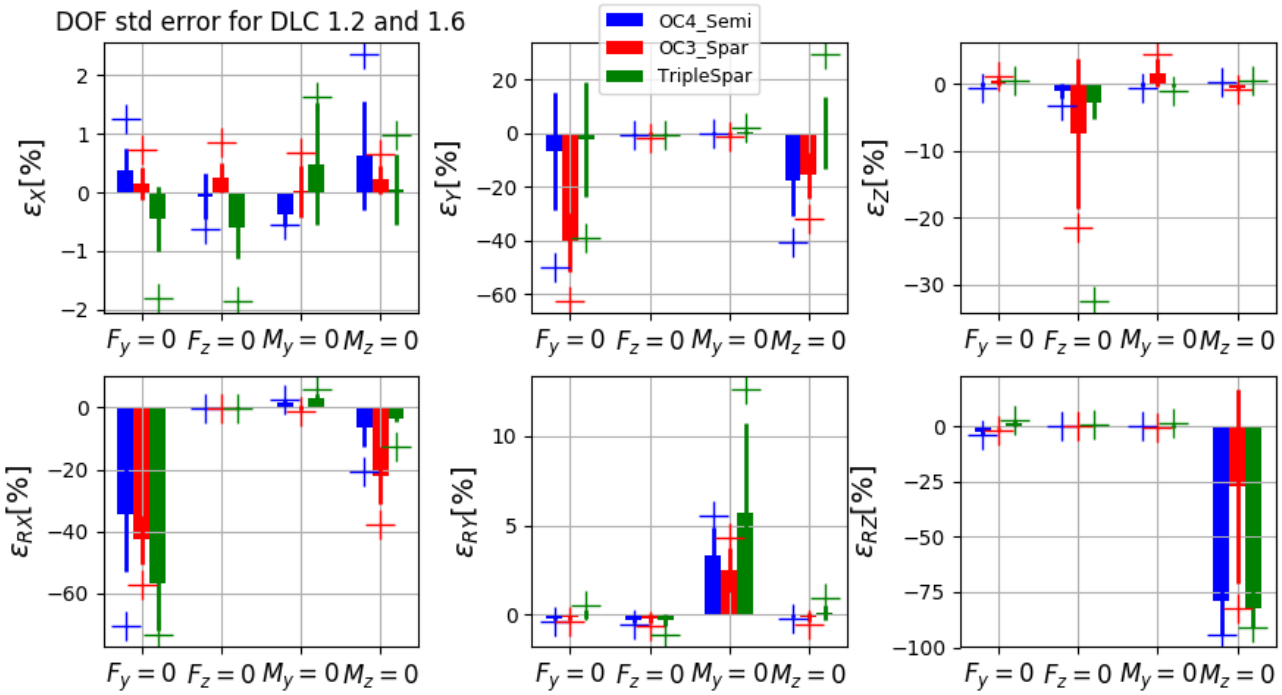

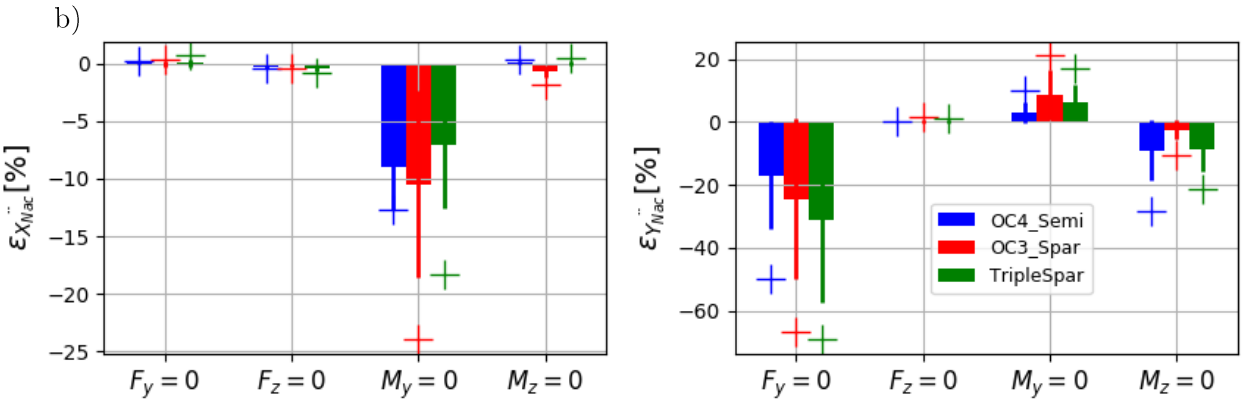

Figure 26: Effect of removal of aerodynamic load component. Relative errors on mean the standard deviations of a) the motions and b) Nacelle accelerations.

3.3.2.2 Effects of deteriorated performances

The purpose is to check the influence of the actuators dynamics (cut-off frequency) on the obtained performances. The deteriorated performances which have been mimicked are a low pass filtering effect. The low pass filtering effect is due to the actuator dynamics. For the low pass filtering effect, a first order low-pass filter is applied to each component of the load tensor. f_c is the cut-off frequency at -3dB. In Laplace domain, the transfer function between the i^{th} actuated tensor $F_{rotor\ actuated,\ i}$ and the setpoints $F_{rotor\ setpoint,\ i}$ is then represented by Eq. (3.19).

$$\frac{F_{rotor\ actuated,\ i}(s)}{F_{rotor\ setpoint,\ i}(s)} = \frac{1}{1 + \frac{1}{2\pi f_c} s} \tag{3.19}$$

This filtering procedure has been implemented within the OpenFAST structural module ElastoDyn with a simple Euler scheme for the derivative. All the load components are filtered at the same time. In the scope of this study, the M_x component has not been filtered due to a certain complexity in the interaction with the servo module.

Five values of the cut-off frequency have been simulated $f_c \in [0.14,\ 0.2,\ 0.3,\ 0.5,\ 1.0]\ Hz$. The error levels for the nacelle fore-aft acceleration and the platform pitch are plotted on Figure 27 as those quantities of interest are the most affected ones by the low-pass filtering effect. The average of the relative errors between the baseline and deteriorated cases are represented by the bars and the maximum by the crosses (+). A cut-off frequency between 0.2 and 0.3Hz affects the standard deviation of the platform pitch motion up to 5% on load cases types 1.6. A cut-off frequency of 0.5Hz the nacelle acceleration of the wind turbine affects up to 5%, when the mast is considered flexible. As a consequence, for scale 1:30 assuming Froude scaling, the actuator cut-off frequency should reach at least 2Hz to correctly achieve global motions and 5Hz for nacelle accelerations.

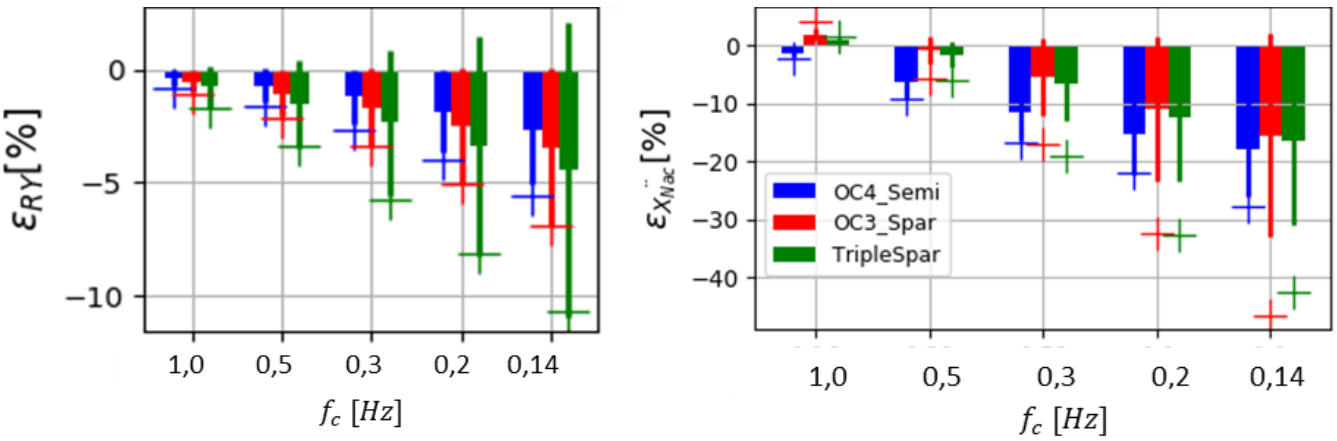

a) b)

Figure 27: Relative error on the standard deviation of a) the platform pitch motions and b) the nacelle acceleration, as function of actuator cut-off frequency

The methodology of representing actuator effects as a global low pass filter between the setpoint load to the actuated load gives a coarse overview of the overall effect of the on-board aircraft propellers technical solution. This 1st order low pass filter modeling for the actuators will be discussed in chapter 4.

3.4 Conclusions

In this chapter, the loads that have to be reproduced in a SIL setup by the actuators have been identified and characterized. The characterization of the setpoint loads for the actuators was based on a review of important physical phenomena and a parametrical study using aero-hydro-servo-elastic computations. The frequency content of the loads to reproduced and how the different modeling assumptions impact the frequency content have been illustrated. Illustrations on the spectral content of different quantities of interest were presented in part 3.1.2, while in part 3.2.2, the requirements for different floating wind turbines in different wind/wave conditions were concisely presented. The original contributions of these studies are about the different load cases and floating wind turbines under study. Those specifications constitute an important input for the choice and the design of the actuation system.

In part 3.3, the parametrical study was extended to mimic the experimental setup limitations. Those limitations, highlighted in chapter 2, were of two kinds: load component removal and deteriorated performances (low pass filtering effect) of the actuators. Important ratios and orders of magnitude are exhibited for different FWTs in different types of loads cases. This constitutes the second important input for the choice and the design of the actuation system, which will be developed in Chapter 4.

4 Experimental methodology

Contents

In this chapter, the main objective is the development of the experimental methodology and the design of the subsystems. From the SIL systems identified in the literature (see chapter 2), Figure 28 presents a conceptual overview of the interactions between the different subsystems. The bottom dashed boxes represent the coupled "software-in-the-loop" case, and the top feedback box is dashed as it has not been used for the present tests (feedback control is discussed in part 6). The following boxes are presented along this chapter:

- The *numerical model* which does the real-time computation of the full scale wind turbine, from the measured motions of the platform (denoted $X, \dot{X}$). It is presented in part 4.1.
- *Force allocation*: how to define the setpoint for each actuator (denoted T_{set}) from the load tensor output of the numerical model (denoted $F_{rotor\ set}$). It is presented in part 4.3.
- *Control strategy* denotes the control system developed to transform the setpoint for each actuator into a suitable input for the actuator (denoted β). It is presented in part 4.3
- The coupling point is between the actuator and the FWT. Due to the *actuator* loads, (denoted T_{act}), the *FWT* in the wave tank will move, creating some motions (denoted $X, \dot{X}$). The *real-time environment,* presented in part 4.2, includes a *force observer* (to estimate the load tensor produced by the actuators) and a *motion observer* to estimate the FWT motions for the *numerical model.*
  The loop is finally closed.

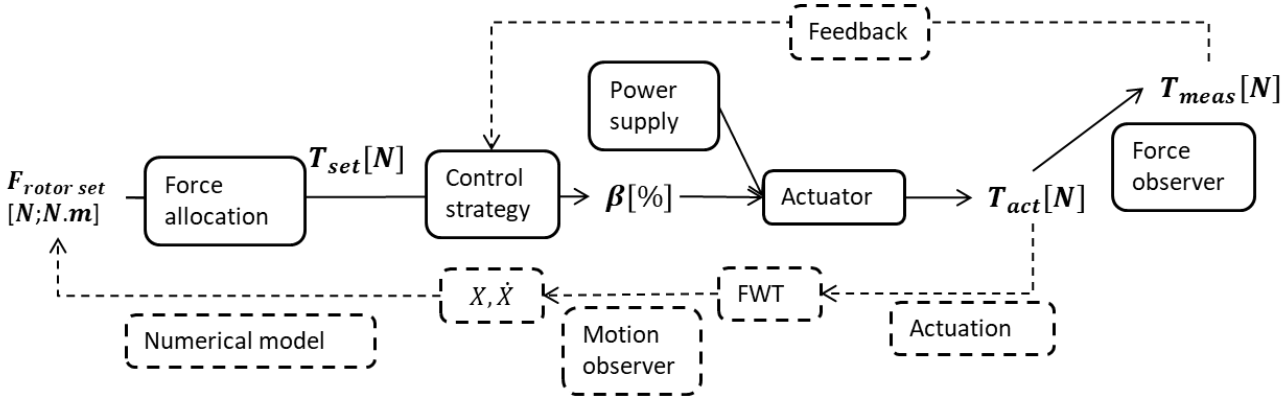

Figure 28: Overview of the SIL subsystems interactions

In part 4.1, the different options for the numerical models and the requirements are presented. Then, in part 4.2, the requirements for the real-time environment (force observer, motion observer, and hardware-software architecture) are presented. Finally, in part 4.3, the design of an actuation system is presented. This includes the choice and the characterization of each individual actuator but also the force allocation procedure to move to a multi-actuators design to generate a full load tensor at the tower top.

4.1 Appropriated numerical tool

The loads setpoints have been defined in chapter 3. The next step is about the use of a suitable numerical tool to compute those loads in real-time. The main requirements that have been identified for a SIL system are listed below. Those requirements should ensure an acceptable accuracy and the main following functionalities:

- run in real-time (with a Froude scale factor on the time) on an on-board PLC;
- robust and stable solvers, even for complex wind fields and highly dynamic inflow conditions;

- suitable aerodynamic theory with a validated implementation and state-of-art empirical corrections of unsteady aerodynamics;
- similar inputs to the numerical tools used at the different design stages;
- easy modifications of control laws parameters;
- simple interfacing with pre-processing turbulent wind fields;
- ability to impose measured platform and tower motions.

The main contributor to the load setpoints is the aerodynamic loading. Particular attention is given to the aerodynamic model assumptions. Firstly, a short review of aerodynamic models leads to the identification of suitable theories for SIL applications. Then, the selected numerical tool OpenFAST (NREL, no date; Jonkman, 2013) is presented, with the different modeling assumptions and modeling strategies.

4.1.1 Suitable aerodynamic models

Different models exist for calculating aerodynamic loads acting on wind turbines blades. From engineering models to high-fidelity models based on Navier-Stokes equations, different families of models have been identified. The different available models for aerodynamic load calculations are summarized in Table 16, inspired from (Schepers, 2012; Schepers and Sieros, 2017).

Model Name	Assumptions	Required data	Main limitations	CPU Time
Blade **E**lement **M**omentum	Blade elements + momentum theory Potential Flow; Stationary	C_l and C_d of each airfoil section. Each empirical correction has a proper set of inputs.	No vorticity and quasi-static assumption → *dynamic inflow* impacts need to be modeled elsewhere No viscous effects → *dynamic stall* needs to be modeled elsewhere 3D blades effects partially reproduced.	**short**
Generalized **D**ynamic **W**ake	Blade elements + Potential Flow; Dynamic inflow partly modeled	Eventually C_l and C_d of each airfoil section Each empirical correction has a proper set of inputs.	No vorticity → *dynamic inflow* approximated No viscous effects → *dynamic stall* needs to be modeled elsewhere Unstable for high induction factors	**short**
Dynamic **B**lade **E**lement **M**omentum	Similar to BEM + Dynamic inflow impacts partly modeled	Similar to BEM + additional specific inputs.	Similar to BEM *dynamic inflow* approximated	**short**
Free **V**ortex **W**ake	Potential flow Lifting line theory	C_l and C_d of each airfoil section Each empirical correction has a proper set of inputs.	*Dynamic inflow* and proper calculation of modified induction due to blades–wake interaction *Dynamic stall* needs to be modeled elsewhere	Medium
Computatio nal **F**luid **D**ynamics	Viscous Fluid	Depends on the description of the blades. Eventually exact geometry of the blades, hub, …	Depends how: • The turbulence is modeled (RANS, LES, ..) • The blades are described, either physically or by coupling with blade elements theories (e.g. actuator lines)	Long to very long

Table 16: Different state of the art models for aerodynamic loads calculations

An illustrative graph representing the CPU time requirements versus the fidelity of the different models is depicted in Figure 29.

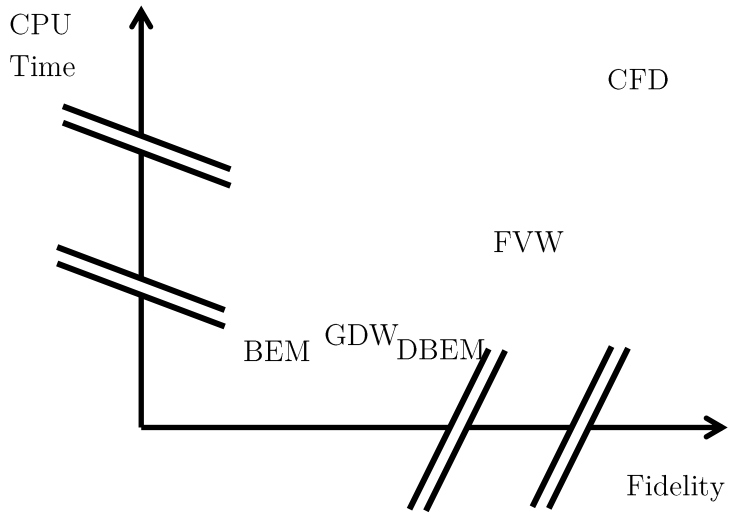

Figure 29: Computational time versus physics fidelity for different aerodynamic models. Inspired by [4]

For our purpose, only the engineering models with strong assumptions and empirical corrections - BEM, GDW and DBEM - could be used because of the real-time constraints. Different BEM implementations exist, either in commercial codes (DeepLinesWT, OrcaFlex, Bladed) and also in open access or open source codes (HAWC2, OpenFAST,…). OpenFAST, an open source framework for wind turbines developed by the NREL (NREL, no date; Jonkman, 2013), was considered to be a suitable option for different reasons:

- The aerodynamic module (AeroDyn) is under active development and includes all the empirical corrections;
- Different comparisons have been done between experimental data and AeroDyn results;
- The most important reference wind turbine have open source verified and partially tuned (with model scale experiments) models for OpenFAST;
- It is widely used by the wind energy community and consequently providing the numerical inputs for a test campaign with the SIL system was considered to be possible;

OpenFAST includes a complete framework for floating wind turbine simulations, with the possibility to perform aero-hydro-servo-elastic simulations. A drawing of the OpenFAST framework is presented in Figure 30. Additional modules exist for others kinds of modeling (integration into FAST.Farm, SubDyn substructure modeling, BeamDyn FEA for the blades and the tower, as well as different pre-processors and post-processors). The offshore features depicted in the figure are not used for the SIL system.

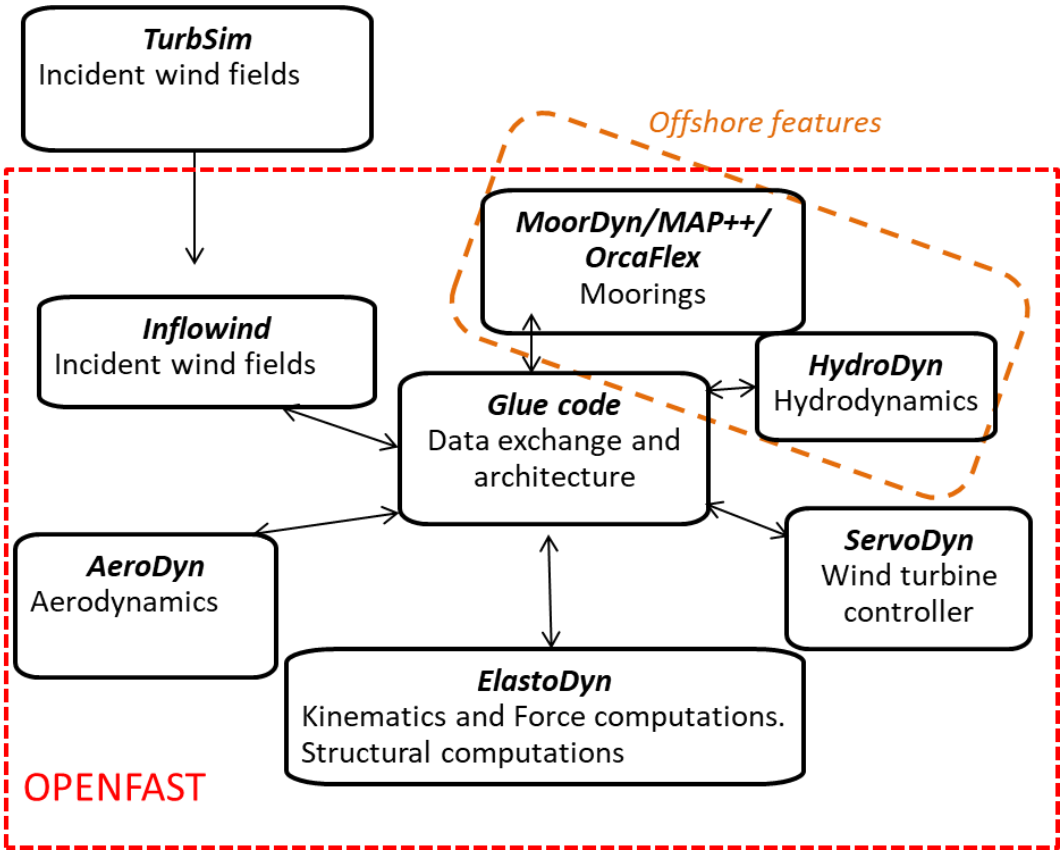

Figure 30: OpenFAST framework

4.1.2 OpenFAST for real-time computations

For the full scale numerical model of the wind turbine, the OpenFAST code is compiled as a shared library on the CompactRIO controller. Minor modifications are set through the OpenFAST glue code to supply measured displacements and velocities at each time step. Those modifications to the OpenFAST code and the validation process are detailed in appendix A. The inflow, aerodynamics, servo and structural modules are used in the real-time computation. A schematic drawing of the OpenFAST tool with its different modules and its integration to the real-time environment system is depicted in Figure 31. For the different experimental and numerical studies of this work, the latest available version of OpenFAST has been used. Consequently, depending on the study, the versions change. In this work this covers OpenFAST v1.0 to OpenFAST v2.3. The changes between the different versions are relatively minor and concern robustness, stability and some bugs corrections. More details about the aerodynamic models within OpenFAST are given hereafter with their inputs and outputs. Different convergence studies to find a trade-off between CPU time, accuracy and stability are presented in part 4.1.2.2.

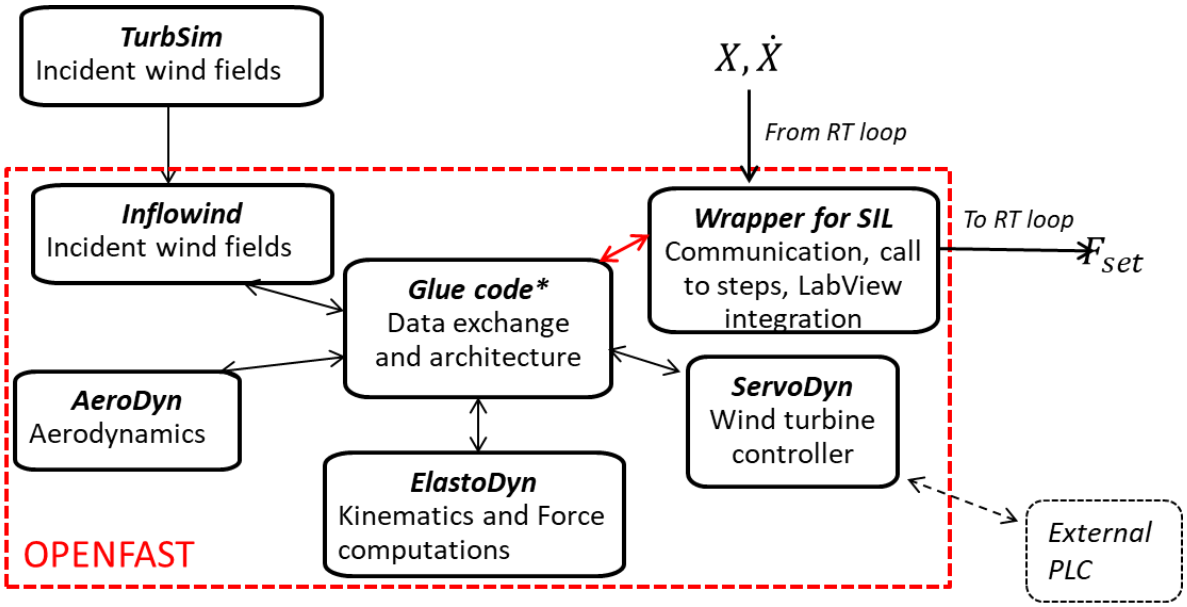

Figure 31: OpenFAST integration in the real-time environment.

4.1.2.1 Aerodynamic model description

For the selected versions of OpenFAST, two versions of the aerodynamic module exist, *AeroDyn v14* and *AeroDyn v15*. They are based on the same kind of approaches: BEMT, GDW, DBEMT. They are slightly different in implementations, especially concerning the empirical corrections (unsteady aerodynamics, …) and the mandatory assumptions (straight or prebend blades, …). Both versions have been used in the present work, depending on the available open source validated models of the reference wind turbines.

The required inputs of those modules are:

- The blade elements velocities – defined by the hub velocities, the blade pitch controller and the blade deformations.
- The blade element positions and orientations – defined by the hub positions, the blade pitch controller and the blade deformations.
- The incident freestream wind field, usually from pre-processor (i.e TurbSim (Jonkman, 2009)).

Then, the calculation is decomposed in different steps:

- Calculation of the induction factor, which is provided by the momentum or dynamic momentum theory for the BEMT / DBEMT. This induction factor give access to the local perturbed wind velocities for each blade elements.
- Calculation of local 2D forces on the airfoils sections, the blade element theory, with the perturbed *inducted* local velocities for each blade elements. The lift and drag coefficients for each blade element depend on the type of airfoils. Eventual 3D effect corrections on the lift and drag coefficients, as function of the incident angle-of-attack, could be taken into account.
- An iteration process is required between the momentum theory and the blade element theory until a convergence on both results is obtained.

Also, additions of empirical corrections with Hub/Tip loss, skewed wake or dynamic stall are taken into account at the different stages of the BEM calculations. These corrections have been calibrated

against measurements in wind tunnels (Schepers, 2012; Blondel *et al.*, 2016) and with comparisons with more sophisticated computational models (Pegalajar-Jurado *et al.*, 2018).

4.1.2.2 Selection of a suitable time step

When using a BEMT numerical model, typical recommendations are around 200 time steps per revolution (Jonkman *et al.*, 2015). At full scale, the recommended frequency is consequently in the range [20-40]Hz. At model scale, this makes the recommended frequency at which the numerical model is called by the real-time loop in the range of [100 – 300]Hz. As a reminder, the numerical model is run at full scale (full scale frequency of [15 - 45]Hz). Different parameters could influence the CPU time of a BEMT numerical model:

1. Discretization of the blades,
2. Converging criteria between momentum and blade element theories,
3. Compiling strategies (floating number precision, type of compiler, …),
4. Sub-time stepping for the momentum part.

After a first qualitative sensitivity study, from feedbacks of OpenFAST users and from other studies on SIL system (e.g. (Battistella *et al.*, 2018)), two parameters deserve more attention: the discretization of the blades and the compiling strategies.

Many efforts have been deployed to get a successful and optimized OpenFAST code compiling on the compactRIO PLC. Indeed, while LabView provides C/C++ functions integrations, compatibility with Fortran libraries (OpenFAST core modules) has been developed. A full GCC/Gfortran environment is installed on the compactRIO and the compiling process is carefully performed to avoid memory saturations. The settings that have been used to get the lowest CPU time are:

- Single floating point precision: switching from the default double floating point precision to single floating point precision gave a factor of approximately three on the CPU time with a very small influence on the integrated forces.
- Reference BLAS implementation: Different implementations of the mathematical libraries used for the algebra computations (BLAS and LAPACK), have been tested. However, multithreading and parallel computation attempts on the compactRIO were not successful and the reference BLAS implementations have been used.

Once the compiling strategy has been defined and the computational time evaluated, the initial settings of the open source models of the reference wind turbine could not be used directly. Indeed, respecting the default full scale time steps of 0.0125s and 0.025s for the NREL 5MW and the DTU 10 MW, respectively, did not match the real-time requirements on the compactRIO. To go further than the recommendations in the literature about time step and blade discretization choices, different convergence and sensitivity studies have been performed on the numerical model. The main objective is to find a trade-off between a low CPU time, a sufficient accuracy and numerical stability. Because the numerical model is used in real-time, a lack of stability might damage the experimental setup.

The study presented hereafter is a convergence study on blade discretization. Other studies have been performed but stayed at qualitative levels. It concerns:

- Time step convergence study, looking for the maximal admissible time step that ensures the stability and sufficient accuracy. For the full scale time steps under consideration (in the range [60-90]ms) and for rigid blades and drivetrain, no stability problems have been observed;

- Effects on the CPU time, accuracy and stability of solving flexible blades and drivetrain during the simulation. The main outcome is that it is possible to take into account those aero-elastic phenomena without increasing significantly the computational effort. However, the time step needs to be sufficiently small to guarantee the numerical stability.

Blade discretization

A sensitivity analysis on the blade discretization has been conducted to evaluate the differences on the thrust F_x. In the OpenFAST user manual (NREL, no date), the recommendation is 10 to 20 nodes per blades. In (Battistella *et al.*, 2018), a similar convergence study has been done on the number of nodes per blade for the DTU 10MW. The blade discretization varied from 10 to 50. Their conclusion was that 25 nodes per blade is a good trade-off between computational expense and accuracy.

The rotor has been discretized from 10 to 200 nodes per blade. The initial open source model was made of 37 nodes per blade. Instead of a linear spacing between the blade nodes, a geometric distribution has been used between each edge and the middle of the blade in the spanwise direction. The blade discretization is represented in Figure 32. Defining more points at the tip, where the loads are higher, is expected to speed-up the convergence. Because most of the tests in the experimental campaign are done with turbulent wind fields, this convergence study has been done with a turbulent wind defined by $U_w = 18m.s^{-1}; T_I = 20\% ; \alpha_{vert\ shear} = 0.14$. The selected wind turbine is the DTU 10MW, with the AeroDyn v14 aerodynamic module. The wind fields are generated with TurbSim, with a grid dimension of 205m × 230m, centered on the hub location. Initially, a very fine grid has been considered to avoid having differences in the aerodynamic loads only due to the interpolation between the aerodynamic grids (blade nodes locations) and the wind fields grids. However, due to memory requirements, a very fine grid could not be used. The selected grid has 33×36 nodes.

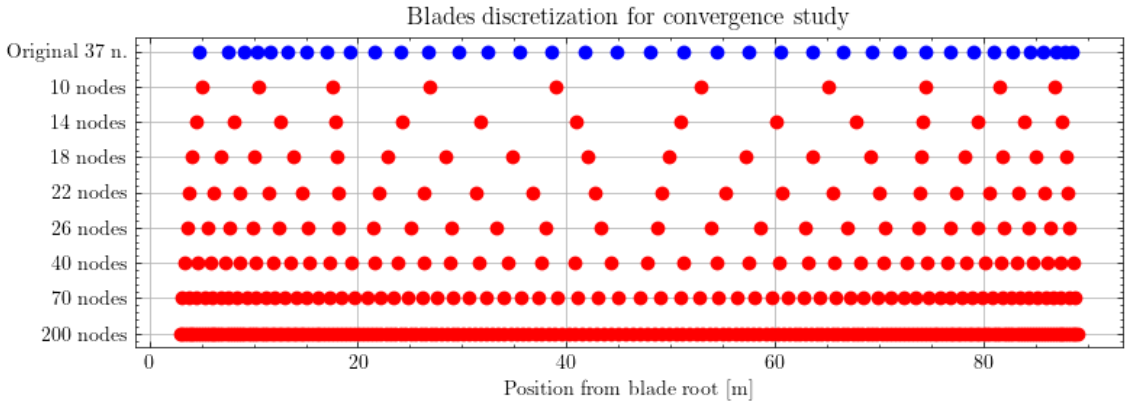

Figure 32: Different discretizations of the DTU 10MW blade

In Figure 33, the thrust force is compared for the different blade discretization and error levels are computed for each characteristic frequency bandwidth. Increasing the number of nodes does not lead to better results.

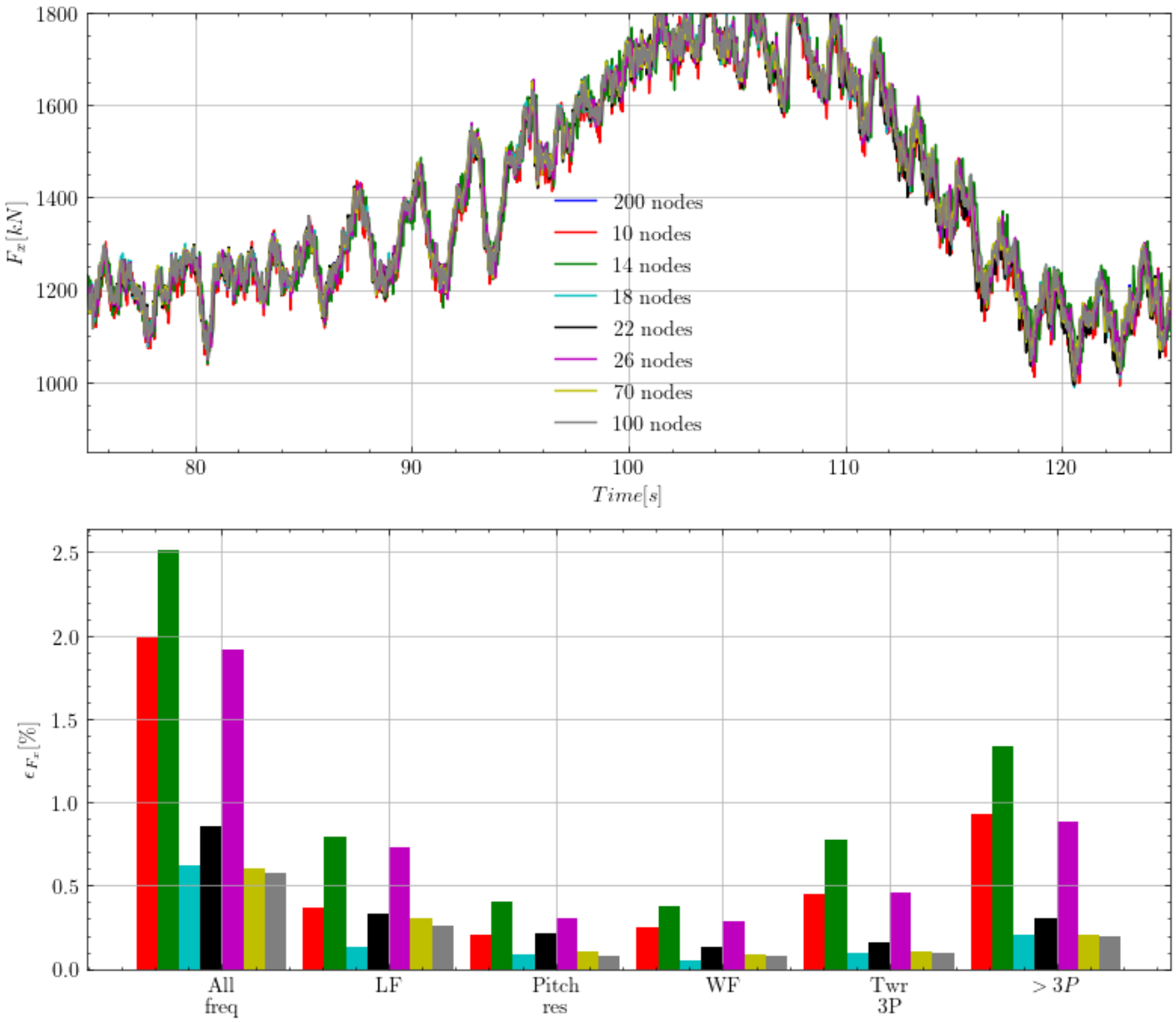

Figure 33: Convergence study for the rotor thrust. Top: Thrust time series. Bottom: Error levels per frequency bandwidth

The dimensionless CPU time for each blade discretization configuration is represented in Figure 34. This CPU time evaluation was conducted on a compactRIO 9049, OpenFAST is compiled in single precision and linked to the original openBLAS shared library and OpenFAST is called via the LabView programming environment.

The dimensionless CPU time is obtained by computing the ratio between the CPU time and the experimental real-time for a 1:40 scale factor. This ratio increases linearly with the number of nodes, it should be lower than one to ensure that the aerodynamic simulation can be performed faster than the experiment.

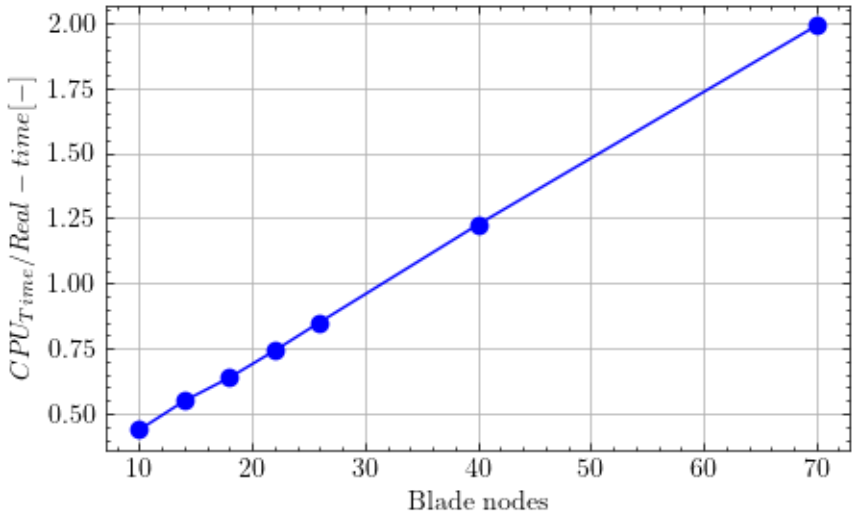

Figure 34: OpenFAST CPU time compared to real-time on the compactRIO 9049

To conclude, blade discretization has a significant impact on the computational time. For this wind condition on the DTU 10 MW rotor, using 18 nodes per blades is considered to be sufficient in terms of accuracy. However, to properly compare the different blade discretizations, higher resolution wind fields' grids and corresponding time steps should have been used. Indeed, the differences might arise from the interpolation of the local velocities from the wind field grid.

4.1.3 Using simplified aerodynamics for real-time computation

The aforementioned theories compute the full aerodynamic load tensor acting on the rotor. However, among the different tensor components, the rotor thrust F_x is the most preponderant one (Burton *et al.*, 2011; Chabaud, 2016). Even with the use of a simplified aerodynamic theory such as the (D)BEM, it is still challenging to do those computations in real-time at a sufficiently high time resolution. Moreover, those computations require a significant amount of inputs, and for some test campaigns, a simplified wind turbine modeling could be preferred.

One of the most common parametrizations of the aerodynamic force F_x on the rotor (see e.g. (Manwell, McGowan and Rogers, 2010)), corresponds to the case where the rotor swept area is seen as an actuator disc with a fixed thrust coefficient C_T (also equivalent to a porous disc with a fixed drag coefficient) for a given wind speed U_0 at hub height. The thrust force is expressed by Eq.(4.1):

$$F_x(U_0) = \frac{1}{2}\rho_{air} C_T(U_0) A_{rotor} U_0^2 \tag{4.1}$$

with A_{rotor} the rotor swept area and ρ_{air} the air density.

While this expression does not introduce any assumption for steady state values – this is just the definition of the thrust force coefficient - using it for varying incident wind speed should be done with a special care. To get the dynamic thrust variation to a small variation of the incident wind speed Δ_u. This expression could be extended by using different possible assumptions. Harmonic linearization (Lupton and Langley, 2019) and linearization capabilities of aero-servo-elastic codes (Pegalajar-Jurado, Borg and Bredmose, 2018) around a given operating point are promising methodologies. Introducing dependency to the TSR and the blade pitch angle $\beta_{Bld\ pitch}$, with 2D surface $C_T(TSR, \beta_{blade})$ values might also keep a part of the physics.

In the present subsection, we consider a "drag disc" formulation, i.e. with the strong assumption of *a constant thrust coefficient*. The objective of this drag disc formulation is to highlight some physical

phenomena (aerodynamic damping,...) and to provide order of magnitudes of thrust variation for the parametrical study, which has been presented in chapter 3.

The accuracy of the constant thrust coefficient assumption depends on the *controller region* of the wind turbine:

- Below-rated region: The steady state values of C_T are relatively constant and set to a high value, maximizing the power capture.
- Above-rated region: The steady state value of C_T varies significantly, due to the pitched blades. The accuracy of a constant C_T strongly depends on the characteristic frequency of wind speed variation. If this frequency is bigger than the natural frequency of the wind turbine controller, this approximation gives meaningful results for small change of the TSR. If the frequency is smaller than the natural frequency of the wind turbine controller, the thrust coefficient is not constant anymore and follows in a quasi-static way the steady state values.

To provide insights into the fluctuations of the thrust force, we are looking for expressions of the thrust variation Δ_{F_x} and of the thrust time derivative $\frac{\partial_{F_x}}{\partial_t}$ around a mean incident wind speed U_0. The mean incident wind speed defines an operating point characterized by $(U_0, \beta_0, \Omega_0, C_{T\,0})$ for the mean wind speed, mean collective blade pitch angle, mean rotor speed and the corresponding mean thrust coefficient, respectively.

A small variation of the incident wind speed Δ_u will change the force in $F_x(U_0 + \Delta_u)$ as in Eq. (4.2):

$$F_x(U_0 + \Delta_u) \approx \frac{1}{2}\rho_{air} C_T(U_0 + \Delta_u) A_{rotor}(U_0 + \Delta_u)^2 \tag{4.2}$$

With a Taylor expansion around the operating point, this force could also be expressed as in Eq. (4.3):

$$F_x(U_0 + \Delta_u) = F_x(U_0) + \left(\frac{\partial F}{\partial U}\right)_{U_0} \Delta_u \tag{4.3}$$

As explained here above, the question is how to express the variation of the thrust force with variation of the incident wind $\left(\frac{\partial F}{\partial U}\right)_{U_0}$. Two simplified limit cases are considered in those developments: the constant thrust coefficient assumption (corresponding approximately, for small variation of the wind speed, to a non-responding controller (β_0, Ω_0 constants) and the steady-state thrust assumption (corresponding, approximately, to a very fast-responding controller). The wind speed derivative of the thrust is developed in Eq. (4.4):

$$\left(\frac{\partial F}{\partial U}\right)_{U_0} = \frac{1}{2}\rho_{air} A_{rotor}\left(C_T(U_0) * 2U_0 + \left(\frac{\partial C_T}{\partial U}\right)_{U_0} U_0^2\right) \tag{4.4}$$

For the constant thrust coefficient, the term $\left(\frac{\partial C_T}{\partial U}\right)_{U_0}$ is neglected. For the steady-state thrust assumption, this term is taken into account. The constant thrust coefficient assumption leads to the Eq. (4.5) for expressions of the thrust variation Δ_{F_x} and of the thrust time derivative $\frac{\partial_{F_x}}{\partial_t}$ as a function of the incident wind speed variation Δ_u.

$$\begin{cases} \Delta_{F_x} \approx \dfrac{2 * F_x(U_0)}{U_0}\,\Delta_u \\ \dfrac{\partial_{F_x}}{\partial_t} \approx \dfrac{2 * F_x(U_0)}{U_0} * \dfrac{\partial(\Delta_u)}{\partial t} \end{cases} \tag{4.5}$$

When looking at those simplified expressions of the variation and derivative of the thrust force, different comments could be made:

- The thrust variation Δ_{F_x} is approximately proportional to the change in incident velocity. In this incident velocity, there will be the platform velocities $\dot{X}$. Consequently, a part of the aerodynamic loading is a damping term, called aerodynamic damping. The contribution of this damping to the overall damping depends on the operating point defined by U_0. From Eq. (4.5), the damping expression for the x component of the force is approximately $B_{aero\,x} \sim \frac{2*F_x(U_0)}{U_0}$
- The maximum thrust variations will occur for the maximum platform velocities, and the maximum thrust derivatives will occur for maximum platform accelerations and maximum incident wind speed changes.

These observations are used for the evaluation of the aerodynamic loads produced by the numerical model of the SIL system and in chapter 3 for the selection of wave conditions to get the maximum requirements for the actuators.

4.1.4 Aerodynamic characteristics of the DTU 10 MW RWT

The simplified damping expression for the *drag disk* is applied to the DTU 10MW RWT, for different operating points, and depicted in Figure 35, together with the x-rotor force $F(U_0)$. The *steady-state* curve corresponds to the interpolation of the steady-state x-rotor force curve. From control point of view it corresponds to the case of a very reactive controller, whatever the frequency of the input hub wind speed fluctuations. To compute the *steady-state* damping, the x-rotor force from the DTU 10MW RWT report (Bak *et al.*, 2013) (which is the thrust curve minus the gravity contribution due to the shaft tilt) is simply computed from a central 1st order scheme from the coarse force/wind speed curve. Overall, the aerodynamic damping significantly varies for the different operating points and is completely different between the steady-state and the drag disk approaches. For the steady-state operating points, this illustrates the *negative platform pitch damping* in case of a non-adapted controller (too reactive). For the three operating points under considerations, the value of the drag disk damping at the rated wind speed ($11\,m.s^{-1}$) is twice the value at $U_{hub} = 14\,m.s^{-1}$ and four times the value at $U_{hub} = 18\,m.s^{-1}$.

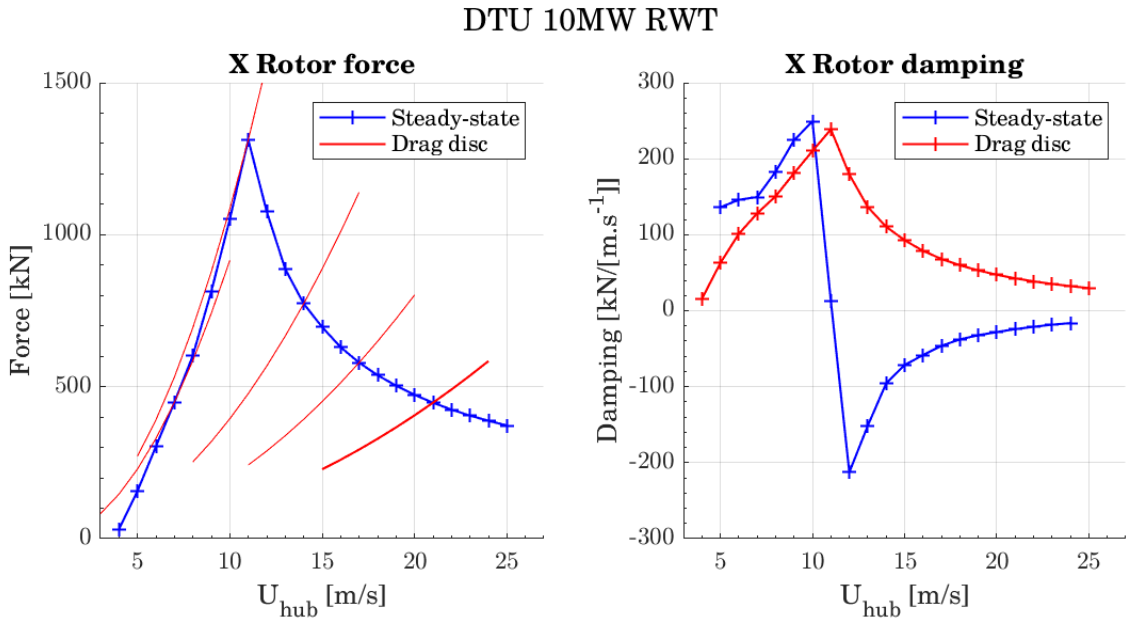

Figure 35: Rotor x-force (left) and simplified aerodynamic damping (right) for the DTU 10MW RWT at different operating points

To get a first comparison between the drag disk, the thrust curve and the OpenFAST numerical models, the damping component is compared by means of the following OpenFAST simulations procedure.

OpenFAST simulations are run with sinusoidal imposed motions, at different working points for different characteristic frequencies. To ease the understanding and decouple the physics, the imposed motion is the platform surge to bypass projected swept area and skew inflow impacts on the x-component of the rotor load due to platform pitch motions. The methodology is based on (Bayati *et al.*, 2016; Leroy, 2018). In this work, similarly to (Souza and Bachynski, 2019), the wind turbine controller is active to get the overall rotor load effect and not only the aerodynamic loads variations for fixed blade pitch angles and rotor speed. The same amplitude $(0.3\, m.s^{-1})$ of the velocity signals is considered for four characteristic frequencies: LF (0.0084Hz), R_Y NF (0.03Hz), WF (0.09Hz) and Twr (0.38Hz) and three operating points ($U_{hub} \in [11, 14, 18]\, m.s^{-1}$). . Note that in the simplified selected case, the hub wind speed variations ΔU_{hub} corresponds to the platform surge velocity $-\dot{X}_1$.

The selected graphical representation is based on the variation of the x-rotor force ΔF as function of the variation of the apparent wind speed $\Delta_{U\,hub}$. On this figure, the main characteristics and corresponding physical effects are:

- The slope of the ellipsoids indicates the damping component of the force, but also the excitation force. Indeed, if the hub wind speed fluctuation comes from the FWT motions, this is a damping term. If the hub wind speed fluctuation comes from the incident wind field, this is an excitation term. If the slope is positive (respectively negative), a positive (respectively negative) damping is reproduced.
- The widths of the ellipsoids indicate out of phase component of the force, with an analogy of a stiffness / added mass term. This term has an impact on the natural frequency of the system.

These explanations are summarized in Figure 36.

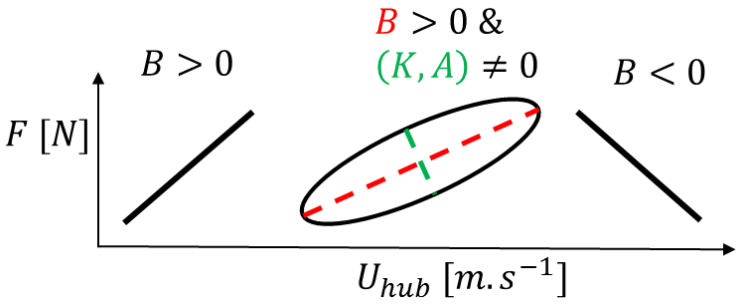

Figure 36: Analysis of thrust variation as function of incident hub wind speed.

The results for this study are depicted in Figure 37. The *drag disk* and the *thrust curve* aerodynamic dampings are represented by dashed lines (--). The OpenFAST forces are represented by continuous lines (-). The damping from the OpenFAST simulations is fitted from the slope of the ***Twr*** oscillations. We can see that, for LF fluctuations of the hub wind speed, the force computed by OpenFAST is close to the thrust curve results, as the frequency of the fluctuations is small enough to let the wind turbine controller adapt to the hub wind speed variation. Firstly, none of the frequencies leads to a pure damping term from the OpenFAST simulations. The force variations are not perfectly in phase with the hub wind speed variations. At the *Twr* characteristic frequency, the drag disk formulation overestimates, estimates correctly and underestimates the damping for hub wind speeds of respectively **11, 14** and 18 m/s.

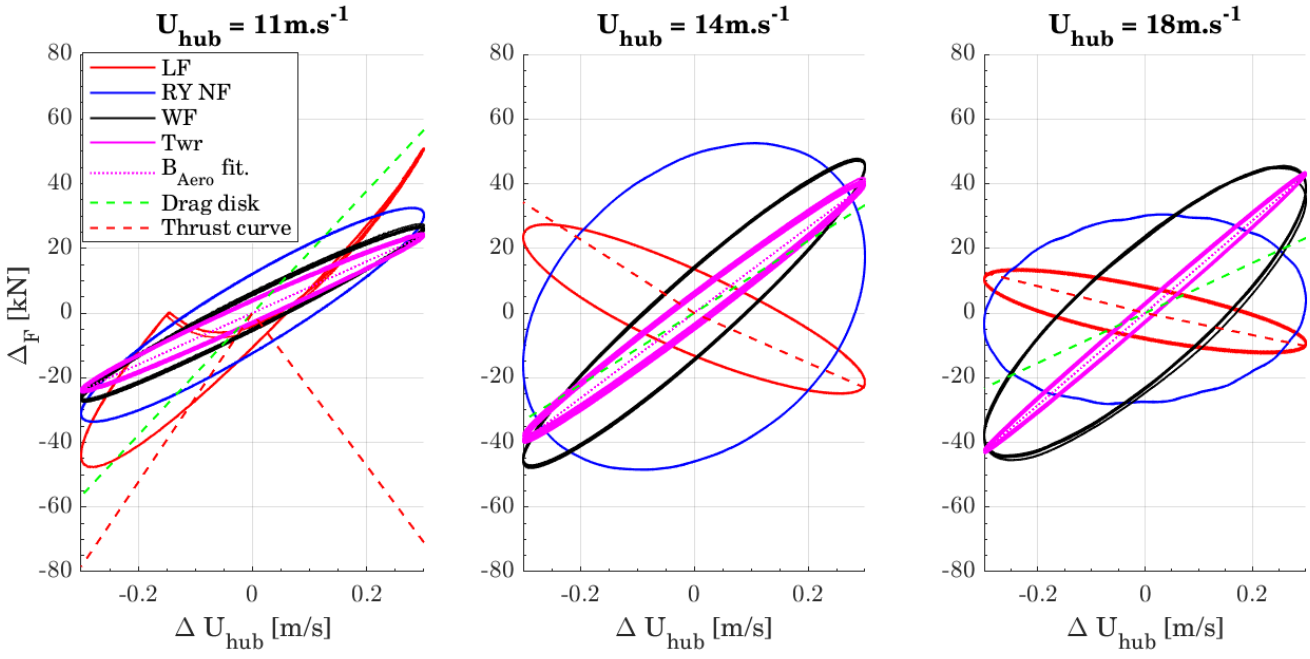

*Figure 37: Variation of the x-rotor force **ΔF** versus the variation of the apparent wind speed **ΔU**$_{hub}$ for three operating points and four characteristic frequencies of oscillations.*

4.1.5 Conclusions about appropriated numerical tool

Different aerodynamic theories have been developed in the literature for the modeling of wind turbine loadings with different open source implementations. However, for real-time computations on an on-board PLC, only low-fidelity or very-low fidelity models can be envisaged. The two options have been investigated by looking at the components of the F_x rotor load, i.e. the damping and out-of-phase

components. In the SOFTWIND project, it has been decided that very simplified theories such as the ones presented in part 4.1.3 limit the accuracy and the investigation possibilities of the setup. Indeed, the need to reproduce the wind turbine controller effects on platform dynamics was a prerequisite. To explore the impact of the FWT motions, a comparison on the quantities of interest is presented in chapter 7 from wave tank testing results.

Additionally, different sensitivity analyses have been presented to find a trade-off between real-time computation (CPU time) and accuracy. This indicates that, compared to the different sources of uncertainties of the method, using coarse blade discretization to speed up the computational time is not a strong assumption.

4.2 Real-time environment and DAQ integration

The real-time environment and the data acquisition system (DAQ) are described in this part, in terms of architecture and developments performed.

4.2.1 Architecture hardware/software

A SIL system is composed by different subsystems. The interaction between each subsystem needs to be carefully considered to avoid important error propagation. In Figure 38 are depicted an overview of the communication protocols and frequency of acquisition.

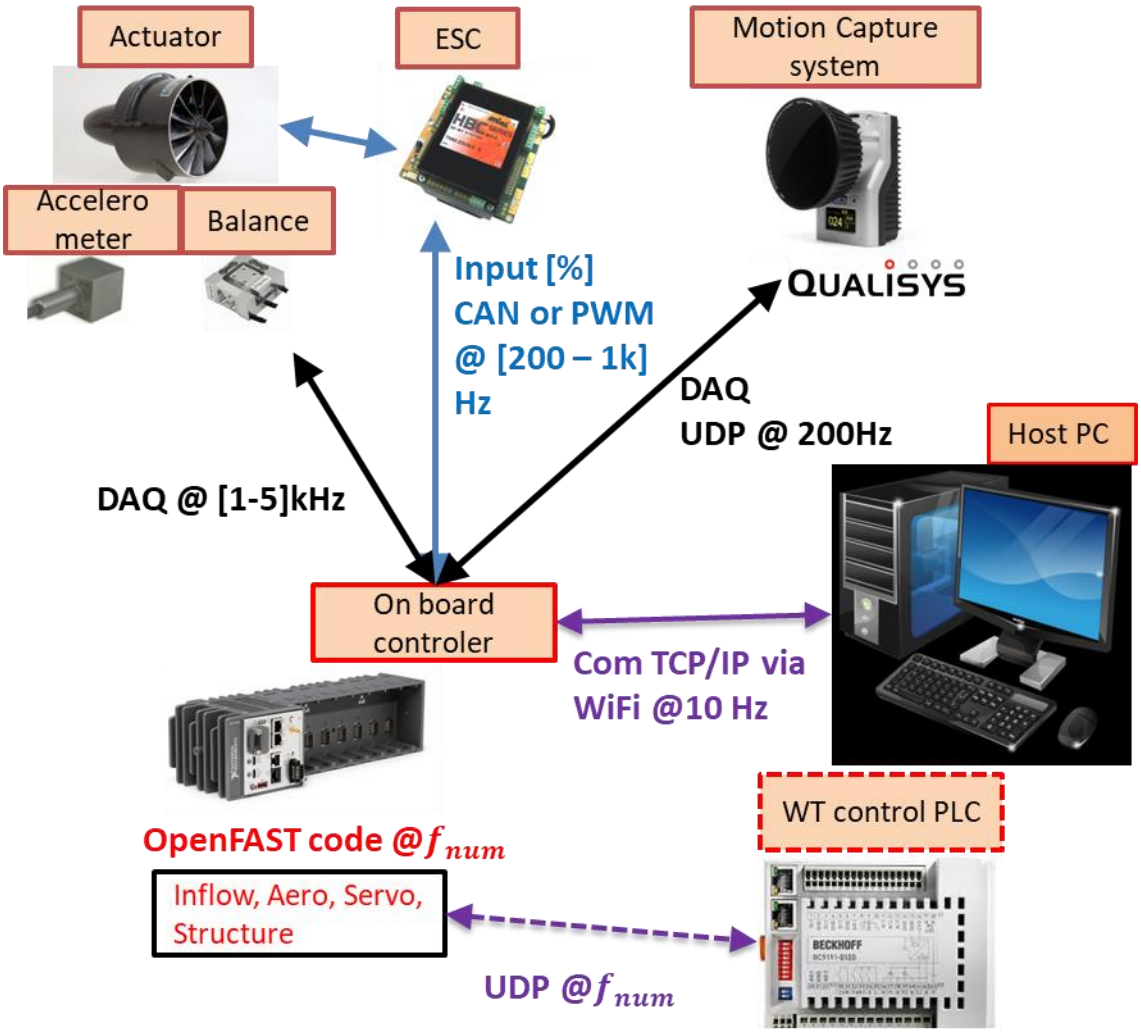

Figure 38: Overview of the DAQ and actuator control

Different real-time loops are running on the Linux real-time operating system of the compactRIO controller at different frequencies:

- The main control loop. It masters most of the data acquisition and the actuator control. The acquisition frequency is $f_{control}$. In this work, different tests were conducted, depending on the type of communication protocol between the compactRIO and the ESC (CAN message or PWM signals). This frequency has varied from 200 Hz to 1kHz.
- A dedicated loop for the MOCAP system integration. The acquisition frequency is $f_{MOCAP} = 200\,Hz$ for the different setups we have used.
- A dedicated loop for the numerical tool. The acquisition frequency is f_{num}. This frequency was not constant for the different setups. This frequency was 100 Hz for the floating setups, and 70 Hz for the forced motions setup (Hexapod),

On the HOST PC, another real-time loop runs at a lower frequency. A graphical interface has been developed to choose the different control mode of the actuators and switch between identification tests and SIL tests.

The corresponding communications have been established:

- Between the HOST PC and the compactRIO via a WIFI communication and a TCP/IP protocol at a low sampling frequency (10 Hz).
- Between the MOCAP computer and the compactRIO, via an UDP protocol and a dedicated Local Area network (LAN). This UDP protocol ensures the motions received by the compactRIO are the freshest. If the network is overloaded, some packets may be lost but the real time would not be delayed. The use of a dedicated LAN and the low data rate (200Hz and 44 bytes per packets) prevent packet loss.
- Between the compactRIO and another PLC, specifically dedicated to the control law part. It is denoted *WT control PLC* in Figure 38. This development has been done to give the opportunity to integrate a wind turbine controller on its hardware. This communication is real-time, via a UDP protocol. The communication is activated by a dedicated library called by the servo module of the numerical tool. This communication is optional and the servo module operations of the numerical tool could also be performed on the compactRIO. Again, a dedicated LAN and a low data rate are applied.

The National Instruments® framework has been used. It consists of:

- The Labview programming environment on the HOST PC and on the CompactRIO controller.
- Dedicated modules for the data acquisition.
- Additional modules for the control and the monitoring of the actuator (CANOpen protocols, PWM signal generator,…)

This architecture has been used to have only one Ethernet cable between the dry side of the wave tank and the model. This cable is used for MOCAP UDP transfer, synchronization and safety. All the conditioners for the on-board sensors are embedded on the model.

4.2.2 Motion capture system and observer

In the SIL methodology, the motions of the FWT (positions and velocities) are used in real-time by the numerical model. The main concern is to capture the aero-hydro coupling with the computed rotor loads that will depend on these motions. Basically, the aerodynamic loads include a damping term for

most of the DoF, and consequently the FWT velocities need to be correctly measured in real-time. Compared to other wave tank experiments of freely floating bodies, the additional requirements about the motion tracking are a real-time achievement and very fine target level of accuracy.

The key challenge for the motion observer is to provide non noisy positions and velocities to the numerical model while limiting the induced delay. Different solutions have been developed:

- Positions are captured by the MOCAP system. Velocities are assessed by a simple first-order finite difference scheme. Positions and velocities are low pass filtered with a 2nd order Butterworth filter. The cut-off frequency of the filter is adjusted to get only the significant part of the motions
- Kalman filter (Fossen, 2011), merging the IMU and MOCAP systems to get a state estimate of the positions and velocities.

In terms of target specifications for this motion observer, the main parameters are:

- The admissible delay at the highest frequency of interest.
- The required attenuation for different frequencies.

The admissible delay is based on a phase threshold for the highest frequency of interest. This admissible delay has been illustrated for different frequencies of interest in Chapter 3. The delay induced by the motion observer is only a portion of the total SIL delay. Consequently, the admissible phase at the highest frequency of interest needs to be relatively small. A maximal phase of $\frac{\pi}{8}$ was a target in the settings of the motion observer. Concerning the required attenuation, it will depend on the numerical model sensitivity and modeling assumptions to ensure numerical stability. A notch filter might also be useful if vibrations of the markers are experienced.

In this work, a MOCAP system based on the Qualisys® environment has been used. The Qualisys environment is composed of different components:

- Several cameras, at least three for accurate triangulation, sending infrared pulses;
- Reflecting markers, basically 4cm-diameter spheres with a given layout;
- The QTM real-time processing software.

The different cameras take frames at the acquisition rate, detect the relative marker positions and using their calibration properties, compute the 3D positions of each marker. The processing software takes the 3D positions of the different markers as inputs, applies some trajectory smoothing techniques (gap fill,…), and then computes the 6 DOF positions of each body. The procedure is based on a least-square fitting on the available markers and cameras.

To reach accurate results, the experimenter must pay attention to the errors and bias introduced at the different steps to set-up the MOCAP system. Quantification of these errors has been thoroughly investigated for the different setups. The different steps and their challenge are:

- Positioning of the cameras and of the markers. Defining a suitable arrangement is challenging.
    - Capturing 2 bodies – the platform and the nacelle – without being too far.
    - The reflecting markers should not hide each other, otherwise the least square fitting procedure leads to jumps in the computed 6 DoF positions.
    - Similarly, a constant number of cameras need to track the 6 DoF bodies.
    - The markers should be connected to the platform and nacelle with stiff supports, to avoid high frequency vibrations.

- Calibration of the cameras and adjustment of their settings. This has to be performed regularly if the conditions (temperature, humidity, positions of the fixation points) slightly change.
- Definitions of the reference frame, and orientation of the platform. This was a difficult step to reach a sufficient accuracy, especially for the rotations.
    - A small change in the yaw orientation directly induces a misalignment between the wind and the nacelle orientation, leading to different aerodynamic computations;
    - Small changes in the platform trim and platform heel also affect the computation in the numerical model, and change the operating points (platform pitch, incident wind speed). This might affect the wind turbine controller behavior.
- Selection of a suitable acquisition frequency and verification of real-time operation.

The second solution developed is based on Kalman filter techniques. The idea is to use different sensors and sensor types to get a state estimation of the positions, velocities and accelerations. The development and implementation of the Kalman filter follows (Six, 2018) and was done by Félicien Bonnefoy, supervising this PhD work. Kalman filters are used for a broad range of applications, e.g. in dynamic positioning of ships. A Kalman filter has two steps: prediction and correction. The prediction is based on the accelerations signals, whereas the correction uses the positions of the MOCAP. Basically, if only the accelerometers are used, it introduces drift in the positions and velocities. On the other part, using only the MOCAP introduces high frequency noise, especially in the FWT velocities signals.

The main parameters of a Kalman filter are:

- The two sampling frequencies, for the predictor-corrector steps. They are not necessarily the same and quite often the accelerometers have a higher sampling frequency. Consequently, the correction is done every n time steps.
- The *confidence* in each sensor. Mathematically, this is expressed by the noise covariance matrices of the processed data (accelerometers and gyrometers) and the measured data (MOCAP). They might be estimated from standard deviations of measurements without motions. It corresponds to a certain level of noise. Typical values are summarized in Table 17.

Quantity	Value
$\sigma_{gyro}\ [mrad.s^{-1}]$	0.9
$\sigma_X\ [mm]$	0.1
$\sigma_{Rot}\ [mrad]$	0.3
$\sigma_a\ [m.s^{-2}]$	0.2

Table 17: Typical values for Kalman filters covariance matrices

The motion observers are evaluated with post processing perfect filtering and with the sensor redundancy. This is presented in chapter 5.

4.2.3 Force observer

To estimate the loads generated by the actuators, it is important to have a real-time measurement with a sufficient acquisition frequency. The actuators based on aircraft propellers could generate high frequency fluctuations due to mass imbalance or aerodynamic masking effect. However, one of the main challenges is to get the actuator thrust only, by removing the gravity forces and the inertial forces also measured by the force transducer. This compensation is called *inertial compensation* hereafter.

Additional specificities of the setup include:

- The force transducer is connected to the Compact RIO with an AI Bridge NI 9237 module. This module introduces a delay inversely proportional to the sampling frequency (4ms at 10kHz and 20ms at 2kHz). In order to minimize the delay, the data is sampled at 10kHz and an average on 10 points is used to downsample at 1kHz. This gives a 5ms total delay.
- The flexible tower for the floating setup induces large accelerations at the tower natural mode. This makes inertial contributions at this frequency well above the thrust fluctuation setpoints for the actuator, as it has been shown in chapter 3.

The inertial compensation is described for the $\overrightarrow{e_x}$ component of the load tensor. This load tensor is expressed in the shaft frame that is tilted from the tower top frame. The force transducer measures a force F_{meas}, at a certain point. At another point, an accelerometer, ideally an Inertial Measurement Unit (IMU), measures the acceleration (minus the gravity acceleration) and possibly the angular velocities. This accelerometer also measures the gravity component due to the shaft orientation in the inertial frame. Both measurements locations could be different but are connected to the same rigid body. The measured force and the acceleration are transported to a target reference point.

The actuator F_x is obtained by Eq. (4.6).

$$F_{act\,x} = F_{meas\,x} - m_{seen} \times a_x \tag{4.6}$$

With:

- m_{seen} the mass seen by the force transducer.
- a_x the x component of the measured acceleration and transported to the correct reference point in the shaft frame.

The mass seen by the force transducer m_{seen} has been estimated by different ways:

- On the Hexapod system, different steady-state values of the measured force for different inclinations. The measured force is only the gravity force in that case.
- Identification of the mass could also be calculated for wave only tests, for which the actuator force should be zero along the test. Waves + steady thrust tests have also been used for this identification, keeping in mind that varying inflow conditions due to the nacelle motions could also generate a certain force.

4.3 Actuation system design

In this part, the actuation system design is presented. The actuation system include the different actuators and the supporting frame. The main topics are:

- characterization of these actuators, in terms of dynamics and control,
- force allocation procedure, to get the setpoint for each actuator from the target load tensor,
- frame design and actuators selection, i.e. optimization of the actuation system layout, efficiency of over-actuated layout compared to fully-actuated.

4.3.1 Loads generated by aircraft propellers

As presented in chapter 2, on-board actuators have been selected for this work. With the development of small scale Unmanned Aerial Vehicles (UAV) based on multi-propellers systems (quadcopters, hexacopters or even octacopters), aircraft propellers constitute a suitable actuator solution. Those actuators are now well-known, light, robust, and affordable.

The objective of this part is to present the specificities of those actuators, how they work, what are the main describing parameters, and how could they be modeled.

4.3.1.1 Working principle and characterization of the actuators

A picture of a small-scale aircraft propeller and its component for small UAV applications is depicted in Figure 39.

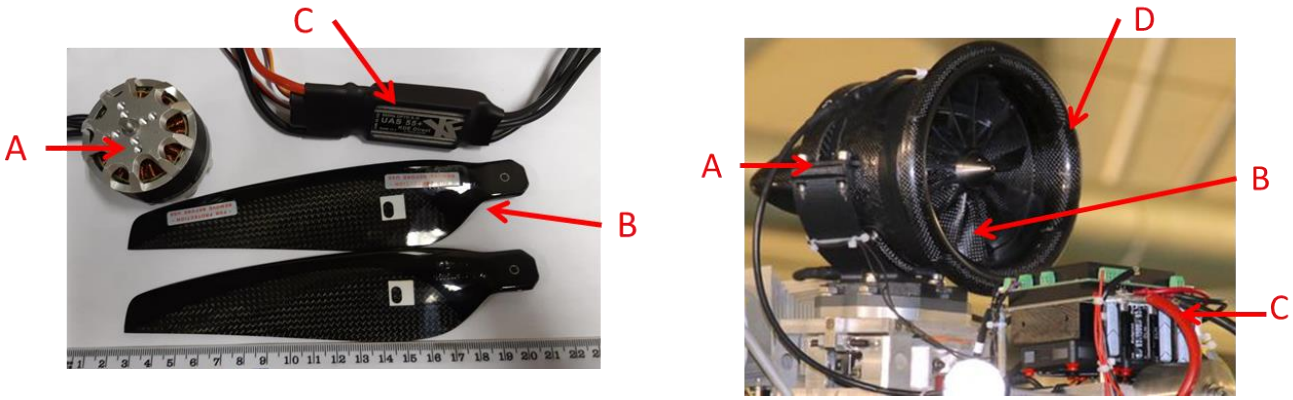

Figure 39: Typical aicraft propellers for small scale UAV applications. A) BLDC motor; B) Blades; C) Electronic Speed Controller ; D) Duct

This actuator is composed of different subsystems as depicted in Figure 39:

- The electrical motor (BLDC) A)
- The propeller itself B)
- The Electronic Speed Controller (ESC) C)
- Possibly, a duct for the flow control D)
- The power supply (possibly battery)

For UAV application, an additional autopilot masters the attitudes and trajectories of the vehicle. In the SIL application, this autopilot is the real-time environment.

Different solutions of aircraft propellers have been developed. They have been designed for UAV applications, from remote controlled model airplanes to very small *FPV (first-person view) racing* multicopters. For most of the applications, the thrust-to-weight ratio is more important than the dynamic characteristics of the thrust. Consequently, many technical steps have been overcome to increase the duration of each flight and the payload capacities of those UAVs but improving the dynamic characteristics was not the main priority.

These small UAVs are, to some extent, similar to helicopters. A helicopter has two working principles to vary the thrust generated by its rotor:

- Increase or decrease the rotor speed at a fixed blade pitch angle. The actuator mechanism is a motor that generates a torque transmitted via a shaft to the propeller.
- Increase or decrease the blade pitch angle via a dedicated actuator (so-called blade pitch actuators).

Most of the developments for small multicopters use the rotor speed variations to change the thrust. The other mechanism, based on blade pitch actuators, has not been widely investigated up to now. However, as shown by (Cutler and How, 2015), this actuator solution seems very promising in terms of dynamic features. Figure 40 is extracted from (Cutler and How, 2015), and shows the fast dynamics of a blade-pitch solution on a step response compared to the varying rotor speed solution. However, one of

the limitations is the ability to efficiently predict the thrust produced. For wave tank SIL application, the predictability - linked to the suitability of feedforward-only control strategy – is an important advantage of rotor speed variation solution. Finally, the blade pitch actuator solution can significantly improve the actuator bandwidth. However, the varying rotor speed solution is better controlled and widespread. This is the solution that has been followed for the system developed. Note that helicopter rotor heads have complex collective blade pitch motors that control the thrust but also two moments.

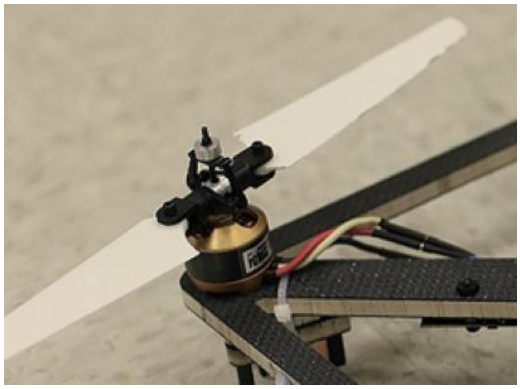

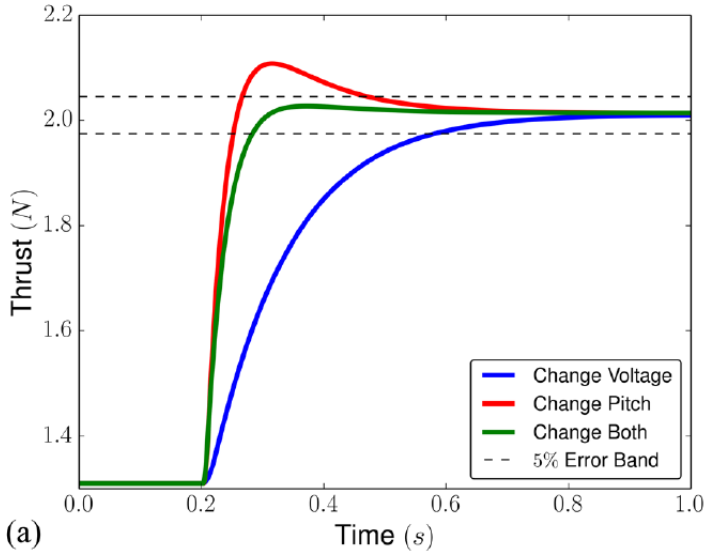

Figure 40: Blade-pitch actuator dynamics compared to rotor speed dynamics, from (Cutler and How, 2015)

One of the important questions about the loads generated by these propellers is about the relative importance of the torque compared to the thrust. For a helicopter, this torque is not negligible: the small secondary perpendicular rotor at the back of a helicopter counterbalances the rotational motion induced by the rotor torque. This relative contribution of the torque of each motor to the integrated load tensor needs to be addressed. The contributions of the gyroscopic moments are also a concern that needs to be addressed.

A box diagram of the actuator is depicted in Figure 41. From an input duty-ratio β [%] specified by the real-time environment, the actuator produces a thrust T, a torque Q and due to its angular velocities in the inertial frame, some gyroscopic moments M_{gyro}.

The main quantities that might be measured and potentially controlled are indicated. For the target size of the propellers, we have access - at a sufficiently high frequency - to the following values:

- Input duty ratio β [%] ;
- Output thrust T_{meas} $[N]$; $Q_{meas}[N.m]; M_{gyro}[N.m]$ from a force observer.

The current intensity, rotor speed, motor torque are not outputs in real-time at a high frequency from these small sensorless electrical motors. Those variables are estimated by the ESC but their algorithms are often a black box with only high-level parameters to adjust the settings. This means the rotor speed, current intensity or motor torque cannot be used as control variables.

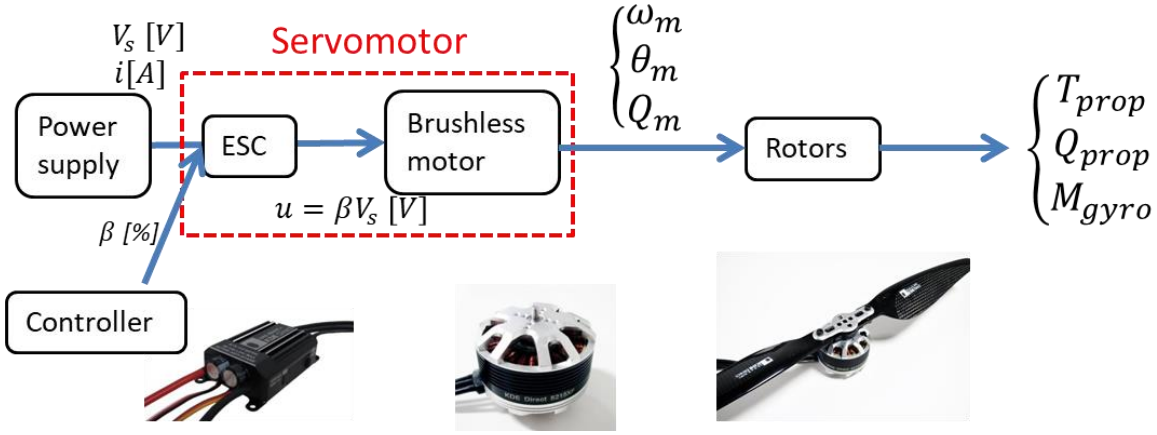

Figure 41: Box diagramm of the actuator

Different quantities characterize those actuators. Information found in supplier documentation is summarized in Table 18. These characteristics have been used in the selection and design of suitable configurations.

Motor	ESC	Propeller	Power supply
Motor constants Ke, K_t, K_v, i_{idle}, R_m being the motors electrical constant, torque constant, speed constant, idle current and internal resistance, respectively. Each motor has a certain range for admissible input voltage and current. The mass of the motor m_{motor} is also an important parameter.	• Frequency of the PWM signals • Type of commutation (trapezoidal, sine-based, …) • Throttle discretization • The mass of the ESC m_{ESC} is also an important parameter.	• Inertia J_{prop} and mass m_{prop} • $C_{T\,prop}$ and $C_{Q\,prop}$ the torque and thrust coefficients • $Diam$ the diameter of the propeller • Overall properties: materials, flow control (duct), number of blades	• U_c the rated voltage of the power supply • i_{max} the maximal current draw.

Table 18: Aircraft propeller actuator main characteristics

4.3.1.2 Modeling of actuator thrust dynamics

An analytical model of the dynamics of the actuator thrust has been derived. This analytical model was used to:

- Predict actuator performances, in terms of frequency bandwidth and maximal thrust variation.
- Highlight the main driving parameters to help in the choice between one {propeller + motor + ESC} configuration to another.

We are looking for an Ordinary Differential Equation (ODE) of the output thrust T from the input duty-ratio β. With suitable approximations, a transfer function between both variables is obtained. Positive and negative saturations of the thrust and thrust derivative are also derived to complete the model. The main assumptions and limitations as well as the derivation of the analytical model is in appendix C. Only the results are summarized in this part.

The characteristic ODE is expressed in a canonical form by Eq. (4.7). It is the characteristic equation of a 1st order low pass filter between the input duty-ratio β and the output thrust T with gain K and characteristic time τ. Two saturation mechanisms of the thrust variation $\frac{\partial T}{\partial t}$ have been taken into

account for positive saturation (maximal torque, characterized by i_{max}) and negative saturation (no braking). This modeling is valid around a working point defined by $(\omega_0, T_{prop\,0}, Q_{prop\,0})$.

$$\begin{cases} \tau\dot{T} + T = K\beta \\ \tau \sim \dfrac{J_{prop}}{\left(\dfrac{30}{\pi K_v^2 R_m} + 2\dfrac{K_t(i_0 - i_{idle})}{\omega_0} - b_f\right)} \\ K \sim \dfrac{K_t \times U_c * 2\overline{C_T}\omega_0}{R_m * \left(\dfrac{30}{\pi K_v^2 R_m} + 2 * \dfrac{K_t(i_0 - i_{idle})}{\omega_0} - b_f\right)} \\ \left[\dfrac{\partial T}{\partial t}_{max}\right]^+ = \dfrac{2T_0}{J_t\omega_0} * \left(K_t(i_{max} - i_{idle}) - \overline{C_Q}\omega_0^2 - b_f\omega_0\right) \\ \left[\dfrac{\partial T}{\partial t}_{max}\right]^- = -\left(\omega_0\left(\dfrac{2\overline{C_T}K_t i_{idle}}{J_t} + b_f\right) + \overline{C_Q}\omega_0^2\right) \end{cases} \quad (4.7)$$

In terms of application, the different motor constants are usually accessible. J_{prop}, the propeller inertia around its axis of rotation, can be computed from mass properties and approximated geometry. $\overline{C_Q}$ and b_f can be estimated from tabulated steady-state characteristics of the {motor + propeller} assembly.

4.3.1.3 Control perspective

A load analysis of this actuator has been developed. The next concern is to use and control in real-time the actuator in an experimental setup. The inputs of those on-board propeller actuators are the *duty-ratio* β, also called *input PWM* or *throttle*. It is expressed in %. The main output is the thrust T generated by those propellers, expressed in Newtons. As explained above, they also generate a torque Q and gyroscopic moments. The setpoint for each actuator is a target load, made of the torque and the thrust. The control variable for each actuator is unique and is the duty-ratio β. If the thrust and the torque are totally correlated, there is only one setpoint parameter for each actuator.

The identified disturbances are the platform motions (variations of inflow conditions) and the aerodynamic interactions between the different actuators.

Open-loop control and closed-control could be envisaged, depending on the requirements in terms of bandwidth, static error, overshoot, ….The open-loop control in this work uses a feedforward strategy. In other works (Azcona *et al.*, 2014; Meseguer and Guanche, 2019) it is denoted as *calibration* procedure. The feedforward strategy is based on an identification of the actuator behavior. The corresponding identification methodology for the static behavior and the dynamic behavior is described in chapter 6. The main drawback of this methodology is about unmeasured disturbances that may introduce discrepancies between the identified behavior of the actuator and the actuated forces.

Feedback control of the actuators might increase the actuator bandwidth and take into account any disturbances. Several design techniques for Proportional Integral Derivative (PID) controllers have been established by the engineering control community. In terms of additional requirements, the *force observer* needs to run in real-time and filter the unwanted frequencies. For aircraft propeller that spins at high rotational velocities, oscillations and vibrations at 1P (mass imbalance) or $n_{blades} * P$ (imbalance in the input or outputs section for the flow) might be a challenge for an accurate, stable and robust feedback control strategy.

4.3.1.4 Comparison with another actuation solution

To sum-up this load analysis, a qualitative comparison between the on-board propeller type actuator and the earth-fixed cable actuator solution is presented in Table 19. (+) denotes an advantage

compare to the other solution and (-) denotes a drawback. This synthetic table is based on a qualitative analysis. To go further and quantify those differences, a comparative test campaign with the different actuator solutions is required.

	Aicraft propellers	Cables
Force allocation	(+) Might be simple	(-) The force allocation depends on fixation point around the wave tank; Systems are usually overactuated
Installation	(+) very easy	(-) is adapted to each facility
Highest frequency captured	(-) To be characterized. This depends on the inertia versus torque characteristics of the motors	(+) and (-) The adapted DC motor can have large torque characteristics. However, vibrations of the cables or ropes could impose a threshold.
Force control characteristics		
Sensitivity to delay	(+) sensitive	(-) very sensitive
Calibration of the actuator system	(-) a dynamic feedforward is preferred	(+) simple (springs)
Disturbance rejection due to platform motions	(+) minor influence	(-) major influence
Determinism (via sensors, simple laws,…)	(-) Sensors are complex and the force observer needs to be carefully designed. The thrust produced is less deterministic.	(+) One uni-directional load cell per cable. The tension produced is relatively deterministic.
Control strategies	(+) Feedforward control mandatory but feedback control not necessarily required.	(-) Need of feedforward and feedback control strategies.

Table 19: Qualitative comparison between aircraft propellers and cables actuator solution

4.3.2 Force allocation - framework

The load analysis of part 4.3.1 has been developed for a single actuator. The next development concerns the procedure to get the setpoint load for each actuator from the setpoint load tensor, output of the integrated real-time numerical model. This procedure is called force allocation.

Different aspects of the force allocation are presented:

- The analytical formula to switch from the numerical setpoint load tensor to the actuators individual setpoint and vice-versa;
- The different options that could be followed, i.e. under-actuated, fully-actuated or over-actuated layout. This covers the different required methodologies, its advantages and drawbacks.

Notations and conventions

Different notations are introduced for the following developments. The reference frame is the shaft frame defined by the unit vectors ($\overrightarrow{e_x}, \overrightarrow{e_y}, \overrightarrow{e_z}$). The reference origin is the hub Apex and denoted O_{hub}

The following subscripts are used:

- $rotor$ stands for the loads generated in the shaft frame. Either target loads from the numerical tool or actuated load by the actuators;
- $prop$ stands for the propeller loads;
- act stands for actuated – realized/produced – load;
- set means it is a setpoint.

The following variables are used:

- T stands for the thrust of each actuator;
- Q stands for torque of each actuator;
- $P_{T_i}$are the coordinates x_i, y_i and z_i of the thruster i in the shaft frame;
- $\overrightarrow{e_{Ti}}$ are the orientations of each thruster in the reference frame. They are unit vectors.

They are $\boldsymbol{n_{prop}}$ propellers and the number of load component is $n_{rotor\ load}$ (≤ 6).

$T_{prop\ act} = \left(T_{1\ act} \dots T_{n_{prop}\ act}\right)$ is the thrust produced (actuated) by n_{prop} propellers.

$T_{prop\ set} = \left(T_{1\ set} \dots T_{n_{prop}\ set}\right)$ is the thrust setpoint for the n_{prop} propellers.

As a propeller i generates a thrust T_i, a torque $Q_{m,i}$ and gyroscopic moments $M_{gyro\ prop\ i}$ the total loads produced by the propellers are denoted $F_{prop\ act}$ and the total loads setpoints are denoted $F_{prop\ set}$

4.3.2.1 Definition of the force allocation procedure

In the general case, each propeller is producing a thrust oriented along the orientation $\overrightarrow{e_{Ti}}$. $\overrightarrow{T_i} = T_i \begin{bmatrix} \overrightarrow{e_{Ti}}.\overrightarrow{e_x} \\ \overrightarrow{e_{Ti}}.\overrightarrow{e_y} \\ \overrightarrow{e_{Ti}}.\overrightarrow{e_z} \end{bmatrix}$. It is also producing a torque around the $\overrightarrow{e_{Ti}}$ axis and due to the motions of the shaft in the inertial frame, some gyroscopic torques are acting. The torques applied at the actuators locations are denoted $\overrightarrow{M_{prop,i}} = \begin{bmatrix} M_{prop\ x,i} \\ M_{prop\ y,i} \\ M_{prop\ z,i} \end{bmatrix}$ for each actuator i. In a first approach, the torques and gyroscopic moments are neglected. This makes $F_{prop\ act} = T_{prop\ act}$ and $F_{prop\ set} = T_{prop\ set}$.

Once the layout of the different actuators has been defined, a relation could be defined between the rotor loads effectively produced $F_{rotor\ act}$ and the propeller loads $F_{prop\ act}$. Denoting J_F (Jacobian) this transformation matrix, we have the Eq. (4.8):

$$F_{rotor\ act} = \boldsymbol{J_F} * F_{prop\ act} \tag{4.8}$$

The Jacobian J_F expresses the contribution of each actuator thrust to the total load tensor expressed in the shaft frame. Then, the question is how to get, at each time step, the setpoint loads $F_{prop\ set}$ for the actuators from the SIL setpoint loads $F_{rotor\ set}$. The procedure to get $F_{prop\ set}$ from $F_{rotor\ set}$ is called the force allocation procedure. Depending on the number of actuators and their layout, the force allocation procedure differs. The different options for the system *under-actuated*, *fully-actuated* or *over-actuated*.

Firstly, the force allocation procedure is derived in the general case. Secondly, this force allocation procedure is applied to some specific fully-actuated and over-actuated layout.

To compute the moments induced by the thrust, the relation: $M_{\overrightarrow{T_i}/O_{hub}} = \overrightarrow{OP_{T_i}} \wedge \overrightarrow{T_i}$ is used. It leads to Eq. (4.9):

$$M_{\overrightarrow{T_i}/O_{hub}} = \begin{bmatrix} x_i \\ y_i \\ z_i \end{bmatrix} \wedge T_i \begin{bmatrix} \overrightarrow{e_{Ti}}.\overrightarrow{e_x} \\ \overrightarrow{e_{Ti}}.\overrightarrow{e_y} \\ \overrightarrow{e_{Ti}}.\overrightarrow{e_z} \end{bmatrix} = T_i \begin{bmatrix} y_i\overrightarrow{e_{Ti}}.\overrightarrow{e_z} - z_i\overrightarrow{e_{Ti}}.\overrightarrow{e_y} \\ z_i\overrightarrow{e_{Ti}}.\overrightarrow{e_x} - x_i\overrightarrow{e_{Ti}}.\overrightarrow{e_z} \\ x_i\overrightarrow{e_{Ti}}.\overrightarrow{e_y} - y_i\overrightarrow{e_{Ti}}.\overrightarrow{e_x} \end{bmatrix} \quad (4.9)$$

In the general case, the relation between the propellers' thrust and torque and the load tensor generated in the hub frame is defined by Eq. (4.10). The corresponding Jacobian is expressed in Eq. (4.11).

$$\begin{cases} F_{prop\ act\ x} = \overrightarrow{e_{T1}}.\overrightarrow{e_x}T_1 + \overrightarrow{e_{T2}}.\overrightarrow{e_x}T_2 + \cdots + \overrightarrow{e_{Tn_{prop}}}.\overrightarrow{e_x}T_{n_{prop}} \\ F_{prop\ act\ y} = \sum_{i=1}^{n_{prop}} \overrightarrow{e_{Ti}}.\overrightarrow{e_y}\,T_i \\ F_{prop\ act\ z} = \sum_{i=1}^{n_{prop}} \overrightarrow{e_{Ti}}.\overrightarrow{e_z}\,T_i \\ M_{prop\ act\ x} = \sum_{i=1}^{n_{prop}} \left(y_i\overrightarrow{e_{Ti}}.\overrightarrow{e_z} - z_i\overrightarrow{e_{Ti}}.\overrightarrow{e_y}\right)T_i \\ M_{prop\ act\ y} = \sum_{i=1}^{n_{prop}} \left(z_i\overrightarrow{e_{Ti}}.\overrightarrow{e_x} - x_i\overrightarrow{e_{Ti}}.\overrightarrow{e_z}\right)T_i \\ M_{prop\ act\ z} = \sum_{i=1}^{n_{prop}} \left(x_i\overrightarrow{e_{Ti}}.\overrightarrow{e_y} - y_i\overrightarrow{e_{Ti}}.\overrightarrow{e_x}\right)T_i \end{cases} \quad (4.10)$$

$$J_F = \begin{bmatrix} \overrightarrow{e_{T1}}.\overrightarrow{e_x} & \cdots & \overrightarrow{e_{Tn_{prop}}}.\overrightarrow{e_x} \\ \overrightarrow{e_{T1}}.\overrightarrow{e_y} & \cdots & \overrightarrow{e_{Tn_{prop}}}.\overrightarrow{e_y} \\ \overrightarrow{e_{T1}}.\overrightarrow{e_z} & \cdots & \overrightarrow{e_{Tn_{prop}}}.\overrightarrow{e_z} \\ \left(y_1\overrightarrow{e_{T1}}.\overrightarrow{e_z} - z_1\overrightarrow{e_{T1}}.\overrightarrow{e_y}\right) & \cdots & \left(y_{n_{prop}}\overrightarrow{e_{Tn_{prop}}}.\overrightarrow{e_z} - z_{n_{prop}}\overrightarrow{e_{Tn_{prop}}}.\overrightarrow{e_y}\right) \\ \left(z_i\overrightarrow{e_{Ti}}.\overrightarrow{e_x} - x_i\overrightarrow{e_{Ti}}.\overrightarrow{e_z}\right) & \cdots & \left(z_{n_{prop}}\overrightarrow{e_{Tn_{prop}}}.\overrightarrow{e_x} - x_{n_{prop}}\overrightarrow{e_{Tn_{prop}}}.\overrightarrow{e_z}\right) \\ \left(x_i\overrightarrow{e_{Ti}}.\overrightarrow{e_y} - y_i\overrightarrow{e_{Ti}}.\overrightarrow{e_x}\right) & \cdots & \left(x_{n_{prop}}\overrightarrow{e_{Tn_{prop}}}.\overrightarrow{e_y} - y_{n_{prop}}\overrightarrow{e_{Tn_{prop}}}.\overrightarrow{e_x}\right) \end{bmatrix} \quad (4.11)$$

$\boldsymbol{J_F}$ is then a n_{prop} -by-$n_{rotor\ load}$ full matrix.

As a conclusion, a layout is characterized by the orientation $\overrightarrow{e_{Ti}}$ and the coordinates $P_{T_i}$of each propeller. In the general case there are $\boldsymbol{n_{prop} * (3+3)}$ parameters for this layout.

Under-actuated layout

The system is *under-actuated* if the rank of the Jacobian J_F is less than the number of load components to reproduce. It is due to the number of actuators n_{prop} and their layout compared to the number of load components to reproduce $n_{rotor\ load}$. The force allocation procedure is based on a optimization to minimize the global level of errors on the actuated tensor compared to the target tensor.

Fully-actuated layout

The system is *fully-actuated* if the rank of the Jacobian J_F is equal to the number of load components to reproduce and the number of actuators equals the number of load components to reproduce. The Jacobian is a square matrix with a nonzero determinant. The force allocation procedure only depends on the layout of the actuators.

Over-actuated layout

The system is *over-actuated* if the rank of the Jacobian J_F is equal to the number of load components to reproduce and if the number of actuators is larger than the number of load components to reproduce. The force allocation procedure is based on an optimization to minimize the global level of errors on the actuated tensor compared to the target tensor. Over-actuated systems are well–studied topic in the control science community, for instance applied to parallel cable robots as it becomes possible to avoid negative tensions in the cables. There is not a unique solution for the propeller thrust setpoint, and either real-time optimization or additional relations are used to define the setpoint for each actuator. Different optimization strategies are presented and implemented on a simplified case in part 4.3.4.3 for eight propellers and the six rotor loads to reproduce.

The different layout possibilities and the main consequences for the setpoint of the actuators is presented in Table 20.

Under-actuated system	Fully-actuated system	Over-actuated system
$rank(J_F) \leq n_{rotor\ load}$ $\boldsymbol{F_{prop\ set}}$ is obtained from an optimization performed at each time step or on additional constraints	$\begin{cases} n_{prop} = n_{rotor\ load} \\ rank(J_F) = n_{rotor\ load} \end{cases} \Leftrightarrow \det(J_F) \neq 0$ This leads to Eq (4.12): $\boldsymbol{F_{prop\ set}} = J_F^{-1}\boldsymbol{F_{rotor\ set}}$ (4.12) J_F^{-1} is unique and fixed once the layout is fixed.	$\begin{cases} n_{prop} > n_{rotor\ load} \\ rank(J_F) \geq n_{rotor\ load} \end{cases}$ $\boldsymbol{F_{prop\ set}}$ is obtained from an optimization performed at each time step or on additional constraints

Table 20: Different layout configurations and consequences on the setpoints.

4.3.2.2 Inclusion of the torque and gyroscopic moments in the force allocation

As explained in part 4.3.1, these actuators produced not only thrust but also small torques and due to their angular velocities in the inertial frames, gyroscopic torques. Firstly, the modifications due to these additional loads produced by the actuators on the force allocation procedure are presented. Secondly, evaluation of the different contributions in terms of order of magnitudes are used to simplify the problem.

The relation between the actuators forces and the load tensor generated is then slightly modified from Eq. (4.10) to Eq. (4.13).

$$\begin{cases} F_{prop\ act\ x} = \overrightarrow{e_{T1}}.\overrightarrow{e_x}T_1 + \overrightarrow{e_{T2}}.\overrightarrow{e_x}T_2 + \cdots + \overrightarrow{e_{Tn_{prop}}}.\overrightarrow{e_x}T_{n_{prop}} \\ F_{prop\ act\ y} = \sum_{i=1}^{n_{prop}} \overrightarrow{e_{Ti}}.\overrightarrow{e_y}\,T_i \\ F_{prop\ act\ z} = \sum_{i=1}^{n_{prop}} \overrightarrow{e_{Ti}}.\overrightarrow{e_z}\,T_i \\ M_{prop\ act\ x} = \sum_{i=1}^{n_{prop}} \left(y_i\overrightarrow{e_{Ti}}.\overrightarrow{e_z} - z_i\overrightarrow{e_{Ti}}.\overrightarrow{e_y}\right)T_i + \sum_{i=1}^{n_{prop}} M_{prop\ x,i} \\ M_{prop\ act\ y} = \sum_{i=1}^{n_{prop}} \left(z_i\overrightarrow{e_{Ti}}.\overrightarrow{e_x} - x_i\overrightarrow{e_{Ti}}.\overrightarrow{e_z}\right)T_i + \sum_{i=1}^{n_{prop}} M_{prop\ y,i} \\ M_{prop\ act\ z} = \sum_{i=1}^{n_{prop}} \left(x_i\overrightarrow{e_{Ti}}.\overrightarrow{e_y} - y_i\overrightarrow{e_{Ti}}.\overrightarrow{e_x}\right)T_i + \sum_{i=1}^{n_{prop}} M_{prop\ z,i} \end{cases} \quad (4.13)$$

$M_{prop,i}$ is due to the motor torque $Q_{m,i}$ of the i[th] actuator and to the gyroscopic torques $M_{gyro,i}$. Each source of torque and their dependencies are presented.

Gyroscopic torques:

$M_{gyro,i}$ is a function of $\left(\dot{X_{FWT}}, \sqrt{T}\right)$ as it depends on the angular velocities of the propeller $\omega_{m,i}$. Indeed, for a propeller oriented in the $\overrightarrow{e_{Ti}}$ direction, with angular speed $\omega_{m,i}$ and with platform rotational speed vector $\overrightarrow{R_p}$, we get Eq. (4.14):

$$\overrightarrow{M_{gyro,i}} = J_{prop} \times \omega_{m,i} \times \overrightarrow{e_{Ti}} \wedge \overrightarrow{R_p} \tag{4.14}$$

with:

- J_{prop} the actuator inertia around its shaft
- $\overrightarrow{R_p} = (\dot{X_{FWT\,4}} \quad \dot{X_{FWT\,5}} \quad \dot{X_{FWT\,6}})$

To simplify, two assumptions are introduced:

- rotational velocities due to the tower deflections are neglected;
- platform roll and yaw velocities are negligible compared to the platform pitch velocity.

From these assumptions, the rotational speed vector simplifies to $\overrightarrow{R_p} = (0 \quad \dot{X}_5 \quad 0)$.

Then, the gyroscopic torques simplify to Eq. (4.15):

$$\overrightarrow{M_{gyro,i}} = J_{prop} \times \omega_{m,i} \times \dot{X}_5 \times \begin{pmatrix} -\overrightarrow{e_{Ti}}.\overrightarrow{e_z} \\ 0 \\ \overrightarrow{e_{Ti}}.\overrightarrow{e_x} \end{pmatrix} \tag{4.15}$$

To evaluate the significance of the gyroscopic torques, orders of magnitude have been computed for one load case and one actuator. The application case is based on the SOFTWIND SPAR experiments, at scale (1:40), with environmental parameters $H_s = 5.8m; T_p = 10.9s;\ U_{hub} = 18m.s^{-1}; T_I = 17\%$. The actuator is the KDE5215-XF220 with the KDE-CF155-DP propellers and oriented in the $\overrightarrow{e_x}$ direction. For the estimation of the angular velocity of the propeller, the tabulated performance data from the manufacturer documentation has been interpolated based on the input force. From the manufacturer documentation, the propeller has an inertia about the central axis (including propellers, mounting hardware, and adapter) of $J_{prop} = 2.9\,\mathrm{E}-4\ \mathrm{kg.m^2}$. For this application case, the maximal gyroscopic torque acting on the actuator is $0.02N.m$ while the maximal setpoint load component $M_{rotor\,set\,z}$ is $18N.m$. This makes the gyroscopic torque 3 orders of magnitude below the setpoint $M_{rotor\,set\,z}$. These gyroscopic torques could then be safely removed from the force allocation.

Motor torque

For steady-state values, there is a direct link between the motor torque and the thrust. The steady-state relation could be obtained by the results of static calibration, experimentally determined (see chapter 6) or provided by the manufacturer. However, the relations between the dynamic torque and the dynamic thrust are not obvious. A short reasoning is presented to identify the main dependencies of the motor torque.

From a torque momentum equation on the motor shaft we have Eq. (4.16)

$$Q_m + Q_{aero} + Q_f = J_{prop}\dot{\omega_m} \tag{4.16}$$

With the same notations as before and with Q_f a friction torque that is neglected in a first approach. Following the approximations presented in part 4.3.1.2, we have:

- $Q_{aero} \sim \frac{C_Q}{C_T} \times T$
- $\frac{dT}{dt}$ proportional to $\dot{\omega_m}\omega_m$

This makes the motor torque Q_m dependent on the thrust T and to the temporal derivative of the thrust $\frac{dT}{dt}$. This dependency is denoted by $Q_m \sim \mathcal{L}_{TtoQ_m}\left(T, \frac{dT}{dt}\right)$. The Jacobian can be extended by adding the thrust derivatives to the thrusts in the actuated forces. A state vector $Y = \left[T_1 \quad \dots \quad T_{n_{prop}} \quad \frac{dT_1}{dt} \quad \dots \quad \frac{dT_{n_{prop}}}{dt}\right]$ is introduced and the Jacobian is now of dimension $n_{rotor\ loads} \times 2n_{prop}$. The developments are not pursued and instead, to provide some insights about the feasibility of the force allocation procedure, the dependency on $\frac{dT}{dt}$ is neglected and the steady-state relation between the motor torque and the thrust is used. $Q_m \sim \mathrm{C(T)} \times T$ with C(T) a coefficient that depends on the operating point.

The term $\sum_{i=1}^{n_{prop}} M_{prop\,x,i}$ in Eq. (4.13) is re-expressed by Eq. (4.17)

$$\sum_{i=1}^{n_{prop}} M_{prop\,x,i} = \sum_{i=1}^{n_{prop}} Q_{m,i}\overrightarrow{e_{Ti}}.\overrightarrow{e_x} = \sum_{i=1}^{n_{prop}} \mathrm{C_i(T_i)\,T_i}\,\overrightarrow{e_{Ti}}.\overrightarrow{e_x} \tag{4.17}$$

The Jacobian is consequently slightly changed and is represented in Eq. (4.18)

$$J_F = \begin{bmatrix} \overrightarrow{e_{T1}e_x} & .. & \overrightarrow{e_{Tn_{prop}}e_x} \\ \overrightarrow{e_{T1}e_y} & .. & \overrightarrow{e_{Tn_{prop}}e_y} \\ \overrightarrow{e_{T1}e_z} & .. & \overrightarrow{e_{Tn_{prop}}e_z} \\ y_1\overrightarrow{e_{T1}e_z} - z_1\overrightarrow{e_{T1}e_y} + \mathrm{C_1T_1}\,\overrightarrow{e_{T1}e_x} & .. & y_{n_{prop}}\overrightarrow{e_{Tn_{prop}}e_z} - z_{n_{prop}}\overrightarrow{e_{Tn_{prop}}e_y} + \mathrm{C_nT_n}\,\overrightarrow{e_{Tn}e_x} \\ (z_i\overrightarrow{e_{Ti}e_x} - x_i\overrightarrow{e_{Ti}e_z}) + \mathrm{C_1T_1}\,\overrightarrow{e_{T1}e_y} & .. & z_{n_{prop}}\overrightarrow{e_{Tn_{prop}}e_x} - x_{n_{prop}}\overrightarrow{e_{Tn_{prop}}e_z} + \mathrm{C_nT_n}\,\overrightarrow{e_{Tn}e_y} \\ (x_i\overrightarrow{e_{Ti}e_y} - y_i\overrightarrow{e_{Ti}e_x}) + \mathrm{C_1T_1}\,\overrightarrow{e_{T1}e_z} & .. & x_{n_{prop}}\overrightarrow{e_{Tn_{prop}}e_y} - y_{n_{prop}}\overrightarrow{e_{Tn_{prop}}e_x} + \mathrm{C_nT_n}\,\overrightarrow{e_{Tn}e_z} \end{bmatrix} \tag{4.18}$$

If the coefficients C_i depend on the working point, the Jacobian changes at each time step. Evaluation of the motor torque influence has not been investigated. Experimental characterization of the motor torque is presented in chapter 6.

4.3.3 Frame design and actuators selection

The general framework for the actuation system design is described hereafter. This concerns the frame design and the selection of the actuators. The related topics are the optimization variables, the main objectives and constraints. The general objective of the actuation system design is to find a high-performance, easy-to-build solution that generates high quality forces and is lightweight.

The frame design includes the definition of the geometry and the properties of frame components. The corresponding characteristics and criteria to evaluate are:

- mechanical strength of the frame to withstand maximal and varying loads with minor deflections and sufficiently high resistance,
- limited deflections and vibrations for the frequencies of interest,
- limited mass and inertia of the overall frame.

The optimization variables are the parameters of the frame to be optimized. Each actuator is described by its position (3 variables) and its orientation (3 variables). This makes the total number of parameters up to $n_{prop} * 6$.

The actuator selection needs to be done in accordance to the frame design, as their choice highly depends on the force allocation procedure. The main characteristics of each actuator solution are:

- the thrust range, defined by the high and low saturation $[T_{min}, T_{max}]$,
- the mass of the {motor, propeller, ESC} assembly. Note that the ESC is not necessarily at the actuator location, but could be at the tower top or tower base of the FWT,

- the dynamics of each actuator, in terms of thrust derivative saturation and bandwidth.

Each actuator has its own properties and these properties could hardly be modeled as a function of their dimensions or mass. Attempts to introduce such dependencies led to unsatisfactory results. The optimization is instead a loop on different actuators solutions with their main characteristics.

4.3.3.1 Frame design: objectives and constraints

The objectives of the frame design are first introduced and then the constraints are described. Note that, mathematically, different techniques exist to modify a constraint in an objective, by using e.g. weighting functions around the constraints boundaries (penalty methods for constrained optimization).

The most important objective is the error between the targeted loads and the actuated loads. A L2 norm with weighting coefficients has been considered, expressed in Eq. (4.19)

$$\epsilon_{total} = \sum_{j=1}^{n_{rotor\ load}} \alpha_j \, \epsilon\left(F_{rotor\ j}\right) \tag{4.19}$$

With:

- α_j the weighting coefficient for the j[th] load component. If all the rotor loads have the same significance, $\forall j \in [1 - n_{rotor\ load}], \alpha_j = 1/n_{rotor\ load}$.
- ϵ the error between the actuated load and the setpoint load. The choice which has been made here is to use the Euclidian norm $\epsilon\left(F_{rotor\ j}\right) = \left\| F_{rotor\ set\ j} - F_{rotor\ act\ j} \right\|_2$.

Minimizing this error inherently assumes to have an estimation of $F_{rotor\ act\ j}$. This could be obtained either from a model of the actuator or from feedback control. Regarding feedback control, in a first approach it is envisaged to have only one 6-component balance be placed atop of the wind turbine mast. Consequently, the thrust of each propeller will probably not be measured. For a fully–actuated layout, this is not a problem since the Jacobian is invertible. For over-actuated layouts, there is not a unique solution of actuated thrusts from a single measurement. For exploration purposes, the choice that has been made is to assume a certain actuator model based on the simplified model presented in 4.3.1.

The actuated error objective is the main objective for the evaluation of the setup quality. However, additional and complementary objectives which do not necessarily require an actuator model could be used to have an efficient evaluation of different frames. (Chabaud *et al.*, 2018) mentioned, for cables, staying away from slacks and peaks for the setpoints vector improved the overall quality. For fans, if the main problem is the actuator dynamics and the thrust saturations, then a minimization of $\frac{\partial F_{setpoint}}{\partial t}$ and of $\left|F_{setpoints}\right|_{max}$ could provide interesting results for a pre-screening of the design space.

Additional objectives for the frame design could be introduced, for instance to limit the power consumption and the total economic cost of the solution.

In terms of constraints, different criteria are defined:

- location of the actuators, to avoid collision and aerodynamic interactions between the propellers and to have an efficient force allocation procedure,
- stiffness and frequency characteristics of the frame, with the most important frame mode natural frequencies not conflicting with an important source of solicitation. The deflections at any of the frequencies need to be relatively small.
- Mass and inertia budget compared to the target RNA.

Concerning the aerodynamic interaction, it (Meseguer and Guanche, 2019) observed an overall decrease of the actuated thrust when one or four out of four propellers are running for a multi-propeller setup. At the maximal payload (100% input), the overall decrease between the measured force produced by the four propellers compared to the sum of the individual thrust is 15% in their configuration. They tackle this problem by using a calibration of the thrust loss when using several actuators. However, it is better if this phenomenon that severely decreases the overall predictability of the actuators thrust could be avoided.

Concerning the suitability of a given layout to the force allocation, the requirements are on:

- the rank and the conditioning of the Jacobian,
- avoiding the 0N zone. If a selected actuator can only work in forward or in backward mode, this imposes a strong constraint of the same sign of the targeted force along the tests.

For the frequency characteristics of the frame, the important sources of excitations are:

- any FWT natural modes, including second tower mode if its response is not negligible;
- the actuator thrust setpoint;
- the imbalance of the propeller (propeller mass imbalances induce 1P frequency content and obstacles in the upstream or downstream zones of the propellers induce $n_{blades}\,P$ frequency content). Note that in the system developed by IH Cantabria (Meseguer and Guanche, 2019), polymer dampers have been used to limit the vibrations between the actuator and the frame.

Consequently, for the scale of interest, it is important to have the lowest natural mode of the frame above ~[10-15]Hz, with the additional constraint of exclusion zone (i.e. around 29Hz for the SOFTWIND SPAR setup described in chapter 5). For accurate force measurements, the deflections of the frame need to be relatively small, otherwise inertial loads due to the deflections of the frame will be measured.

Concerning the mass and inertia budget, the force transducers and the mechanical interfaces with the tower top needs to be incorporated with the comparisons to target wind turbine RNA properties.

4.3.3.2 Actuator selection

The actuators selection needs to be done in accordance with the given layout. The methodology that has been followed in the SOFTWIND project has been to establish different characteristics of a set of commercially available actuators. Those characteristics, ranked in decreasing importance, are:

- Thrust range,
- Mass of the {motor, propeller, adapter} assembly,
- Estimated bandwidth from the model presented in part 4.3.1.2.,
- ESC tuning parameters accessibility and documentation from the manufacturer,
- Power supply requirements (rated voltage, intensity requirements),
- Monitoring possibilities.

It has been noticed that most of the actuators for multicopters are working in forward-only or in backward-only modes.

A set of actuators has been estimated with the model presented in 4.3.1.2. From the available online documentation, the motors, ESC and propellers from two manufacturers have been checked: KDE-Direct and T-Motors. The database is presented in Appendix C.

4.3.4 Evaluation of layouts and actuators

In this part, different layouts and actuators are tested for specific (simplified) configurations. The overall objective is to provide guidelines to:

- select appropriated actuators;
- explore the design space of the actuators layout;
- compare fully-actuated versus over-actuated framework.

4.3.4.1 Single actuator, thrust actuated

For the floating setups and for the forced motions setup presented in chapter 5, only a single actuator and one force component $F_{rotor\,x}$, oriented in the shaft direction, of the setpoint load tensor have been considered. If the actuator has the right orientation (tilted as the wind turbine shaft) and right position (limited offset to avoid thrust-induced moment), the relation between $F_{prop\,set}$ and $F_{rotor\,x}$ simplifies to $F_{prop\,set} = F_{rotor\,x}$. If the actuator is not correctly oriented and positioned, there is no possibility to get the correct setpoint force.

4.3.4.2 Six actuators, fully-actuated

The force allocation procedure is first explored for a fully-actuated case with the assumption that all the rotor load components are important, i.e. $n_{rotor\,load} = 6$. A fully-actuated layout has the main advantage of freezing the allocation procedure. Each actuator thrust setpoint only depends on the rotor loads setpoints and on the layout of the different actuators. The setpoint thrusts are obtained by Eq. (4.12) with the condition $\det(J_F) \neq 0$. The Jacobian is a square matrix. A very simplified version of this layout has been considered to illustrate the actuators setpoints. Different assumptions are introduced hereafter to reduce the number of parameters. To simplify the problem, the propellers are assumed to be oriented on one axis $\overrightarrow{e_x}, \overrightarrow{e_y}, \overrightarrow{e_z}$ only: T_1 and T_2 on $\overrightarrow{e_x}$; T_3 and T_4 on $\overrightarrow{e_y}$; T_5 and T_6 on $\overrightarrow{e_z}$. To further simplify the problem, another restriction is used: one actuator would only affect one force and one moment. This is done by selecting appropriate positions of the actuators. The advantage of this simplified layout is to simplify the force allocation procedure to three decoupled problems, each problem made of two unknowns (the two thrust setpoints). Now the question is about the associations between the different forces and moments. Several options exist and the choice is based on a sorting of different criteria. The most important criteria which have been identified are:

- The lowest error between the setpoint rotor loads $F_{rotor\,set}$ and the actuated rotor loads $F_{rotor\,act}$. This is, by far, the most important criterion. Attention should be paid to the most important rotor loading components. This is mathematically introduced as weighting coefficients in the norm for the evaluation of the error levels.
- The mass budget should be respected (avoid unnecessary large actuators)
- Other aspects such as the power consumed by the different propellers or the price of the setup are also of interest.

To get the lowest level of error, it is expected that the setpoint of the actuator should stay away from very low values (low cut-off frequency and low maximum rate of thrust change around 0). Moreover, some aircraft propellers can rotate forward and backward in the same test, some others cannot. The possibility to have forward and backward operation relies on:

- The ESC (ideally four quadrants);
- The shape of the propellers and the aerodynamic performance of the airfoils.

One of the possibilities is to associate the forces and moments in such a way that at least one component has the same sign during a test. With an adequate layout, this should ensure the setpoint thrust to keep the same sign during a test. From a brief analysis of the rotor load setpoint, the important observations are:

- F_x and $M_x > 0$ whatever the incident wind speed.
- $M_y \sim > 0$ in case of a significant vertical shear, especially above rated. This is not the case for highly turbulent wind fields.
- Above rated wind speed, F_y has a small negative mean value, F_z has a small positive mean value, and M_z has a small negative mean value. However, the variations are in the same order of magnitude as the mean values.

An example is to associate F_x and M_z; F_y and M_x ; F_z and M_y. This combination leads to the Jacobian expressed in Eq. (4.20) and a schematic illustration is represented in Figure 42.

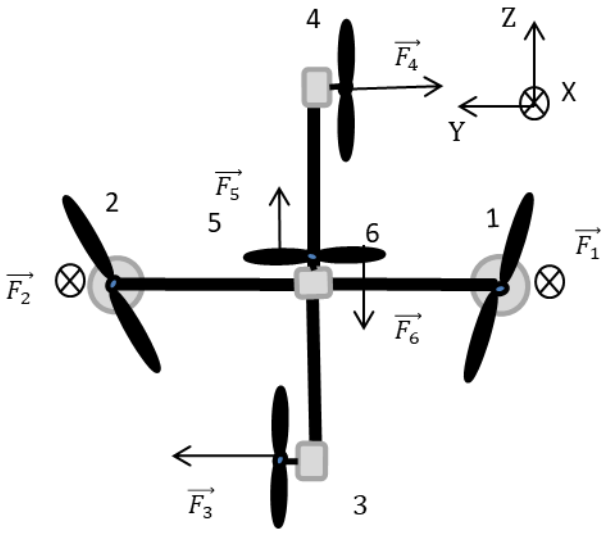

Figure 42: Schematic drawing of the six actuators fully-actuated simplified layout. OYZ projected view

$$J_F = \begin{bmatrix} 1 & 1 & 0 & 0 & 0 & 0 \\ 0 & 0 & 1 & -1 & 0 & 0 \\ 0 & 0 & 0 & 0 & 1 & -1 \\ 0 & 0 & -z_3 & z_4 & 0 & 0 \\ 0 & 0 & 0 & 0 & -x_5 & x_6 \\ -y_1 & -y_2 & 0 & 0 & 0 & 0 \end{bmatrix} \tag{4.20}$$

To provide some insights about actuator selection and frame dimension, this layout is applied to a given wind turbine load case. Firstly, the actuators are fixed and the actuators locations $(y_1, y_2, z_3, z_4, x_5, x_6)$ vary. Secondly, the locations are fixed and the actuators vary to see the differences between different actuators. The objective of this preliminary work was to highlight the key factors and relevant metrics for the selection of different layouts.

The selected load case is the illustrating case on the OC3-Hywind FWT, with the NREL 5MW, as presented in chapter 2 and 3. The load tensor is then scaled down using a scale ratio of 1:30.

Determined actuators and varying dimensions

In this first study, the objective is to get order of magnitude for the acceptable lengths. The main criteria to select acceptable lengths are:

- the ratio between the I_{zz} inertia of the actuators and the I_{zz} inertia of the target RNA,
- the error on the actuated rotor load component.

The inertia of the actuators and its frame are calculated according to Eq. (4.21):

$$I_{zz\ RNA\ actuators} = 1.5 * \sum_{i}^{n_{prop}} m_{prop,i} * \sqrt{\left(\overrightarrow{P_{Ti}}.\overrightarrow{e_x}\right)^2 + \left(\overrightarrow{P_{Ti}}.\overrightarrow{e_y}\right)^2} \tag{4.21}$$

The 1.5 correction factor is taken into account to roughly approximate the frame contribution into the total inertia. The target RNA is that of the NREL 5MW RWT: $I_{zz\ RNA\ target} = 2.5E + 7\ kg.m^2$

The inputs actuators are the KDE-Direct 5215-XF220 with CF-155-DP propellers. To get a first insight, the problem is first reduced to the (F_x, M_z) problem for two actuators. To get only one input parameter a symmetrical layout is assumed, i.e. their input locations are $y_1 = -y_2 = L$, with L a characteristic length. Their mass (including cables, ESC, motor and prop) is approximately 0.42kg.

In Figure 43 top, the error on M_z and M_x are presented for a length L varying in the range [0.3 - 2]m. The higher the error on F_x, the higher the error on M_z. On the bottom plot, the error on F_x is represented as function of the $I_{zz\ RNA}$ ratio ($\frac{I_{zz\ RNA\ actuators}}{I_{zz\ RNA\ target}}$). The higher the inertia, i.e. the higher the length L, the lower the error on the force F_x. This could be explained by the impact of the M_z load component on the target actuator setpoint. If the length increases, a small change of the thrust of one actuator has a bigger impact on the generated moment M_z. Consequently, with large lengths, the torque induce setpoint is relatively smaller. This will be illustrated in a following study. An acceptable limit of the $I_{zz\ RNA}$ ratio has been arbitrary fixed to 3 and is represented by the black dashed line on the figure. For scale ratios of 1:30, 1:40 and 1:50, the maximal lengths are respectively [0.3, 0.5 and 1.2]m. The selected actuators have diameters of 0.4m. To limit the aerodynamic interactions, a minimal length of one diameter is preferred. This makes the design not appropriate for a scale ratio of 1:50. For the following studies, the length range is reduced to $[0.5 - 1]m$.

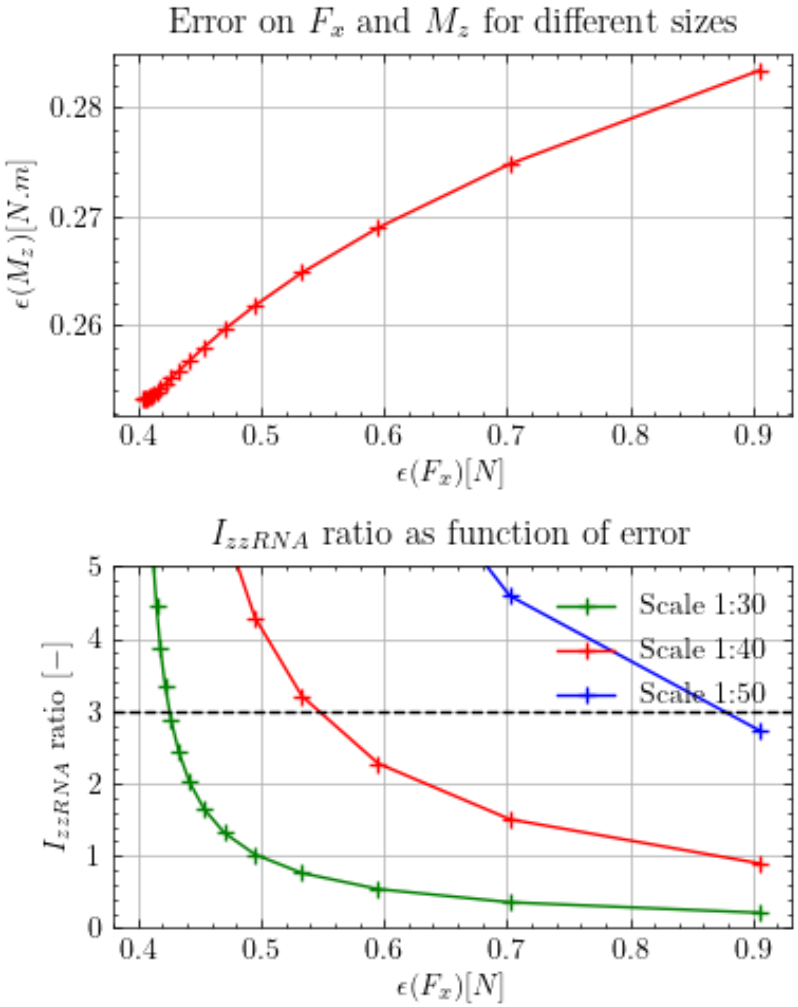

Figure 43: Error on the actuated forces depending on the input spacing between the actuators

Fixed dimensions and varying actuators

The same two load components F_x and M_z are considered. L is fixed to 0.5m. Different actuators are used:

- KDE-Direct 5215-XF220 with CF-155-DP propellers,
- KDE-Direct 4215-XF465 with CF-125-DP propellers,
- T-motor MN501S with propellers,
- T-motor PV60 with propellers.

The time series of the rotor loads (F_x,M_z) and of the thruster loads (T_1,T_2) are represented in Figure 44. The time series are plotted on a short period of time to see how the propellers follow their setpoint. From the setpoints of the rotor loads, it is clear that the M_z component has a 3P frequency content (approx. 0.3s at this scale) much more pronounced than the F_x component which is dominated by the wave frequency variations approx. 2s at this scale). With this actuator model, the behavior is not symmetrical between increasing setpoint and decreasing setpoint, the low saturation of the thrust derivative (freewheel) being important around time = 26s. The actuators have close behavior for increasing setpoints but differ for decreasing setpoint. The wave frequency variation of the rotor loads are relatively well captured (except the low saturation). However, the 3P variations are roughly captured, ass seen on the actuated M_z component compared to the M_z setpoint.

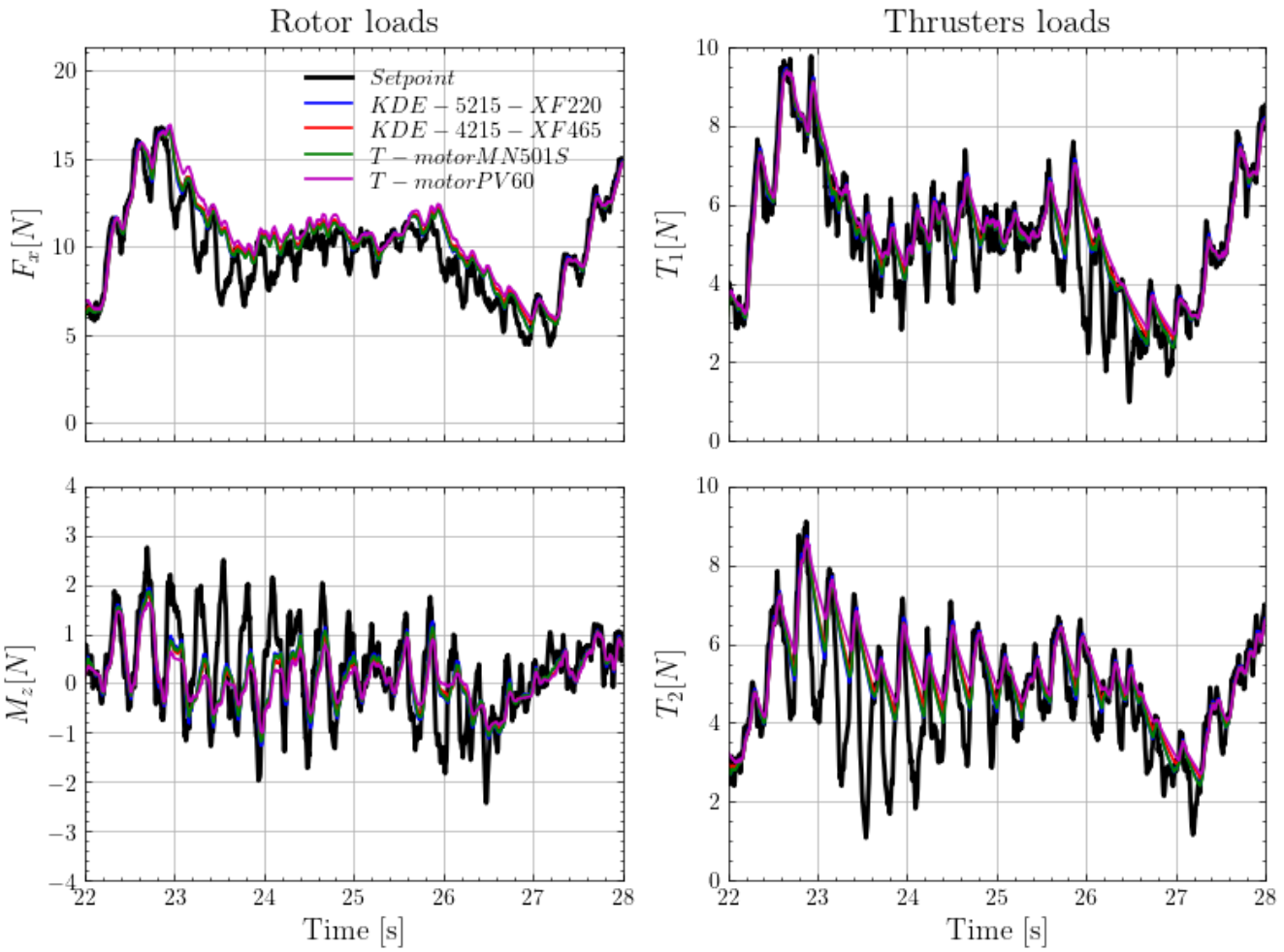

Figure 44: Rotor setpoints and actuated loads versus time for different actuators

The time series and error levels of the six actuator loads and six actuated rotor loads are depicted in the next subsection with comparison with the over-actuated solution.

4.3.4.3 Eight actuators, over-actuated system

In the case of an over-actuated system, the number of equations ($n_{rotor\ loads}$) is less than the number of unknowns n_{prop}. To define the force allocation procedures, there are different possibilities. An *intuitive* constraint on the distribution of the loads could be used. This constraint defines additional equations to close the system and to have a unique solution for each thruster. This is the solution retained by (Meseguer and Guanche, 2019) to limit the torques produced by the propellers. Or, another option is to implement an optimization procedure that has to be solved at each time step. The objectives and constraints of this optimization problem are expressed in the next subsection.

For exploration purpose, two propellers in charge of the F_x rotor load component have been added to the simplified six actuators fully-actuated layout. To avoid aerodynamic interaction, the locations of actuators 1 and 2 now have negative z values and the actuators 7 and 8 have positive z values. The orientations need to be carefully selected. Two configurations have been retained:

- Actuators 1, 2, 7 and 8 generate a positive unidirectional load in the $+\overrightarrow{e_x}$ direction. This configuration is denoted C_1 in the following figures;
- Actuators 2 and 7 have a positive thrust in the $+\overrightarrow{e_x}$ direction. Actuators 1 and 8 have a positive thrust in the $-\overrightarrow{e_x}$ direction. This configuration is denoted C_2 in the following figures

The new Jacobian is expressed in Eq. (4.22) and reflects the influence of the eight actuators thrust on the six rotor load components. This Jacobian is the one of C_2. A schematic illustration is depicted in Figure 45.

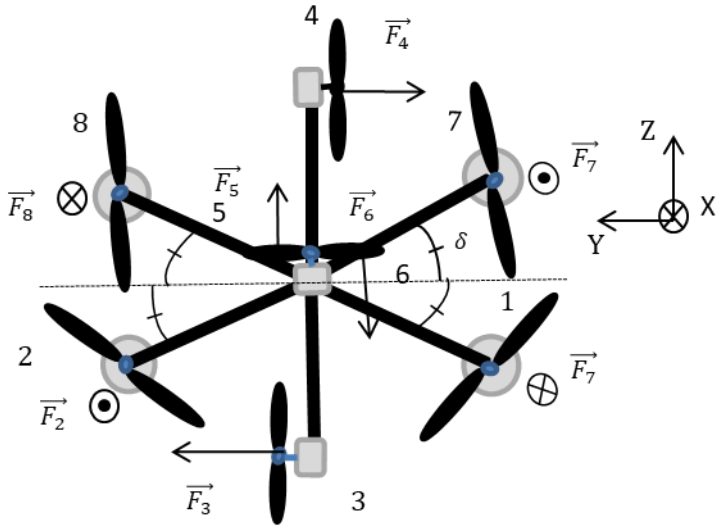

Figure 45: Schematic drawing of the 8-actuator over-actuated simplified layout. OYZ projected view

$$J_F = \begin{bmatrix} 1 & -1 & 0 & 0 & 0 & 0 & -1 & 1 \\ 0 & 0 & 1 & -1 & 0 & 0 & 0 & 0 \\ 0 & 0 & 0 & 0 & 1 & -1 & 0 & 0 \\ 0 & 0 & L_3 & -L_4 & 0 & 0 & 0 & 0 \\ z_1 & z_2 & 0 & 0 & L_5 & -L_6 & z_7 & z_8 \\ -y_1 & -y_2 & 0 & 0 & 0 & 0 & -y_7 & -y_8 \end{bmatrix} \tag{4.22}$$

The selected objectives and constraints of the optimization problem are listed hereafter.

Objectives: The error objective presented in Eq.(4.19) is directly implemented. To estimate the actuated loads at each time step, the actuator models (thrust range, dynamics) have been used. The weighting coefficients for the norm evaluation of the rotor loads which have been used are $\alpha = [100, 5, 1, 6, 3, 5]$.

Constraints: The only constraints that are implemented are the thrust ranges for each actuator.

The optimization problem has been implemented in the Python Optimize SciPy package. After different tests to select suitable algorithms, the SLSQP (Sequential Least Squares Programming) algorithm has been considered as enough robust and time-efficient. This algorithm could be applied because the selected norm make the optimization problem a least-square-based optimization problem, widely studied in the literature.

To evaluate the gains obtained by using 8 actuators instead of 6 actuators, a comparison has been done with similar layouts and similar actuators. The actuators in charge of $\overrightarrow{e_x}$ are the KDE-Direct 5215-220 CF-155-DP, and the others are the KDE-Direct 4215-465 CF-125-DP. The reference length is 0.7m. For the 8 actuator configurations, the actuators 1, 2, 7, 8 are symmetrically located following the illustrative drawing in Figure 45, with an angle $\delta = 45°$ with the y-axis. Concerning the actuator models, a pure delay of 20ms is assumed for this comparison case.

The results are compared for the rotor loads $F_{rotor\ act}$ and the propeller thrusts $T_{prop\ act}$. The time series are depicted in Figure 46 and in Figure 47, respectively.

Different observations could be made:

- For the F_y and M_x rotor loads components, both configurations give the same results. These two load components are decoupled fromthe rest of the load components.
- On F_x:
  - The results are better with the 6 actuators than with the 8 actuators C_1. This is due to (i) the poorer performances (bandwidth) of the KDE-Direct 4215-XF465 than the KDE-Direct 5215-XF220, (ii) the fact that the optimization tries to minimize the error done on the M_y and M_z components, consequently the actuators 1, 2, 7 and 8 try to minimize the overall error (iii) the mean thrust for actuator 1 and 2 is lower for the 8 actuators configuration than for the 6 actuators configuration, leading to lower frequency bandwidth and relatively more important saturation;
  - However, the 8 actuators C_2 gives better results than the two others. This is due to the low saturations of the actuators generating in positive $\overrightarrow{e_x}$ counterbalanced by the actuators generating in negative $\overrightarrow{e_x}$;
- On M_y and F_z the results obtained with the 8 actuators C2 is much better than the 6 actuators configurations. With only 6 actuators, negative M_y could not be achieved while it is possible with the 8 actuators configurations.

These observations strongly depend on the actuator models. Indeed, as seen in Figure 47 for actuators 2, 5 and 6 the saturation mechanisms significantly deteriorate the actuation of the 6 actuators configuration and the 8 actuators C_1. This saturation (freewheel) mechanism needs to be investigated to see how it could be efficiently balanced (regenerative or dissipative braking ,…).

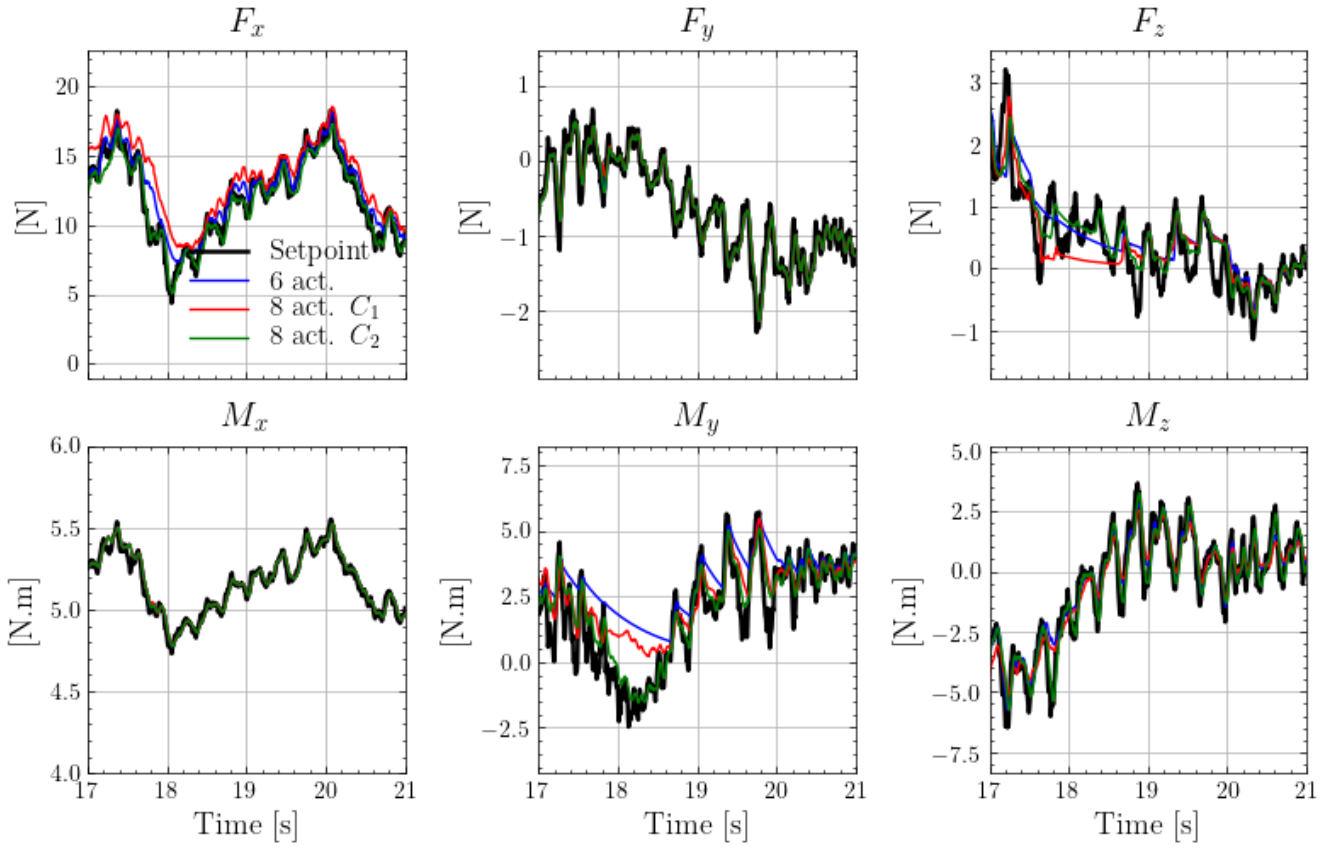

Figure 46: Rotor setpoints and actuated loads versus time for the 6 and 8 actuators configurations

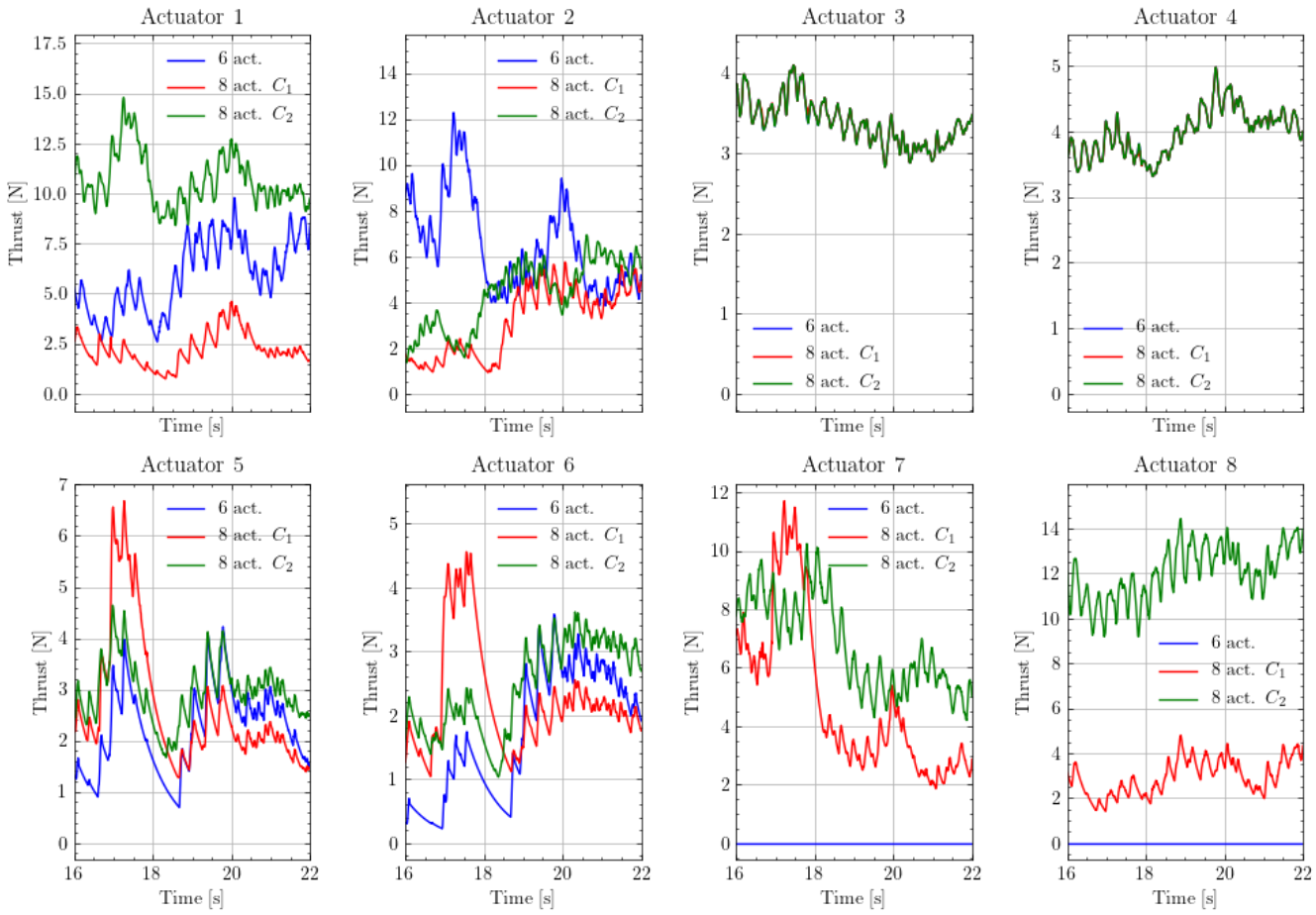

Figure 47: Actuated thrusts versus time for the 6 and 8-actuator configurations

To define additional indicators about the adaptability of a set of actuators to a given rotor loads test case, histograms of the different actuators throttles are depicted in Figure 48. These histograms show that, for most of the actuators, the mean operating point is quite low (in the range [10 - 30]%), and with a part of the time series in the range [0-10]%, which is problematic for the actuator dynamics. Indeed, it has been observed experimentally (see chapter 6) than below a certain throttle (in the range [5-15]%), the performances of the actuators collapse. For the 8-actuator configuration C_2, the histograms are narrower for actuators 1 and 2, indicating that the variations of the setpoints throttle is smaller for these actuators. This is a very valuable result that needs to be investigated further.

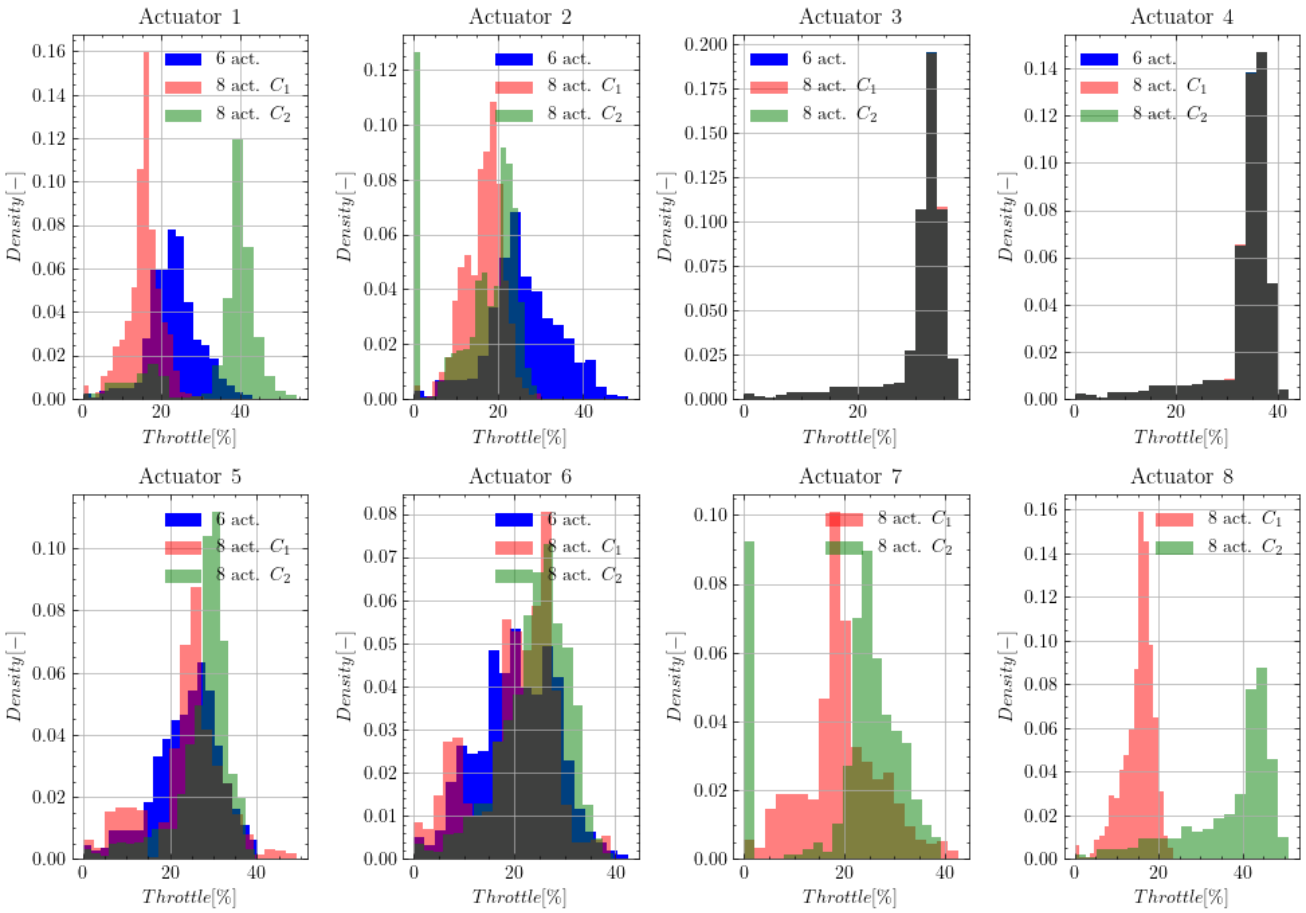

Figure 48: Throttle histogram of the different actuators, 8 and 6 actuators configurations

To conclude on this analysis, a simplified comparison between an 8-actuator and a 6-actuator configurations has been conducted. The over-actuated layout changes the force allocation and requires the use of an optimization at each time step. This optimization has been successfully implemented in a Python framework. The 8 actuators configuration improves the performances for some load components (M_y) but also deteriorates the performances on other load components (F_x). The throttle range of the different actuators is not well adapted to the rotor loads setpoints. This comparison has been done to provide guidance for suitable actuators layout and to check the overall added-value of over-actuated layouts. The main conclusions are that an over-actuated layout could improve the overall error levels by making the setpoint load for each actuator in a better suited regime zone, away from the very low regimes (0N).

4.4 Conclusions

In this chapter, the different subsystems of the SIL methodology have been presented. The three main subsystems are:

- The *numerical model* for the rotor loads full scale simulation,
- The *actuators* that reproduce the setpoint load computed by the *numerical model*,
- The *real-time environment* that integrates the *numerical model*, masters the data acquisition (DAQ) and corresponding *observers* and controls the *actuators*.

The different options and the choices that have been made are presented for each subsystem. The main conclusions per subsystem are now summed-up.

Numerical model

The role of the numerical model is to compute the full scale rotor loads depending on the incident wind fields, the control strategy, and the real-time measured motions of the FWT. Different models exist, but a real-time computation need to be performed. This restricts the number of suitable numerical models.

Then, a comparison of the rotor loads physical phenomena (damping, etc…) has been performed between a state-of-the-art medium fidelity model (OpenFAST, based on the BEMT) and different simplified models that require less inputs. The main outcomes are that the differences between the simplified models and OpenFAST depend on the characteristic frequency of the hub wind speed fluctuations. The integration of the wind turbine control law is mandatory to get the correct damping and out-of-phase components of the F_x rotor force.

Actuators

On-board actuators have been selected for this work. A load analysis is first presented, with a simplified analytical model to get the main driving factors for the actuators performances. Then, the force allocation procedure, i.e. the relations between the setpoint rotor loads tensor in the hub frame to each actuator thrust setpoint, is presented. The consequences on the actuators layout are investigated, with comparison between a fully-actuated layout and an over-actuated layout.

Real-time environment

The architecture for the software-hardware integration is the first item to consider. This depends on the type of actuators (on-board or earth-fixed). Then, the motion observer and the force observers are presented, with their main characteristics.

5 Experimental apparatus development

Contents

In this chapter, the implementation of the SIL methodology for different campaign is presented. The main underlying goals are:

- The design process and the as-built system characterization for the SOFTWIND SPAR 10MW FWT
- The specificities of the different set-ups and how they facilitate the understanding and the characterization of the SIL system performances,
- The characterizations and identifications performed, about the SIL subsystems and the experimental set-up specificities;

The identifications presented here don't include the actuators performance identifications, which are presented in chapter 6. The theoretical and practical background about system characteristics identification (mass, damping, stiffness) is given in appendix B.

The different set-ups presented in this chapter can be divided into two categories:

- The test benches, completely dedicated to the evaluation of the SIL subsystems (actuators and real-time environment) performances and the test of different implementations. They include the Hexapod and the multi-propellers set-ups.
- The floating set-ups. They have also been used for the debug and validation of the system development. Coupled physics between the hydrodynamics and the rotor loads could only be analyzed with these set-ups.

5.1 FWT design for model testing

5.1.1 Wind turbine design

The model-scale wind turbine has been designed for the Blue Growth Farm project. The same wind turbine has been used for the SOFTWIND SPAR experiments.

The wind turbine design covers the following elements:

- Tower,
- RNA,
- Wind turbine controller.

For the conceptual stage of the project, the DTU 10MW RWT (Bak *et al.*, 2013) has been considered for the wind turbine.

RNA

The target RNA is the same as the full-scale DTU 10MW RWT. The RNA characteristics for the scaling procedure include:

- Mass,
- Inertia,
- Dimensions,
- Shaft orientation (tilted axis).

Wind turbine controller

The wind turbine controller is the DTU Baseline controller (Hansen *et al.*, 2005), already compatible with the OpenFAST numerical tool. The only parameters to tune are the gains of the Gain Scheduled Proportional Integral (GSPI) controller, to satisfy different requirements as negative platform pitch damping. To simplify the design process, it has been decided to take only one set of parameters for

the two floating set-ups. As the design of wind turbine control law is out of scope of the present work, parameters tuned for other FWT using the DTU 10MW are considered satisfactory. The PI parameters optimized for the public definition of the Olav Olsen 10MW FWT *(Oo–Star)* (Müller, Lemmer and Yu, 2018) are used, as the platform pitch natural frequencies of the *Oo–Star* and of the SOFTWIND SPAR platform are close. For the Blue Growth Farm (BGF) multipurpose platform, this choice concerning the controller gains is less suitable:

- the platform has a pitch natural frequency higher than the *Oo–Star* platform;
- the platform is expected to have a lot of excitation and damping from the waves. Consequently, the radiation damping and drag damping are probably sufficient to not be counterbalanced by controller-induced negative platform pitch damping (of an onshore-based controller).

Nevertheless, this choice has been made for simplicity.

Tower

The target tower is based on the onshore DTU 10MW RWT tower (Bak *et al.*, 2013). The design procedure to get a suitable model scale system and the identification of the as-built system are presented hereafter. The tower characteristics for the scaling procedure include:

- height,
- mass,
- flexible properties (rigid, structural similitude, modal similitude,…).

The BGF project specifications for the wave tank testing campaign include:

- Respect a modal similitude for the tower;
- A 6-component tower base force transducer.

Ideally, a structural and aerodynamic scaling of tower would ensure that the tower behavior is respected. However, a structural scaling requires a Young modulus smaller than the full scale (Courbois, 2013). As the aerodynamic loads acting on the tower are not reproduced, one possibility is to change the tower diameter and shell width to get the correct distributed mass, stiffness and damping properties. Because of the instrumentation size and mass and because of the different materials at full scale and model scale, those distributed properties could be hardly achieved. A simpler possibility is to follow a *modal similarity*. This similarity respects the main mode characteristics of the tower. Only the 1st fore-aft and 1st side-side modes are considered. Ranked in a decreasing order of importance, the mode characteristics are:

- Natural frequency,
- Amplitude of the deformations,
- Shape of the mode.

To stay within acceptable ranges for the different characteristics, some criteria have been defined:

- For the natural frequency of the 1st fore-aft and side-side tower modes, an acceptable range should be defined around the target natural frequency. One has to make sure that any important excitations will not excite the natural frequency of the tower;
- For the amplitude of the deformations, the integrated stiffness of the tower should be of the same order of magnitude as the target one. The structural damping was not evaluated at the design stage.

In Figure 49, the frequency map for the tower design illustrates the acceptable zones (in green) and the forbidden zone (in red) for the 1st natural frequency of the tower. The orange zones correspond to the zones to avoid, taking into account fluctuating operating points due to the rotor speed fluctuations. The values are given at scale 1:40. The main sources of excitations are the wave frequencies, the 3P frequency and the 1P frequency. The 1P and 3P ranges of the DTU 10MW RWT and the IEA-10-198 are represented. The foreseen significant wave frequencies of the BGF project and SOFTWIND SPAR (denoted SW SPAR, see part 5.2.3) are also represented. Two acceptable solutions are defined (Hegseth, Bachynski and Martins, 2020):

- « Stiff-soft » solution, when the 1st natural frequency of the tower falls between the 1P and the 3P frequency.
- « Stiff-stiff » solution, when the 1st natural frequency of the tower is above the 3P frequency.

The solution that has been retained is a “stiff-soft” solution, similarly to the original tower of the DTU 10MW RWT, as the tower was primarily designed for the BGF multipurpose concept and then closer, in terms of coupled platform- tower mechanical system, to a bottom-fixed offshore wind turbine.

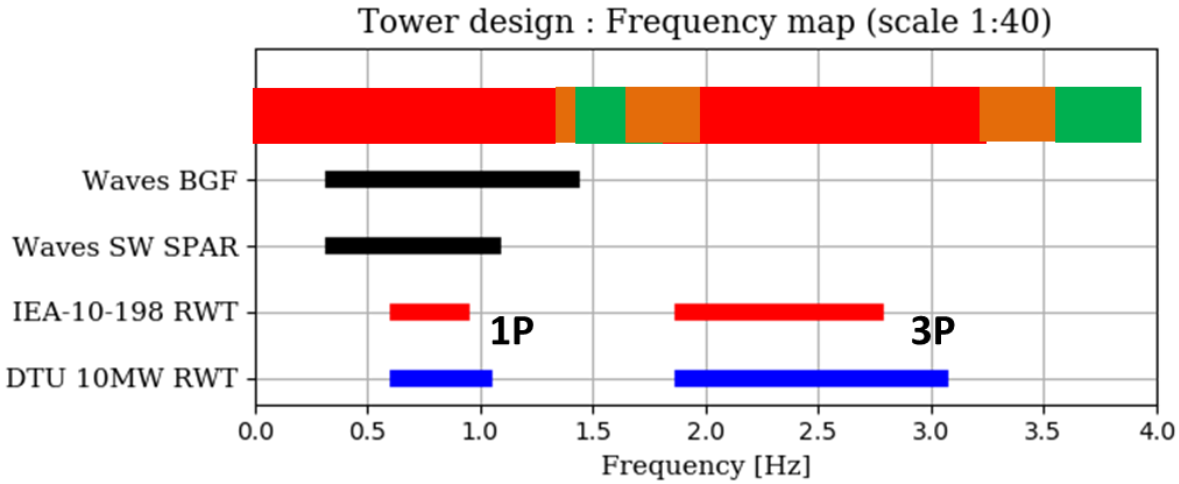

Figure 49: Selection of an appropriate natural frequency for the tower 1st fore-aft mode. The two green zones are the “stiff-soft” and the “stiff-stiff” configurations

The design process was iterative to find a suitable section of the flexible aluminum beam. It was based on a Finite-Element Analysis (FEA), with the NREL’s BModes code (Bir, 2005), of the model-scale aluminum beam and RNA. Then, an experimental validation with the target aluminum beam and equivalent RNA mass has been performed (hammer tests). The identification tests are presented in the next part.

5.1.2 SOFTWIND SPAR FWT design

The SOFTWIND SPAR FWT was designed to get the representative behavior of a 10 MW floating wind turbine at scale 1:40. The SPAR platform, its mooring system and a flexible tower in modal similarity have been built and characterized for the test campaign purpose. The design process was not fully integrated as, for instance, in (Hegseth, Bachynski and Martins, 2020), but stayed at a simplified conceptual stage. The designed key-components include:

- The floater,
- The mooring system,

- The tower.

The wind turbine is the same as presented for the Blue Growth Farm set-up in part 5.1.1. This concerns the tower and the RNA.

5.1.2.1 Floating foundations

The selected floating foundation is a SPAR. This choice has been made to simplify the design process and reduce cost compared to a semi-submersible platform. TLP platforms, while being attractive, have been considered as too demanding in terms of sensitivity to the SIL system performances for a validation design of a floating wind turbine. However, the design process was based on realistic constraints and criteria. Moreover, to get the expected behavior and hydrodynamic loads on a SPAR FWT structure, the main dimensions are based on existing SPAR FWT. Particularly the OC3 Hywind SPAR platform (Jonkman, 2010) and the *Hywind Scotland* platform have been considered as reference systems.

Static design parameters include:

- A sufficient metacentric height GM,
- Trim angle due to the rated rotor thrust.

Frequency design parameters include:

- Natural periods in heave, roll and pitch,
- Platform motions RAO. A frequency-domain model based on the Boundary Element Method diffraction-radiation solver NEMOH (Babarit and Delhommeau, 2015) has been developed.

Additional constraints are driven by logistic aspects specific to the wave tank facilities. Limiting the mass and the height of the FWT facilitates its transport.

The values for the different criteria that have been used are recalled in Table 21. They are based on observations for other similar floaters or design guidelines.

Static criteria	**Frequency criteria**	**Wave tank constraints**
• GM >1 • 2° < Trim < 5°	• Heave, roll and pitch natural periods in the range [25 – 35]s, with sufficient separation between heave and pitch and heave and roll. • Realistic platform motions RAO, with verification of typical coupling effects, and limited motions for small wave periods.	• Maximal draft of 2.5m • Maximal mass of 4Tons for crane requirements

Table 21: Criteria and constraints for the floater design

Wind turbine

In Figure 50, the different sub-systems and their assembly are illustrated, for the target floating wind turbine, and the corresponding envisaged system at model scale. The describing parameters are also indicated (hub height, SPAR dimensions, …).

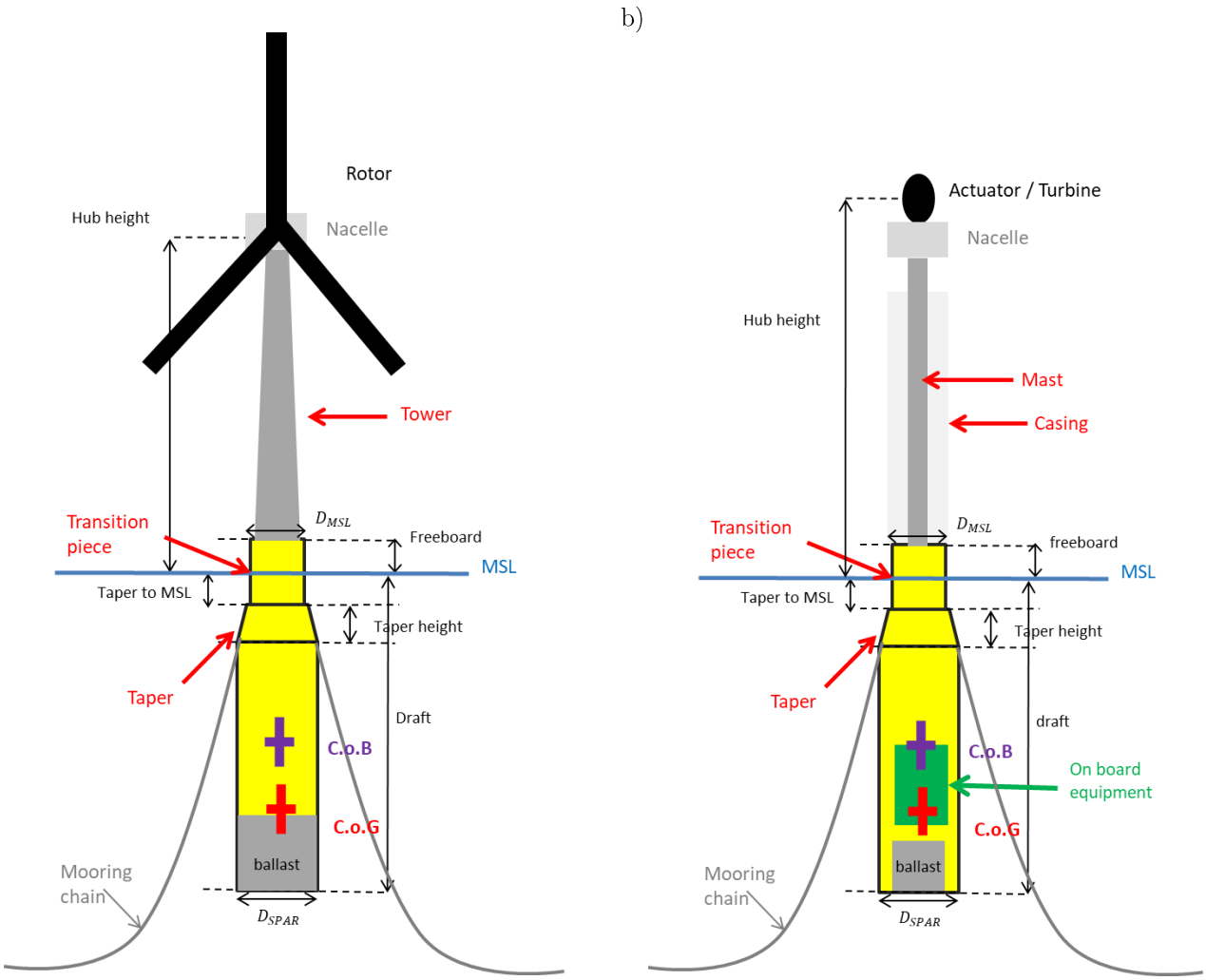

Figure 50: Characterizing parameters of the SOFTWIND SPAR FWT. a) target system. b) model scale system

The main dimensions and mass properties of the floater and wind turbine are summarized in Table 22. The target values at full scale and model scale are indicated.

	Values	
	Scale 1:1	Scale 1:40
Floater		
CM Location Below MSL along platform centerline [m]	-73.7	-1.84
Mass [kg]	1.94E+07	303.1
Ixx [$kg.m^2$] around CoG FWT	1.00E+10	97.7
Iyy [$kg.m^2$] around CoG FWT	1.00E+10	97.7
Izz [$kg.m^2$] around CoG FWT	6.00E+08	5.9
D_{MSL} [m]	11.2	2.80E-01
D_{SPAR} [m]	18.0	4.50E-01
Taper top from MSL [m]	4.0	0.10
Taper height [m]	8.0	0.20
Draft [m]	90.0	2.25
Freeboard [m]	4.0	0.10
Wind turbine		
Hub height above MSL [m]	119	2.98
Tower height [m]	111.63	2.79
Tower mass [kg]	6.28E+05	9.82
Tower CoG Z [m]	47.6	1.19
RNA mass [kg]	6.77E+05	10.58
RNA CoG X from tower centerline[m]	-0.6	-0.016
RNA CoG Y from tower centerline[m]	0.0	0.00
RNA CoG Z from tower top [m]	1.8	0.045

Table 22: Target main characteristics of the floater and of the wind turbine

5.1.2.2 Mooring system

Once the floater properties have been defined, a suitable mooring system has been defined. The mooring system aims at limiting horizontal motions (surge, sway and yaw). For wave tank experiments, different options could be envisaged:

- An aerial mooring system, to facilitate the design process and the understanding of the FWT behavior. Such aerial system, basically made of lightweight ropes and calibrated springs, facilitates the fit of a numerical model as only the horizontal motions are impacted. Consequently, the coupling between the different DoF decreases. Moreover, the behaviors of these springs are nearly linear and not submitted to hydrodynamic loadings, reducing the modeling complexity.
- A model scale realistic mooring system, either catenary, semi-taut or taut for SPAR platform. This imposes the same kind of complexity than a full-scale mooring system, with hydrodynamic loadings, and coupling between the DoF (especially platform surge and pitch). However, this option reproduces with a higher fidelity the expected behavior of a FWT.

For this set-up, a catenary system was preferred to an aerial mooring system. The main reason is that the low frequency motions of the platform could be quite sensitive to the hydrodynamic loads acting on the mooring lines (Le Boulluec *et al.*, 1994). As found in (Azcona *et al.*, 2017), change of the

Reynolds number and its effect on the hydrodynamic loads on the mooring lines is expected to be small, with similar chains and similar scale ratio. The selected solution is a mooring system composed of three clusters in steel chains. Each main line is composed of a main mooring line attached to the bottom of the wave tank, and connected to two "bridles" – which are part of a delta-connection – attached to the SPAR floater. The mooring system architecture and the characteristic dimensions are inspired from the Hywind Scotland system. Additionally, the design process is inspired from the STATIONIS software methodology (STATIONIS, 2020), to find a suitable system. The criteria and constraints are summarized in Table 23. The associated important values for the different constraints and criteria are detailed in Table 24 and have been arbitrary defined but inspired from typical FWT mooring systems found in the literature.

Design constraints	**Frequency criteria**	**Chain selection criteria**
• The anchor does not accept vertical loads. This imposes a touchdown point sufficiently far from the anchor point • Admissible tension at the fairleads • Limited heading angle • Low sensitivity to non-symmetric mooring layout	• Natural periods in surge, sway and yaw • Natural periods of the mooring lines	• Maximal anchor radius defined by the wave tank dimensions. • Realistic range of chain diameters • Realistic shape of the chain links.

Table 23: Criteria and constraints for the mooring design

	scale 1:1	**scale 1:40**
Mooring stiffness		
Surge [min–max] nat. period [s]	[60 - 120]	[9.5 -19.0]
Yaw [min-max] nat. period [s]	[10 - 20]	[1.6 - 3.2]
Admissible offsets		
Hor. offset due to steady wind force [m]	20	0.5
Hor. offset due to steady wind force and dynamic motions [m]	30	0.75
Max heading angle [deg]	5	5
Dimensions and properties of the lines		
Maximal anchorage radius [m]	750	18.75
Max tension at fairleads [% MBL]	50	50
Min laid length on the seafloor in offset max [m]	50	1.25
Chain diameters range [mm]	[120 - 200]	[3 - 5]
First nat. period of the mooring line [s]	< 3	<0.5

Table 24: Main inputs for the different criteria and constraints of the moorings

Based on those criteria and constraints, quasi-static and frequency domain computations have been conducted to partially cover the design space. Those computations have been conducted using MAP ++ (Masciola, Jonkman and Robertson, 2013) and an in-house python wrapper to perform frequency domain computations. The mooring chain properties (lineic mass, dimensions, stiffness, etc.) are based on the OrcaFlex software documentation. The resulting mooring system is described in Table 25.

	Scale 1:1	Scale 1:40
Anchor radius [m]	600	15.0
Fairleads depth [m]	12	0.30
Fairleads radius [m]	10.5	0.26
Diameter chain [m]	0.16	0.0040
Bottom chain length [m]	600	15.0
Bridle chain length [m]	48	1.2
Mass lineic in air [kg/m]	510	0.32

Table 25: Properties of the target moorings system

5.1.2.3 Coupled floater-tower behavior

The modification of the tower properties when clamped on the SPAR compared to the cantilevered condition is detailed in this part. This change of the boundary condition at the tower base affects the tower natural frequency. Indeed, the tower is no more cantilevered to a fixed frame but constitutes, together with the rigid floater a coupled mechanical system (DNVGL, 2019; Hegseth, Bachynski and Martins, 2020). This has not been taken into account in the design of the tower and has been discovered during the SOFTWIND SPAR tests. Basically, concerning the increase of the tower natural frequency with the *clamped on the SPAR* condition, the new value of 2.42 Hz becomes a problem for all the below-rated operating points. On this graph, the tower natural frequency is represented for (i) fixed (cantilevered on soil) condition, (ii) clamped on the SPAR condition and (iii) a possible "stiff-stiff" configuration. The natural frequency of the 1st blade flapwise mode is also depicted on this figure, and is very close to the tower natural frequency for the *clamped on the SPAR* condition. The consequence of this new "apparent" tower frequency is to make it not adapted to the SPAR platform. The "floating condition" should have been taken into account at the design stage. The consequences are the impossibility to include in the numerical model the 1st blade flapwise mode and the tower shadow effect, in order to avoid instability of the tower deflections. For the same reason, all the below-rated operating points could not be run with a turbulent wind with a vertical shear.

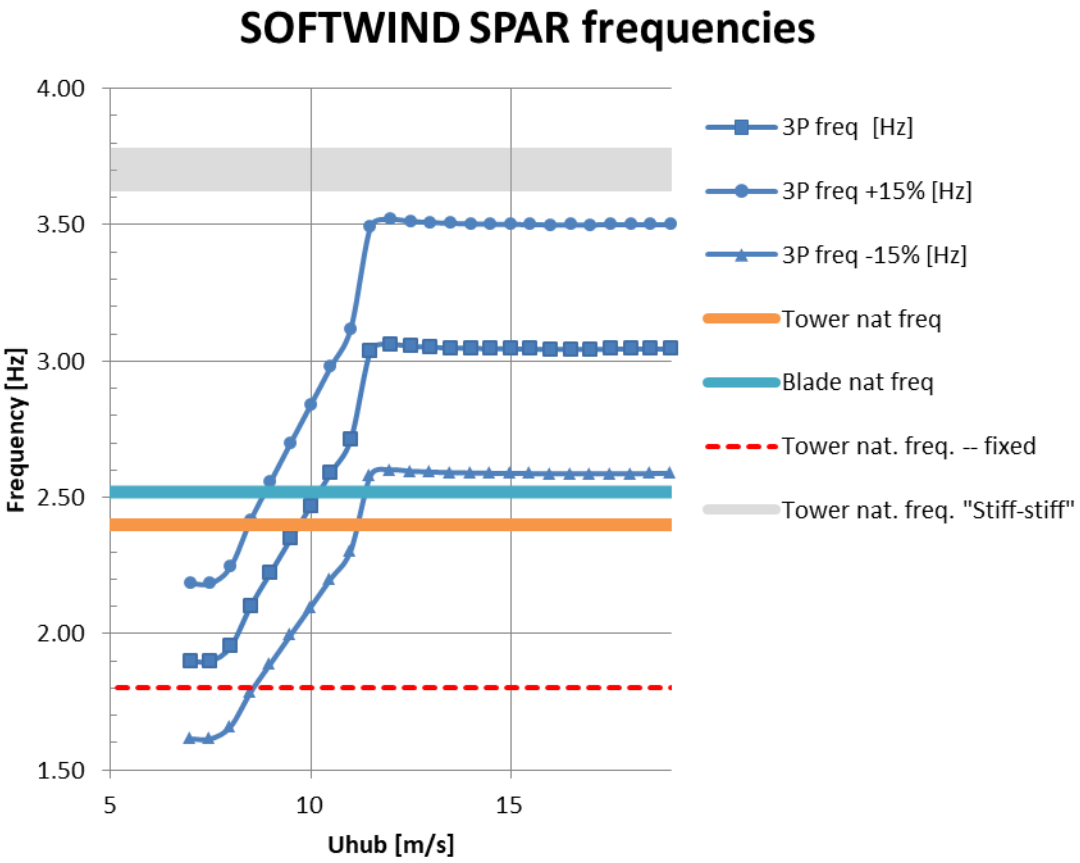

Figure 51: SOFTWIND SPAR 3P rotor frequency and tower natural frequencies. The Blade natural frequency is that of the collective 1st flapwise mode.

All the as-built properties, for the floater, wind turbine and the mooring system are presented in appendix D.

5.2 Set-ups description

In this section, the different set-ups that have been built and used are presented.

5.2.1 Forced motions set-up #1: Hexapod

In the validation process adopted, a first test bench with forced motions has been designed and set up. The different subsystems used in a SIL wave tank campaign are implemented except that the floater is replaced by the 6 DoF Hexapod. The set-up represents, at scale 1:30, the 5MW OC3-Hywind Spar FWT (Jonkman, 2010) and the Hexapod is used to replay different scenarios of FWT motions. Sinusoidal motions and realistic floating wind turbine motions are reproduced. Those motions are obtained thanks to prior fully coupled numerical simulations, for a given sea state. When used on the test bench, similar input files (initial conditions, wind inflow conditions) are used in order to have the aerodynamic forces corresponding to the motions provided by the Hexapod.

This test bench and its findings constitute an original contribution of the SOFTWIND project to the FWT SIL system development, with a fine characterization of the different elements of the SIL apparatus. This methodology has then be extended for the floating set-ups. The main goal is to validate the full chain of the SIL system (real-time execution of the numerical model with measured motions, force observer design, validation of the communication protocols,…). Imposing the motions allows assessing in a very controlled environment the performances of the system; however, possible mechanical

instabilities on the FWT motions could not be checked (due, e.g. to an non-adapted force feedback control strategy).

The objectives of this test campaign are to define a validation process of the multi systems identification methodology of actuators performance. It includes the following items:

- MOCAP real-time delay quantification,
- Adjustment of motion observer settings (cut-off frequency),
- Validation of communication protocols,
- Integration and timing of the numerical model,
- Force observer settings,
- Quantification of the actuators performances, definition of a suitable identification methodology:
    - Steady-state identification,
    - Frequency domain and time domain identification methodologies,
    - Mostly open-loop but also closed-loop control tests.

Different existing elements have been gathered to build the set-up:

- A "rigid" mast (3m height, natural bending mode at 10Hz),
- A ducted fan – a Schübeler DS-94-DIA HST with a BLDC motor DSM6745-700,
- An Electronic Speed Controller (ESC) - the MGM HBC 25063-3. The ESC is controlled with CAN bus message at 1 kHz.
- Stabilized power system at 48V, with current intensity saturation at more than 150A (burst value ~300A),
- A 6 DoF Symétrie Hexapod (also called a *Stewart platform*),
- An unidirectional accelerometer,
- A Qualisys motion capture system with associated cameras and markers. For this set-up, it consists in 4 MIQUS cameras and 5 markers located along the tower,
- An in-house force transducer (also called balance)
- A CompactRIO 9045 PLC for the data acquisition and to run the real-time numerical simulation.

The force transducer and the accelerometer are placed atop of the mast and are rigidly connected to the ducted fan.

A functional drawing and a picture of the set-up are represented in Figure 52.

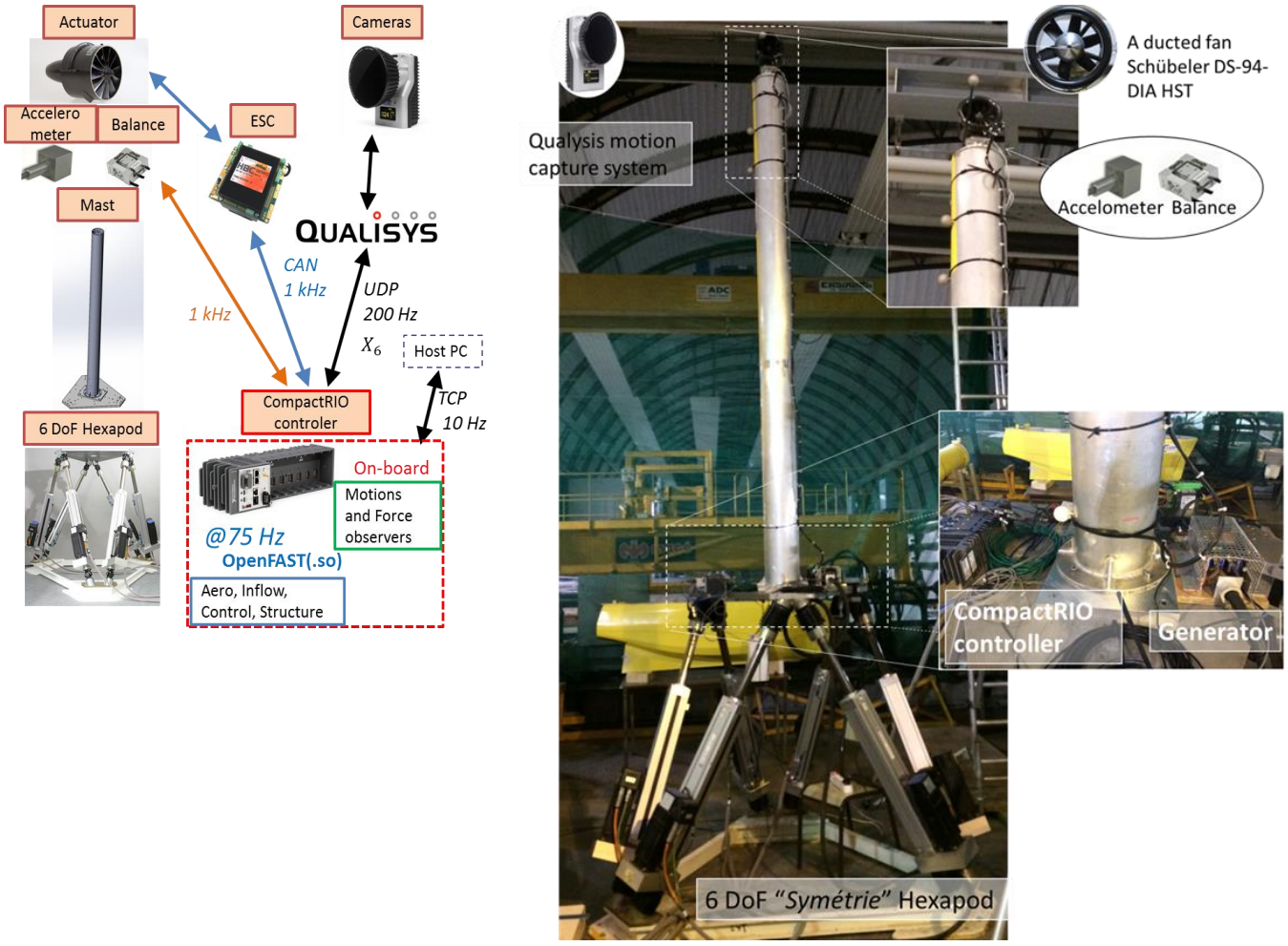

Figure 52: Overview of the test bench with motions forced by a Hexapod

5.2.2 Floating set-up #1: Blue Growth Farm project

A multipurpose floating platform has been tested in the frame of the H2020 project Blue Growth Farm (Lagasco *et al.*, 2019). The aim of the project is to produce advanced industrial knowledge about a fully integrated & efficient offshore multipurpose floating platform. The platform provides a central protected pool to host automated aquaculture system, as well as a large storage and deck areas to host a commercial 10 MW wind turbine and a set of wave energy converters.

A 1:40 scale model of this multipurpose floating platform was designed and built by Centrale Nantes team, according to specifications provided by the project consortium. A view of the platform is presented in Figure 53. The platform was tested at autumn 2019 in the ECN ocean engineering wave tank. For the wind turbine modeling, the SIL methodology developed in this work has been used. Due to its large mass, inertia and dimensions, the hydrodynamic, gravity and inertial loads acting on the platform are expected to be several time higher than the wind turbine loads. However, among the specification of the project consortium, the need of a modal similarity of the tower modes has been specified. Regarding the aero-hydro coupling, representing wind turbine loadings might influence the resonant motions of the platform (low frequency motions, tower deflections) and the tower base loads. Influence on the mean positions (platform tilt under rated rotor thrust) of wave-induced motions is expected to be negligible.

In terms of development of the SIL methodology, this test campaign was the first opportunity to test the system in a wave tank environment with a 2-body configuration; the platform and the nacelle. This brought additional complexity and required a deep understanding of the different subsystems (MOCAP, numerical model, …). Moreover, the natural frequency of the tower being higher than the wave frequencies, it imposes stronger constraints on the admissible delays and actuator control.

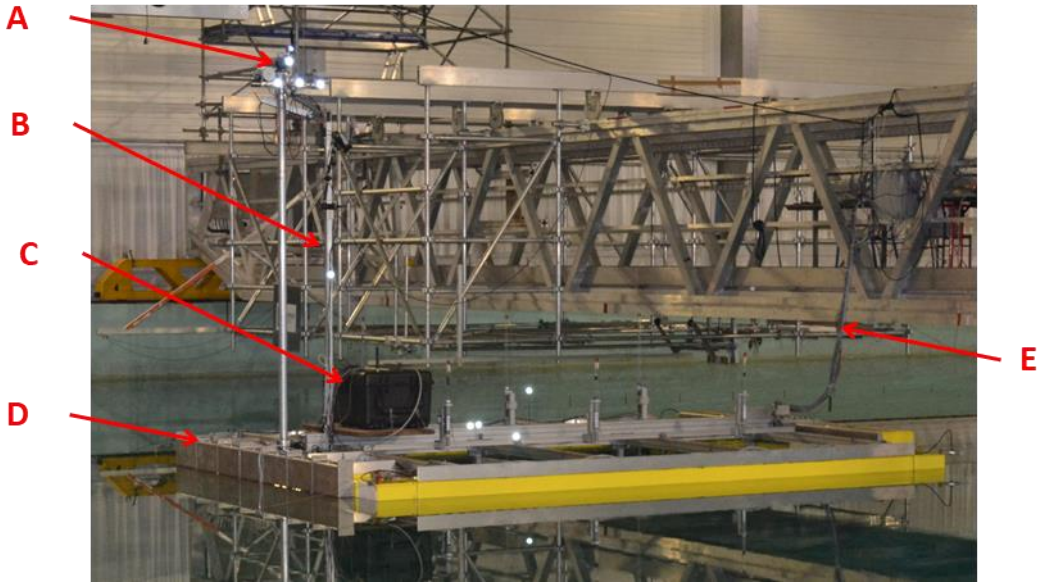

© *Centrale Nantes*

A: actuator with four reflecting markers for the MOCAP system
B: additional mast to avoid weight effects of the different cables
C: on-board acquisition wallet
D: instrumented Oscillating Water Columns (WEC)
E: suspended cables connected to the Host PC and stabilized power system.

Figure 53: Overview of the Blue Growth Farm set-up

Different configurations of the multipurpose platform have been tested during the test campaign, with and without the wind turbine. The tests considered in this work relate mostly to the platform without fishnets but with active WECs.

The different tests performed in each configuration are similar to the typical tests of a classical floating wind turbine:

- Decays,
- Hammer tests,
- Pull-out,
- Regular waves,
- Irregular waves,
- Regular waves with wind,
- Irregular waves with wind.

The objectives of these different tests are described in chapter 7 and 8.

In the SIL development and validation perspective, the most important aspects are:

- Identification of the performances of an actuator solution.
- Identification of the motion observer properties in realistic conditions.
- Tuning of the force observer with a flexible tower.

Different elements constitute the set-up:

- The platform with:
  - wave energy converters (Oscillating Water Columns), equipped with pressure sensors and wave probes,
  - fishnets,
  - 4 aerial mooring lines, made of lightweight dyneema and calibrated springs.
- A flexible aluminum mast for the wind turbine tower. The mast characteristics are described in the next subsection.
- An actuator solution developed by KDE-Direct. This includes the KDE5215XF-220 motor, the KDE-UAS85UVC ESC and the KDE-CF155-DP 2 bladed aircraft propeller.
- Stabilized power system at 48V, with current saturation at more than 150A. Alimentation cables connect the dry side of the wave tank to the ESC.
- A 3-component accelerometer ASC OS-315LN-002, range $2g$, located atop of the tower.
- An SBG Ellipse Inertial Measurement Unit (IMU) located at the tower base.
- The Qualysis motion capture system with associated cameras and markers. For this set-up, it consists in 4 OQUS cameras for the tracking and 4 markers for each 6 DoF body. The platform constitutes one body, and the nacelle constitutes the second body.
- The same 2-component force transducer as for the Forced motions set-up #1, connected to the compactRIO with an AIBridge on the NI module 9237.
- A compactRIO 9049 PLC to run the real-time loop on LabView.

Note that, initially, the same ducted fan as used in the forced motions set-up #1 was planned to be used However, after an over-heating failure of the Schubeler DS-94-DIA HST ducted fan, a KDE-Direct solution has been used instead. As it was a last-minute adjustment, the mechanical interface between the actuator and the nacelle was not as stiff as the ducted fan mechanical interface. This induces vibrations at the natural frequency of this transition piece around 30 Hz.

The ESC is controlled with PWM signals at 200 Hz. A CAN Bus message has been used for the monitoring of internal ESC quantities.

5.2.3 Floating set-up #2: SOFTWIND SPAR

The 2nd floating set-up has been done on a 1/40 scale 10 MW SPAR floating wind turbine between November 2019 and March 2020.

The objectives of this test campaign were:

- Validation of the SIL approach and implementation of the developed system on a 10MW FWT.
- Evaluation of the actuator performance and its effects on the floating wind turbine behaviour.
- Characterization of the experimental behaviour of a 10 MW Floating Offshore Wind Turbine at a relative large scale (1/40) for the validation of aero-hydro-servo-elastic numerical models of FOWT in realistic wind and waves conditions.
- Experimentally evaluate the influence of wind turbine controller on FWT global motions.

The set-up is depicted in Figure 54.

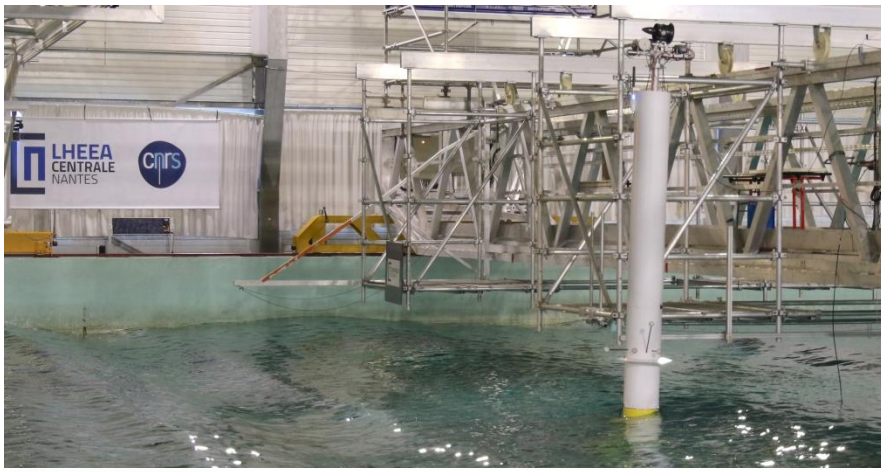

© *Centrale Nantes*

Figure 54: Illustration of the SOFTWIND SPAR set-up

Different elements constitute the set-up for the SIL specific part:

- A ducted fan – a Schübeler DS-98-DIA HST with a BLDC motor DSM6043-650
- An Electronic Speed Controller (ESC) - the MGM HBC 25063-3. This ESC could be controlled with CAN Bus messages or PWM signals.
- A 3-component accelerometer ASC 5521-005, range $5\boldsymbol{g}$, located atop of the tower.
- The compactRIO, tower top IMU, MOCAP system and tower top force transducer are the same as in the BGF set-up.
- A Lithium – FePho4 battery, rated tension 52V, energy capacity of 72Ah, mass of 40kg, with dimensions $\mathbf{200 \times 150 \times 300}\,\boldsymbol{mm}$. A Battery Management System (BMS) makes the discharge uniform in the different battery cells. The current intensity saturation is estimated at more than 70A by the manufacturer.

The set-up also includes elements and instrumentations mandatory to perform wave tank test of a FWT:

- The SPAR buoy,
- Three chains and a delta-connection for the mooring lines,
- The tower with its casing for transporting the RNA cables,
- Wave probes to measure the free surface elevations.
- The wave tank itself, dimensions $\mathbf{50 \times 30 \times 5}\boldsymbol{m}$ for the length, width and depth. 48 hinged-flap wavemakers generate the waves. For the SOFTWIND SPAR set-up, they are controlled in position-mode;
- An absorbing beach to limit the reflection.

A drawing of the set-up is presented in Figure 55.

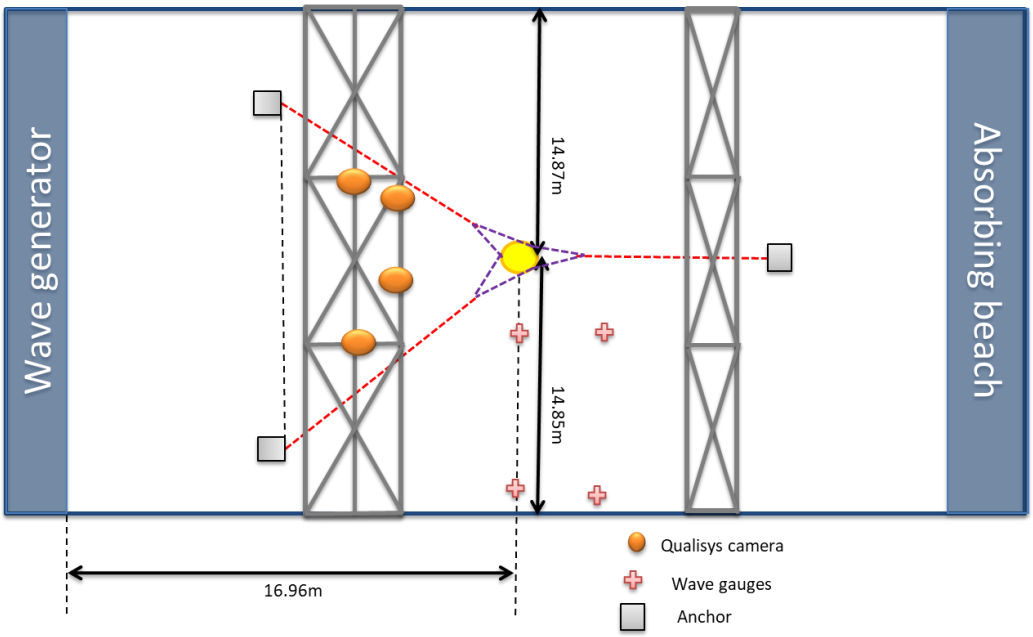

Figure 55: SOFTWIND SPAR set-up general layout

A detailed presentation of the set-up characteristics could be found in appendix D.

5.2.4 Fixed multi-propellers test bench #1

To pursue the development of the SIL system, a test bench has been designed in spring 2020, to study different aircraft propellers on a 6-component force transducer. The propellers are fixed on a rigid frame with different configurations. The test bench design and the experiments have been performed by Mohamad Hmedi for his MSc thesis and supervised by Félicien Bonnefoy.

The objectives of this test campaign are:

- Increase in the complexity with a first version of a multi-propellers set-up. The actuators setpoints use not only the thrust component from the wind turbine numerical simulation, but also the other setpoint load components.
- Use of a 6--component force transducer for proper evaluation of actuators torques.
- Test different combinations of lightweight two-bladed aircraft propellers with different configurations of motors, ESC and blades.
- Extend the identification methodology developed for one actuator to a multi propeller layout.
- Explore if the interactions between the different propellers may modify the thrust generated by several propellers compared to the sum of individual thrusts. This deviation from a summation principle has been observed for their multi-propellers set-up by Meseguer et al. (Meseguer and Guanche, 2019).

The set-up is depicted in Figure 56.

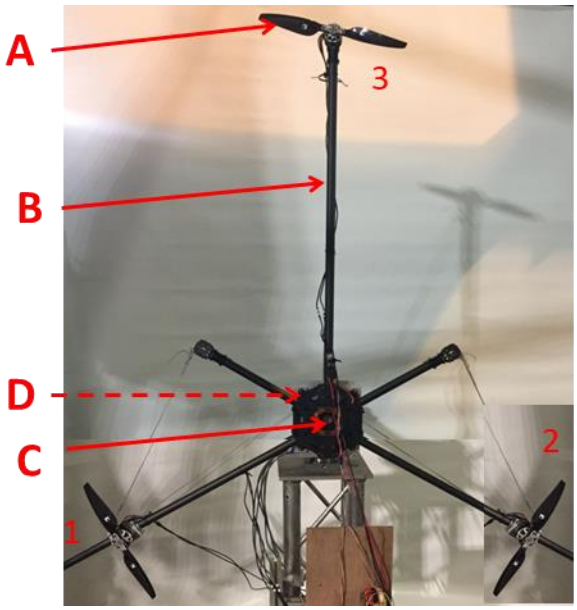

A: Actuator
B: carbon fiber tube
C: frame origin
D: 6-component force transducer

Figure 56: Multi-actuators test bench. The actuators are numbered 1, 2 and 3.

The test matrix includes different characterization and identification tests of the actuators. Firstly, different single actuator identifications are conducted. Then, the identification procedure is extended for several actuators running at the same time. Tests include white noise, steps, sine, and realistic setpoints from the SOFTWIND SPAR campaign. The main outcomes of this test campaign deal mostly with the actuators performances. They are presented in chapter 6.

The test bench is made of different elements:

- A TARROT T810 TL810A frame to place and connect the different actuators. This frame is initially designed for hexacopter and is made of circular carbon fibers beams of section $\phi = 25mm$ and thickness $\epsilon = 2mm$.
- Three actuators designed by KDE-direct, with different combinations of motors, ESC and propellers. The ESC are driven by PWM signals.
- A HBM BG2 6-component force transducer, with useful range [0-5] kN and [0-5] kN.m
- A compactRIO 9049 PLC to run the real-time loop on LabView.

Concerning the actuators, for most of the test the three used actuators are the following:

- Actuator 1: KDE 5215-XF220 motor, KDE85UAS-UVC ESC, KDE-CF-155-DP propeller.
- Actuator 2: KDE 5215-XF460 motor, KDE55UAS-HVC ESC KDE-CF-155-DP propeller.
- Actuator 3: KDE 4215-XF465 motor, KDE55UAS+ ESC, KDE-CF-155-DP propeller.

As the test bench is ground-fixed, there is no more need of accelerometers to remove the inertial contributions in the measured forces. Note that the force transducer is not centered on the frame center. Consequently, the different measured moments are transported from the balance origin to the frame center.

The test bench has been built to provide insights for a multi actuators set-up. A simplified layout has been considered in order to limit the aerodynamic interactions between the propellers and to reproduce 3-load components with those three actuators. Two scenarii have been envisaged for the selected load components:

- $[F_x, M_y, M_z]$, with the sketch on Figure 57 left. It is denoted configuration 1

- $[F_y, F_z, M_x]$, with the sketch on Figure 57 right. It is denoted configuration 2

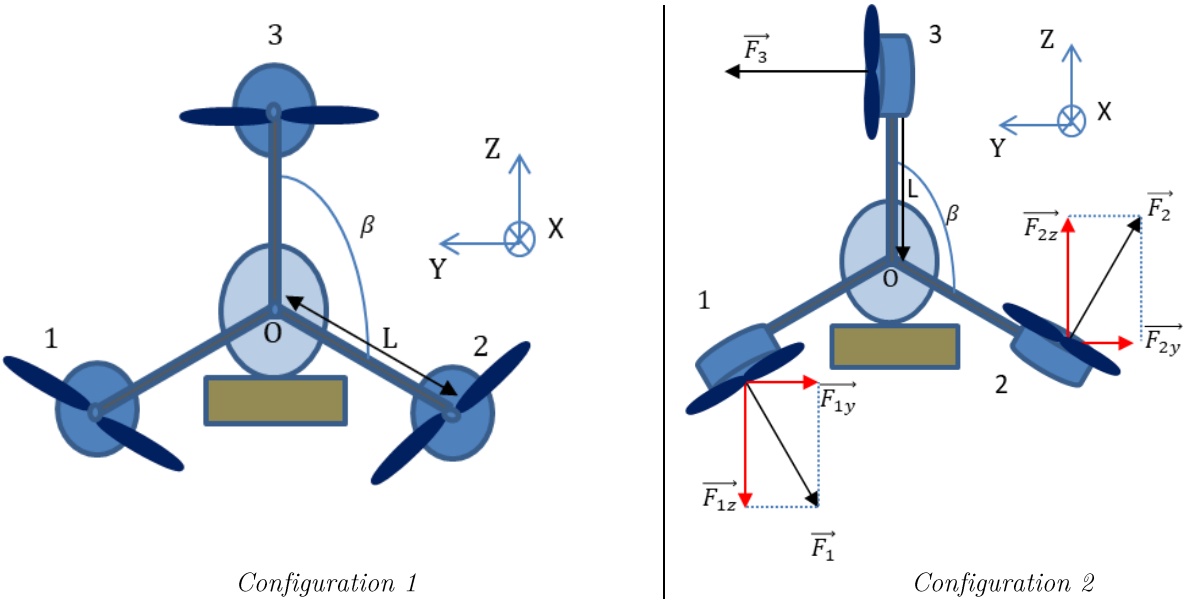

Configuration 1 *Configuration 2*

Figure 57: Envisaged layout configurations for the multi-propellers test bench #1

These two configurations are fully-actuated. The two describing parameters, the distance L from the frame center to the actuator location and the angle β between the different beams have been set to $L = 0.7m$ and $\beta = 120°$. All the results presented in chapter 6 have been done with the configuration 1.

5.2.5 Specificities

The specificities of the different subsystems for each set-up are described hereafter.

5.2.5.1 Motion observer

Hexapod

6-DoF positions and velocities of the platform are fed to the numerical model after low-pass filtering of the MOCAP (Qualisys) real-time outputs. A 2nd order Butterworth filter with a cut-off frequency of 10Hz has been used.

BGF and SOFTWIND SPAR

Kalman filters have been designed to build a state-estimation of the positions and velocities. This was applied for the platform 6 DoF motions and for the relative nacelle 6 DoF motions. The sensors which have been used for the two bodies are:

- 6-DoF platform: Qualisys (cameras + 4 markers) and an SBG Ellipse IMU.
- 6-DoF nacelle: Qualisys (same cameras + 4 markers) and the 3-component accelerometer. Another SBG Ellipse IMU was intended to be used at the nacelle but it did not work due to interferences on the CAN bus at the ESC startup.

5.2.5.2 Force observer

The thrust is low-pass filtered at 40 Hz to remove the mass imbalance vibrations of the propeller and the 50 Hz oscillations of the electrical supply

To estimate the thrust generated by the turbine, the inertial compensation is performed with:

- a unidirectional accelerometer for the Hexapod set-up,
- a 3-component accelerometer for the BGF and SOFWTWIND SPAR set-ups.

5.2.5.3 Numerical model

Hexapod

OpenFAST v1.0 has been used for this test campaign. The input files of the NREL 5MW have been used directly, without changing the aerodynamic blade discretization and the structural discretization. The reference numerical model of the NREL 5MW uses the AeroDyn v15 module. The modeling assumptions include, among others:

- No tower drag but rotor-tower aerodynamic interaction (tower shadow effect) has been taken into account;
- Rigid blades and rigid drivetrain,
- OpenFAST runs at 67 Hz due to real-time constraints on a medium performance CompactRIO. The corresponding full scale time step in the numerical simulation is 82.2 ms. The incident wind field used the same time step as the OpenFAST glue code on a 31*41 nodes grid, with crosswise dimensions 145m * 190m.

BGF and SOFTWIND SPAR

OpenFAST v2.1 and 2.2 have been used for these test campaigns. The reference input files of the DTU 10MW RWT have been used, validated for the AeroDyn 14 module, with only a change of the aerodynamic blade discretization and of the structural blade discretization.

For the BGF set-up, the rotor-tower aerodynamic interactions (tower shadow effect, influence of the tower on the upstream wind field) are taken into account. For the SOFTWIND SPAR, this influence has not been taken into account due to resonance of the 1st fore-aft tower mode (see section 5.1.2.3 for details).

The modeling assumptions include, among others:

- Rigid blades and rigid drivetrain.
- OpenFAST runs at 100 Hz to respect real-time constraints. At scale 1:40, the full scale time step is 63.2 ms. The incident wind fields have been generated with TurbSim v1.5 using the OpenFAST glue code time step on a 32*36 nodes grid, with crosswise dimensions 205m * 240m. Note that the glue code time step means the simulation time step, the time step at which the different submodules exchange data.

5.3 Performances characterization

The different characterizations performed on the different SIL subsystems are presented hereafter. Note that the actuator performance identification is presented in a dedicated part, in Chapter 6.

To avoid any redundancy in the manuscript, the force observer and motion observer performances are presented for the SOFTWIND SPAR set-up and Hexapod set-up only. They have also been checked for the BGF set-up with similar conclusions.

5.3.1 Motion observer performances

The identification performed on the motion observer concerns the evaluation of the delay and the sensitivity of the numerical model to noisy velocities.

The motion observer characterization is conducted, including the MOCAP system and the Kalman filters on different important aspects. This characterization includes:

- Static properties: the steady heel, trim and heading angles. It is completely linked to the calibration procedures of the MOCAP system and of the IMU.
- Dynamic properties:
    - Frequency distribution of the MOCAP system and of the IMU disturbances,
    - Delay induced by filtering techniques (1st order low pass filter or Kalman filter),
    - Latency of the MOCAP system processing and RT communication protocol,
    - Impact of the motion observer frequency content on the load tensor produced by the numerical model.

Firstly, the static properties are briefly investigated. Then, to address the dynamic performances of the motion observer, two aspects are considered. Firstly, the performances of the motion observers using the Kalman filters are analyzed in terms of gain and phases. Considering the poorer performances than expected, the frequency content of the motions are analyzed, both from the MOCAP system and the Kalman filters. These performances have been thoroughly investigated to provide guidance for next development steps of the SIL system.

5.3.1.1 Static performances

The steady heel, trim and heading angles impact directly the force computed by OpenFAST:

- The heading creates a nacelle yaw misalignment. This makes the wake more skewed and consequently increases in-plane rotor forces (F_y, M_x and M_z)
- The trim increases the rotor inclination, changing the rotor loads components, in particular the M_y component.
- Impacts of the heel angle need to be characterized.

These angles also impact the fidelity of the results and the characterization of the set-up for the following reasons:

- The heading angle is linked to imbalance in the horizontal plane mooring line tensions. Moreover, the added heading angle due to the aerodynamic loads (in particular M_z), especially above the rated wind speed, may be hidden by the uncertainty on the equilibrium angle.
- The trim and heel angles reflect the position of the FWT center of gravity and the imbalance in the vertical plane mooring lines tensions. Moreover, the added trim but also heel angle due to the aerodynamic loads (in particular M_x, F_y, F_x and M_y), may be hidden by the uncertainty concerning the equilibrium angles.

The SOFTWIND SPAR tests have been performed on two separate phases, to evaluate the repeatability of the static angle characterization. These angles are compared to steady angles obtained with numerical models based on the mass, inertia, CoG and mooring lines measurements. These models are described in chapter 8. Note that the MOCAP calibration procedure is the same for both periods but the cameras layout changed between the two periods due to wave tank facility logistic constraints. A comparison of the three static angles is presented in Table 26. Between the two periods, the heel angle has a variation of +0.6 deg and the heading angle of -0.4 deg. The equilibrium trim angle is at the same value for the two periods. However, when comparing with expected values, there is a non-negligible discrepancy concerning the heel and heading angles. Different alternative measurements have been investigated to cross-check these equilibrium angles but, as it was not defined in the initial specifications for the test campaign, they fail to give angles with a better accuracy than the MOCAP system.

	MOCAP value, period 1	MOCAP value, period 2	Numerical values from experimental measurements
Heel (R_X) [°]	0.4	1.0	0.05 ± 0.1
Trim(R_Y) [°]	-0.29	-0.29	-0.35 ± 0.1
Heading (R_Z) [°]	-1.3	-1.7	0.1 ± 0.1

Table 26: Equilibrium FWT angles for the two periods of the SOFWTIND SPAR tests and comparison with numerical values from other experimental measurements (mass, CoG, ...)

To conclude, some discrepancies have been noticed in the equilibrium angles for the FWT, both for two MOCAP cameras layouts and between expected values (from CoG, mass and mooring line tensions). This is related to the calibration procedure of the MOCAP system. For next test campaigns, anticipation of verifications measurements are recommended.

5.3.1.2 Latency

The Qualisys MOCAP system operation was described in part 4. The QTM user guide (Qualisys, 2016) specifies the different operations performed by the cameras and by QTM. The image capture rate of the cameras is 200Hz. The motions processing delay is made of different parts:

- Latency between the image capture and the 6DoF output motions of QTM,
- Transfer and reading by the real-time control loop of the compactRIO.

The estimation of the latency between the image capture and the QTM output is presented in a histogram format in Figure 59. We can see that the most probable latency is 3ms for this camera set-up. Note that similar values were obtained for other camera set-ups. It includes the image capture, the 2D marker calculation, the TCP/IP transfer to the QTM computer and the different operations performed on the QTM computer. The timeline of these operations is depicted in Figure 58.

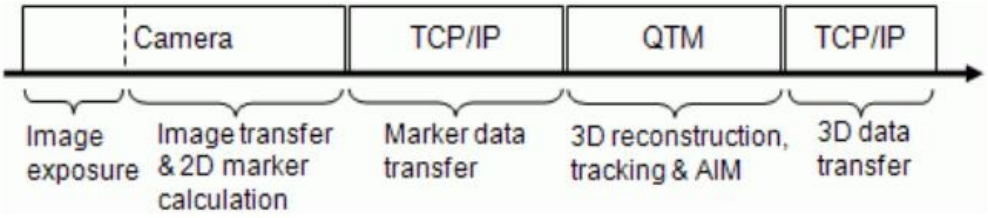

Figure 58: Timeline of Qualisys image capture and processing, from (Qualisys, 2016)

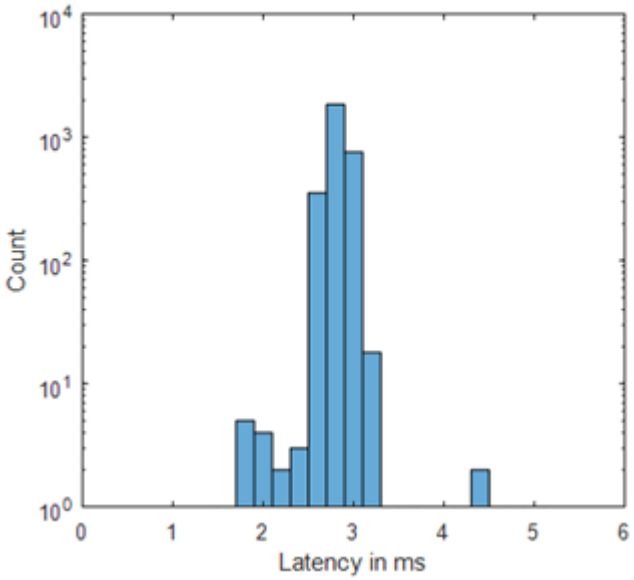

Figure 59: Qualisys latency in real-time mode

A UDP protocol at the same acquisition rate sent the data to the compactRIO as soon as it is available. However, the real-time control loop is not synchronized with the reception of the UDP message. This means that the physical motions (image capture) are red by the RT control loop after a given delay. This delay being between the Qualisys signal latency and this latency summed to the time step of the real-time control loop in the worst synchronization case. For the Hexapod (respectively BGF and SOFTWIND SPAR) set-up, the real-time loop was running at 1kHz (respectively 200Hz), consequently this physical delay is in the range $[3-4]$ ms (respectively [3-8]ms).

5.3.1.3 Dynamic performance

As presented in chapter 3, the different sources of delay can significantly impact the overall performance of the SIL methodology. The most important source of delay is due to the actuators performances, as presented in chapter 6. However, the settings of the motion observer need to be carefully adjusted to avoid any contribution of the motion observer to the total delay. The different contributors to the motion observer delay are:

1. The latency of the MOCAP system (estimated at approximately 4ms for the QTM system),
2. The synchronization between the real-time control loop running on the PLC and the real-time protocol of the MOCAP system. This may induce a delay of up to one time-step of the control loop (up to 5ms in this set-up),
3. The phase lag due to the filtering technique implemented in the motion observer.

To estimate the last contribution, comparisons between real-time filtered signals and post-processed, zero-phase filtered signals are presented in frequency and time domains. A transfer function is defined between the physical motions X_{phys} and the motions observer motions X_{obs}. The motion observer transfer function $H_{motion\,o.}(s)$ is expressed in Eq.(5.1). As there is no ideal mean to evaluate the true physical motions, the strong assumption that is made is to take X_{phys} as the Qualisys perfectly filtered (zero-phase) motions. This transfer function is computed in post-processing. Note that in case of simple low pass filtering, this phase lag could be easily computed from the cut-off frequency value.

$$H_{motion\,o.}(s) = \frac{X_{obs}(s)}{X_{phys}(s)} \tag{5.1}$$

In Figure 60, the force observer transfer functions of the hub X-positions and X-velocities are depicted on the left and on the right, respectively. The coherence of the two identified transfer functions is very close to 1, making the identification of a transfer function trustful. Firstly, the two transfer functions are not similar, because the state estimation of the position and of the velocities are not performed in the same way in the Kalman filter. For the velocities, the angular velocities and accelerations of the IMU have relatively important weights compared to the derivatives of the MOCAP angular positions. The hub X-position presents a gain overshoot at the tower natural frequency (2.4 Hz) while for the velocity, the Kalman filter attenuates the amplitude of the motions. Secondly, the two transfer functions have a phase slightly larger than the phase characteristics of a 1st order low pass filter. The corresponding delay is approximately [20-25]ms, and the 22deg phase at the tower natural frequency equals the threshold of $\frac{\pi}{8}$, which was the maximal admissible limit envisaged.

To conclude, with the set of parameters employed for the Kalman filters, the phase lag is larger than expected and reaches a value of $\frac{\pi}{8}$ for the tower natural frequency. The attenuation is different between the velocity (attenuated) and the position (amplified). The added value of the Kalman filter is related to the platform angular velocities, for which the tower base IMU gives significantly less noise than the derivatives of the MOCAP 6DoF rotations. Those conclusions are valid for the MOCAP signals taken as references. However, the true physical motions are not necessarily the MOCAP captured motions.

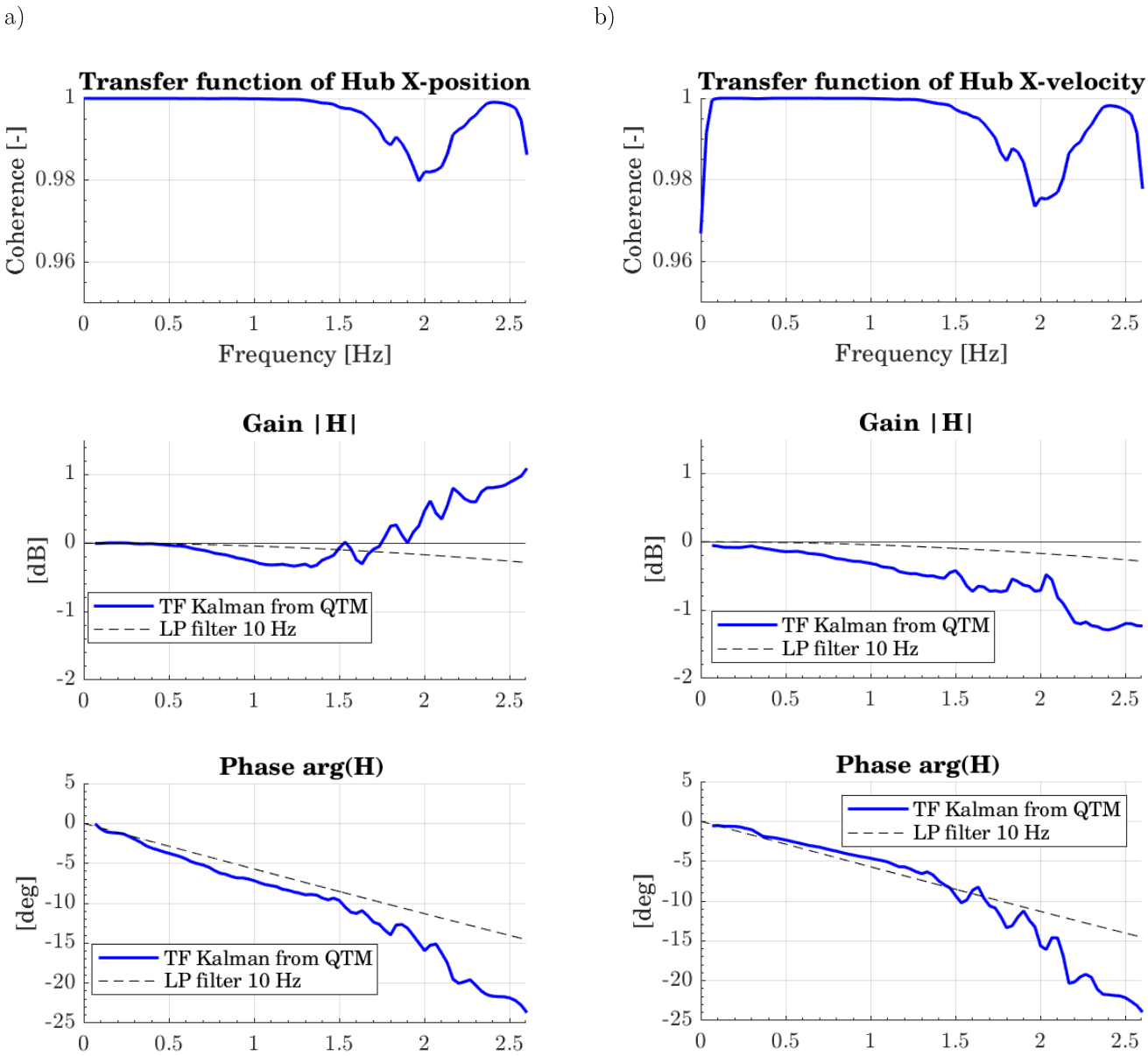

Figure 60: Estimated transfer function of the motion observer. a) hub x-position; b) hub x-velocity.

To further investigate if the Kalman filters applied to the motions are mandatory, the frequency content of the estimated motions (either captured or state-estimated) is investigated.

5.3.1.4 Frequency content of the measured motions

The MOCAP system disturbances are due to the oscillations in the 6DoF tracking of the cameras (projected view of the spherical markers, least-square fitting performed by QTM to reconstruct the 6DoF body, …) but also to the physical vibrations of the markers. To illustrate the frequency content of the disturbances, the velocities are computed for a given load case by different means:

- Kalman filter state estimations. It is denoted *Kalman* in the following analyses.
- First-order finite difference scheme from the MOCAP positions without filtering. It is denoted *MOCAP raw* in the following analyses.
- First-order finite difference scheme from the MOCAP positions, low pass filter with $f_c = 10Hz$. It is denoted *MOCAP filt* in the following analyses.

The 6 platform DoF velocities, the tower deflection velocities in the X and Y direction and the total hub X velocity time series are depicted in Figure 61 for a load case with $H_s = 0.113m; T_p = 1.73s\,; U_w = 18m.s^{-1}; T_I = 17\%$. The corresponding PSD are depicted in Figure 62.

A wind and wave case is considered for the illustration to get the induced vibrations of the actuator. The total hub x-velocity is defined in chapter 2, and includes the relative tower deflection, the platform pitch and surge velocity.

For the different DoFs, the Kalman filter and filtered MOCAP outputs superimpose well in the frequency range of interest. The 2.4 Hz peak is the first fore-aft tower mode (coupled with the floater) and the 28Hz peak is the 2nd fore-aft tower mode (coupled with the floater). On the total hub velocity, this 2nd peak is quite pronounced with the Kalman filter, and its amplitude is even larger than the raw MOCAP signal. The raw MOCAP system without any filtering leads to high platform angular velocities (roll, pitch and yaw velocities, d), e), f). However, for the total hub velocity, the MOCAP raw signal is not so noisy.

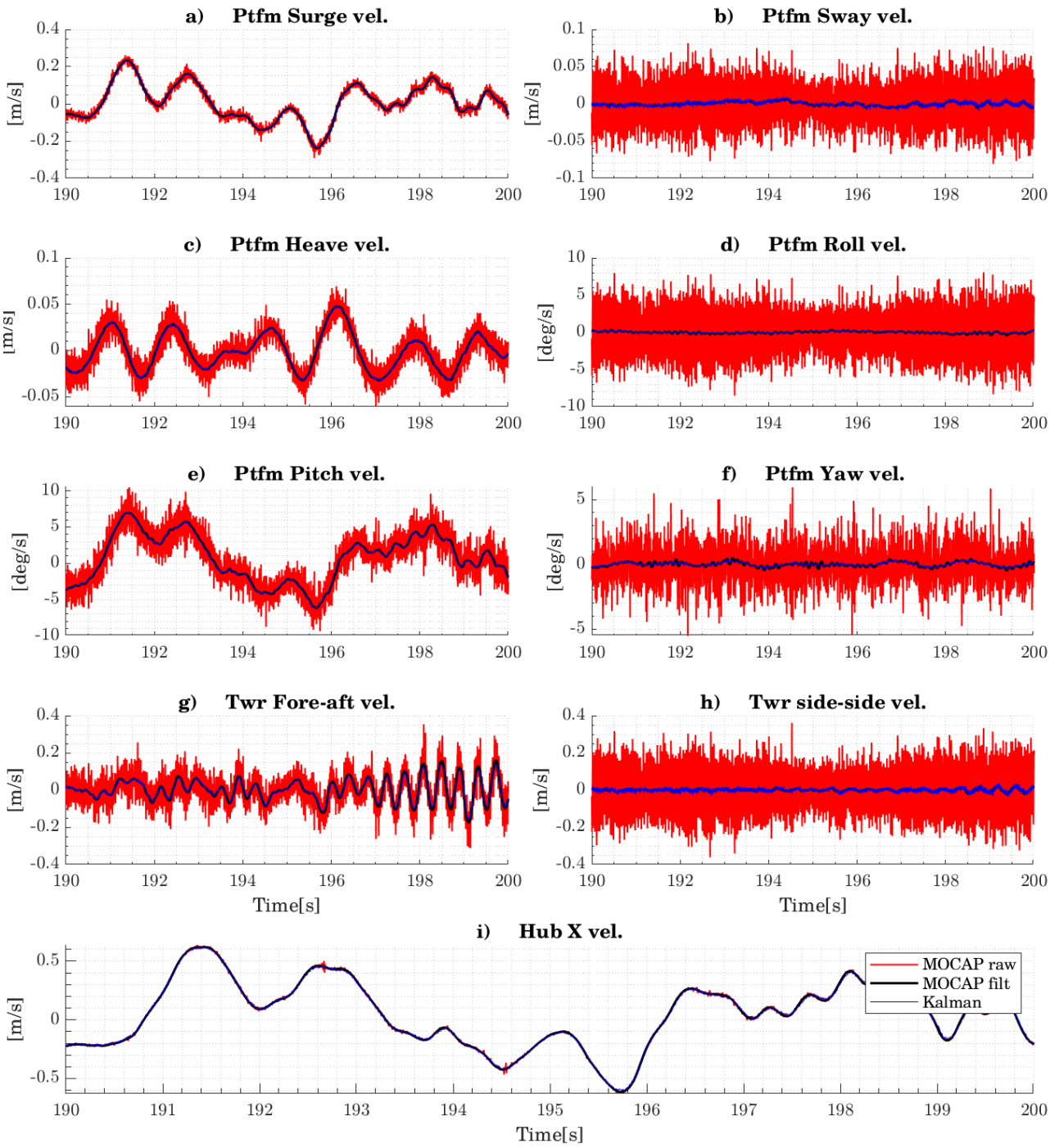

Figure 61: Motion observer performance, FWT DoF velocities time series.

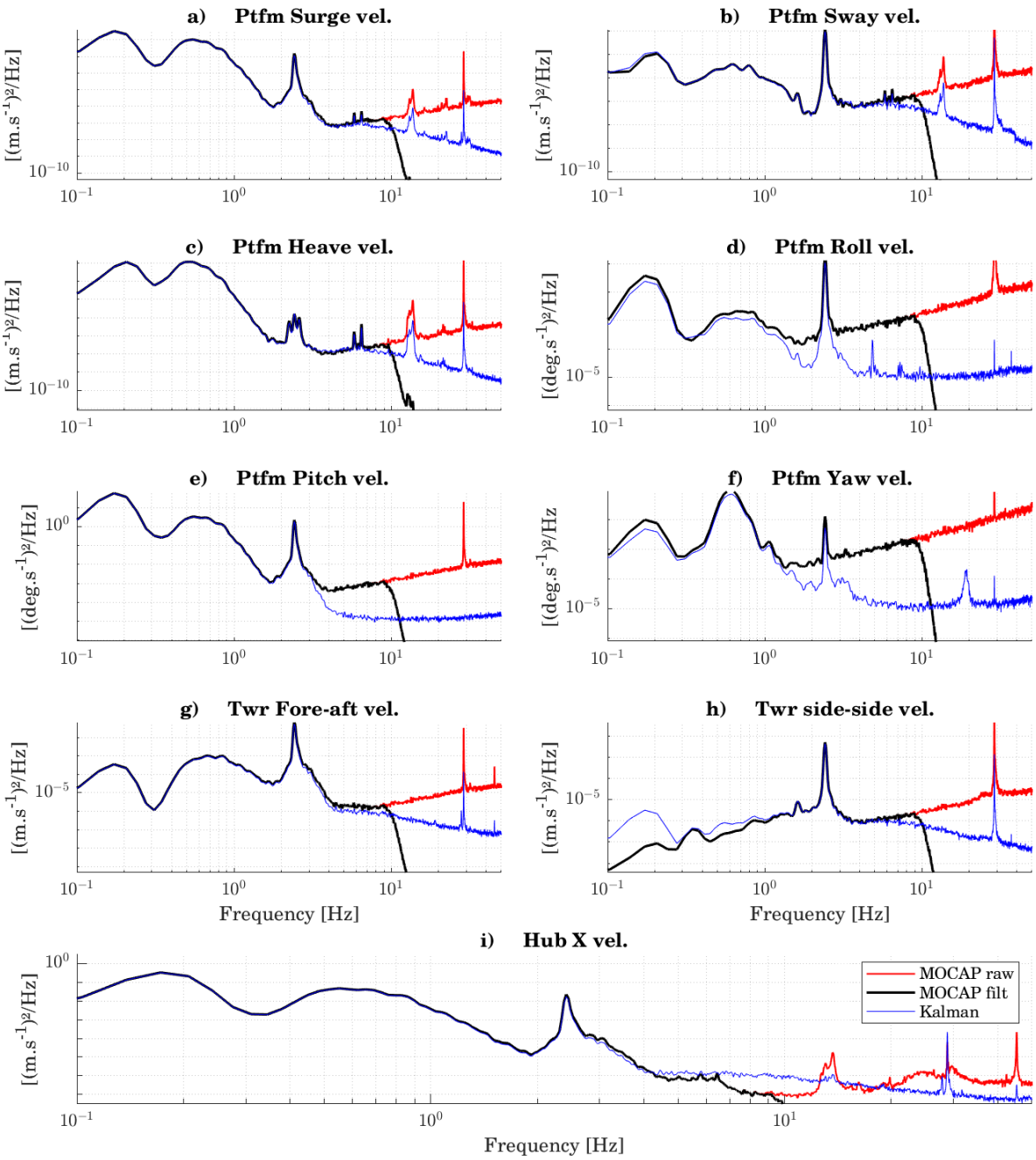

Figure 62: Motion observer performance, FWT DoF velocities PSD

This is confirmed in Figure 63, with the different components of the hub x-velocity plotted. The hub velocity related to the platform pitch velocity ($h * \dot{X}_5$, h being the tower top height above MSL) is counterbalanced by the tower top velocity $\dot{X_{twr}}$. This makes the resulting total hub velocity less noisy. A small peak is observed around 13 Hz for the platform translation velocities in the *MOCAP raw* signals. Vibrations of the Qualisys marker supports might explain this component.

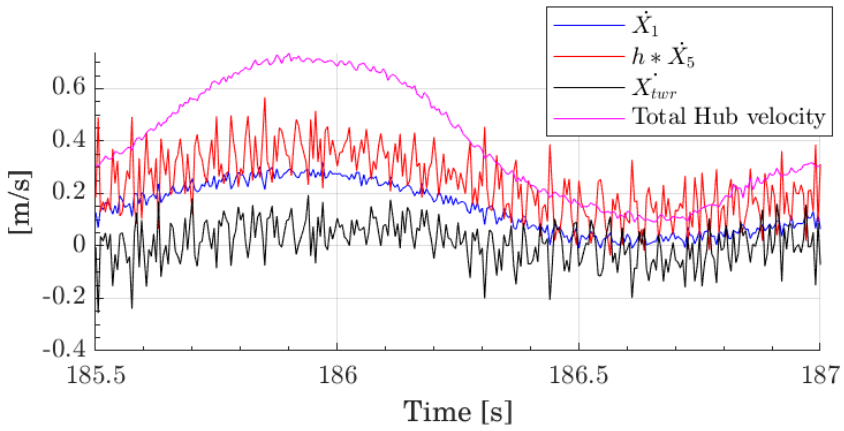

Figure 63: Details of the Hub x-velocity for the MOCAP raw

One possibility could be to disregard the impact of the high frequency fluctuations in the velocity signals on the force produced by OpenFAST. If the wind turbine is considered as a linear system and if the rotor loads are, around an operating point, proportional to the fluctuations of the incident wind velocity, a summation principle for the different frequencies could be applied. Both motion scenarios, *MOCAP raw* and *Kalman,* have been replayed by OpenFAST simulations. The full-scale forces outputted by OpenFAST are depicted in Figure 64 for these two scenarios. The last curve, denoted *MOCAP raw + LP filt*, is the MOCAP raw OpenFAST but the forces are filtered in post-processing at 20 Hz. The noise in the motions adds some high frequency content (*MOCAP raw* versus *Kalman*), but it does not change the lower frequency fluctuations of the forces. Indeed, the *MOCAP raw + LP filt* forces superpose very well with the *Kalman* forces. This indicates that filtering the motions is not mandatory, and a filter directly applied on the forces or on the command for the actuators (see chapter 6) is sufficient. Those conclusions are valid for this two-body configuration, and different forces fluctuations have been qualitatively obtained for a rigid-body configuration (Hexapod set-up). This might be explained by the large oscillations in the hub velocity related to the platform pitch velocity which are not counterbalanced by the nacelle motions. Deeper investigations are required to corroborate these conclusions.

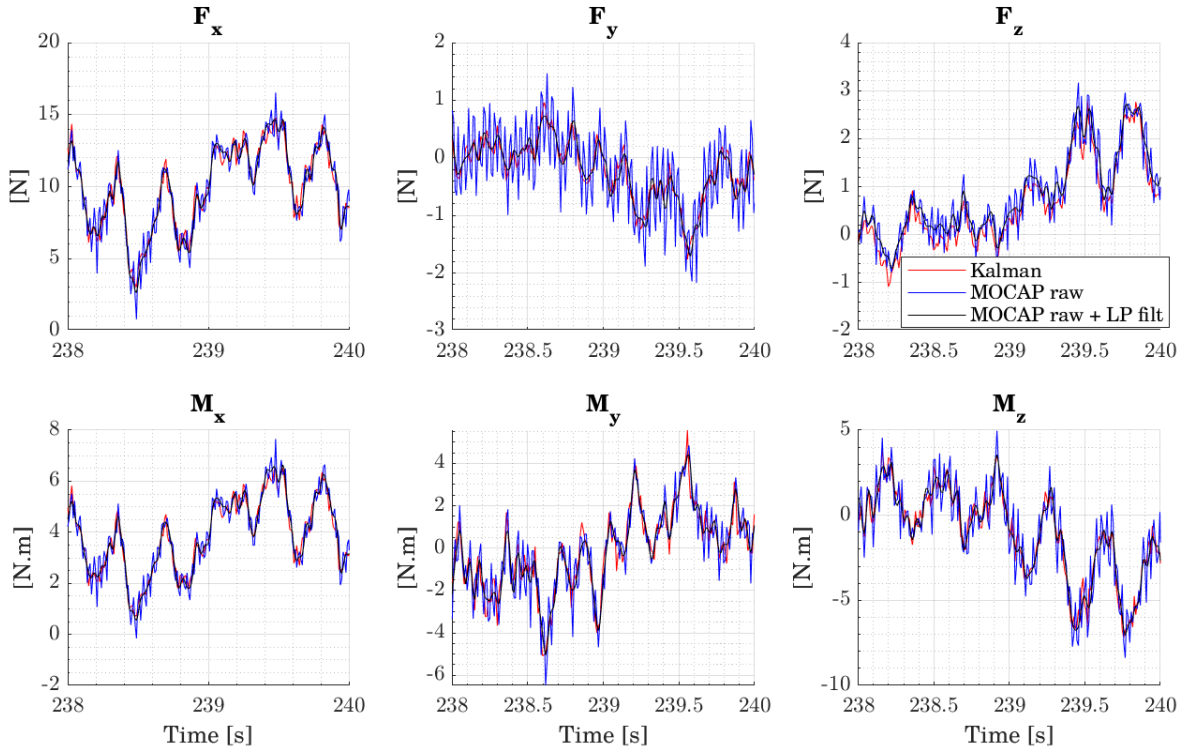

Figure 64: Forces output by OpenFAST for both motions scenarios MOCAP raw and Kalman

5.3.1.5 Conclusions

Many efforts have been deployed to get a high resolution, reliable and reproducible motion tracking system. The methodology to define a correct camera layout and 6-DoF body definition has been defined for a two-body configuration. Kalman filters have been successfully implemented on the floating set-up for a two-body configuration. However, the additional complexity brought by the Kalman filters has not been counterbalanced with significantly better performances. Different technical problems made the performance of the motion observer lower than expected:

- Kalman filters operations performed in the RT loop have caused minor real-time mismatches (jitter) that were not taken into account. The consequence was a delay increment in the motion observer, leading to an overall increment of the SIL system delay. This has caused, additionally to other bugs, unrealistic tower oscillations for the SOFTWIND SPAR set-up;
- The nacelle IMU was not working, due to interference on the CAN Bus, with the actuator ESC. An accelerometer with relatively poor performances has been used for the SOFTWIND SPAR set-up, making the motions state estimations not as accurate as expected;
- The synchronization of the sensors has not been thoroughly investigated. Due to differences in the processing time and communication protocols, the MOCAP outputs are used with a delay between 4 and 9ms in the set-ups used compared to the IMU outputs. This might cause discrepancies and inaccurate state estimations.

It has to be noted that merging an IMU and a MOCAP system has a significant interest concerning noise reduction for the platform angular velocities and for counterbalancing missing data from the MOCAP system.

An important outcome is about the sensitivity of the numerical model to unfiltered MOCAP signals. It was found, a posteriori, to have less impact on the forces output by the numerical model than expected.

5.3.2 Force observer performances

The performances of the force observer are crucial to understand the loads produced by the actuators in different kind of tests. For the inertial compensation, as explained in chapter 4.2.3, one parameter needs to be adjusted (the mass seen by the force transducer m_{seen}). Then, the quality of the inertial compensation is assessed by looking at the residual force (compensated) when the turbine is off. The inertial force deduced from the accelerometer signal ($m_{seen}a_x$) and the inertial force measured by the force transducer must agree. Investigations have been conducted for the SOFTWIND SPAR set-up as certain discrepancies in the inertial compensation have been noticed. The different discrepancies and corresponding identifications are detailed in this part.

5.3.2.1 Selection of the force transducer

An important aspect is the frequency content of the force generated by the propeller. The frequency content for the different actuators are presented in chapter 6. The highest important frequency - especially the 1P turbine frequency, see chapter 6 - has been computed for different mean thrust (operating point) values of the propeller to be sure that the sampling frequency is sufficiently high (to avoid aliasing).

For the SOFTWIND SPAR and the BGF set-ups a 2-component force transducer has been used. The main problem is that the torque component could not be properly identified. Except the buffering delay due to the NI9237 module explained previously, the SNR was good and the range of measurement appropriate.

For the multi-actuators set-up, a 6-components force transducer has been used. However, it was not well adapted to the forces and torques range of interest. Indeed, for the force, the amplitude of interest is approximately [1/100 - 1/1000]th of the nominal force range of the balance. Consequently, the SNR is relatively low. Additionally, another observation deals with the coupling terms in the calibration matrix of the force transducer. For this relatively compact force transducer, the coupling between the forces and the torques is not negligible. This creates off-diagonal terms in the calibration matrix. The problem is when one wants to get a fine resolution on the torques, the thrust of the propellers together with their arm effects could easily mask the torque production. For future set-ups, a preferred force transducer should be:

- less compact (with limited mass increase)
- with smaller force ranges.

5.3.2.2 Static performances and mass tuning

The main inputs of the *inertial compensation* are the mass seen by the sensor m_{seen} and the acceleration measured by the accelerometer. The accelerometer calibration and the identification of m_{seen} are done in the same test by imposing different steady-state trim angles θ to the nacelle. For this identification, it is assumed that there is no steady-state error in the prescribed Hexapod motions. The force measured by the force transducer is represented in Figure 65, with the X axis being the projected gravity acceleration on the hub frame x-axis $g_x = g\sin(\theta)$. A linear fit of the force evolution gives access to the mass seen by the force transducer. $m_{seen} = 2.40\,kg$ has been identified for the Hexapod set-up.

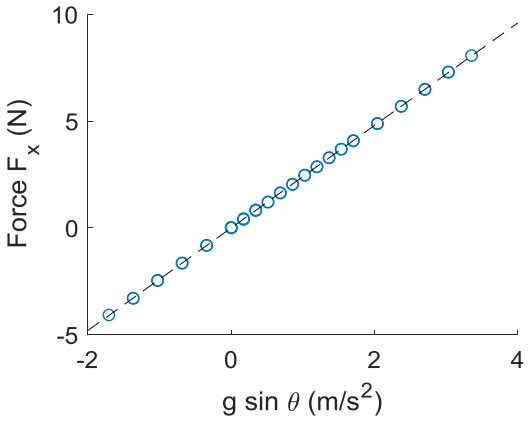

Figure 65: Identification of the mass seen by the force transducer. Hexapod set-up.

5.3.2.3 Dynamic performances

The dynamic performances have been investigated for the SOFTWIND SPAR and the BGF set-ups.

Two indicators have been used to check the success of the inertial compensation when the turbine is off:

- The force estimated after the inertial compensation (residual force) should be close to zero;
- The identified transfer function between the force measured and the mass times acceleration should be very close to 1 in the frequency bandwidths of interest. This transfer function $H_{force\ o.}$ is expressed in Eq. (4.6):

$$H_{force\ o.}(s) = \frac{F_{meas\ x}(s)}{m_{seen} a_x(s)} \tag{5.2}$$

The force observer transfer function $H_{force\ o.}$ is identified using dynamic motions of the platform and tower (motions-driven accelerations).

The mass is identified by two ways:

4. Using quasi-static motions of the platform (gravity-driven acceleration). In this set-up, those quasi-static platform motions are the steady-state trim angles of the platform and of the tower top, obtained in the static calibration tests as described in chapter 6.
5. By looking at the static gain of the force observer transfer function expressed in Eq. (4.6).

The mass is expected to be very close to the identified mass on the Hexapod set-up of $m_{seen} = 2.40\ \text{kg}$. For the SOFTWIND SPAR set-up, the gravity contribution leads to an identified mass of $m_{seen} = 2.35\text{kg}$, and the static gain of the transfer function leads to an identified mass of $m_{seen} = 2.40kg$. This uncertainty of $\Delta m_{seen} = 0.05\ \text{kg}$ is in the range of the mass measurement uncertainties (due to the rough estimation of the suspended cables between the nacelle and the mast casing). Note that the uncertainties in the equilibrium position provided by the MOCAP system, as described in the next subsection, have a very limited influence on the identified mass seen by the force transducer. The latter is approximately ¼ of the target RNA mass. This mass is composed of the actuator mass itself and approximately half the force transducer mass. Note that the force transducer and the actuators are tilted of 5° compared to the tower top frame, while the accelerometer is oriented along the tower top frame. This rotation is taken into account into the inertial compensation.

The frequency content of the force observer transfer function $H_{force\ o.}(s)$ is investigated. It is similar, on the frequencies of interest, to a 1st order low-pass filter transfer function with a cut-off frequency of 5 Hz. However, it has a phase near zero on the frequencies of interest. Then, to improve the

inertial compensation fidelity, the correction brought to the force observer is to use the inverse of a low pass filter. The negative delay introduced by this inverse low pass filter is counterbalanced to avoid a phase difference between the signals. Results are shown hereafter for *very severe waves only* test, with full scale environmental parameters $H_s = 9.4m$ and $T_p = 13.8s$.

In Figure 66 the time series of the superimposition between $F_{meas\,x}$, the raw force seen by the force transducer in the x-direction, and $m_{seen}a_x$, the mass times the acceleration seen in the x direction, are represented. Looking at the original results, (left or a)), the upper plot shows that the residual force, is rather small $[\pm 0.4N]$ compared to the force seen by the force transducer $[\pm 8N]$. However, using the inverse of the force observer transfer function gives significantly better results, with a residual force of $[\pm\, 0.07N]$ (top right or b)). The bottom graph illustrates the superimposition per frequency bandwidth, with LF denoting the low frequency including platform pitch natural frequency, WF the wave frequency and Twr_1 the first tower fore-aft mode. The LF inertial forces are very small compared to the WF and Twr_1 inertial forces. For the WF bandwidth, the superimposition is nearly perfect for both cases, but for Twr_1 an attenuation of $m \times a$ compared to the force could be observed of the left part of the figure (original force observer). This attenuation disappears for the improved force observer.

a) *Original force observer* b) *Improved force observer*

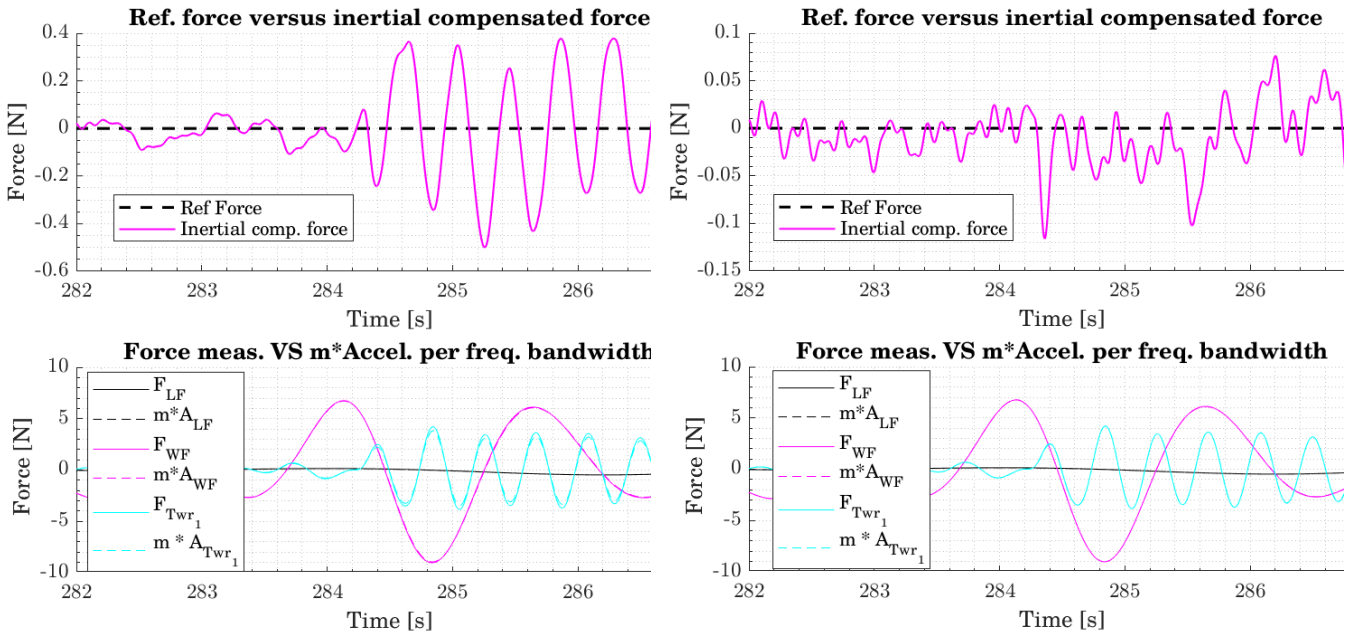

Figure 66: Force observer validation for waves-only tests. Top: residual force after inertial compensation versus reference (zero) force. bottom: force measured per frequency bandwidth versus mass times acceleration. a) original force observer results. b) improved force observer results

The identified force observer transfer functions are represented in Figure 67, with the coherence being at 1 ± 0.002 in the frequency bandwidths of interest. A low-pass filter with cut-off frequency of 5 Hz is superimposed to the gain and phase plots, and superimposes very well with the gain plot for the original force observer but does not superimpose with the phase plot. The improved force observer has a transfer function being very close to 1.

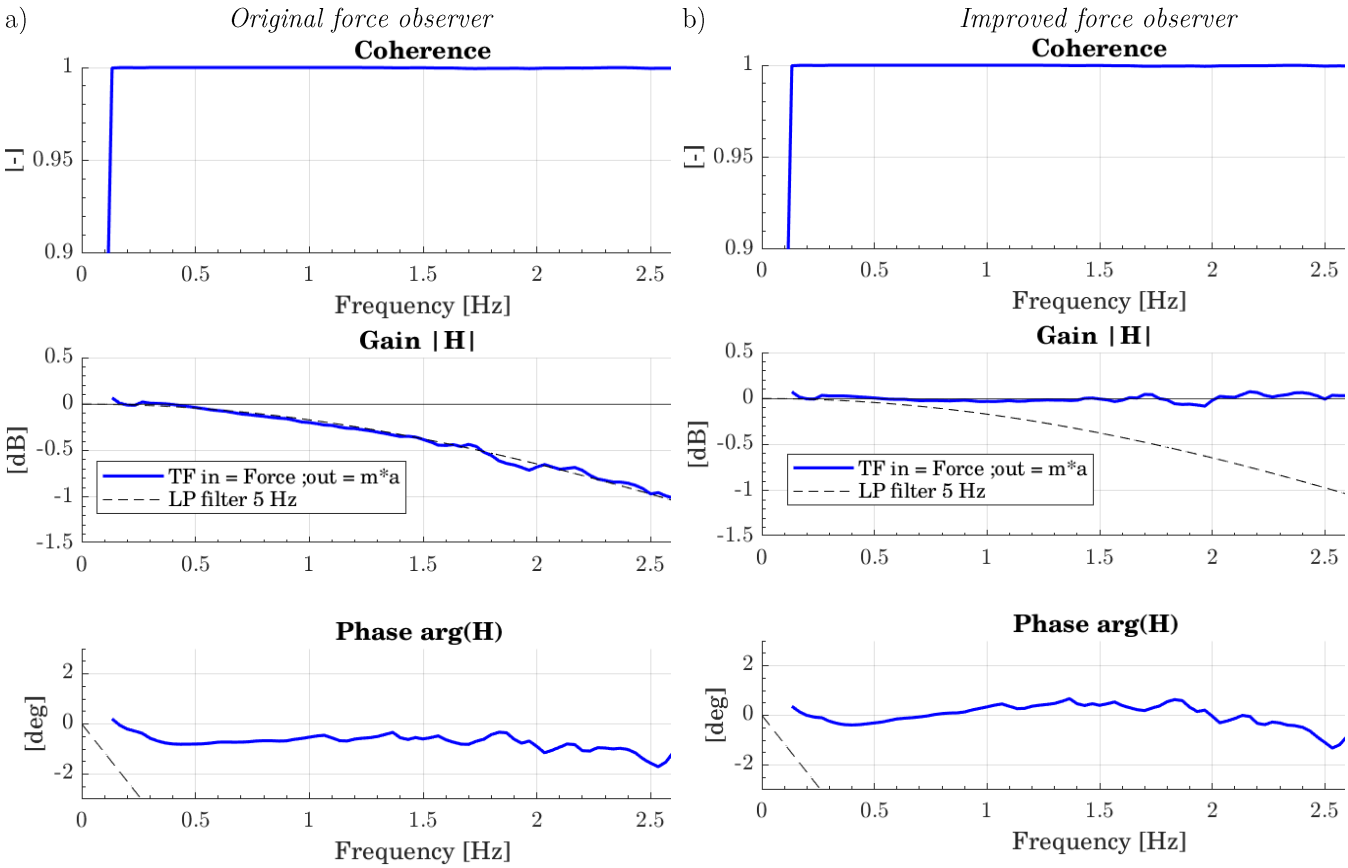

Figure 67: Force observer validation for waves only tests. Transfer function between the input force measured and the output mass times acceleration. A fitted 1st order low pass filter is superimposed. a) original force observer transfer function. b) improved force observer transfer function

The results are very satisfactory using the improved force observer and are used in the performances evaluation of the actuators.

5.3.2.4 Conclusions

The different test campaigns have shown how the accuracy of the force observer is crucial for a proper identification of the loads produced by the actuators. Most of the tests have been performed with a single actuator and a 2-component force transducer, and it has been extended to a multi-actuators configurations on the last test bench with a 6-component force transducer. The range of torques and forces are not necessarily compatible with the appropriate ranges of typical force transducers (such as the HBM BG-X serie). Designing or selecting an appropriate force transducer (relatively low force range but high torque ranges) is a prerequisite before using the force observer for feedback control. Moreover, in this work we were not able to properly identify the dynamics of the torque produced the actuator. This measure is required to easily reproduce the experiments in numerical simulations (see chapter 8).

Another important sensor of the force observer is the accelerometer or IMU used to withdraw the inertial forces. For a proper identification of the actuated loads with FWT motions (disturbances), this in-situ measurement is required. However, as illustrated in chapters 2 and 5, the significance of the inertial loads due to the RNA mass makes *inertial compensation,* and consequently actuated loads estimation, highly sensitive to the acceleration measurements. The selection of the accelerometer should be based on:

- appropriate range,
- bandwidth effect (low-pass filtering),

- redundancy with IMU,
- acquisition signal sufficiently high to avoid actuator loads-imbalance vibrations.

5.4 Conclusions

Different experimental set-ups have been designed and used to evaluate the feasibility, the performances and the relevance of the SIL methodology. The objectives and specificities of each set-up are summarized in Table 27.

The overall methodology was based on different characterization, identifications and validations. The SIL experimental apparatus has been tested and used for different set-ups. Its development requires the creation of dedicated test benches, to properly characterize the performances of the actuators and to facilitate the implementation by limiting the number of interfaces.

	Objectives	**Main characteristics**	**Main outcomes**
Forced motions #1, Hexapod	• Verification of communication protocols, • Evaluation of a single actuator performances in a controlled environment, • Characterization of the motion and force observers, • Testing feedback control strategies.	• Forced motions set-up (6 DoF hexapod) • Actuator #1 (ducted fan)	• Validation of the communication between the different SIL subsystems • Understanding of Force observer and motion observer behaviors • System identification of the actuator thrust
Floating #1, Blue Growth Farm	• Implementation of the SIL approach on a 10MW wind turbine, • Motion and force observer design for a 2-body configuration (platform and flexible tower)	• Platform weakly dependent on the rotor loads, • Flexible tower, • Kalman filter, • Actuator #2 (two-bladed aircraft propeller)	• Deal with a 2body system (platform and tower), • Motion observer tuning, • Application of the Hexapod campaign outcomes to another single actuator.
Floating #2, SOFTWIND SPAR	• Implementation of the SIL approach on a 10MW FWT, • Characterization of the behaviour of a 10MW FWT in realistic wind and waves conditions, • Evaluation of the actuators performances and its effects on the floating wind turbine behaviour, • Experimentally evaluate the influence of the wind turbine controller on FWT global motions.	• Flexible tower • Kalman filter • Actuator #1 (ducted fan) • Full FWT.	• Comparison of different numerical models in a fully-coupled SIL system, • Influence of the actuator performances also for low frequency (pitch natural frequency), • Comparisons of different controller effects,
Fixed multi-actuators set-up #1	• Extension to multi-propellers set-up • Setpoints of the actuators using not only the thrust but also the rotor loads torques, • Use of a 6 load components force transducer for proper evaluation of actuators torques.	• Several two-bladed aircraft propellers tested, • 6-component force transducer, • Three actuators running at the same time to model F_x, M_y and M_z.	• Recommendations for force transducer selection and frame mechanical design, • Securing the development of a 6-components rotor loads modeling system.

Table 27: Summary of the different experimental set-ups, objectives, characteristics and outcomes

6 Actuators performance identification

Contents

This chapter covers the calibration of the actuator thrust and the quasi-static and dynamic identification of the actuation system performances. Firstly, the methodology is explained. Then, this methodology is applied to two different actuator models, a ducted fan and different 2-bladed aircraft/drone propellers. Results in this part are presented at model scale. For the frequency bandwidths of interest and for the force range of interest, the considered scale ratios cover the range [1/50 – 1/30].

The original scientific contribution in this part is about applying known methodologies for system identification to these kinds of actuators, with key indicators defined by the FWT physics. A particular effort has been deployed to get an overall good consistency between different identification methodologies. The use of a simple frequency-dependent feedforward strategy gives promising results for this kind of actuators and is thus recommended for such systems.

6.1 Calibration and identification of actuator performances

In this part, the calibration and identification procedures are detailed. These procedures are mandatory for the feedforward part of the actuator control. A box diagram of the control loop of the actuator is depicted in Figure 68. The two implemented strategies are a feedforward only and feedback combined with feedforward. T_{set} , β, T_{act} and T_{meas} are respectively the target setpoint thrust, the input-duty ratio to the actuator, the actuated thrust and the measured thrust. $H_{ffwd}(s)$, $H_{act}(s)$, $H_{force\ o.}(s)$ and $H_{PID}(s)$ are the transfer functions of respectively the feedforward strategy, actuator, force observer and PID feedback control. Feedback control is widely used in the control engineering community to improve dynamic and steady-state performances. Existing strategies range from simple Proportional Integral Derivative (PID) control to advanced nonlinear control. In this work, a PI controller has been implemented and tested on the first test bench (Hexapod), but developments and settings adjustment were not pursued. Indeed, due to the initial misunderstanding of the NI module 9237 induced delay (see part 4.2), the trade-off between a higher bandwidth and an acceptable overshoot were not satisfactory. Moreover results using the feedforward only strategies, especially using the dynamic compensation procedure, have been considered satisfactory and its implementation easier and shorter (fewer parameters to adjust) for forthcoming test campaigns.

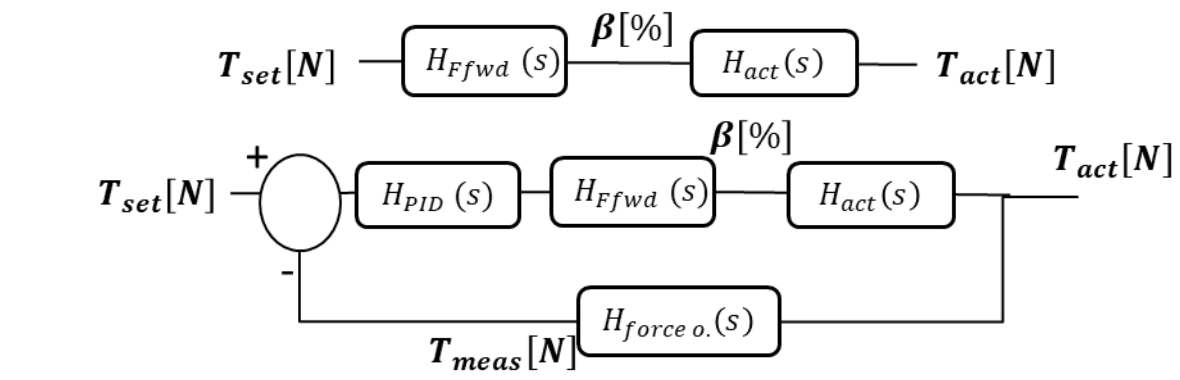

Figure 68: Box diagram of the actuator. a) feedforward only diagram. b) Feedforward and feedback diagram

The objectives of the identification procedures are also to identify the performances of the actuators. These performances are based on the loads generated, both on steady-state and dynamic characteristics. To get consistent force results during the tests, the calibration of the actuators is one of the key stages of actuators control (Meseguer and Guanche, 2019). This calibration is called “quasi-static identification” for the steady-state properties and “dynamic identification” for the dynamic

properties. The challenge was then to understand the main behavior of the actuator in order to efficiently pre-compensate the input duty ratio for a target thrust.

The identification is performed for the full actuation chain. It includes the power system, ESC, BLDC motors and propellers. Intermediate identification has not been possible due to the proprietary "black-box" ESC.

6.1.1 Quasi-static identification

The first kind of identification performed links the static thrust [N] to the input duty ratio β [%]. The duty-ratio can also be called *throttle* or *input PWM*. Two kinds of tests were performed to get this static relation:

- Increasing and decreasing duty-ratio levels, to get the steady-state discrete operating points of the actuator;
- Linear ramp of duty-ratio, with a very gentle slope. Operating points could be determined and it also checks if they are any dead-zones between the duty-ratio and the produced load.

The same methodology has been applied by Azcona et al. (Azcona *et al.*, 2014) applied to a 1:40 scale 6 MW semi-submersible platform. More recently, for the development of a multi-fan system developed by IHCantabria (Meseguer and Guanche, 2019), the static calibration procedure has been extended to take into account aerodynamic interactions between different propellers.

Special attention is given to the following items:

- A dependency on the input power supply voltage when batteries system is used. This might be investigated by repeating the quasi-static identifications at different charge levels.
- When the identification is performed directly atop of the wind turbine tower fixed to the floater, the duration of the plateau and the amplitude of the steps should be carefully selected to avoid exciting too much any natural frequencies.

This quasi-static identification defines a relation between the setpoint thrust T and the input duty-ratio β for different operating points. This is presented in Eq. (6.1):

$$\beta = \frac{1}{K[T]} * T \tag{6.1}$$

With $K[T]$ the gain between the input duty-ratio and the output thrust. To implement this strategy, both 2nd order polynomial fit of $K[T]$ and tabulated values have been tested. The fidelity of the polynomial fit depends on the actuator, while a fine discretization of tabulated values has been considered to be consistent. Then, the feedforward correction consists in using this quasi-static identification to get the appropriated input duty-ratio $\beta_{static}(t)$ from the setpoint thrust $T_{target}(t)$. This is presented in Eq. (6.2).

$$\beta_{static}(t) = \frac{1}{K[T_{target}(t)]} * T_{target}(t) \tag{6.2}$$

In that case, the feedforward correction H_{Ffwd} is only a static gain.

6.1.2 Dynamic identification

Different kinds of time-varying setpoints have been used to characterize the dynamics of the actuator. Those setpoints include:

- Step signals of different amplitudes, both for rising and falling setpoints

- Sine setpoint with varying frequencies and amplitudes. This is equivalent to regular waves when computing the motion RAO of a floating body.
- White noise signals, different frequency ranges and amplitudes.
- Realistic setpoint load (equivalent to irregular waves when computing the motion RAO of a floating body). Different scenarii of increasing complexity were simulated, from steady wind-only to turbulent wind, wind shear and wave-induced velocities.

The main indicators for the dynamic identification are:

- Transfer function of the actuator, between the setpoint force and the actuated force $H_{actuator}(s) = \frac{F_{measured}(s)}{F_{setpoint}(s)}$. This identification is performed with different methodologies:
  - Frequency-domain identification using the Bode diagram (Gain and phase) of the actuator
  - Time-domain « black-box » fit to a suitable model.
  - Rising time, overshoot and dead-time from unit-step response.
- Saturations of the thrust derivative $\frac{\partial F_{measured}}{\partial t}$
- Frequency content of actuator thrust, by looking at the PSD of the generated thrust. This indicates if higher harmonics or unexpected loads of the actuators are generated, compared to the setpoint thrust.

The transfer function has been estimated using different widely-known methodologies depending on the input signal:

- a cross spectrum methodology, using Welch method, for the white noise signals
- a RAO estimation at the 1^{st} harmonic frequency, using a Fourier transform for the sine setpoints.

Details are given in appendix B. For a linear system, the indicators identified from the tests with the different setpoints are expected to be consistent. Indeed, only nonlinearities (due to saturations, intrinsic nonlinear behavior, large change of the operating points, etc…) can explain differences between different frequency domain methods and with time domain methods.

The identification was considered successful when the different analyses converged to the same overall model of the actuator. For simplification, the system was considered, around an operating point defined by the mean thrust $T_0\ [N]$, to an equivalent pure delay and 1st order model identified by Eq. (6.3).

$$H_{actuator}(s) \approx \frac{K'[T_0]}{1 + \tau[T_0]s} \mathrm{e}^{-T_{delay}s} \tag{6.3}$$

This is a 3-parameter model, with:

- $K'[T_0]$ the static gain, dependent on the operating point
- $\tau[T_0]$ the rising time, dependent on the operating point. The corresponding cut-off frequency is $f_c[T_0] = \frac{1}{2\pi\tau[T_0]}$.
- T_{delay} a pure delay, independent on the working point.

The main limitations of this simplified model are:

- Different behaviors between acceleration and deceleration of the motor (saturations mechanisms) are neglected;

- Validity around an operating point while variations of the setpoint can be very important for highly turbulent wind conditions;
- A n-order system could be easily simplified to a 2nd-order system, with the same overshoot, resonance frequencies and static gains. With a 1st-order system, overshoot and other characteristic responses cannot be taken into account.

A higher order model would require additional parameters. This could capture the physics in a better way but would lead to different sets of parameters for each test. The 1st-order system is convenient for the *dynamic compensation* procedure described in the next part and is considered as acceptable on the frequency range of interest.

6.1.3 Dynamic compensation

Once the model of the actuator dynamics has been identified, this information could be used to improve the command of the actuator in order to reach a higher fidelity. This procedure is referred as *inverse dynamics*, *dynamic compensation* or *model-based feedforward compensation for closed loop* in the literature. This procedure is first introduced and then is applied to the identified actuator model.

Let $H_{system}(s) = \frac{y}{u}$ be the identified transfer function of the system with input u and output y. The general idea of an adapted controller (feedback control or feedforward control) is to generate the inverse of a process (Goodwin, Graebe and Salgado, 2007). The dynamic compensation procedure used in this work takes the identified transfer function of the actuator to adapt the input u. This input becomes $u_{corrected}$.

$$u_{corrected}(s) = H^{-1}{}_{system}(s) * u(s) * H_m(s)$$

With:

- $H^{-1}{}_{system}(s)$ the inverse transfer function of the system
- $H_m(s)$ a corrective transfer function to ensure stability and robustness to any disturbances.

Consequently, the new transfer function between the input u and the output y is represented in Eq. (6.4):

$$H_{corrected}(s) = \frac{y}{u} = \frac{y}{u_{corrected}} * H^{-1}{}_{system}(s)\, u(s)\, H_m(s) = H_m(s) \tag{6.4}$$

Despite being very basic because limited to linear systems without saturation mechanisms, the dynamic compensation can make the resulting transfer function $H_{corrected}(s)$ closer to 1.

This procedure is now applied to the identified actuator model. Concerning $H_m(s)$, a 1st order low pass filter with cut-off frequency $f_{c\,m}$ (corresponding characteristic time τ_m) is selected. The transfer function of the system was already described in Eq. (6.3). The input to the actuator command is the target thrust represented by its transfer function $T_{target}(s)$. The adapted duty-ratio β_{dyn} could be expressed in the Laplace domain by Eq. (6.5). The dependency of the gains and cut-off frequency to the operating points is denoted by $[T_0]$, the thrust at this operating point.

$$\beta_{dyn}(s) \approx T_{target}(s) * H_{system}{}^{-1}(s) H_m(s) = \frac{T_{target}(s)}{K[T_0]} \frac{1 + \tau[T_0]s}{1 + \tau_m s}\, e^{T_{delay}s} \tag{6.5}$$

The term $\frac{T_{target}(s)}{K[T_0]}$ corresponds to the result of the static identification as presented in Eq. (6.2). The term $e^{T_{delay}s}$ requires knowing the setpoint at a horizon T_{delay}. Computing the setpoint in the future at $(t + T_{delay})$ could be approximated by several techniques (e.g. Padé approximant, polynomial approximations (Chabaud, 2016)) depending on the ratio of T_{delay} compared to the periods of interest. In a first approach, this has been neglected but will be studied at the next development steps. Switching

to time domain leads to the command $\beta_{dyn}(t)$ presented in Eq. (6.6). Note that the corrective low pass filter $H_m(s)$ is applied after this equation on $B_{dyn}(t)$ and is not detailed for the two following equations.

$$\beta_{dyn}(t) = \frac{1}{K[T_{target}(t)]}\left(T_{target}(t) + \tau[T_{target}(t)]\frac{dT_{target}(t)}{dt}\right) \tag{6.6}$$

Reorganizing the terms to get the static relation expressed in Eq. (6.1) leads to Eq. (6.7):

$$\beta_{dyn}(t) = \beta_{static}(t) + \frac{\tau[T_{target}(t)]}{K[T_{target}(t)]}\frac{dT_{target}(t)}{dt} \tag{6.7}$$

Compared to the static relation, a dependency to the time derivative of the thrust has been introduced. The dynamic compensation ($H_{ffwd}(s)$ in Figure 68) used in this work simplifies to thrust derivative correction. The derivative is implemented using a simple 1st order finite-difference scheme. This dynamic compensation of the thrust setpoint has been implemented in the real time control loop of the motor.

For clarity, the methodology that used the steady-state relation between the input PWM [%] and the output thrust [N] is called *static calibration* while the other is called *dynamic calibration.*

6.1.4 Conclusion on the identification and calibration

Different input signals have been considered for the calibration and identification of the actuators performance. The different signals with the expected outcomes and metrics are summarized in Table 28.

	Setpoint type	**Objective**	**Outcomes and metrics**	**Main input parameters**
Static identification	Discrete steady state values	- Operating points could be determined	- Input-output gain relation for different operating points. Used as a static calibration curve (for feedforward)	- Duration of the steady-state levels [s] - Min and max values of the input [%] - Input increment [%]
	Quasi-static linear ramp	- Verification of the discrete steady state values. - Check the dead-zones	- Dead-zone in the throttle	- Duration of the ramp [s] - Min and max values of the input [%]
Dynamic identification	Sinus	- This is equivalent to regular waves when computing the motion RAO of a floating body - Visual interpretation of the behavior	- Transfer function in frequency domain	- Mean operating point [%] - Amplitude [%] - Frequency [Hz]
	White noise	- Frequency domain identification - Overall model for a frequency bandwidth	- Transfer function in frequency domain - Black-box fit in time domain	- Mean operating point [%] - Amplitude [%] - frequency bounds [Hz]
	Steps	- Unit-step response identifications - Quantification of positive and negative saturations - Visual interpretation of the behavior: nonlinearities ? different behavior for increasing and decreasing setpoints ?	- Rising time - Overshoot - Dead-time	- Amplitude of the variation [%] - Mean operating points [%] - Duration of steady-state levels [s]
	Realistic multi-frequencies setpoint	The identification (in frequency and time domain, …) are done with appropriated levels fluctuations and associated frequencies	- Transfer function in frequency domain - Black-box fit in time domain - Error levels - Overall validation of the identified models	- Test case defined by the floating wind turbine and the selected load case

Table 28: Identification signals considered and expected outcomes

The dynamic identification signals that have been used in this work are classical setpoints in the system modeling community. Additional identification tests, including pseudo-random binary sequence (PRBS) and chirp signals (Chabaud, 2016) could also be used for the model identification.

6.2 Application: Actuator #1, ducted fan

- The calibration and performance identification procedure has been applied to the Schübeler ducted fans as used in the Hexapod setup and in the SOFTWIND SPAR setup. The motor, fan geometry, the control scheme and the power system slightly differ between the two test campaigns. The different characteristics are listed in Table 29.

Setup	Fan	Motor	Actuator name	Control	Power system
Hexapod	DS-94-DIA HST	DSM6745-700	*Schub. Hxpd.*	CAN Bus, 1kHz	Stabilized power units, 48V, $i_{max} > 150A$
SOFTWIND SPAR	DS-98-DIA HST	DSM6043-650	*Schub. SW SPAR stab.*	PWM, 200Hz	Stabilized power units, 48V, $i_{max} > 150A$
SOFTWIND SPAR	DS-98-DIA HST	DSM6043-650	*Schub. SW SPAR Batt.*	PWM, 200Hz	Battery, nominal voltage 53V, i_{max}~$70A$

Table 29: Schubeler ducted fans used in the Hexapod and SOFTWIND SPAR set-ups

Note that, for the SOFTWIND SPAR set-up, the power system is a Lithium-ion battery with nominal voltage of 53V and maximal current draw around 70A. To isolate the battery effect, some tests have been performed using the same power system as for the Hexapod setup, i.e. stabilized power units with nominal voltage of 48V.

6.2.1 Quasi-static identification

On this actuator, a 2nd order fit between the input duty ratio and the output thrust gave satisfactory results. All the results obtained in the Hexapod forced motions setup #1 have been obtained with the 2nd order fits for the calibration curve. In the SOFTWIND SPAR setup, the static calibration curve is obtained from tabulated values. Initially, it was envisaged to use the 2-component force transducer to estimate the F_x and M_x load components. With the assumption that the turbine is not generating any F_y force, the F_y component of the force transducer could be used to estimate the actuator torque M_x. Due to non-negligible off-diagonal coefficients in the force transducer calibration matrix and due to the preponderance of the F_x force compared to the measured F_y force, this identification was not successful. This torque characteristic has not been evaluated for the ducted fan actuators.

The F_x static force are given for the two setups (three configurations) and are depicted in Figure 69. 2nd order fit are represented by dashed lines. These jet turbines can generate up to 100N, consequently for the scale ratios of interest, only the range [0 - 60]% of the capabilities of these actuators are used. These calibration curves have been averaged along different tests with the same power system, but different test conditions (temperature, …). It has to be noted that test conditions have a negligible influence on the static calibration (less than 1%). The only influencing factor is the input voltage, as it could be seen between the *Schub. SW_SPAR Batt* [52.5V] and *Schub. SW_SPAR stab.* [48V]. The influence of the battery mean voltage is discussed in the next part. Note that the mean aerodynamic thrust are in the range [10-25]N at 1:40 scale ratio for the DTU 10 MW RWT. This corresponds to [15-40]% PWM range. One could think that the actuator is oversized but the test duration adds thermal constraints at the system so that a smaller actuator would not be better suited.

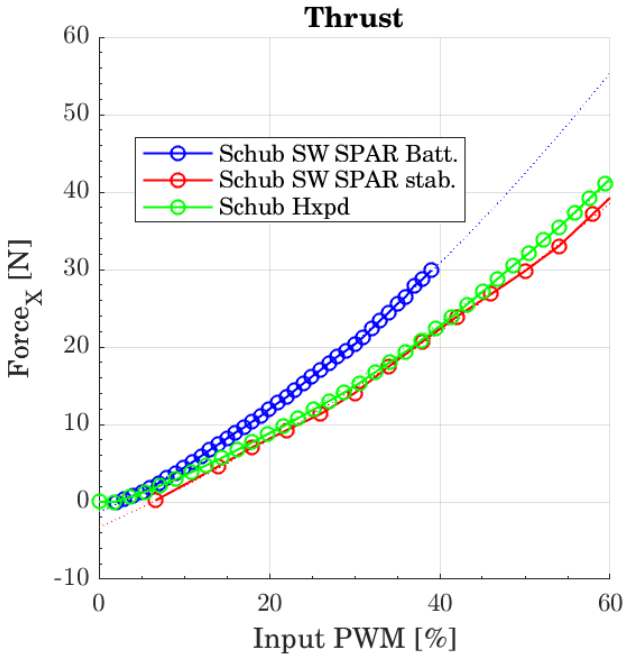

Figure 69: Static calibration of the Schubeler jet actuators

6.2.1.1 Effect of battery voltage variation

In the SOFTWIND SPAR setup, a battery has been used to power the system. The mean voltage in the battery without loads is varying between 52.9V (fully charged) and 50.3V (discharged). The voltage of the battery is recorded by the ESC at a low monitoring frequency.

The quasi-static identification is performed at different mean voltages of the battery to check its influence on the duty-ratio – Thrust calibration curve. This is represented in Figure 70, with the different calibration curves on the left and the relative error compared to the generated thrust from the highest initial voltage (52.9V). The range [50.3 -52.9]V covers most of the battery mean voltage as the Battery Management System (BMS) activates the security around 49.5V. Different tests at the same initial mean voltage (represented on this graph at 52.5V and 52.1V) show limited variations for a given mean voltage. We can observe on Figure 70 right a decrease of thrust with voltage. The decrease between a charged battery and a discharged battery (from 52.9V to 50.3 V, voltage loss of 2.5V) is around 7%. From the simplified model of the actuator presented in chapter 4, a decrease of the generated thrust with the battery voltage is expected with the ratio $\frac{U_{b1}}{U_{b2}}$. The decrease seen on Figure 70 left is approximately proportional to this ratio. We can define a simple strategy to overcome this variation of thrust with battery voltage. At the beginning of each experiment, a correction of the calibration curve with the mean voltage of the battery at rest could be implemented. This has not been implemented in the SOFTWIND SPAR campaign, however, for most of the tests, the battery mean voltage was varying between 51.7V and 53V. In this campaign a maximal decrease of 5% of the mean thrust could be due to the battery voltage.

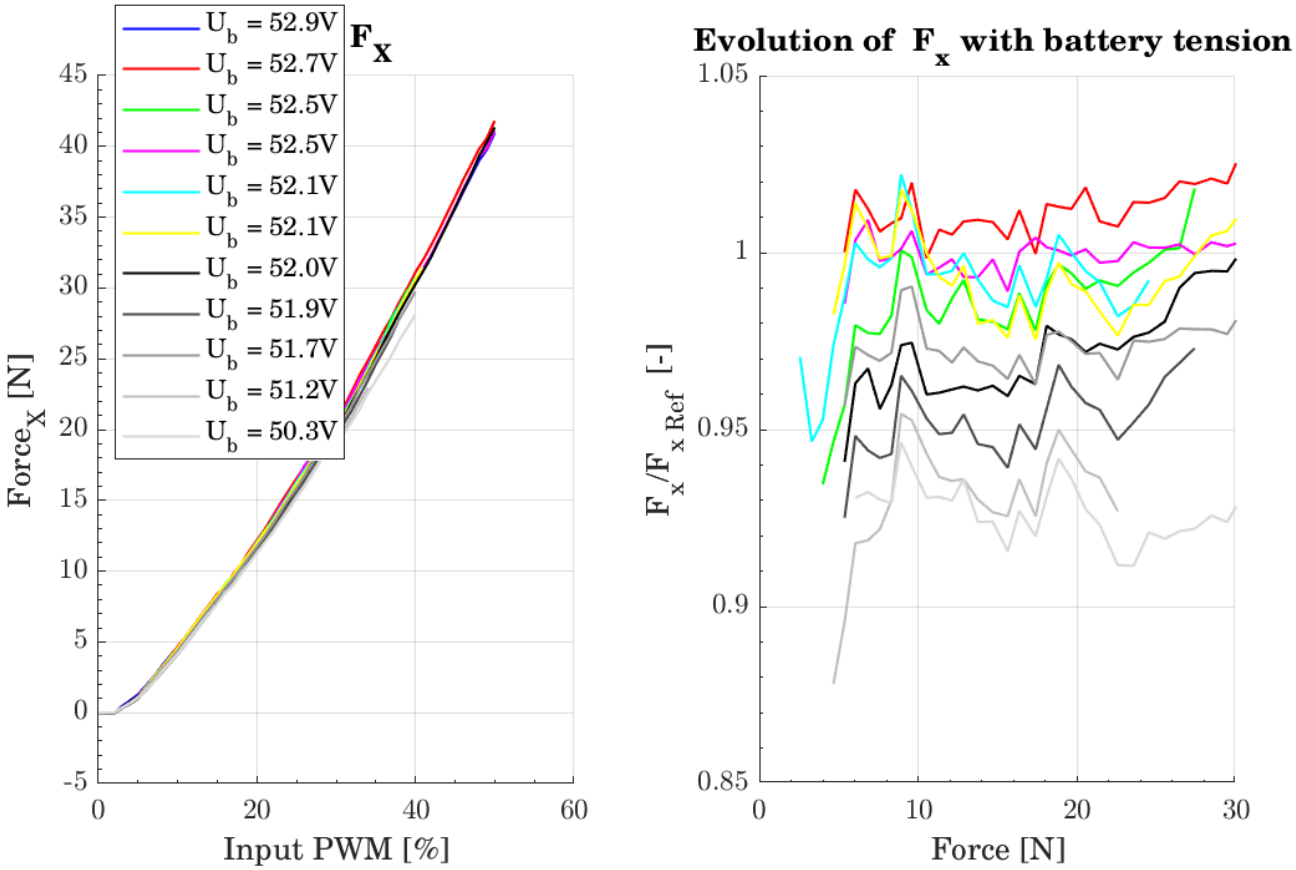

Figure 70: Static identification performed for different battery voltages

6.2.2 Dynamic identification

We apply the procedure described in section 6.1.2 to the ducted fans.

6.2.2.1 Thrust frequency content

The PSD of the x-component of the force measured by the force transducer - without the inertial compensation - is represented in Figure 71 for different constant input duty-ratios. The important frequencies are emphasized by the different peaks. There is a 1P component - due to mass imbalance of the fan, similarly to a wind turbine - at 120Hz for a mean thrust of 7N and at 160Hz for a mean thrust of 12N. Those peaks are also visible on the accelerometer signal which means that the 1P vibration is transmitted to the nacelle. On the accelerometer signal, there is also a peak around 2.4 Hz for the 7N and 12N operating points, which is the mast natural 1st fore-aft natural frequency when coupled to the floater on the SOFTWIND SPAR setup. The mast is slightly excited because of the transient linear ramps between the operating points. The low frequency energetic content is due to platform motions at the surge and pitch natural frequencies, also due to the transient linear ramps.

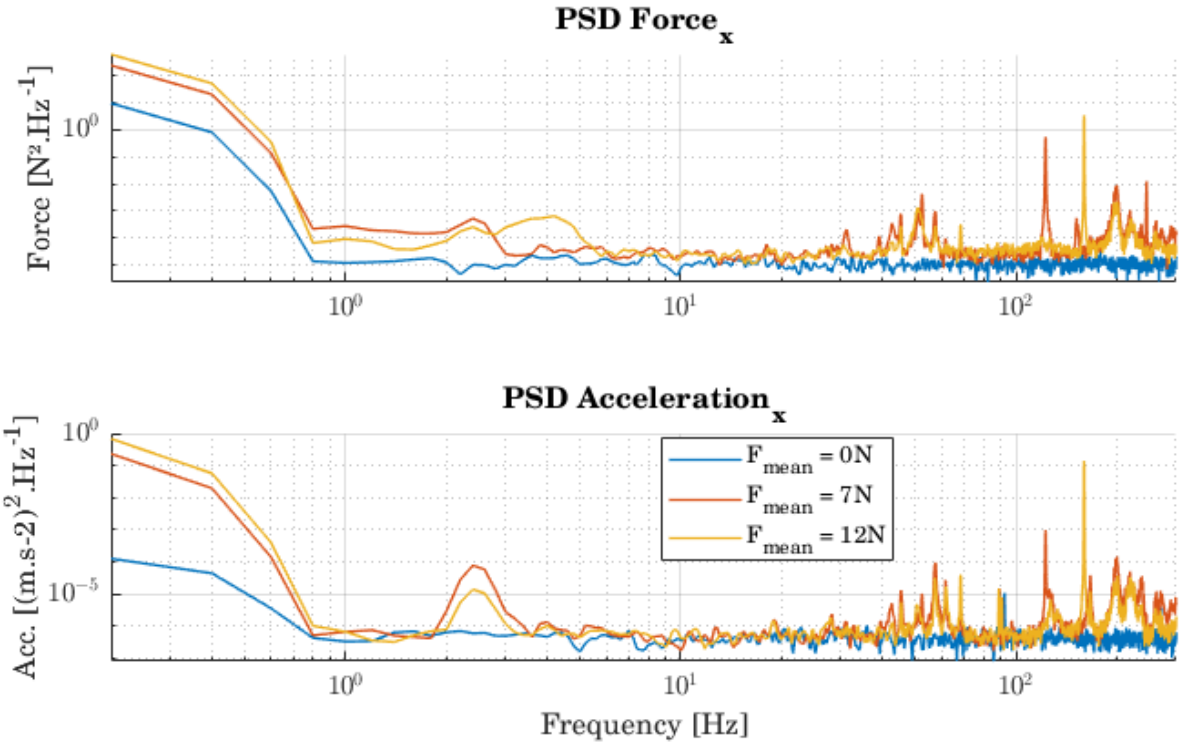

Figure 71: PSD of force and acceleration at different operating points

The 1P frequency as a function of the generated thrust is represented in Figure 72. This 1P frequency is computed by averaging the motor speed given by the ESC at 1Hz for the different steady points. For the loads of interest (range [5 - 40]N), this 1P actuator frequency covers [100 - 250] Hz. A square root fit between the angular velocity and the force is also represented by a dashed black line. The force generated by this turbine fits very well to the square of its angular velocity, validating, for this ducted fan, the constant C_T coefficient.

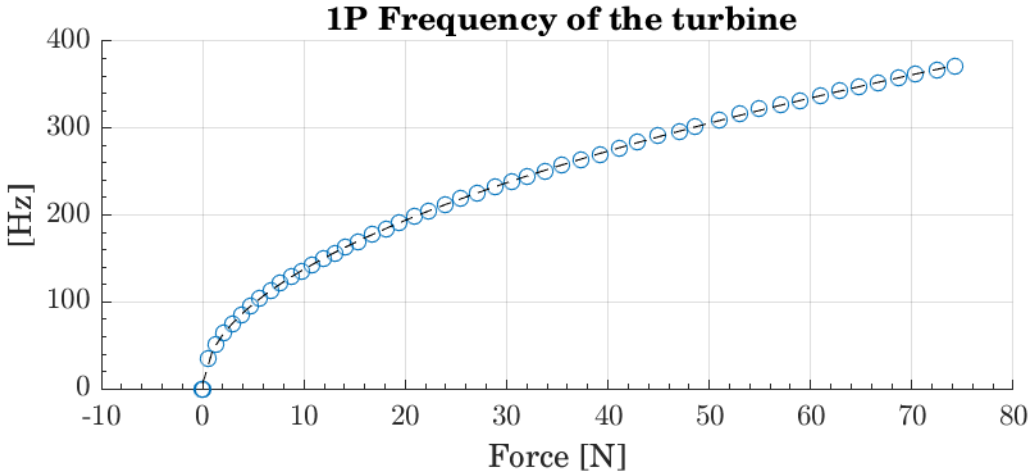

Figure 72: 1P frequency of the Schübeler ducted fan with quadratic fit (dashed line)

In Figure 73, the turbine velocity as function of the input PWM is represented. There is a linear relation between both quantities on the region of interest ([10-60]%), highlighting the velocity control loop of this actuator, run by the embedded STM32 microcontroller within the ESC.

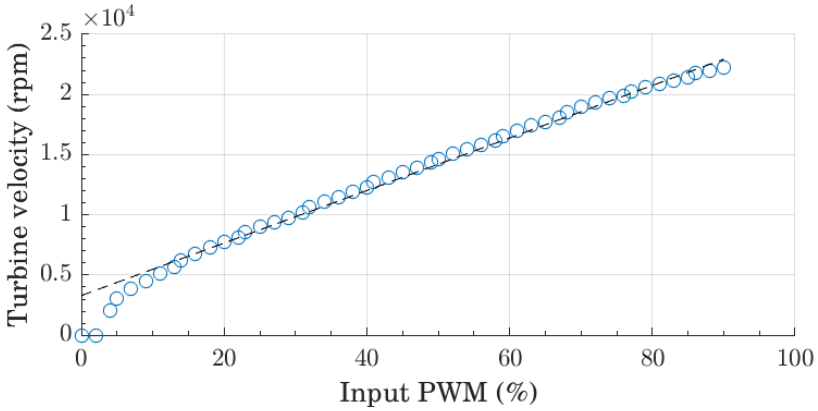

Figure 73: Turbine rotation as function of the input duty ratio. Linear fit on the [10-80]% region

6.2.2.2 Transfer function identification

To identify the actuator's model, from the input duty-ratio [%] to the measured force [N], rising and falling steps, bandpass filtered white noise signals and sine setpoints have been used in the different campaigns. The tests presented in this part use the steady-state calibration curve presented in 6.2.1. The results presented in this thesis differ to the results published in (Arnal *et al.*, 2019), due to a better understanding of the NI 9237 module buffer induced delay as explained in section 4.2.

a. White noise and sine identifications

From the white noise tests, the gain and the phase of the transfer function H of the thrust in open loop are estimated. A graphical estimation of the cut-off frequencies depending on the working points could be deduced from the frequency values where transfer functions fall below -3db. Fitted 1st order low pass filters are superimposed to the evaluated transfer functions to check the validity of the graphically identified transfer function on the frequency range of interest.

This has been applied for the Hexapod setup with the *Schub Hxpd* actuator and is shown on Figure 74. Different operating points have been considered to cover the mean F_x values range for different operating wind speed values. A standard deviation of 10 % of the mean thrust was considered to determine the white noise spectrum frequency components. The upper plot is the coherence between the reference force and the measured force. The coherence is very close to 1, meaning that the identification to a linear system is reliable. The frequency band $[0.05 - 6]Hz$ covers the frequencies of interest from slow wind variations frequencies up to 3P rotor frequencies. The fitted models, represented with dot lines, superimpose very well with the transfer functions identified from white noise tests. A pure delay of 3ms has been added in the fitted models to match the phase characteristics. The gains present unwanted overshoots of around [0.2 - 0.4] dB below 0.5 Hz and corresponds to a magnification of [3-5]% of the low frequency component of the thrust. This might be due to the rather poor quality transfer function identification linked to the insufficient duration of the white noise tests (around 150 s) to conduct an accurate frequency analysis at those frequencies. It could be noticed the fitted gain of 0.95 at 8.5N and 1.02 at 19N, which could be corrected by a better static identification.

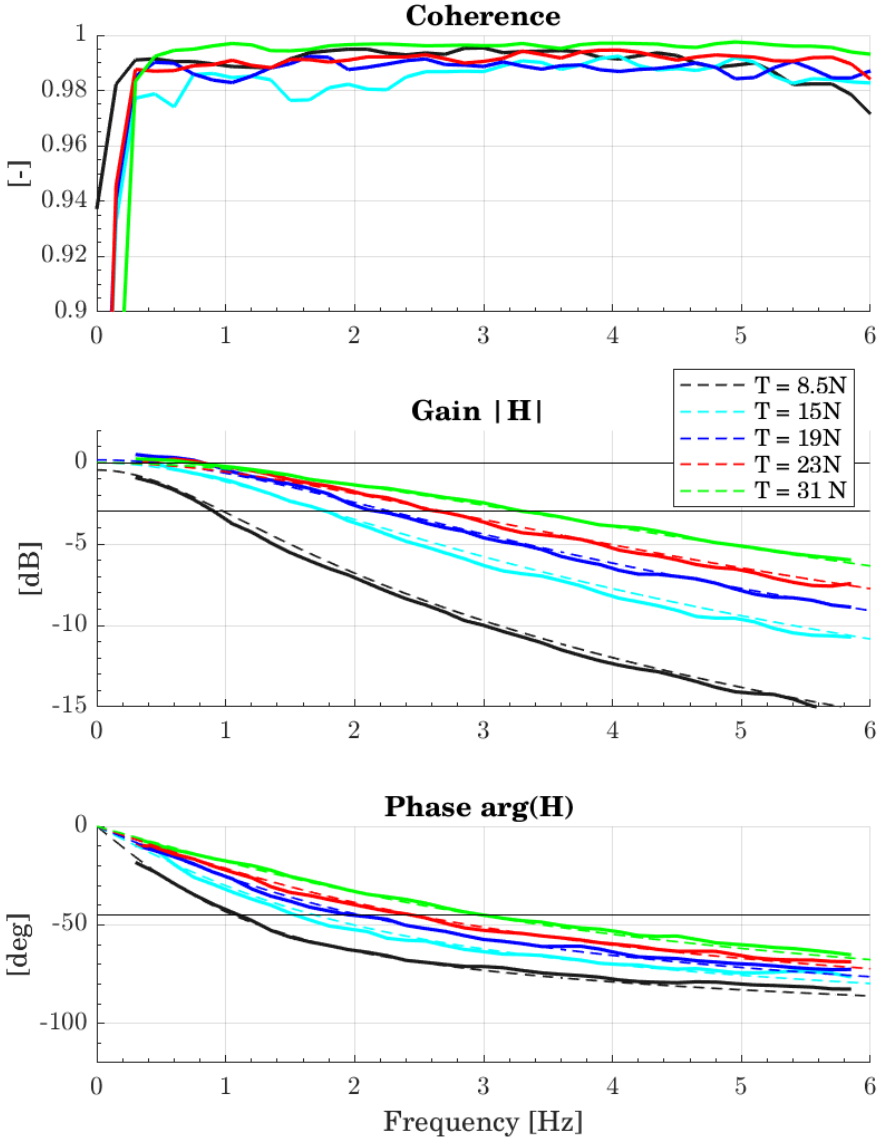

Figure 74: Frequency domain identification, at different working points, of the Schubeler Hxpd actuator thrust. White noise frequency domain and fitted models.

The same methodology has been applied to the *Schub SW SPAR Batt* actuator, with also a transfer function identification from sine setpoints. The frequency domain results are depicted in Figure 75. For the sine identifications, the indicator, similarly to the coherence for cross spectra estimation, to indicate the quality of the identification is the ratio of the 2nd harmonic to the 1st harmonic of the response. If this ratio is above 5%, the corresponding portion of the signal is discarded. On these identifications, the static gain is very close to 1 thanks to the use of tabulated values of the static calibration curve. The sine identifications have been done from 7.5N to 22.5N per step of 2.5N. Fitted first order low pass filters are represented for the operating points 10N, 15N and 20N. The estimations of the transfer functions from white noise and sine setpoints superimpose well, but have some minor differences. The sine estimated gains are slightly more attenuated between 2 and 3 Hz than the white noise identified gains. To match the phase characteristics, the fitted model has a pure delay of 12ms whatever the operating point. Overall, this actuator has slightly smaller cut-off frequencies than the *Schubeler Hxpd* actuator for similar operating points and has larger pure delay response.

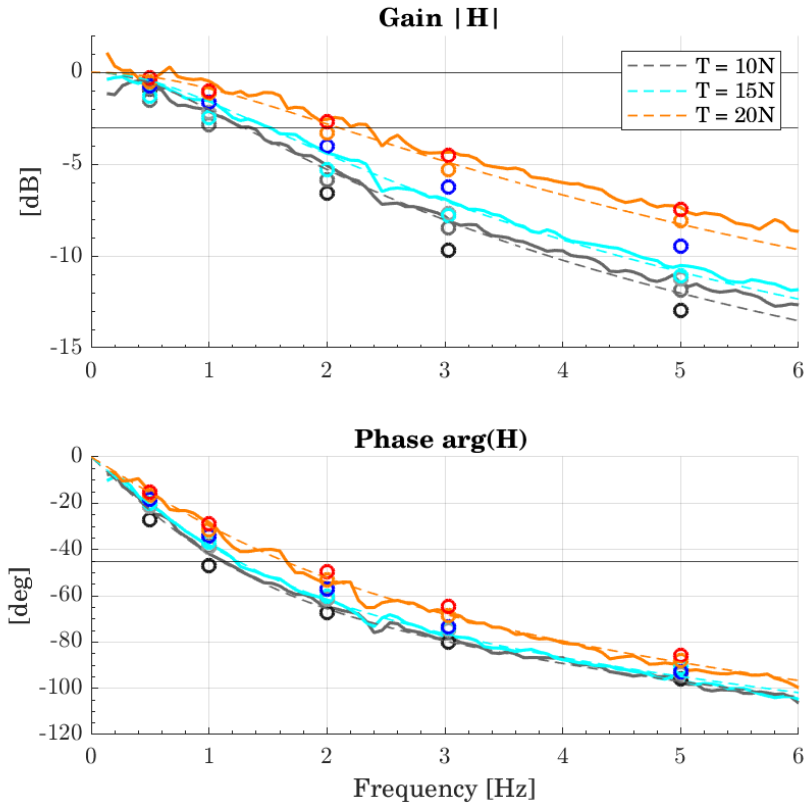

Figure 75: Transfer function identification from white noise and sine setpoints. Schub SW SPAR Batt actuator. *One color per thrust level. Fitted model are represented with dashed lines, sine with (o) symbols, and white noise TF with continuous lines.*

b. Step response

To pursue and validate the actuator model identification, unit-step response of the actuator is analyzed. The dimensionless response to rising and falling steps centered on 25 N and on 12N is plotted in Figure 76, for the *Schub. Hxpd* actuator. Different amplitudes of the steps are considered to look for saturations and nonlinear mechanisms. The measured force is ideally filtered at 35 Hz together with a notch filter centered on 10 Hz to exclude the effect of mast flexible variations. The response of a first order low pass filter with the same rising time, denoted *Fitted model,* is also depicted with dashed lines.

a) b)

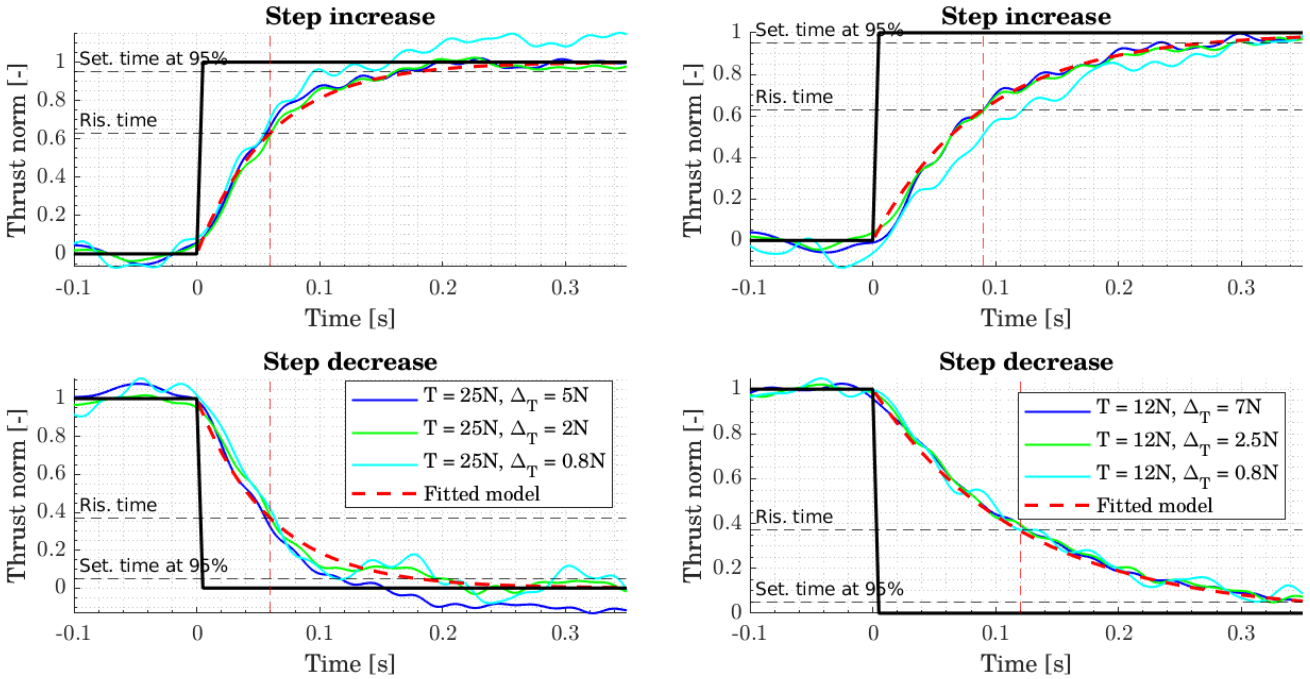

Figure 76: Unit-step response (dimensionless) at 25N (left) and 12N (right) for different step amplitudes. Schub Hxpd actuator. Upper graph for step increase and lower graph for step decrease.

The amplitude of the steps has no effect on the rising and settling times, and the responses superimpose very well with the 1st-order fitted model. The response for a 0.8N step amplitude slightly differs due to a relatively smaller SNR. The characteristic time varies with the operating points as expected. The higher the operating point, the faster the turbine rotates (smaller characteristic time). At 12N, the step decrease is slower than the step increase, but at 25N, values of rising and falling times are very close. For the *Schub Hxpd* actuator, the identified pure delay T_{delay} from the step responses is close to 0ms. This analysis is confirmed by the rising and falling step responses at different operating points of the *Schub. SW SPAR batt.* actuator. They are depicted in Figure 77.

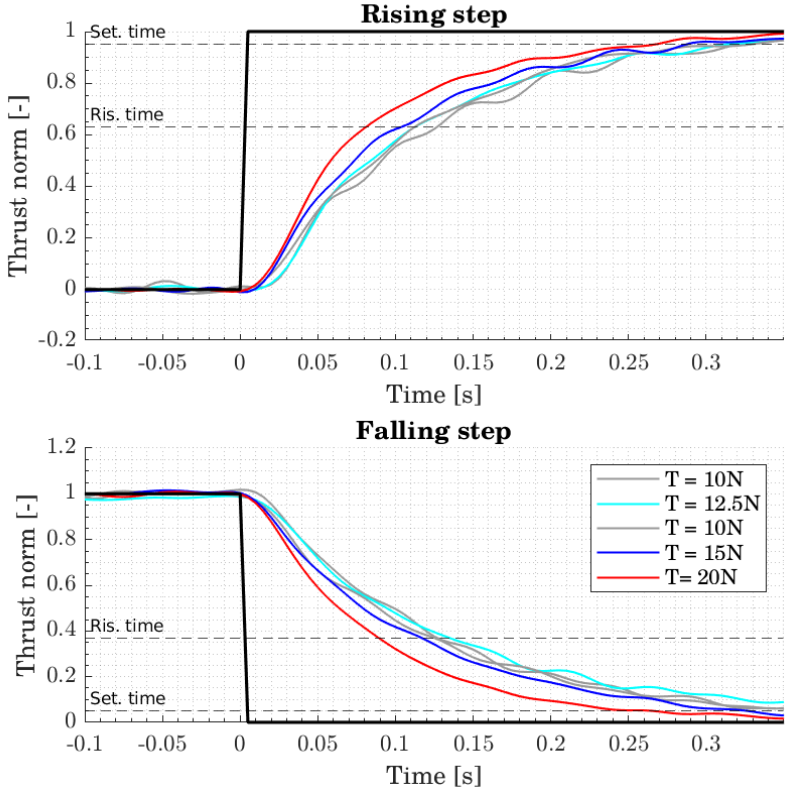

Figure 77: Rising and falling step responses at different operating points for the Schub. SW SPAR Batt. actuator

τ_+ and τ_- are the evaluated time characteristics for respectively rising and falling steps. They are summarized in Table 30. T_{delay} has been visually estimated at 10ms from these steps responses, both for rising and falling steps.

T_0[N]	7.5	10	12.5	15	20
τ_+ $[ms]$	135	115	110	100	80
τ_- $[ms]$	170	130	130	115	90

Table 30: rising and falling time characteristics for different operating points with Schub SW SPAR actuator (model scale data)

Finally, the rising times τ and pure delay T_{delay} are consistent with the bandwidths from the white noise and sine identification.

c. Comparison between different methodologies

A summary of the time characteristic of the equivalent low pass filter depending on the working point is presented in Figure 78. Error bars indicate variability in the identification performed and different behaviors between increase and decrease setpoint.

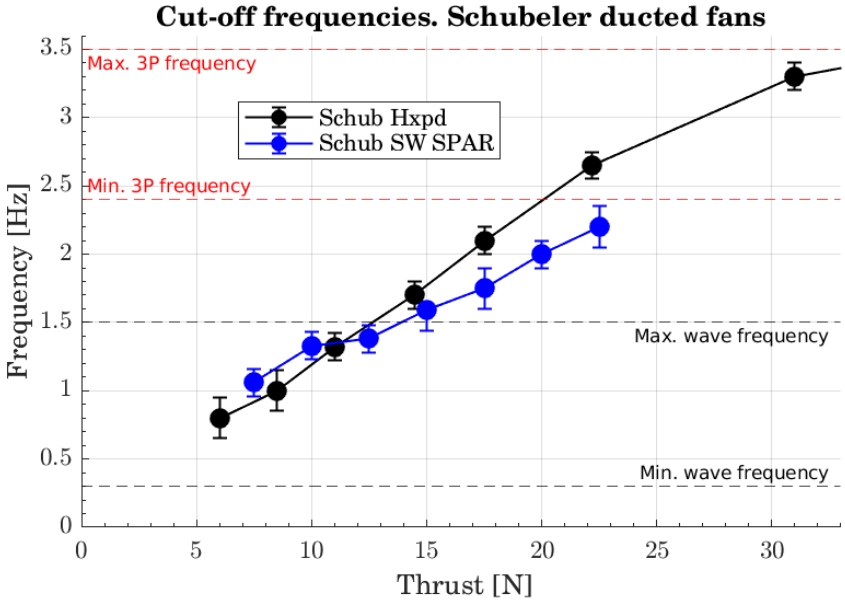

Figure 78: Cut-off frequency as a function of the working point

Depending on the working point, the open loop dynamics of the actuator are either below the threshold for 3P rotor frequency component or below the threshold for wave frequency component. Due to the quadratic dependency of the turbine thrust on the turbine rotating velocity, the higher the operating point, the faster the system. The region we are working in is well below the maximum thrust capacity of 100 N of this ducted fan, which means that a smaller diameter would suit better (same thrust for higher RPM). However, the system must run for 20 minutes long tests so thermal constraints have to be considered.

To conclude, the identification of the actuation system between the input throttle to the motor [%] and the produced thrust agrees well between white noise and sine frequency domain identification, as well as response to steps. A difference between rising steps and falling steps was present but the overall approximation of a 1st order low pass filter is still relevant. The difference between rising and falling steps is due to the incapacity with the current set-up to brake the motor. The braking in dedicated resistances or in the power supply may be investigated for the next steps of the system development.

6.2.3 Using the dynamic compensation procedure

The dynamic compensation is applied to different kinds of tests to identify the resulting transfer function of the actuator. The methodologies have been compared for different input signals. In this subsection, the comparison is performed on the same time history of target thrust, computed with fully coupled numerical simulations. Additionally, considerations about the corrective transfer function (low pass filter) are presented. Then, in part 6.2.4, the dynamic calibration is evaluated on realistic setpoints for the SOFTWIND SPAR campaign.

Concerning practical aspects, note that in order to limit over correction for rising setpoint when using the dynamic compensation, the cut-off frequencies input of the dynamic compensation model is the upper value for each operating point of the curves depicted in Figure 78. Then, a linear interpolation is performed between each working point.

6.2.3.1 Identification of the actuator model with compensation

This time history target thrust is obtained from fully coupled numerical simulations of the following FWT and load case parameters:

Floating wind turbine: OC3 –Hywind SPAR 5MW with its active controller described in (Jonkman, 2010). Blades and tower are rigid.

Wave conditions: JONSWAP spectrum with parameters $H_s = 8.6m; T_p = 13s; \gamma = 1;$

Wind conditions: Mean wind speed $U_w = 18\, m.s^{-1}$, Kaimal wind spectrum with $T_I = 18\%;$ a vertical shear with $\alpha_{shear} = 0.14$;

Time history comparison is presented in Figure 79 and frequency domain comparison is presented in Figure 80. The reference target thrust is represented in black, the blue curve corresponds to the measured thrust using the static calibration only and the red curve represents the measured thrust using the inverse dynamics procedure. Upper plot is the PSD, middle plot the gains on two frequency bandwidths of interest of the computed transfer functions and lower plot represents the phase of the computed transfer functions.

Note that low-pass filtering (below 25Hz) of the measured thrust has been done *a posteriori* using discrete Fourier transform (no delay introduced). The obtained thrust is significantly better in the case where the dynamic compensation procedure is used. When looking at the transfer function characteristics, the cut-off frequency has been switched from 1.5Hz to above 8Hz. When looking at the phase spectra, the dynamic compensation procedure significantly reduces the phase lag of the low pass filter. Those results are highly encouraging, and the need for feedback closed-loop control to increase the bandwidth does not seem necessary. Note that disturbance rejection has not been investigated so far.

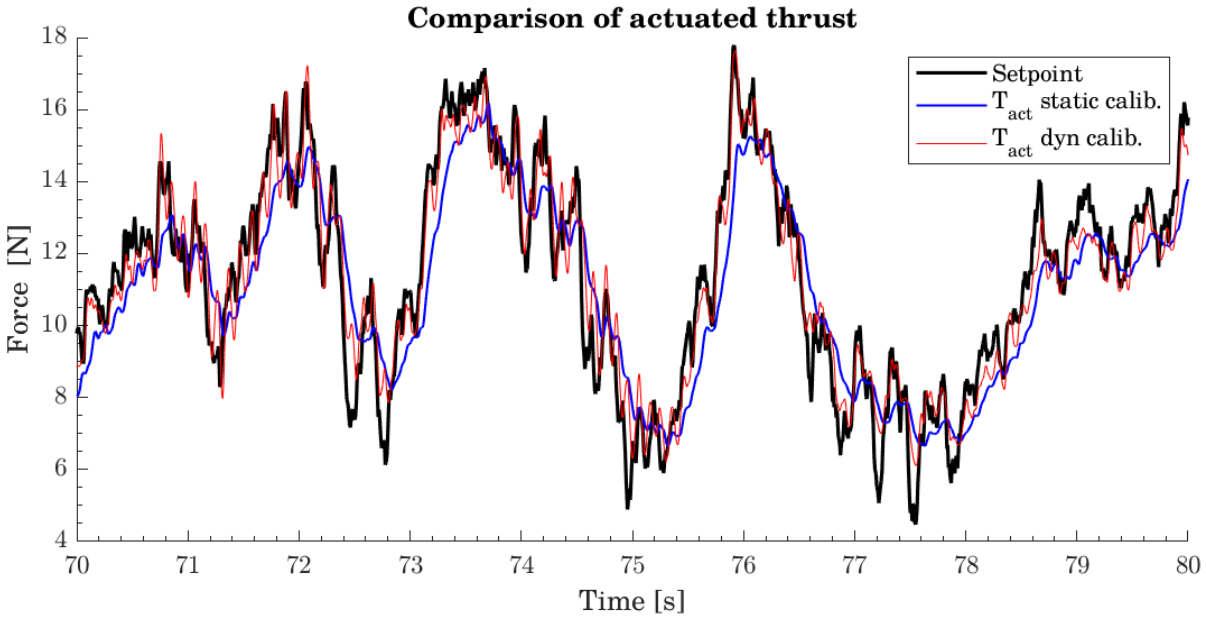

Figure 79: Time series of actuator thrust using the static calibration only (blue) and the dynamic calibration (red). The target force is represented in black.

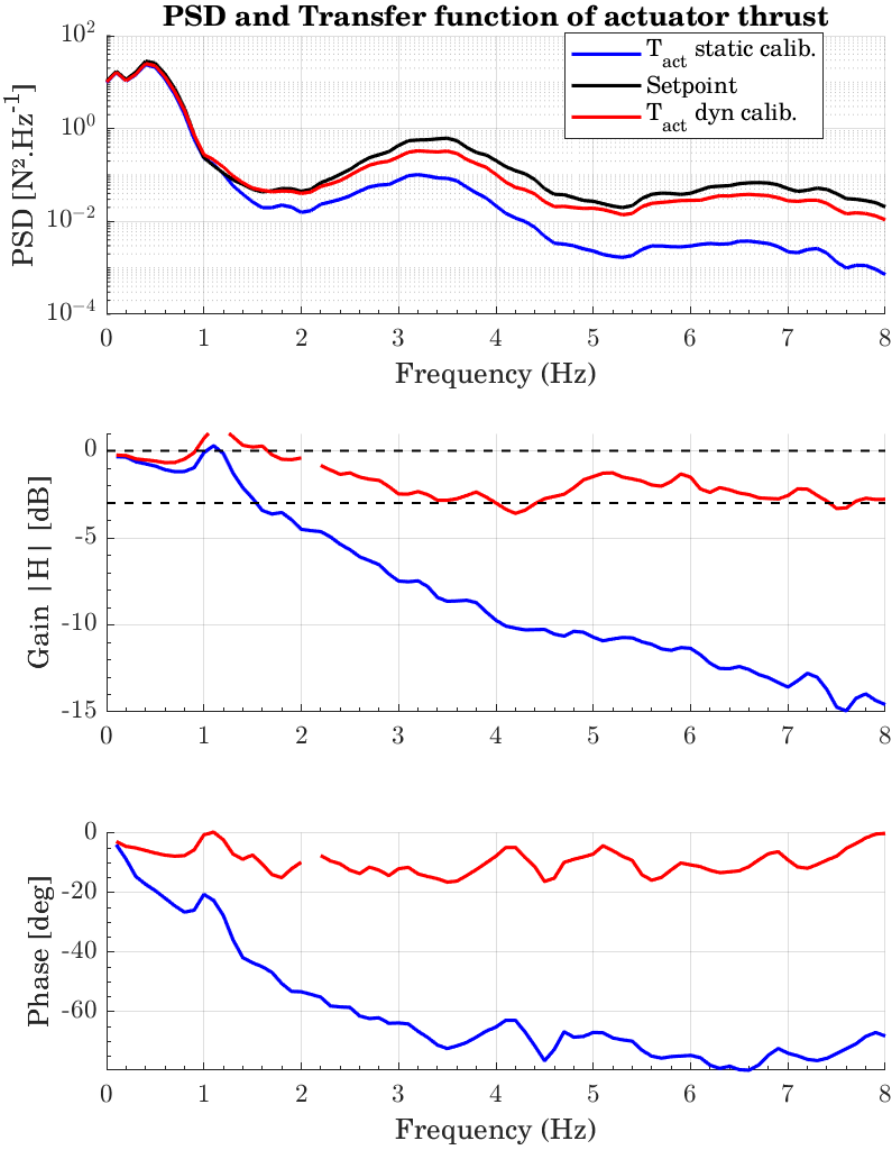

Figure 80: Frequency domain analysis of the actuated thrust. Comparison between static calibration only and dynamic calibration.

6.2.3.2 Adjusting the corrective transfer function

When used in coupled system, the corrective transfer function $H_m(s)$ needs to be carefully designed.

In the SOFTWIND SPAR setup, the 2nd tower mode, which is improperly scaled, has a natural frequency at 29 Hz. The motion observer based on Kalman filter amplifies this component for the hub x-velocity. When summed-up to the bugs in the numerical tool (presented in chapter 7) , this made the resulting OpenFAST F_x force with a non-negligible component at 29Hz. Using a dynamic compensation without corrective low-pass filter made this 29Hz component dominating the input PWM [%] to the actuator. To solve this, the cut-off frequency of the corrective low pass filter was set to ~20Hz, or equivalently $\tau_m = 10ms$. For the frequencies of interest (much smaller), this 1st order low-pass filter induces a phase delay T_m of approximately $T_m \sim \tau_m \sim 10ms$.

6.2.4 Global actuator performances for the SOFTWIND SPAR setup

The performance evaluation, has been applied to the different tests of the SOFTWIND SPAR setup. The main concern compared to the forced motions and test bench identifications are:

- Validity of the fitted model (transfer function) for realistic setpoints,
- Influence of the floating setup disturbances,
- Error level evaluations.

The influence of the actuators control methodology on the FWT behavior is described in chapter 7. In this part, the transfer functions and the error levels are compared to the identification tests results. The load cases considered are listed in Table 31, with the full scale environmental parameters and the model scale mean reference thrust for the actuator. The tests are 10 min long at model scale (~1h full scale). The command of the actuator is either done using the *static calibration* or using the *dynamic calibration*, i.e. without or with the dynamic compensation, respectively. Note that the differences of mean thrust for the 13.9 m/s cases are due to the different turbulence intensity levels.

	Full scale				**Model scale**
LC appellation	$U_w\ [m/s]$	TI [%]	$H_s\ [m]$	$T_p\ [s]$	Mean thrust [N]
Uw 18 LC1	17.9	12.0	4.3	10.0	10
Uw 18 LC2	18.0	17.4	5.8	10.9	10
Uw 14 LC1	13.9	9.0	3.0	12.0	15
Uw 14 LC2	13.9	14.0	3.0	12.0	14
Uw 14 LC3	13.9	14.0	10.5	15	14
Uw 11 LC1	11.4	15.0	2.2	11.0	19
Uw 11 LC2	11.4	15.0	7.7	12.4	19

Table 31: List of load cases for the transfer function evaluation

Firstly, the transfer functions are compared for the same mean wind velocities but different turbulence intensities and wave conditions. The transfer functions are then compared to the identified transfer function for the same mean thrust.

In Figure 81, the transfer functions of the $U_w = [11.4, 14, 18] m.s^{-1}$ load cases are represented, both for the *static calibration* and *dynamic calibration* control strategies. The identified actuator model at the three operating points is represented with a dashed black line. Different observations are made from this figure:

- The fidelity of the identified cut-off frequency from steps, white noise and sine setpoints versus cut-off frequency for realistic setpoints,
- The improvements brought by the dynamic compensation;
- Performances of the dynamic calibration results and ability to estimate a transfer function for realistic setpoints.

These three aspects are reviewed hereafter.

Fidelity of the identified cut-off frequency

The *static calibration* results (continuous lines) and the identified actuator model superimpose very well for all the load cases, whatever the turbulence intensities and the wave conditions. Overall, the frequency domain results of the actuator for the different load cases behave as 1st order low-pass filters with marginally smaller cut-off frequencies. The coherence is very high for the low frequency region up to the wave frequencies (range [0 - 1]Hz), then falls down between 1.5 and 2.3 Hz, and then is high again for both the 3P/tower mode region [2.4 – 3.5]Hz and the 6P region [5 - 7]Hz. Basically, the

coherence is high when the excitation is high. This makes the linear system estimation trust worthy on these frequency ranges. The discrepancy at the tower natural frequency (2.4Hz) on the gain and phase plots, could be explained by:

- Limited force observer performances, even with the corrections presented in chapter 5. Indeed, the amplitude of actuator thrust at this frequency is well below the amplitude of inertial forces at this frequency. This explanation is reinforced by the relatively smaller coherence just before the 2.4Hz frequency. Large increase in the phase is also consistent with this explanation as the inertial forces are shifted by approximately $\frac{\pi}{2}$ with the aerodynamic force (proportional to the velocity).
- The change in operating point within the test due to the turbulent wind. This makes the actuator performance sometimes higher and sometimes smaller for this frequency than the mean performances within the test. Indeed, for a moving average high setpoint thrust, the actuator has a smaller cut-off frequency than for a relatively lower moving average setpoint thrust.
- The disturbances of the actuator inflow, due to the tower deflection velocities. This effect is important to quantify as large deviations to the no-motions behavior of the actuator makes feedback control required. Decay tests analyses with or without the turbine activated have been used to estimate this modification of the produced thrust (see chapter 5); it has been shown the small relative contribution of these disturbances. Moreover, these disturbances are proportional to the input velocity; consequently, they should be in phase with the actuator force, and should increase the resulting force instead of phase shifting the signals.

Identification of dynamic calibration performances

The *dynamic calibration* results (dotted lines) have smaller coherence values than the *static calibration* results on the frequency bandwidth of interest, i.e. with significant energy in the setpoint. This coherence is smaller for the *Uw18* cases (Figure 81 a) top) than for the *Uw11* cases (Figure 81 c) top). For a given operating point, this coherence is smaller when the fluctuations increase (e.g. Uw18 LC2 versus Uw18 LC1 in Figure 81 a) top). This is explained by the amplitude of the dynamic compensation corrections, which are bigger as the fluctuations increase and as the dynamics of the actuator is smaller. This is explained by the nonlinear mechanisms (saturations of thrust derivatives, due to maximal current and freewheel effects) being relatively more important when the "linear dynamics" of the actuator is counterbalanced.

Static versus dynamic calibration results

The *dynamic calibration* results are significantly better than the *static calibration* results. The gain is close to 1 whatever the frequency and the phase is below the 45deg threshold up to 5Hz, making the actuator contribution to the total delay acceptable. At the tower natural frequency, the phase lag is approximately constant at 30deg for the dynamic calibration results and between 60 and 80deg for the static calibration results. The actuator transfer function is approximately the same whatever the operating point when using the dynamic calibration.

a)

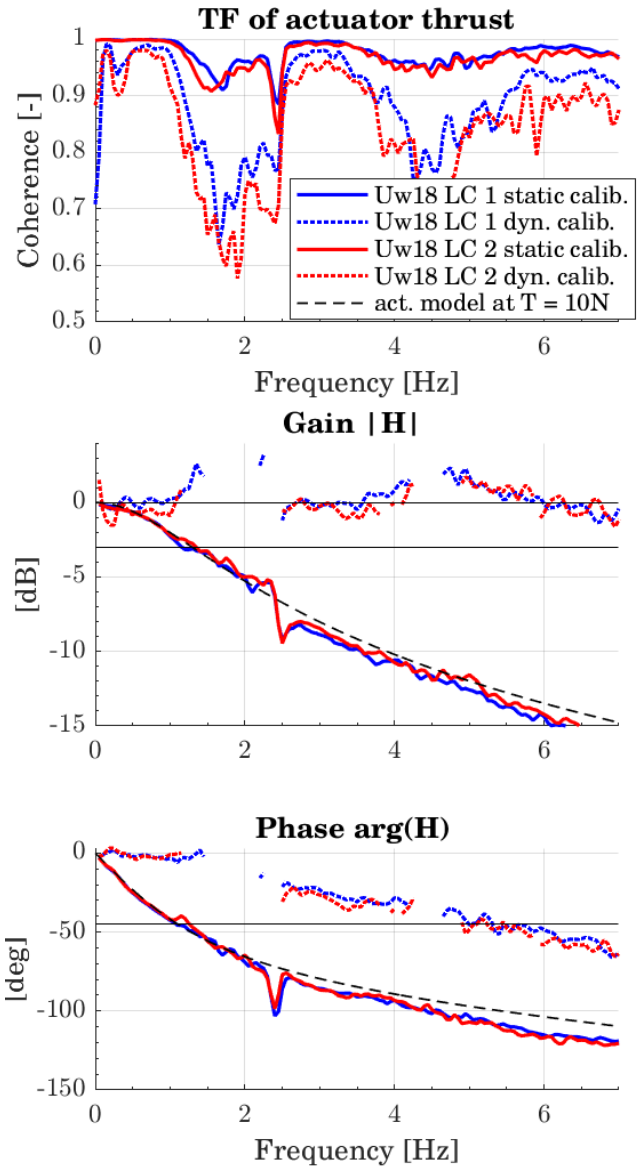
TF of actuator thrust
Coherence [-]
Uw18 LC 1 static calib.
Uw18 LC 1 dyn. calib.
Uw18 LC 2 static calib.
Uw18 LC 2 dyn. calib.
act. model at T = 10N
Gain |H|
[dB]
Phase arg(H)
[deg]
Frequency [Hz]

b)

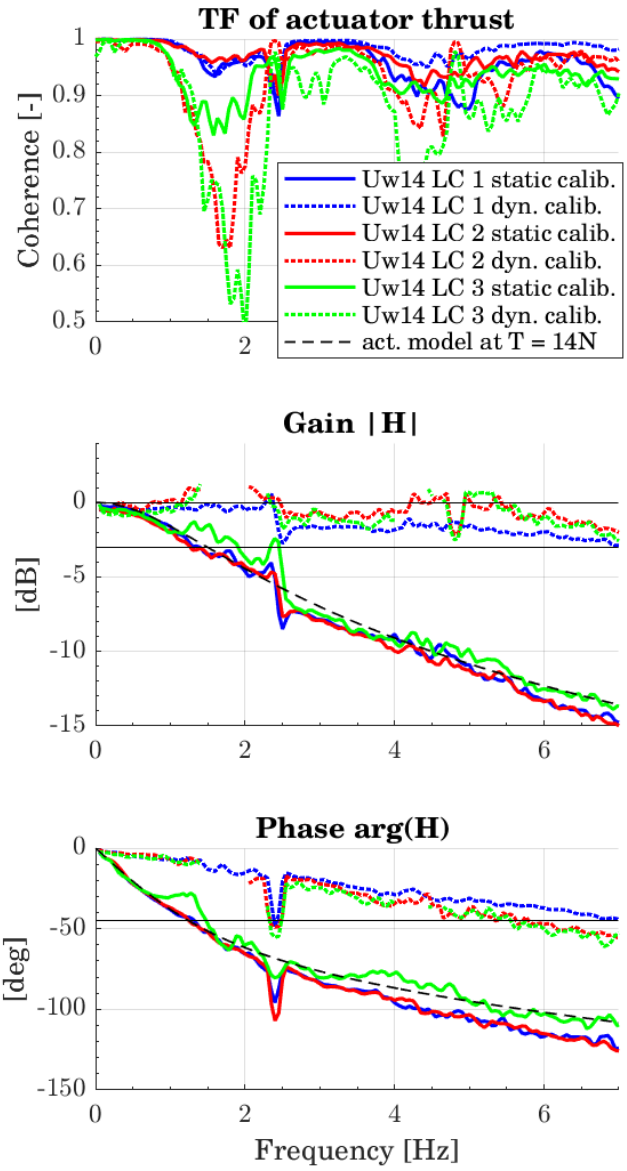
TF of actuator thrust
Coherence [-]
Uw14 LC 1 static calib.
Uw14 LC 1 dyn. calib.
Uw14 LC 2 static calib.
Uw14 LC 2 dyn. calib.
Uw14 LC 3 static calib.
Uw14 LC 3 dyn. calib.
act. model at T = 14N
Gain |H|
[dB]
Phase arg(H)
[deg]
Frequency [Hz]

c)

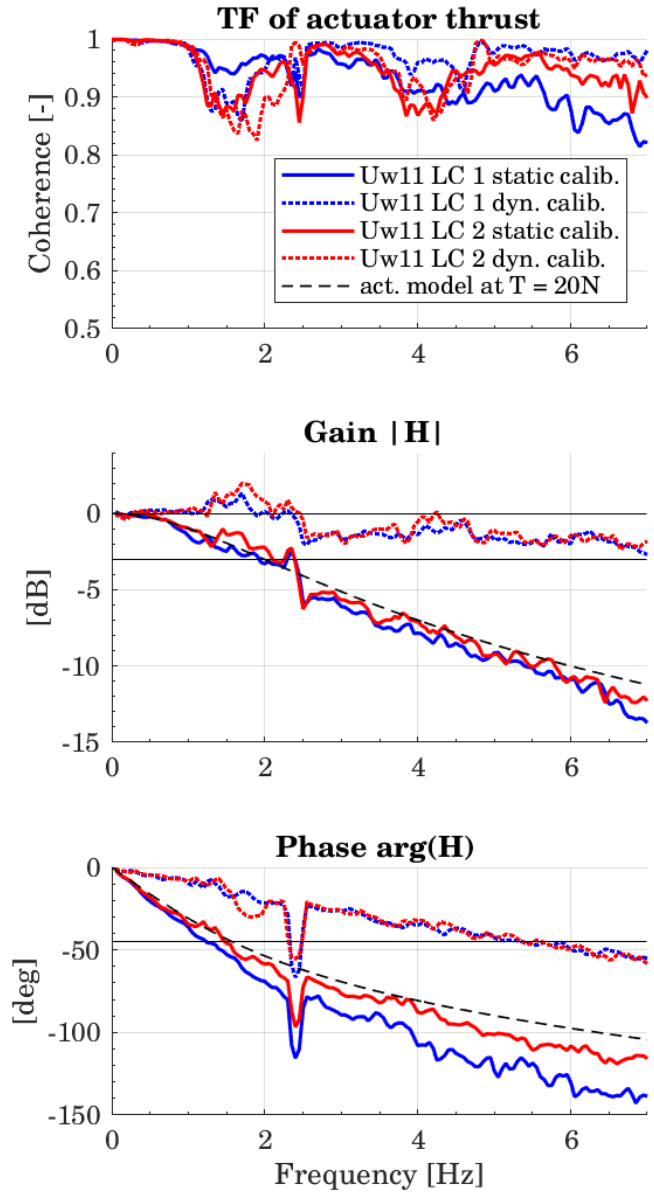

Figure 81: Actuator thrust transfer functions for different load cases. a) $U_w = 18\,m/s$ *load cases; b)* $U_w = 14\,m/s$ *and c)* $U_w = 11.4\,m/s$ *load cases.*

Overall, the frequency-domain characterization methodology developed for the actuator performances is also relevant when looking at realistic setpoints.

Now, the error levels between the reference and the actuated force are addressed. Different options could be followed for computing the error levels:

- Define a global error level indicator indicating the overall match between the reference and the actuated force for a single load case. Basically, this error level can be computed by the standard deviation of the difference between the two forces. This global error level reflects a kind of mean error level, but does highlight the variations of the instantaneous error during the test;
- Define an instantaneous error level between the two forces and compute statistics on this error level (mean, maximum, standard deviation, …). Investigations have been conducted to

compute envelopes of the two forces per frequency bandwidth but have been considered out of scope for the present work.

For a given test, the error level ϵ [%] is then computed using Eq. (6.8)

$$\epsilon = \frac{norm(F_{ref} - F_{act})}{norm(F_{ref})} \tag{6.8}$$

With:

- F_{ref} and F_{act} the reference and actuated forces, respectively
- $norm$ the selected norm.

The selected norm is a L2 norm, $norm(x) = \frac{1}{N}\left(\sum_{i=1}^{N} x_i^2\right)$, with N the number of samples. This error level reflects both the attenuation and the phase delay. The choice to make it dimensionless has been done to take into account the fluctuations of the reference force. Note that both the reference and the actuated forces are low-pass filtered at 9Hz to get only the global frequency bandwidth of interest.

The error levels for the different load cases and actuator calibration strategies are listed in Table 32. The error levels are in the range [3-15]%. The dynamic calibration leads to smaller error levels when the fluctuations are not too important (LC 1 for each operating point compared to LC 2 and 3). As expected, the lower the operating point ($U_w18 < U_w14 < U_w11$), the higher the error levels.

Load case	ϵ [%] static calibration	ϵ [%] dynamic calibration
Uw11 LC1	5.5	3.3
Uw11 LC2	5.8	5.3
Uw14 LC1	5.4	3.6
Uw14 LC2	6.8	6.8
Uw14 LC3	11.2	9.2
Uw18 LC1	14.0	9.4
Uw18 LC2	15.5	12.7

Table 32: Error levels for the different load cases and for the static calibration and dynamic calibration c actuator control cases

To conclude, the performances of the single actuator in the SOFTWIND SPAR setup has been investigated. The frequency domain indicators defined for the identification of the actuator model have been successfully checked for a realistic setpoint. A mismatch at the tower natural frequency concerning the transfer function is probably related to the force observer performances. Global error levels have been computed to complete the performance analysis. Overall, the *dynamic calibration* control strategy of the actuator significantly improves the performances for the highest frequency bandwidths.

6.3 Application: Actuator #2, 2-bladed aircraft propellers

The same methodology is applied to different two-bladed aircraft propellers. These actuators have been used in:

- the Blue Growth Farm project (Floating setup #1), with one KDE-Direct solution,
- the fixed test bench #1, multi-propellers setup, with three KDE-Direct actuators.

6.3.1 Quasi-static identification

The different static relations between the input duty ratio [%] and the actuator thrust and torque are represented in Figure 82. For these two-bladed actuators the fit to a 2nd-order polynomial is less appropriate and tabulated values are used. The torque characteristics should be similar between the

actuator 1 and 2. However, due to a non-perfect alignment of the different actuators along the x-direction (Hub frame) (uncertainty of $\pm 0.5\,\mathrm{deg}$), the measured torques include a part of the $F_{act\,y}$ components and do not correspond exactly to the actuator torques. The actuator number 3, KDE-Direct 4215, generates smaller torque for the same thrust.

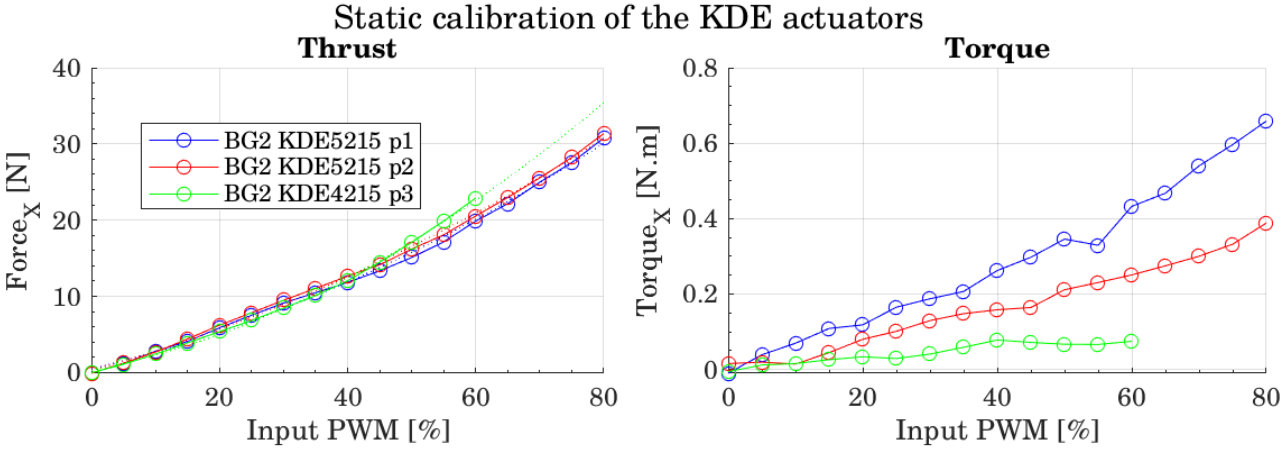

Figure 82: Static calibration of the KDE-Direct actuators

6.3.2 Dynamic identification

The dynamic identification methodology is applied to the different 2-bladed actuators, with step responses, white noise and sine signals. The same indicators are used to define the appropriated actuator models. Note that for the multi-propellers setup, the corrective low pass filter transfer function is defined with $f_c = 5Hz$. The cut-off frequency has been selected relatively low to avoid any amplifications of the frame beams at their natural frequencies (8Hz as shown in chapter 5). To avoid any redundancy with the section 6.2, the focus is on the suitability of dynamic compensation and the definition of the overall actuator model.

6.3.2.1 Step responses

The step responses with and without compensation are addressed. In Figure 83, for a mean thrust of 7N, the responses to rising and falling steps are depicted for the KDE5215 actuator. Note that due to the low SNR, approximately 20 step responses are superimposed and averaged to get the response per operating point. The dynamic compensation improves significantly the rising time, but also the falling time. In both cases, the rising and falling times are similar and even if the regenerative braking is deactivated, the motor is able to efficiently slow down. A pure delay has been identified T_{delay}~$20ms$, but is not completely consistent between the tests. The DAQ system is suspected to have a relatively poor quality for a proper evaluation of this delay.

a) b)

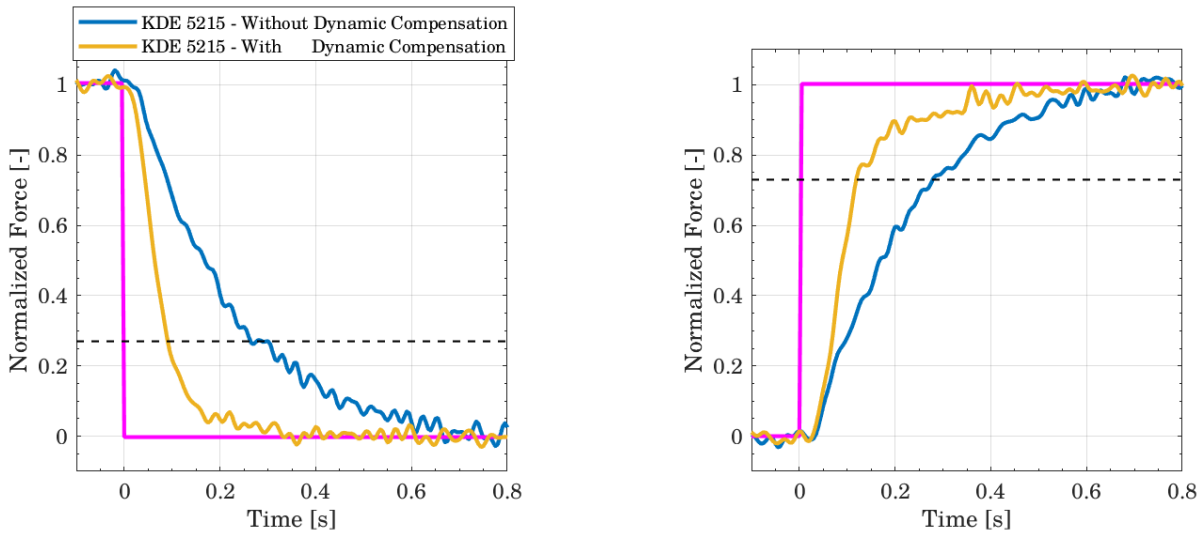

Figure 83: Rising and falling step responses for the KDE-Direct 5215 actuator; mean thrust of 7N. a) falling steps and b) rising steps.

6.3.2.2 White noise and sine response

The white noise and sine responses of the actuator are depicted in Figure 84. Note that due to the low SNR of the force transducer, the white noise identification signals are done for narrow bandwidths (1Hz each) and then assembled. On this Bode diagram, the sine and white noise identified transfer functions superimpose well, with minor discrepancies for the dynamic compensation identification, still due to the low SNR of the force transducer. For the dynamic compensation results, as expected, the identified transfer function superimposes with a low pass filter similar the corrective transfer function ($f_c = 5Hz$) combined to a pure delay of 20ms.

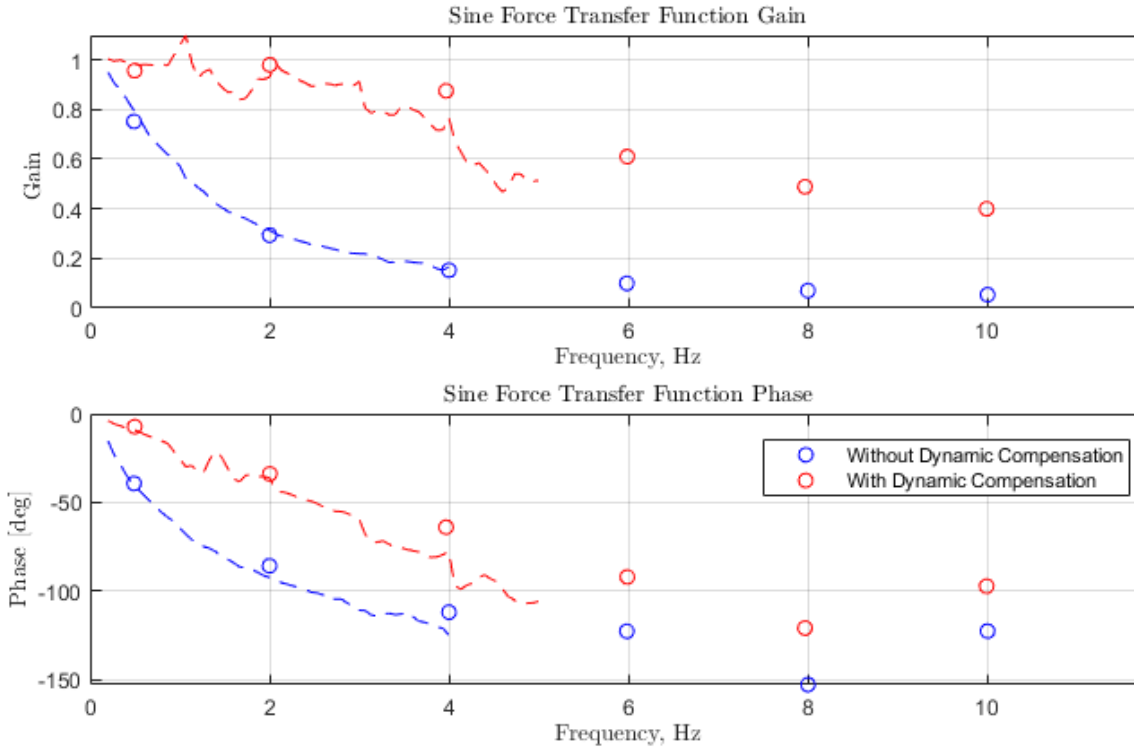

Figure 84: Transfer function computed from white noise and sine. KDE-Direct 5215; mean thrust of 7N.

6.3.2.3 Overall actuator model

The overall results are recalled hereafter. The estimated cut-off frequencies are depicted in Figure 85. For the considered working points, all the cut-off frequencies are below the minimal target 3P rotor frequency of the wind turbine. The different actuators have similar cut-off frequencies for the same mean thrust. The two-bladed propellers exhibit a higher dependency on the working point, with very low cut-off frequencies for low mean thrust and relatively higher cut-off frequencies than the Schübeler ducted fan for higher mean thrust. Note that it was not possible to properly evaluate the actuators model below 5N, due to both the low saturations of the actuators (near 0N, the behavior is erratic) and the poor SNR of the force transducer.

Compared to the analytical model presented in chapter 4 for the actuator performances, the important observations are:

- Low saturations are less important, the motors being able to slow down efficiently. Investigations on this aspect, important for multi-actuators frame design, need to be pursued.
- The cut-off frequency depends on the working point.

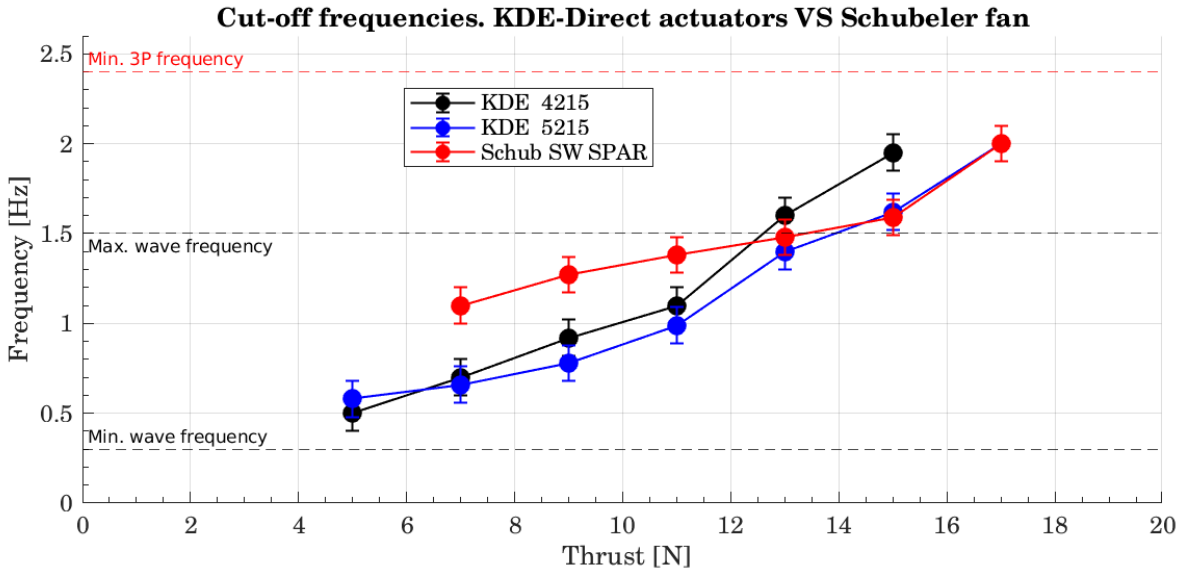

Figure 85: Cut-off frequency as a function of the working point. The two KDE-Direct actuators and the Schubeler ducted fan

6.4 Application: Multi-actuator configuration

The identifications performed for a single actuator have been extended to a multi-actuators setup, i.e. when the different actuators are running at the same time. The quantities and phenomena to look at are:

- The loss in static thrust when the actuators are running at the same time compared to the sum of the individual thrusts, as observed by (Meseguer and Guanche, 2019);
- The transfer functions on the different rotor loads components;
- Application to realistic setpoints for F_x, M_y and M_z.

Not that the actuator thrusts could be computed with the single 6-component force transducer because the actuation system is fully actuated with an invertible Jacobian. Otherwise, if the system is over-actuated, there is an infinite number of possible thrusts to get the measured rotor loads.

6.4.1 Identification

Concerning the static performances, the thrust of the three actuators running at the same time superimpose very well (within +-1%) to the sum of individual thrusts. This is due to the selected large dimensions of the setup, with beam lengths of 0.7m compared to actuator diameter of 0.4m, making the spacing between each actuator center approximately 3 times the actuator diameter.

A MIMO (Multiple Inputs, Multiple Outputs) system is be defined, between the three setpoint rotor loads (inputs) and the three actuated rotor loads (outputs). Around an operating point of 10N for each actuator, white noise F_x, M_y and M_z rotor load components are created. Then, the force allocation is used to define the thrust setpoint for each actuator. In post processing, nine TFs are identified, between the inputs setpoint rotor loads and the output actuated rotor loads. All the off-diagonals components (e.g. TF between $F_{set\,x}$ and $M_{act\,y}$) are negligible because the system is decoupled by construction. The three diagonals TF are represented in Figure 86 both with the dynamic compensation and without the dynamic compensation activated. If the system is strictly linear, similar TFs as the actuator thrust TF are expected. Note that the M_z transfer function couldn't be identified above 4Hz due to too low coherence. The dynamic compensation TFs and static calibration TF are similar to the actuator thrust TF presented in part 6.3.2. The dynamic compensation TFs are still made of the 1st order low pass filter with cut-off frequency of 5Hz and a pure delay of 20ms. The M_y transfer function is slightly above the F_x transfer function, and this could be due to the saturations mechanisms, not impacting the reproduction of the torque M_y.

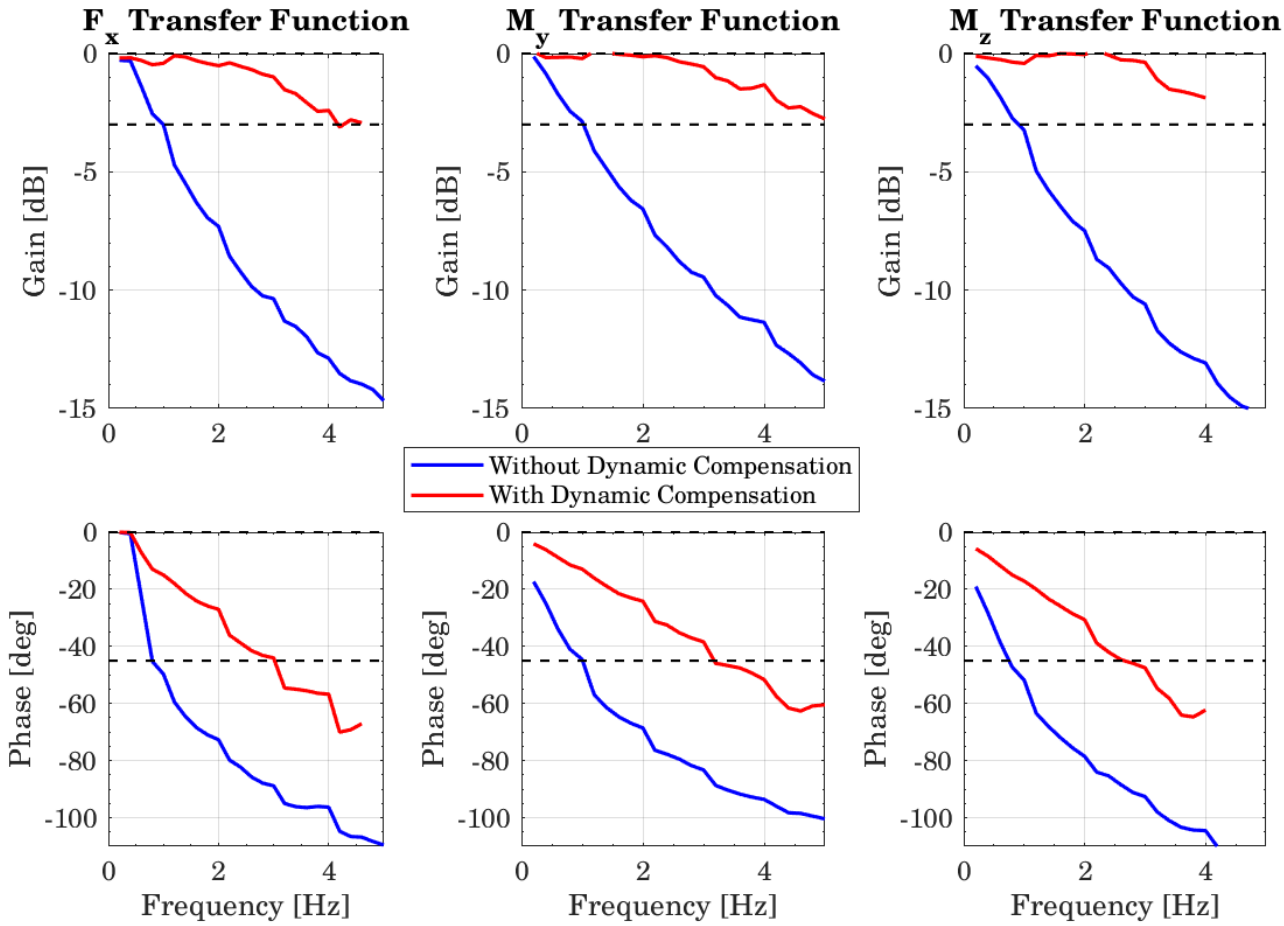

Figure 86: Fx, My, Mz transfer function identifications for a mean thrust of 10N per actuator.

6.4.2 Performances for realistic setpoints

Different time series of the F_x, M_y *and* M_z rotor loads based on the SOFTWIND SPAR test campaign have been taken as setpoints. The load cases are listed in Table 33.

LC appellation	U_w $[m/s]$	TI [%]	H_s $[m]$	T_p $[s]$	MS mean thrust [N]
LC1	11.4	13.8	2.2	11.0	19
LC2	13.9	9.0	3.0	12.0	15

Table 33: Wind and waves conditions for load cases tested for the multi propellers realistic setpoint evaluation

For the two load cases, the mean thrust being 15N (respectively 19N) while the mean M_y and M_z components are close to 0, this makes the average thrust per actuator of approximately 5N (respectively 6.3N). As it has been shown in section 6.3.2, the dynamics of the actuator for this low operating point might be problematic. Additionally, in chapter 4 it has been shown that over-actuated layouts might be better suited by imposing higher mean thrust for each actuator without changing the total F_x force. To mimic such a better suited layout, the same load cases are tested with an increase of 5N for each actuator thrust setpoint. The selection of the additional mean thrust should be based on an over-actuated layout design and on each actuator thrust range. The value of 5N used in this work is arbitrary and based on actuator performances (especially Figure 85).

The temporal evolutions of the actuator thrusts and resulting rotor loads are depicted for LC2 in Figure 87. The actuated loads have been low pass filtered at 20Hz (0-phase filtering) to remove the

frame natural frequencies. At t=98s of this load case, the reference for the actuators 2 and 3 is close to be 0N, at which the actuator has a slow behavior. It is worth mentioning, as in chapter 4, that the 3P rotor frequency component is relatively more important for the M_y and M_z components than for the F_x component. This makes the actuator thrust setpoint (Figure 87 at the right) with an important energy content at the 3P rotor frequency. Concerning the static calibration results, the low pass filtering effect of the static calibration results is clearly visible. The actuators reproduce the WF fluctuations (~ 1.9s i.e. model-scale peak period) without too much attenuation but already with a certain delay. The 3P components are highly attenuated for the baseline LC2 and slightly less for the LC2 + 5N static calibration results, which is consistent with the F_x, M_y, M_z transfer functions obtained in part 6.3.2. Concerning the dynamic calibration results, the 3P component are well captured in terms of amplitude. However, for the baseline LC2 load case, the wave frequencies seem partially amplified compared to the reference forces, especially for the F_x rotor load (Figure 87 a) top). For the LC2 and the dynamic calibration results, the match with the reference forces is much better, for F_x but also for M_y and M_z.

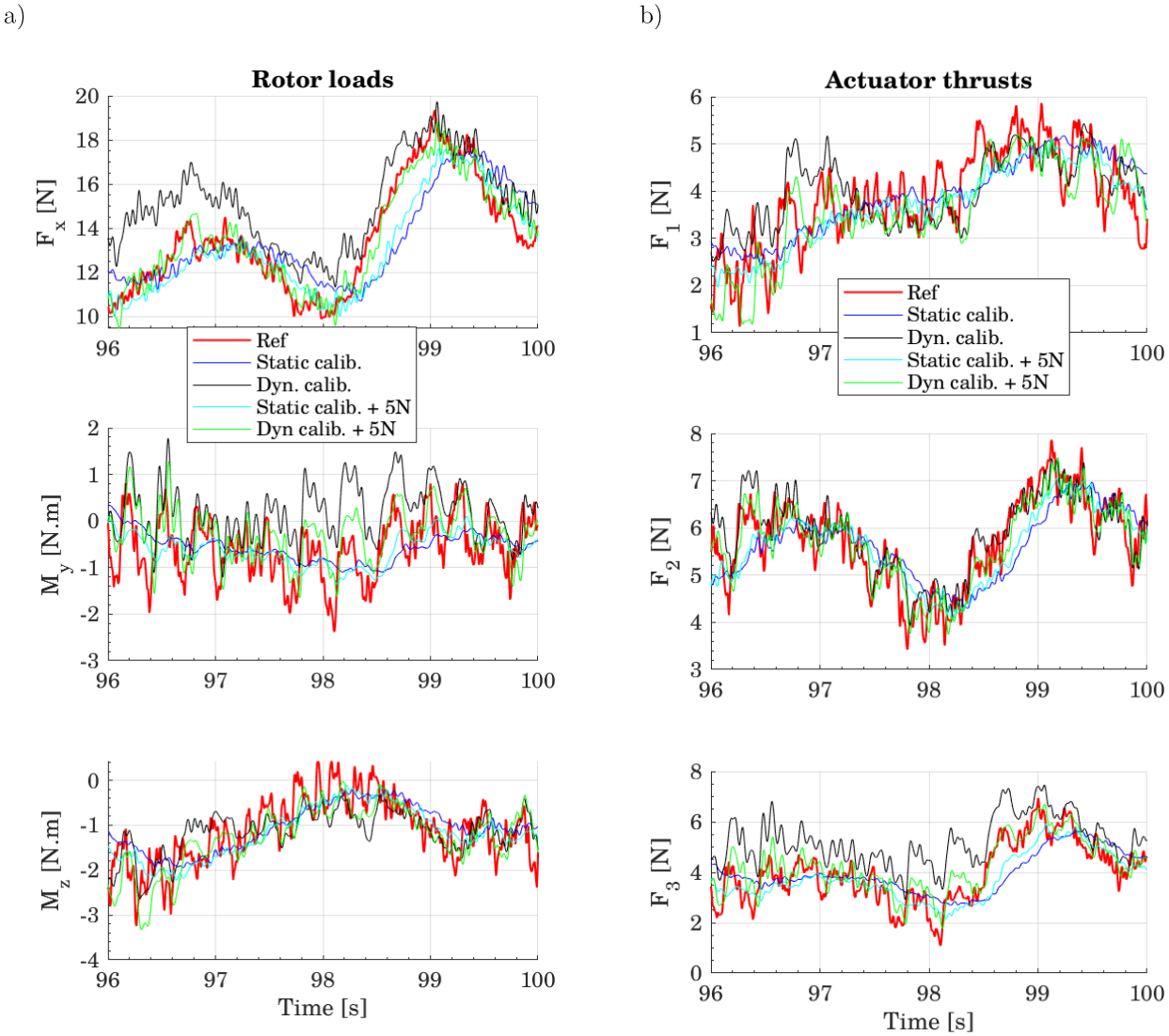

Figure 87: Rotor loads (a) and actuator thrust (b) for the LC 2. Time series

The TFs with and without dynamic compensation, with and without the 5N increase per actuator are depicted in Figure 88. The increase of 5N significantly improves the cut-off frequency of the static calibration results. Consequently, it also increases the coherence on the 3P frequency bandwidth due to the higher gain. All the results have a small coherence between 1Hz and 2.2Hz due to the small

excitation between the wave frequency zone and the 3P rotor frequency zone. Concerning the dynamic calibration results, the coherence is higher with the added force of 5N, making possible the identification of a transfer function on a larger frequency bandwidth. The results on the LF and WF bandwidths are better with the added force of 5N, with gains closer to 1 and higher coherences.

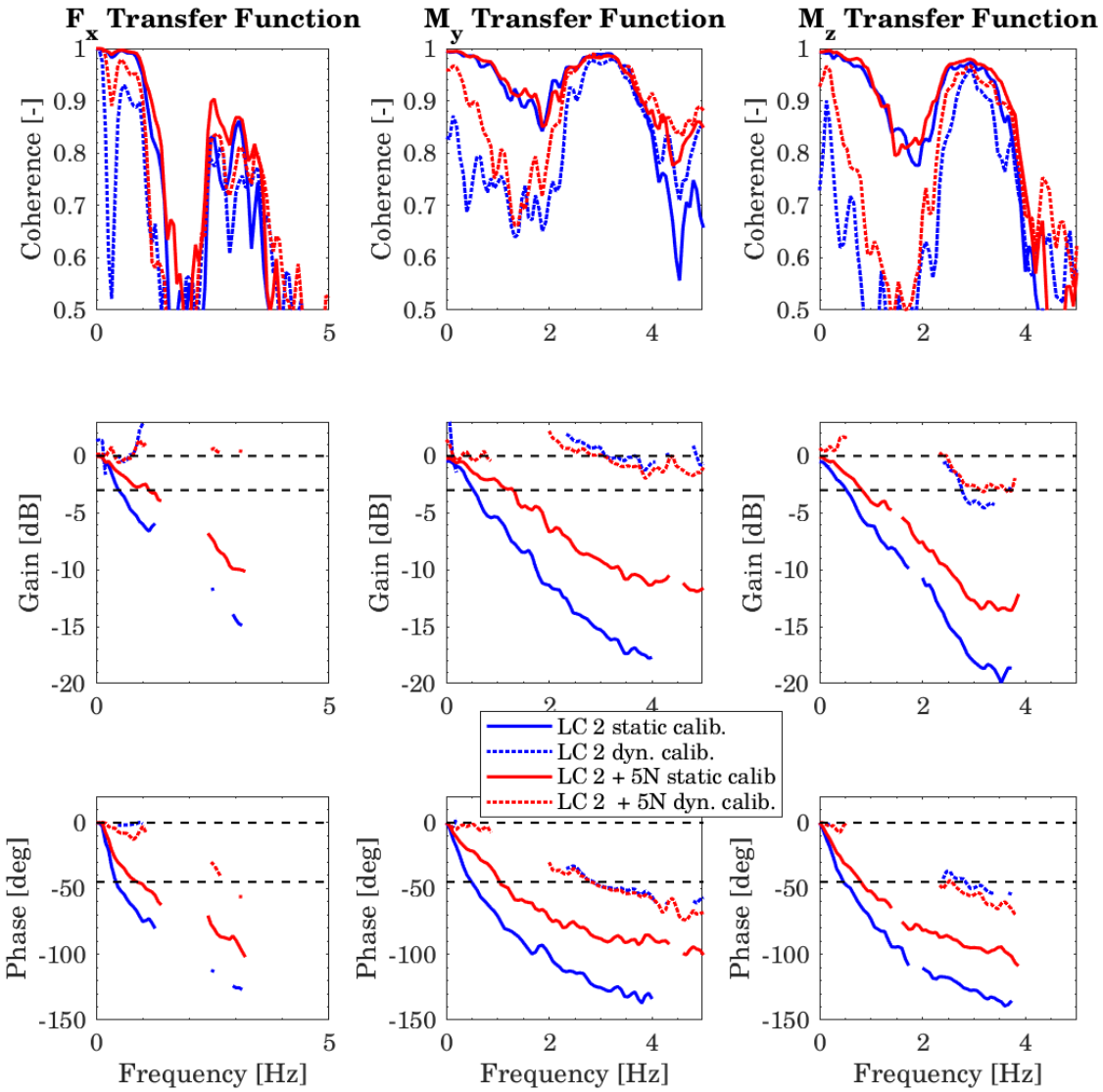

Figure 88: Transfer functions of the actuated rotor loads, LC2,with and without dynamic compensation, with and without the 5N added value

To conclude, the frequency domain identification methodology has been successfully applied to a multi-actuators setup, for the F_x, M_y and M_z rotor load components. The methodology has been applied to identification signals (white noise) but also for realistic setpoints from a wave tank test campaign. The low mean thrust of each actuator is challenging for the dynamic compensation methodology. With a small increase in the mean thrust of each actuator, the dynamic compensation methodology works better.

6.5 Conclusion

The identification of the actuator performances have been conducted by several means, using frequency domain and time domain indicators. The methodology is based on quasi-static and dynamic identifications which are then used in the feedforward control strategy. Inside the feedforward control

strategy, the development which has been done in this work, while not original in the general field of control science, has been successfully developed and applied for on-board aircraft propellers with key indicators defined by the FWT physics. The important outcomes are:

- The different frequency domain methods, based on linear system responses are consistent, also when compared to realistic setpoints.
- For the identification of single actuator performances, the methodology has been validated. The methodology has also been successfully applied and extended to a multi-actuator system.
- The force observer performances, which depend both on the SNR of the force transducer and to the inertial compensation for a moving system, are crucial to have a successful identification of the actuator performances.
- It is important to consider the variability of actuators performances with operating points. The model identification has to be conducted for several operating points. Higher the operating points, faster are the actuators.
- The dynamic compensation significantly improves the maximal frequency well captured by the actuator. It appears that the need for feedback control, to increase the frequency bandwidth and to reduce static errors due to, e.g., disturbances, do not seem important. The dynamic compensation works better when the dynamic of the actuator is not too far from the target dynamic (target cut-off frequency).

7 Sensitivity analysis to rotor loads modeling

Contents

In this chapter, the behavior of the floating wind turbine during the experimental tests is analyzed. The following studies are performed:

- Repeatability analysis,
- Coupling investigations between the hydrodynamics and the aerodynamics,
- Influence of the wind turbine thrust modeling methodology. This define the advantages and limitations of a SIL system with a single actuator;
- Influence of the actuator performances,
- Investigations of different wind turbine blade pitch and generator speed controllers on the global motions of the FWT.

In this chapter, results are presented at full scale.

7.1 Detected bugs and repeatability analysis

Before exploring differences between different tests performed in similar conditions, the repeatability of the system needs to be analyzed. Firstly, some bugs were detected after the test campaigns and consequently, have reduced the number of usable tests for the FWT global motions analysis. These bugs are described, with the reasons why they occur, to provide recommendations for next test campaigns. Secondly, the repeatability of the test is analyzed, taking into account non-corrupted tests. Aero-hydro coupling phenomena are not necessarily dominating the FWT motions. For this reason, comparing small differences for the analyses is relevant only if the repeatability is ensured. The repeatability is evaluated as the variability of the FWT response for the same test conditions.

7.1.1 Bugs

Corrupted tests and bugs in the numerical model have been detected after the SOFTWIND SPAR and Blue Growth Farm campaigns. Details are given in appendix D as it explains discrepancies observed concerning the tower deflection motions. The main conclusions are recalled hereafter.

Real-time mismatches

Two kinds of real-time mismatches have been observed due to a slight overuse of the compactRIO computational resources:

- In the main RT loop. The consequence is an increasing delay for some tests. The tests are considered non valid and have been discarded from the analyses.
- In the OpenFAST RT loop. The consequence is an offset between two similar simulations for the input wind fields.

Bugs in the numerical model

Two bugs have been involuntarily introduced in the SIL wrapper of the OpenFAST glue code. The major effect is that the force at the tower natural frequency is not correctly computed. The consequence is that tower deflections are not correctly reproduced during the tests. The analyses are not performed on these DoFs.

7.1.2 Repeatability analysis

For non-corrupted tests, the repeatability is analyzed. Several tests have been repeated, with only waves, waves and steady thrust, or waves and turbulent wind. Overall, the repeatability of the tests is satisfactory. This is illustrated for the most highly-coupled case, i.e. with waves, turbulent wind and wind turbine control. The environmental parameters are $H_s = 5.8m; T_p = 10.9s; U_w = 18m.s^{-1}; TI =$

17%. The *dynamic calibration* methodology is used for the actuator. The PSDs of the platform surge and pitch are depicted in Figure 89 for two repeated cases. They superimpose well for the three frequency bandwidths of interest: LF (~0.01Hz), R_Y NF (~0.03Hz) and WF (~0.09Hz).

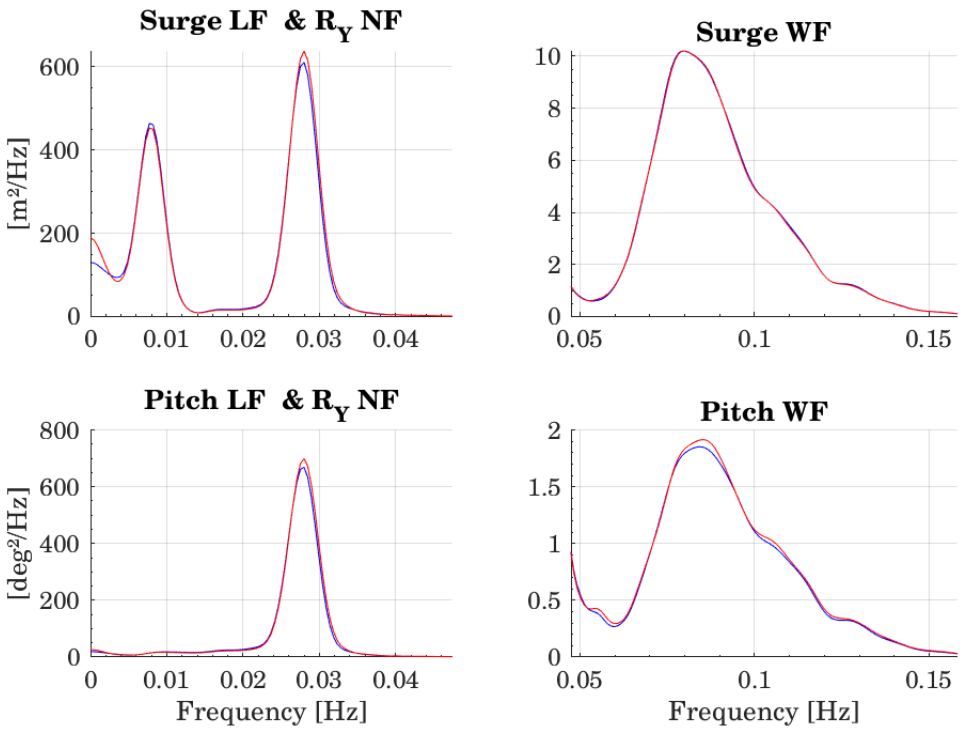

Figure 89: Repeatability for surge and pitch PSD on one load case for two cases

7.2 Aero-hydro coupling

In this part, the coupling between the rotor loads and the FWT motions is investigated. Firstly, the rotor loads characteristics for the selected wind turbine are illustrated. Then, the coupling is investigated for the two floating setups, by comparing waves-only tests, waves and steady thrust and finally waves and turbulent wind cases. Note that the dynamic calibration strategy is considered with the "reference" actuator load case.

The different aspects are analyzed in a perspective of suitable modeling strategies. The corresponding questions are:

- What are the relative contributions of the rotor loads?
- Could the rotor loads contributions superposed to the wave-induced contributions? What about interactions (coupling) between the rotor loads and the wave kinematics?

7.2.1 Blue Growth Farm

In the Blue Growth Farm setup, the coupling between rotor loads and platform motions is expected to be smaller than for a typical floating wind turbine. The key aspects for which rotor loads coupling is expected:

- The low frequency excitation might excite the surge (and possibly pitch) natural frequencies;
- The tower quantities of interest (tower base moments, tower top deflections) are expected to behave differently for waves only tests and wind and waves tests;

- Small steady trim and surge.

Due to the tower deflection problem described in section 7.1, the low frequency motions and the steady trim and surge are the only components to look at.

Different irregular waves and wind conditions have been tested. The illustrative load cases (LC) are listed in Table 34. For the wave fields, JONSWAP spectra are used with a peak shape factor $\gamma = 3.3$. For the input wind fields, Kaimal spectra are considered with an input vertical shear of $\alpha_{shear} = 0.14$.

LC nb	$H_s[m]$	$T_p[s]$	$U_w[m.s^{-1}]$	$T_I[\%]$
LC1	5	8	/	/
LC2	5	8	11.4	0
LC3	5	8	11.4	20

Table 34: Wind and waves conditions considered for the Blue Growth Farm analyses

Steady properties

The steady trim is less than 0.05° for a wind speed of $U_{hub} = 11.4\ m.s^{-1}$, which is really negligible compared to the pitch motion amplitudes. This is due to the high hydrostatic restoring stiffness for the pitch DoF. The steady surge for the same wind speed is 8.5m while in the wave-only case it is approximately 4m. Consequently, the wind-induced offset is not negligible. Note that the potential flow related wave drift force depends on the wave frequency and increases with the square of the wave height.

Low frequency motions:

The PSD of platform surge and pitch are represented in Figure 90. Not those, due to confidentiality, the PSD values have been removed.

Note that all the power spectral densities (PSDs) presented in this part have been computed:

- Using WAFO v2.5 (Brodtkorb *et al.*, 2000) and a Parzen windowing to smooth the PSD peaks;
- Per frequency bandwidth to adapt the number of time averaging segments to the considered frequency bandwidth.

From these PSD, we can see that the low frequency part of PSD are not affected by the wind, with similar peak amplitude at the surge natural frequency (~0.005Hz). Unexpectedly, the turbulent wind case does not induce a larger low frequency response for the surge component. On the platform pitch, the wind cases have slightly smaller response, but the impact is relatively negligible. The numerous peaks on the pitch response are due to the platform moonpool modes and also due to the pitch natural frequency. Note that the increase in the surge $R_Y\ NF$ and WF on the PSD still has a very small overall amplitude compared to the low frequency motions. A similar analysis for the waves conditions $H_s = 6m; T_p = 10s; U_w = 14\ m/s$ leads to the same conclusions.

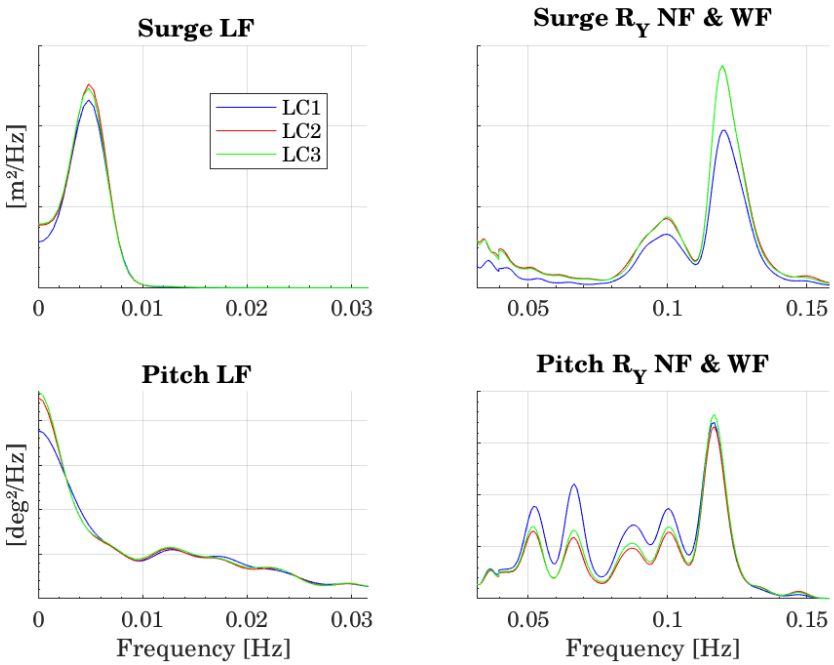

Figure 90: Surge and Pitch PSD for the BGF platform

To conclude, the BGF platform is weakly dependent to rotor loads, even for the low frequency motions. The primary reason is that the platform mass, inertias and dimensions make it much more massive than a typical FWT. Consequently, its behavior is inertia and wave dominated. Representing the rotor loads has a negligible influence on the platform motions.

7.2.2 SOFTWIND SPAR

For the SOFTWIND SPAR test campaign, many load cases have been tested. In this part, the effects of the rotor loads are investigated by differential comparisons between wave-only and waves and wind tests. Different operating points of the wind turbine and waves conditions are investigated. The load cases considered for this analysis are listed in Table 35. The load cases LC1.X and 2.X illustrate the differential comparisons and load cases LC3.X/4.X illustrate the effect of the waves conditions on the low-frequency motions, to explore how much the coupling impact the low frequency motions.

LC nb	$H_s[m]$	$T_p[s]$	$U_w[m.s^{-1}]$ or Thrust [kN]	$T_I[\%]$	controller
LC1.1	5.8	10.9	/	/	/
LC1.2	5.8	10.9	Steady thrust 640	/	/
LC1.3	5.8	10.9	18.0	17.0	yes
LC1.4	5.8	10.9	18.0	17.0	no
LC2.1	9.4	13.8	/	/	/
LC2.2	9.4	13.8	Steady thrust 960	/	/
LC2.3	9.4	13.8	13.9	17.0	yes
LC2.4	9.4	13.8	13.9	17.0	no
LC3.1	2.6	11.0	11.4	15.1	yes
LC3.2	4.5	11.0	11.4	15.1	yes
LC3.3	7.7	12.4	11.4	15.1	yes
LC4.1	3.0	12.0	13.9	13.8	yes
LC4.2	9.4	13.8	13.9	13.8	yes
LC4.3	10.9	15.0	13.9	13.8	yes

Table 35: Wind and waves conditions considered for the SOFTWIND SPAR aero-hydro coupling analyses

Influence of rotor loads on FWT response

In Figure 91, the surge and pitch PSD are depicted for the LC1 (a) and LC2 (b). The different conditions are tested:

- Waves only (LCX.1),
- Waves and steady thrust (LCX.2),
- Waves, turbulent wind and active wind turbine controller (LCX.3),
- Waves turbulent wind and fixed rotor speed and blade pitch angle (LCX.4).

These two load cases comparisons exhibit similar trends:

- The FWT behavior is similar for the WF motions for all conditions. This means a negligible effect of the aerodynamic damping at those frequencies compared to the hydrodynamic related damping.
- Comparing wave-only and wave-only with steady thrust, the PSD are similar. The modifications of the flow characteristics due to the tilted wind turbine do not affect significantly the motions of the FWT, only the mean value. A minor change in the surge natural frequency is visible in Figure 91.a between LC1.1 and LC1.2. It is due to the different mooring stiffness around the steady offset for a 15N mean thrust and the equilibrium position.
- The surge and pitch low frequency motions (left) are dominated by the rotor loads excitation due to the turbulent wind (LC X.3 and X.4 versus X.1 and X.2). The pitch natural frequency is smaller with an active controller (~0.028Hz) than for wave-only tests, decay tests and without control (~0.031Hz).

The influence of the wind turbine controller is thoroughly investigated in part 7.5 but it can already be noticed:

  - the change in the pitch natural frequency as presented above;
  - the much smaller pitch response without control;
  - the different surge response at the surge natural frequency, but this depends on the operating point. For a wind speed of 18 m/s, the surge LF response is smaller with an active controller than without control, while for a wind speed of 14 m/s, the responses are equivalent. This result at 18 m/s may appear in contradiction to the rotor loads induced damping at this frequency; it is due to the difference in the low frequency excitation with and without active controller. See part 7.5 for details.

a)

b)

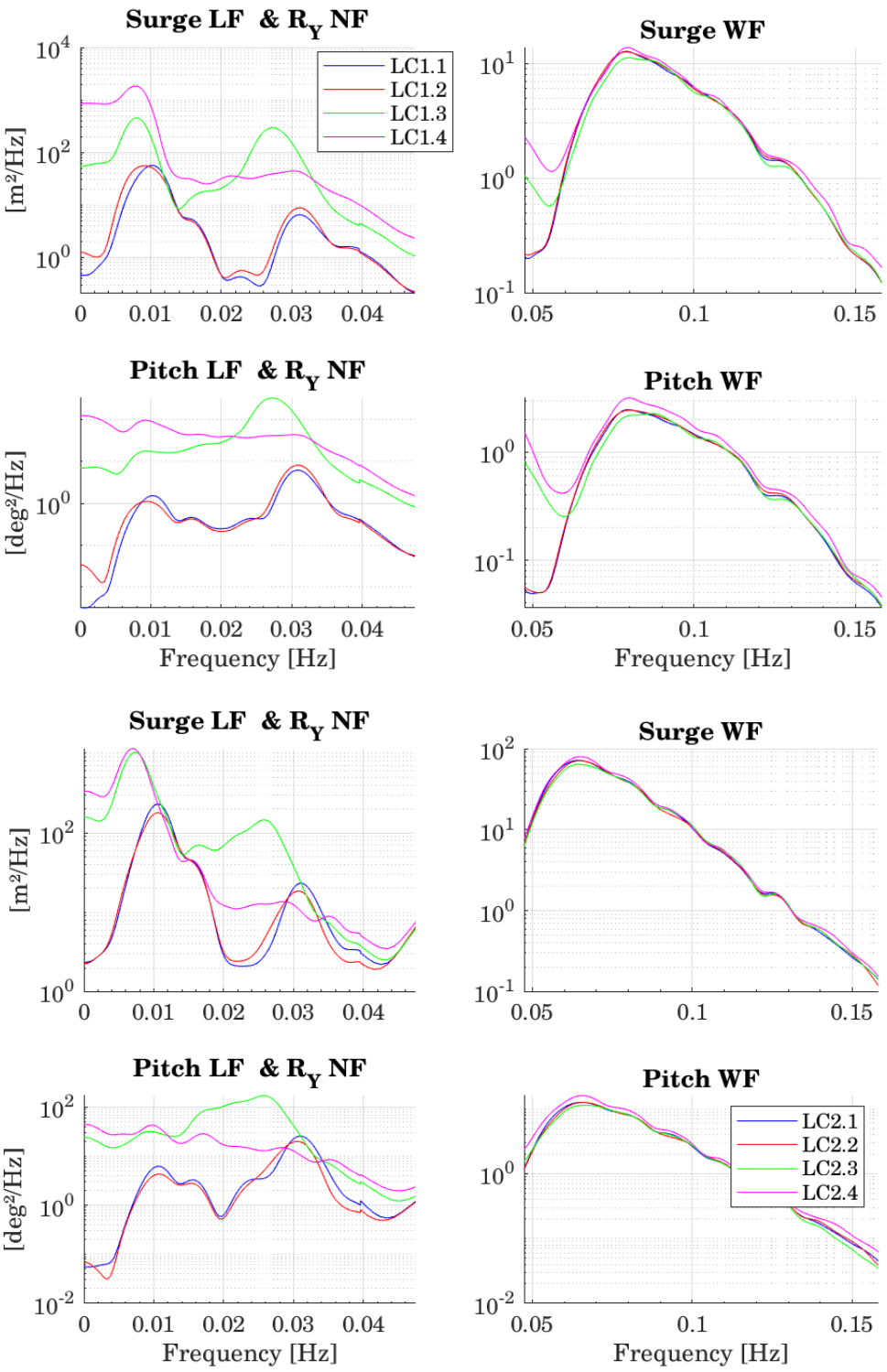

Figure 91: Surge and pitch PSD for different conditions. a) LC1 ($\boldsymbol{U_w}$ = 18m/s) load case, b) LC2 ($\boldsymbol{U_w} = \boldsymbol{13.9m.s^{-1}}$) load case

Evolution of the low frequency motions for the same turbulent wind conditions

The LC3.X and LC4.X are used to illustrate the change in the low frequency motions, for the same wind conditions, due to different wave conditions. Waves conditions vary from small waves, $Hs = 2.6m$ (resp. 3.0m) for LC3.1 (resp. LC4.1), to severe waves $Hs = 7.7m$ (resp. 10.9m) for LC3.3 (resp. LC4.3). In Figure 92, the same PSDs as previously are depicted. The wave induced motions (right) are clearly wave-dependent, but what is of interest for this load cases comparison are the low frequency motions (left part). As seen on Figure 92 a) top left, the surge LF peak located at around 0.008Hz decreases as

the wave height increase. This attenuation is approximately 2/3 on the PSD peak amplitude for the LC3.3 compared to LC3.1, i.e. approximately 0.8 on the standard deviation of the surge motion. For the LC4, this progressive attenuation is well represented by a progressive decrease from LC4.1 to LC4.3 on the surge LF peak amplitudes.

a)

b)

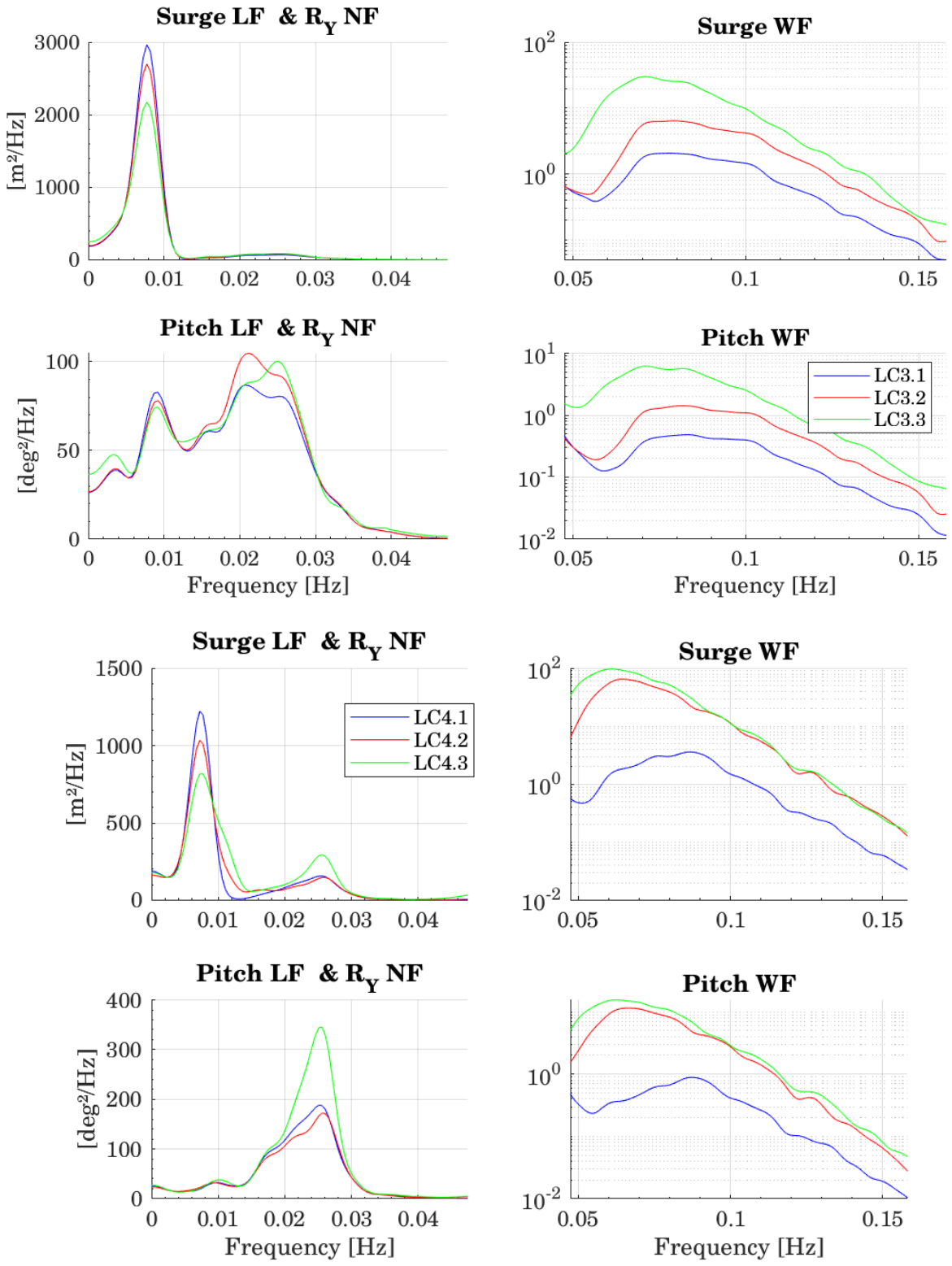

Figure 92: Surge and pitch PSD for the LC3 conditions, i.e. different wave conditions but same wind speed and turbulence intensity. Log scale for WF motions and linear scale for low frequency motions.

To explain those differences, the rotor load F_x reference force PSDs are depicted in Figure 93 for the different load cases (LC3.X and LC4.X). The question is to understand if the differences observed on the motions are due to the rotor loads themselves or due to the hydrodynamic forces. For the same wind conditions, we can expect similar rotor loads forces; however, due to the dependency of the rotor loads to the FWT motions, this is important to check if the rotor loads, in the frequency bandwidth of interest, are similar. At the frequency 0.0084Hz, the different PSD superimpose very well, denoting similar rotor forces. As a consequence, differences in the motions are necessarily due to different hydrodynamic forces. When the wave-induced kinematics increases, the surge LF motion decreases; the LF hydrodynamic related damping is stronger. Note that as the load cases are wind-driven, the increase of the low frequency wave excitation is negligible compared to the rotor excitation. Different options from the hydrodynamic related literature can explain this phenomenon:

- Increase in the viscous forces acting in the splash zone (Lie and Kaasen, 2008; Stansberg *et al.*, 2015). However, this induces both an excitation and a damping: it is hard to conclude.
- A relative "dependent flow" Morison formula instead of an "independent flow" formula (Le Boulluec *et al.*, 1994) concerning the floater drag forces; In that case, comparisons between surge decay tests in waves and surge decay tests in still water can provide some insights.
- An increase of the moorings related low frequency damping due to wave-induced kinematics (Le Boulluec *et al.*, 1994).

This analysis illustrates a part of the coupling between the hydrodynamic forces and the rotor loads. For the load cases LC3 and LC4, a summation principle of rotor-loads-induced response and of the wave-induced response could not take these superimposing phenomena into account.

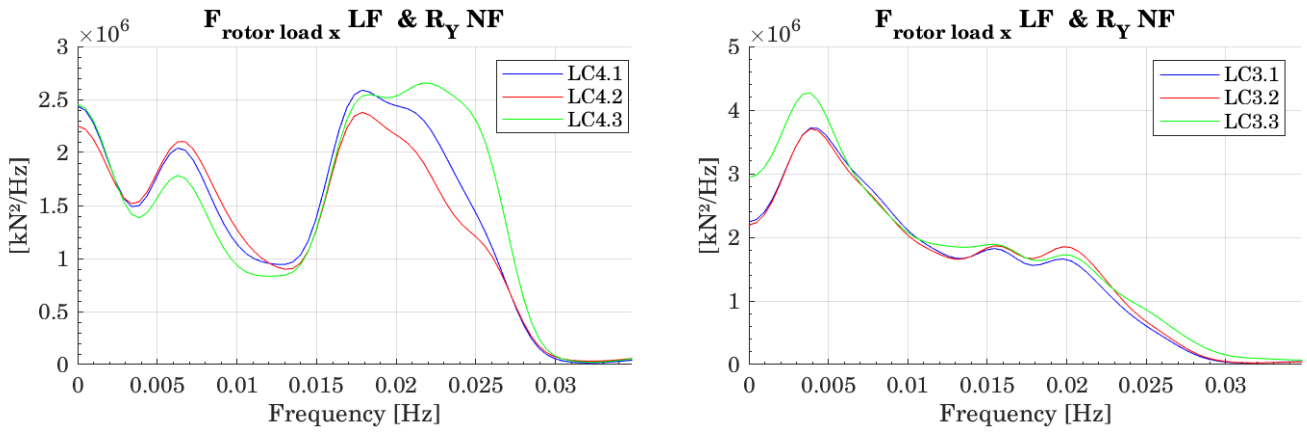

a) b)

Figure 93: Comparison of x-rotor load low frequency PSD. a) LC4 and b) LC3

7.3 Influence of actuators performances

To provide guidelines to the community and help future choices on actuators selection and suitable layout definition, different actuator performances have been tested during the SOFTWIND SPAR campaign. First, many tests have been performed with comparisons between *static calibration* and *dynamic calibration* results (see chapter 6). Additionally, for some load cases the actuator performances are voluntary deteriorated, using two inputs:

- The cut-off frequencyf_c. $f_{c\,1} = 0.16Hz$ and $f_{c\,2} = 0.08Hz$ (full scale).
- a real-time delay Δ_t. $\Delta_{t\,1} = 0.32s$ and $\Delta_{t\,2} = 0.76s$ (full scale).

Note that the effect of actuator performance at the tower natural frequency is expected to be really important. However, due to the problems explained in section 7.1.1, the impact at this frequency could not be reliably investigated. In this part, the objective is to explore the impacts for the LF, R_Y NF and WF bandwidths.

The load cases considered for this analysis are listed in Table 36. For each load case, the following appellations are used:

- LCX *stat.* for the static calibration results,
- LCX *dyn.* for the dynamic calibration results,
- LCX $f_{c\,1}$ (resp. $f_{c\,2}$) for the deteriorated performance with cut-off frequency $f_{c\,1}$ (resp. $f_{c\,2}$),
- LCX $\Delta_{t\,1}$ (resp. $\Delta_{t\,2}$) for the deteriorated performance with added delay $\Delta_{t\,1}$ (resp. $\Delta_{t\,2}$).

LC nb	$H_s[m]$	$T_p[s]$	$U_w[m.s^{-1}]$	$T_I[\%]$
LC1	5.8	10.9	18.0	17.0
LC2	4.5	11.0	11.4	15.0
LC3	7.7	12.4	11.4	15.0

Table 36: Wind and waves conditions considered for the SOFTWIND SPAR actuator performances analyses

The PSDs are depicted in Figure 94. They have similar trends for all load case, which are analyzed per frequency bandwidth.

Surge natural frequency (~0.008Hz)

At the surge natural frequency, the differences among the different cases are quite small. However, the $\Delta_{t\,2}$ added delay case exhibits a larger peak, and the dynamic calibration exhibits a marginally smaller peak. All the other differences at this frequency are within the variability range of the system's repeatability. The dependence of the surge LF response to the actuators performance is small and is due to:

- A slightly stronger negative damping,
- A modification of the "equivalent" wind field time series that are slightly delayed. This is not a real problem when superposing different seeds, as it is recommended in the standards.

Pitch natural frequency (~0.03Hz)

At the pitch natural frequency, the differences are important. Comparisons between static calibration and dynamic calibration results are unexpected. For the $U_w = 11.4\,m/s$ operating point (respectively 18.0 m/s), the actuator full scale cut-off frequency is 0.3Hz (respectively 0.15Hz). This is far away from the pitch natural frequency (factor of 10 (respectively 5)). However, the attenuation of the pitch response is not negligible, and this attenuation is confirmed by the limited bandwidth deteriorated performances cases: the smaller the cut-off frequency (dyn. > stat. > $f_{c\,1}$ > $f_{c\,2}$), the smaller the pitch response at this frequency. This becomes more important as the turbulence intensity increases (LC1 has the highest turbulence intensity). From the dynamic calibration case to the $f_{c\,2}$ case, the attenuation of the PSD amplitude is 80% (resp. 60% and 40%) for LC1 (resp. LC2 and LC3), while the theoretical attenuation of the rotor load frequency content at ~0.03 Hz is only 7% for the $f_{c\,2}$ case. The impact of the added delay is overall small, but also tends to decrease the peak amplitude. This outcome is also counterintuitive, as the added delay should make the rotor force damping smaller. Investigations concerning the discrepancies between dynamic calibration results and static calibrations are pursued hereafter.

Wave frequencies (~0.08Hz)

For the wave frequencies, differences are very small for the surge DoF and small for the pitch DoF. The large added delay and the small actuator cut-off frequency cases have WF motions bigger than the dynamic calibration motions. This must be correlated to the WF aerodynamic damping. With the small bandwidth, the phase lag is important for the wave frequencies (~$\pi/4$), leading to a smaller damping component in the actuated force than in the target (setpoint) force.

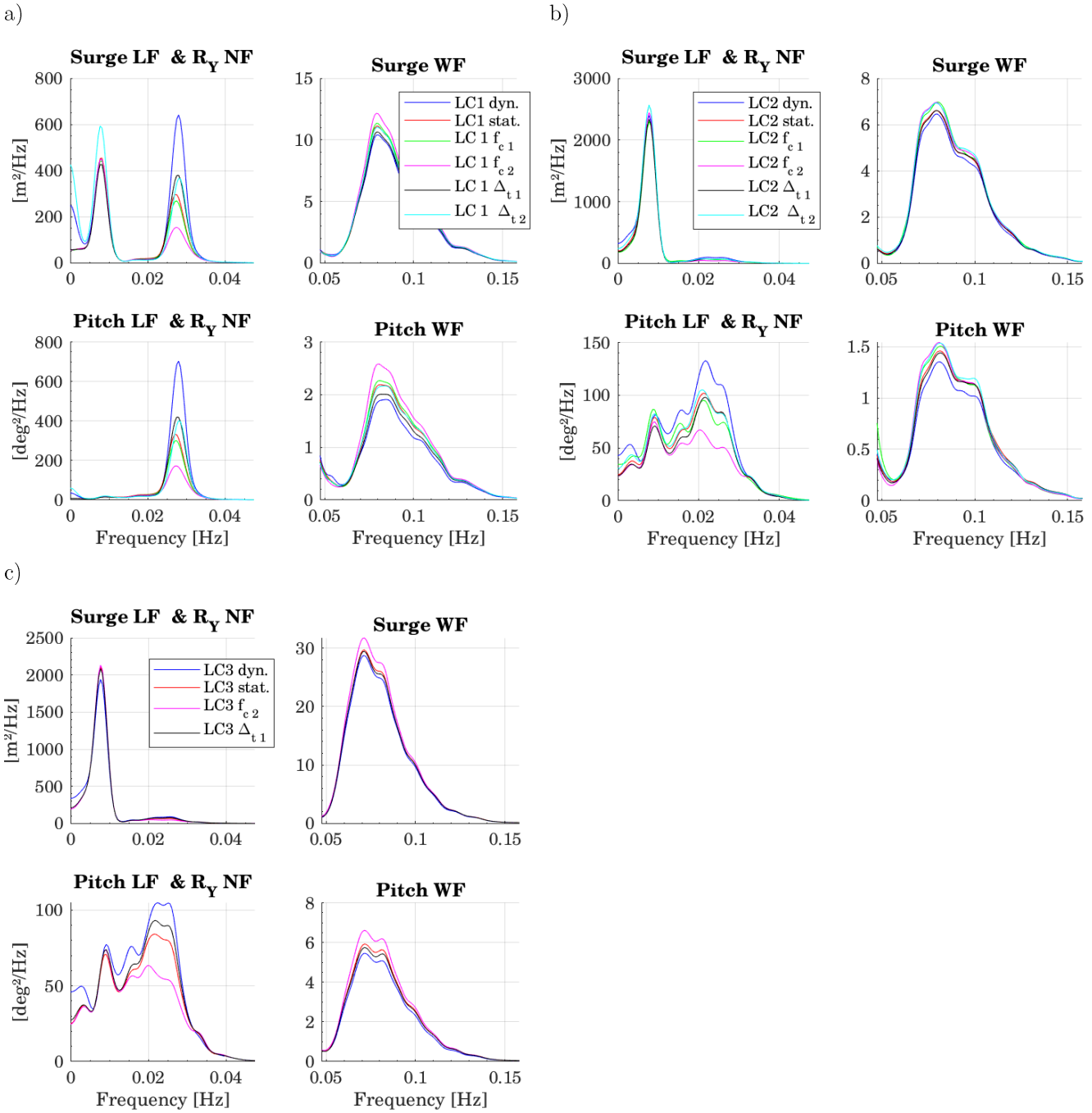

Figure 94: Surge and pitch PSDs for different actuators performances.a) LC1; b) LC2 and c) LC3 results.

All the load cases have been tested with dynamic calibration and static calibration control of the actuators. A ratio $\sigma_{R_Y\ dynVSstat} = \frac{\sigma_{R_Y\ dyn}}{\sigma_{R_Y\ stat}}$ is defined, with $\sigma_{R_Y\ dyn}$ (resp. $\sigma_{R_Y\ stat}$) the standard deviation of the bandpass filtered pitch motions at the pitch natural frequency for the dynamic calibration (resp. static calibration) cases. This ratio is depicted in Figure 95 for the load cases listed in Table 36, as

function of the actuator cut-off frequency (at full scale). For each test, the cut-off frequency is defined by the actuator performances obtained in chapter 6 or by the voluntary deterioration of this cut-off frequency. The size of the markers is proportional to $\sigma_{R_Y\,dyn}$, i.e. the importance of platform pitch motions at the pitch natural frequency for the dynamic calibration results (reference case).

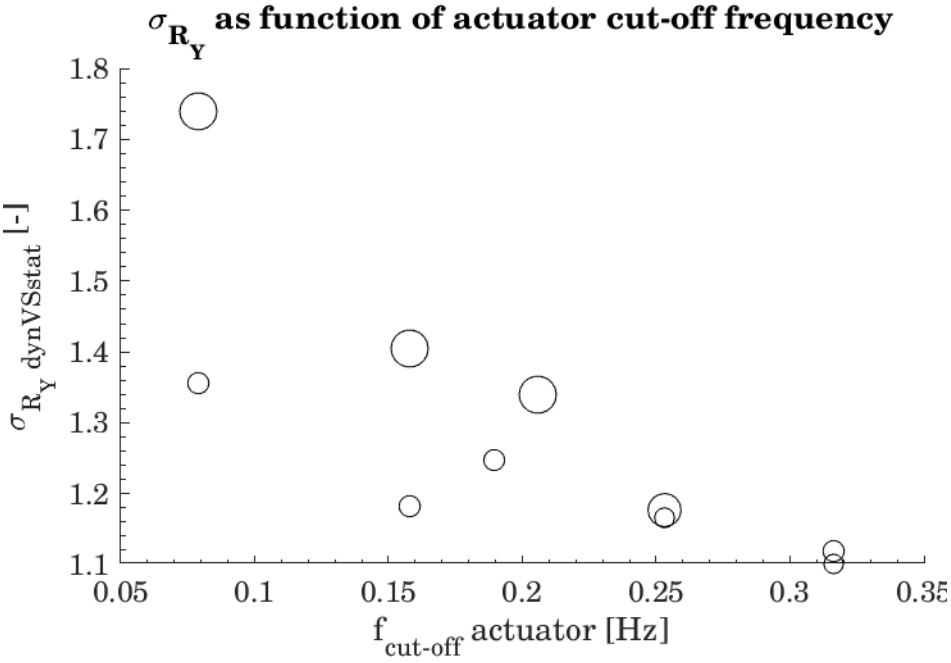

Figure 95: Evolution of the pitch natural frequency ratio as function of the actuator cut-off frequency. The size of each marker is proportional to the standard deviations of the platform pitch motions for the dynamic calibration case.

This ratio varies from 1.1 to 1.75 depending on the actuator cut-off frequency and pitch motion standard deviation. Two trends could be defined:

- The higher the actuator cut-off frequency, the smaller the ratio between dynamic calibration and deteriorated performances platform pitch motions.
- The bigger the platform pitch motions ($\sigma_{R_Y\,dyn}$), the bigger the ratio between dynamic calibration and deteriorated performances platform pitch motions.

These trends are expected. Indeed, a higher cut-off frequency better reproduces both the low frequency excitation force and the damping. However, the pitch natural frequency is far from the actuator cut-off frequency; the attenuation of the force is much smaller than the attenuation of the motions. To further explain this ratio, the x-rotor force setpoint and actuated forces are analyzed. In Figure 96, the rotor loads (setpoints and actuated) and the platform pitch are represented for the LC1, dynamic calibration results versus $f_{c\,2}(= 0.08Hz)$ results. The time series are bandpass filtered around the pitch natural frequency. On the selected portion of the test, at t~920s the platform pitch motions are similar. Then, the pitch motion amplitude increases more with the dynamic calibration actuator command than with the deteriorated actuator command. From the rotor load temporal evolution, we can observe the phase lag between the reference and actuated force. The consequence is a platform pitch natural period that increases in the $f_{c\,2}$ case compared to the *dynamic* case. Finally, the evolution of the platform pitch is not only proportional to the rotor load force attenuation. The phase lag has an important role, and the "memory effect" of the hydrodynamic forces (linked to the retardation function of the platform pitch) may play a role in the overall attenuation of the platform pitch.

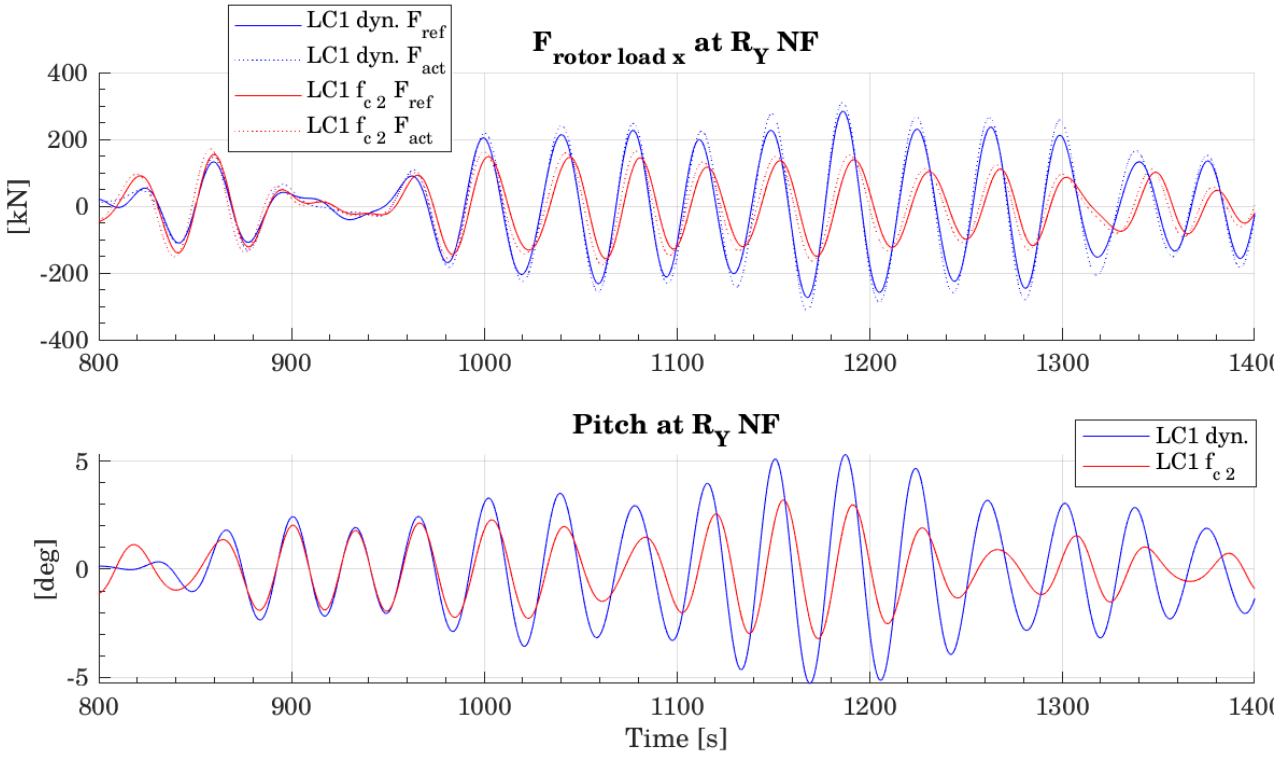

Figure 96: Actuator force (a) and platform pitch (b)

To conclude, the actuator performances have an impact on the FWT motions. For the SOFTWIND SPAR setup, excluding the tower deflection, the actuator performances have an important role on the platform pitch motions at the pitch natural frequency. For the other frequency bandwidth the impacts are much smaller.

7.4 Influence of wind turbine thrust modeling methodology

In order to provide guidelines about suitable methodologies for modeling rotor loads during wave tank testing, comparisons between simplified methodologies and a real-time integration of a state of the art aerodynamic model has been conducted. The different methodologies tested were:

- The reference case, the "software-in-the-loop" methodology, with the OpenFAST numerical model running in real time. The motions of the floater, measured in the wave tank, are sent as inputs to the numerical model. It is denoted "DTU SIL" in the following figures.
- The same case but without any control, i.e. with fixed blade pitch angles and rotor speed dependent on the operating point. It is denoted "control frozen".
- Equivalent of a "drag disk", with a rotor thrust proportional to the square root of the incident hub velocity. It is denoted "drag disk" in the following figures.
- The steady-state thrust curve of the wind turbine, using the total velocity at the hub (sum of the incident wind velocity and of the measured hub motions). It is denoted "steady-state" in the following figures.
- OpenFAST computation of the rotor thrust but without any influence of the motions of the floater. This computation can be performed before the test. It is denoted "DTU Fixed" in the following figures.

Note that:

- For all these tests, the actuator performances correspond to the dynamic calibration results.

- All the *steady-state* configurations were unstable with increasing platform pitch motions. Tests were stopped well before the target duration of 10min and are not represented in the PSDs.

The load cases considered for this analysis are the same as in previous study and are listed in Table 36.

The surge and pitch PSDs are depicted in Figure 97 for the three load cases. The main differences are at the pitch and surge natural frequencies. The two load cases at $U_w = 11.4\,m/s$ have similarities but the evolution differs for the LC1 $U_w = 18\,m/s$.

Concerning the LC2 and LC3 at $U_w = 11.4\,m/s$, Figure 97 b) and c):

- For the surge motion at the surge natural frequency (~0.008Hz):
  - The *DTU fixed* and *drag disk* cases have a peak of approximately same amplitude. The *DTU SIL* case has a bigger peak due to the marginally negative damping due to the rotor loads.
  - The *control frozen* case has smaller amplitude than the *DTU SIL* case. This is due to the positive damping reproduced, similarly to the *drag disk*, but also to the rotor load excitation. Comparison of the rotor loads excitation is investigated hereafter.
- For the pitch motion at the pitch natural frequency (~0.03Hz):
  - The *drag disk* and *control frozen* cases have much smaller amplitudes than the *DTU SIL* case. This is due to the much larger damping provided by those cases.
  - The *DTU fixed* case has a much larger peak amplitude than the *DTU SIL* case due to the lack of damping in the rotor load setpoint,
  - There is no change in the pitch natural frequency for all the cases except the *DTU SIL* case. This is due to the lack of out of phase component in the rotor load setpoint.
- For the WF motions, surge is similar between the different cases and for pitch, the *DTU fixed* case has a slightly smaller amplitude.

Concerning the LC1 at $U_w = 18.0\,m/s$, Figure 97 a):

- For the surge motion at the surge natural frequency (~0.008Hz):
  - The *DTU SIL* and the *DTU fixed* cases have a peak of approximately the same amplitude. The *DTU SIL* case has a bigger peak due to the marginally negative damping due to the rotor loads.
  - The *drag disk* and *control frozen* cases have much higher amplitudes than the *DTU SIL* case. This can be surprising due to the positive damping reproduced by both methodologies and a marginally negative damping for the *DTU SIL* case. However, this can be explained by the different rotor loads excitations. This aspect is detailed hereafter.
- For the pitch motion at the pitch natural frequency (~0.03Hz):
  - The trends are similar to the ones observed for the LC2 and LC3 load cases. However, the amplitude of the *DTU fixed* case changes from 6 times the value of the *DTU SIL* case for LC2 and LC3 to two times for LC1.
- For the WF motions, the trends are similar to those observed for the LC2 and LC3 load cases.

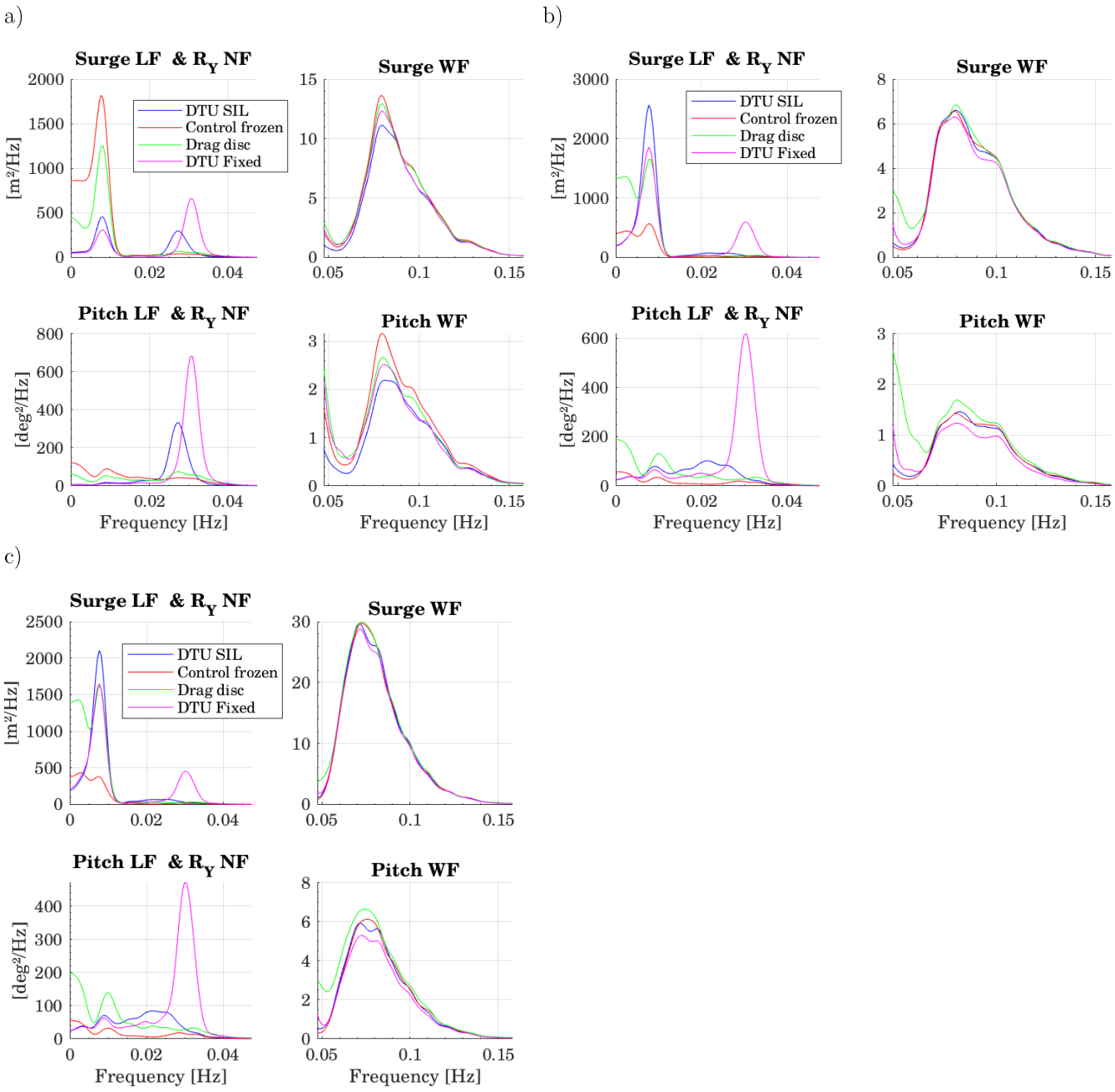

Figure 97: Surge and pitch PSDs for different wind turbine thrust modeling methodology. a) LC1; b) LC2 and c) LC3 results.

To further analyze the differences at the surge and pitch natural frequencies, the PSD of the rotor load setpoint is presented for the different load cases in Figure 98. Regarding the LC1, the amplitudes of the rotor load x-force at the surge natural frequency (~0.008Hz) for the *drag disk* and *control frozen* are one order of magnitude above the rotor load x-force for the *DTU SIL* (and DTU fixed) cases. Around $U_w = 11.4\, m.s^{-1}$ (LC2 and LC3), the amplification is smaller, with the *drag disk* excitation being more important than the control frozen results.

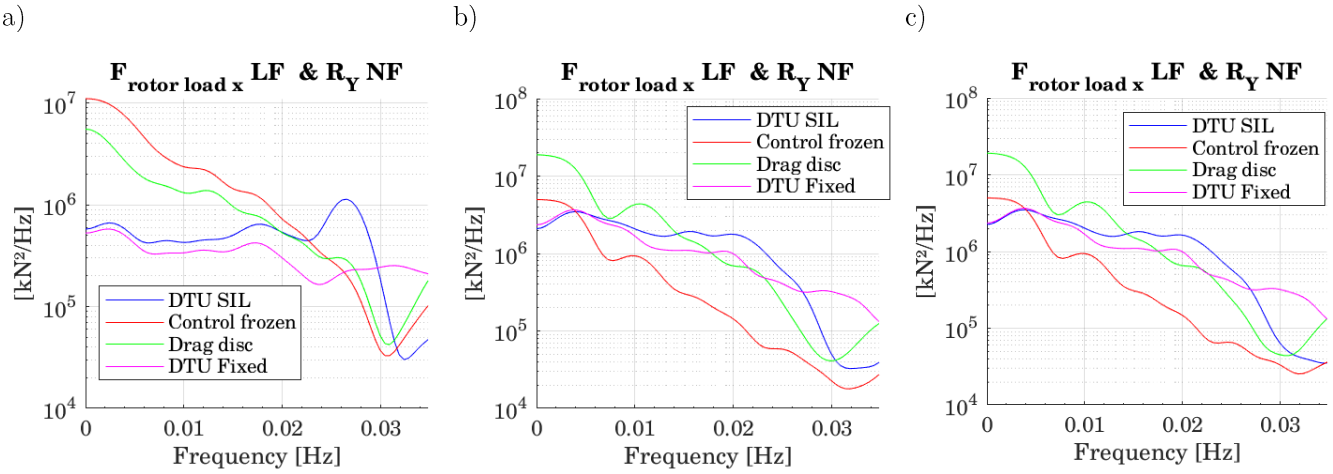

Figure 98: Rotor load x-force PSD for the three load cases a) LC1; b) LC2 and c) LC3

To provide additional insights on the damping and excitation components of the different cases, the surge and pitch natural frequencies fluctuations of the rotor load x-force as function of the hub velocity are represented. This analysis is similar to the sine motions analysis presented in chapter 4. The methodology for turbulent wind and irregular waves that has been defined is:

- Selection of a shorter segment than the full time series with only 10 LF and R_Y NF periods;
- The force and hub wind speed signals are bandpass filtered for the frequency bandwidth of interest. Note that the total hub wind speed is considered (both due to the incident wind fields and to FWT motions)
- To be able to compare the forces to the steady-state thrust curves, the mean incident speed is added to ΔU_{hub} and the mean force on the time serie is added to ΔF.

Figure 99 illustrates the information that could be extracted from this force/wind speed graph. While more details are provided in Chapter 4, the linear assumption behind this is represented in Eq. (7.1):

$$\Delta F_x(U_{hub}) \approx F_{ex\,|u}\big(u_0(t)\big) - B_{aero}\dot{X}_{hub} - A_{aero}\ddot{X}_{hub} - K_{aero}X_{hub} \tag{7.1}$$

With:

- $\Delta F_x(U_{hub})$ the variation of thrust
- B_{aero} the aerodynamic damping
- A_{aero} and K_{aero} the inertial and stiffness terms (out of phase)
- $F_{ex\,|u}\big(u_0(t)\big)$ the excitation force, related to the variation of the incident hub wind speed $u_0(t)$

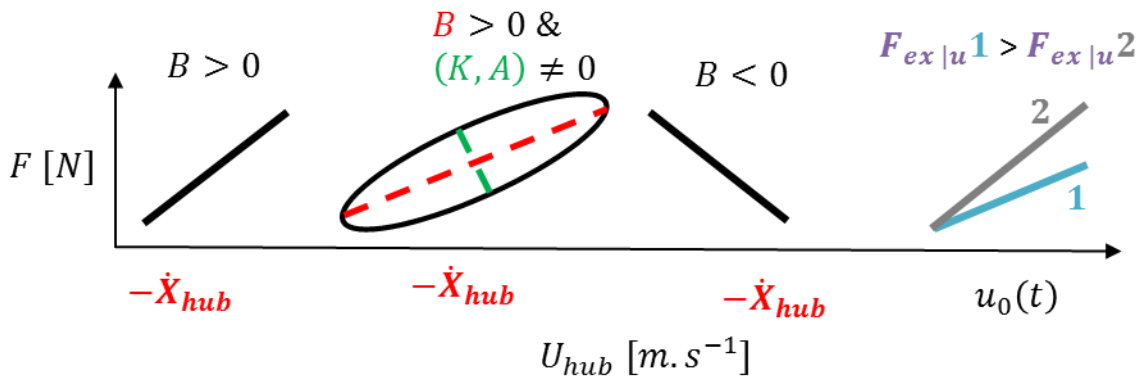

Figure 99: Illustration of thrust variation as function of apparent hub wind speed

This is applied to LC1 (resp. LC2) in Figure 100 (resp. Figure 101).

LC1 ($u_w = 18.0$ m.s^{-1})

At the surge natural frequency (LF, a)):

- The *drag disk* force has a smaller slope than the *control frozen* slope. This corroborates the larger excitation provided by the *control frozen* case, and the larger peak amplitudes on Figure 97 a) top left.
- The *DTU SIL* and *DTU fixed* cases are roughly similar, with negative slopes that are smaller than the *control frozen* and *drag disk* slopes in absolute values. Indeed, the thrust covers 550 to 800kN for the active DTU controller cases, while it covers approximately 400 to 1000 kN for the *control frozen* and *drag disk*. This smaller thrust variation (that is $F_{ex\,|u}$) explains the smaller excitation and induced response (Figure 97 a) top left) for those cases compared to the *control frozen* and *drag disk* cases.

At the pitch natural frequency ($R_Y\,NF$, b)):

- The drag disk and control frozen cases have now similar slopes, which corroborates the same excitation for those two cases. The pitch peak amplitudes on Figure 97 a) are of the same order of magnitude.
- The *DTU SIL* and *DTU fixed* have positive slopes, with certain out of phase component. For the *DTU SIL* case this slope provides a certain damping, while it is only a excitation term for the *DTU fixed* case. That is the reason why the peak amplitude of the DTU fixed case is bigger than the *DTU SIL* case on Figure 97 a). Concerning the out of phase component, it is not related to the FWT motions for the *DTU fixed* case component and consequently, it does not change the pitch natural frequency. However, for the *DTU SIL* case, this decreases the natural frequency.

a) b)

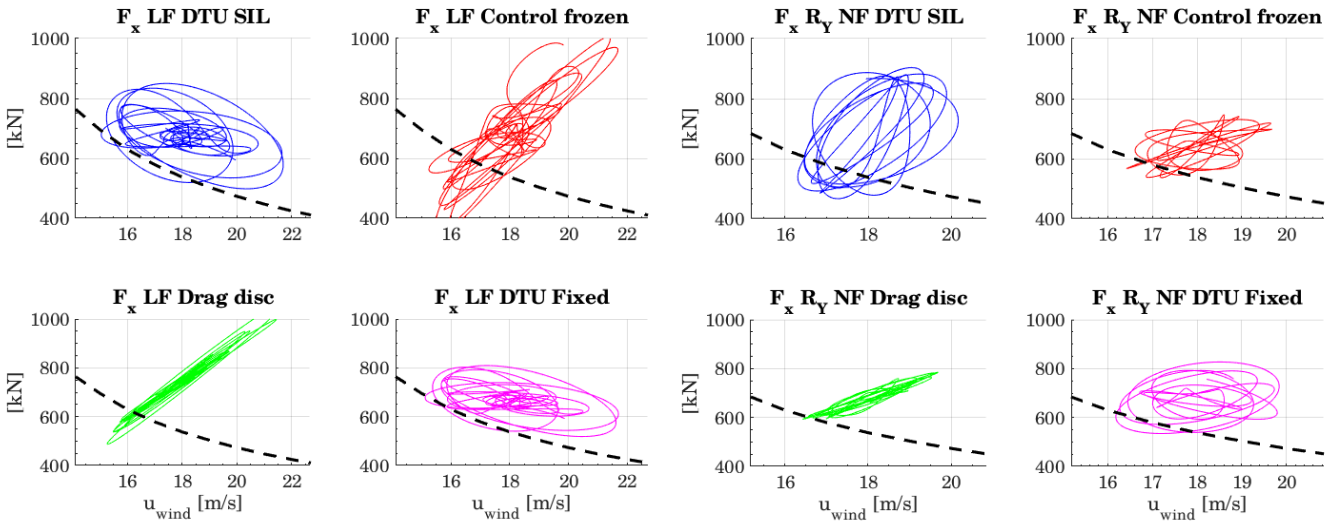

Figure 100: Rotor x-force as function of the hub incident velocity for LC1. a) LF bandwidth; b) $\boldsymbol{R_Y}$ NF bandwidth

LC2 ($\boldsymbol{u_w = 11.4\,m/s}$)

At the surge natural frequency (LF, a)):

- The *drag disk* case has a larger slope than the *control frozen* case, which corroborates the larger peak amplitude of the drag disk on Figure 97 b).
- For the *DTU fixed* and *DTU SIL* cases, it is hard to define a clear mean slope; it is neither negative or positive slope, but includes some excitation, damping as well as out of phase components.

At the pitch natural frequency ($\boldsymbol{R_Y\,NF}$, b)):

- The *drag disk* and *control frozen* cases have now similar slopes: the thrust has a 200kN variation in both cases for the same incident hub wind speed variation. It corroborates the same excitation for those two cases.
- There are no clear trends for the *DTU SIL* and *DTU fixed* cases.

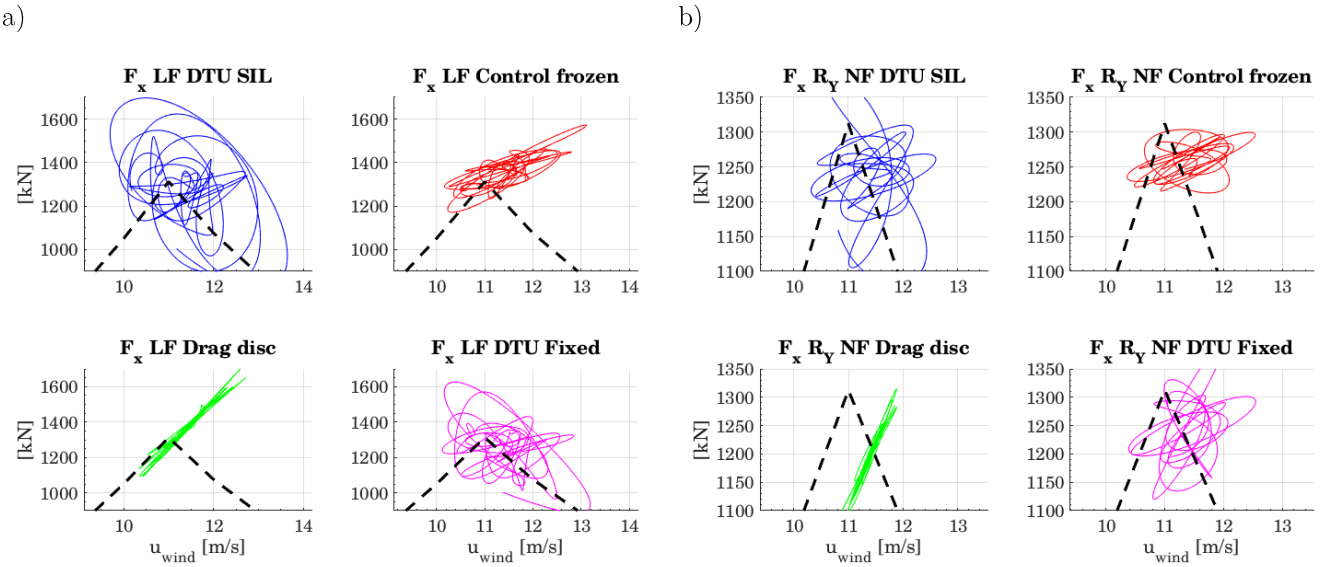

Figure 101: Rotor x-force as function of the hub incident velocity for LC2. a) LF bandwidth; b) $\boldsymbol{R_Y}$ NF bandwidth

7.5 Application: wind turbine controller effect

As stated in the objectives of the SOFTWIND project, testing different wind turbine controllers in the same experimental setup offer valuable experimental data to the wind turbine controller developers. As presented in part 7.2 and part 7.4, the controller effect is important at the platform pitch and surge natural frequencies, for which typical hydrodynamic modeling assumptions make the numerical results differ from the experimental results (see chapter 8 for details). Different controllers have been tested in the SOFTWIND SPAR campaign, including:

- The DTU Baseline controller, with onshore and offshore settings. It is based on a gain scheduled proportional integral (GSPI) controller with the generator speed as the system information, and generator speed and blade pitch angles as controllable quantities. For the offshore settings, the PI gains are the ones tuned for the OO-Star 10MW public design (Müller, Lemmer and Yu, 2018), see chapter 5 for details. It is denoted DTU in this part. Note that the onshore controller has been tested but platform pitch instability has forced to stop the tests very quickly.
- The ODIN controller, developed by the D-ICE company. It is based on model-based nonlinear control. No further details about this controller are given.
- The simplified adaptive super-twisting (SAST) controller, developed by the LS2N laboratory, Centrale Nantes and presented by (Zhang *et al.*, 2019). The advantage of this controller is to reduce the gains tuning efforts.
- The *frozen control* quantities, with fixed blade pitch angles and rotor speed, depending on the mean operating point.

Note that all these control laws use collective blade pitch control.

The objectives of this cross comparison are not to compare the wind turbine controller quantities (blade pitch, power output, …) but to check their effects on the FWT behavior (motions, forces, …).

The load cases considered for this analysis are listed in Table 37. Note that the controllers have not been tested on all load cases.

LC nb	$H_s[m]$	$T_p[s]$	$U_w[m.s^{-1}]$	$T_I[\%]$	DTU	ODIN	SAST	Frozen
LC1	3.0	12.0	13.9	9.0	X	X	X	X
LC2	2.6	11.0	11.4	15.1	X	X		
LC3	4.3	10.0	17.9	12.0	X	X		

Table 37: Wind and waves conditions considered for the SOFTWIND SPAR wind turbine controllers comparisons

The surge and pitch PSDs for the different controllers are depicted in Figure 102 for LC1 ($U_w = 13.9\,m/s$). The SAST and ODIN controllers lead to very different results than the DTU controller, both at the platform pitch and surge natural frequencies. For the WF bandwidth, the responses are close, with a slight amplification for the ODIN case.

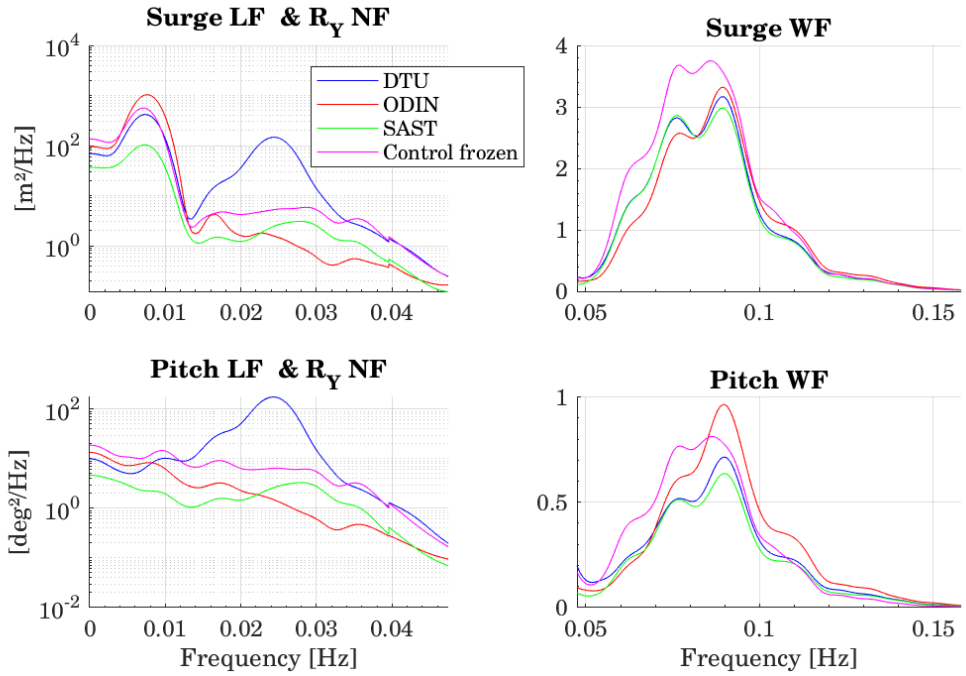

Figure 102: Surge and pitch PSDs for LC1

At the pitch natural frequency, both controllers have much smaller motions amplitude than the DTU controller. At the surge natural frequency, the SAST controller damps the motions compared to the DTU while the ODIN controller amplifies the motions. Overall, the ODIN controller effect is closer to the Control frozen case than the DTU case. To further investigate, the rotor load x-force as function of the incident hub velocity (including the nacelle motions) is represented for each case on the two frequency bandwidths in Figure 103. In each plot, the steady-state force is represented with a black dashed line.

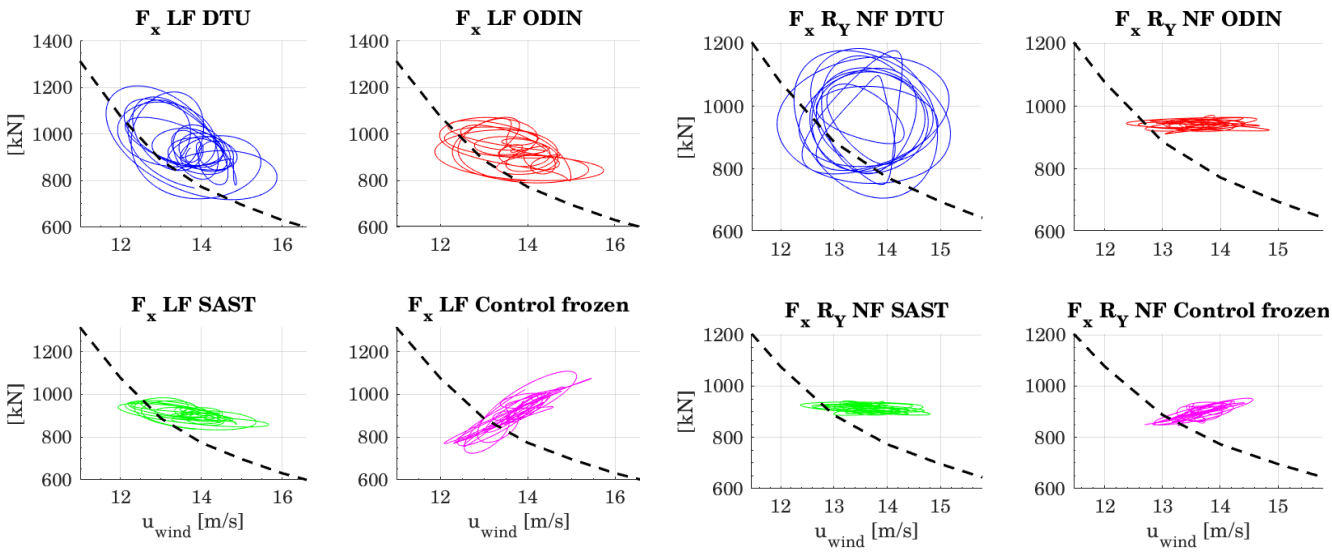

a) b)

Figure 103: Rotor x-force as function of the incident hub velocity for LC1. a) LF fluctuations and b) R_Y NF fluctuations

The following characteristics could be defined:

- At the surge natural frequency (LF, a)):
  - The *control frozen* case has a positive damping and marginally out of phase component
  - The *DTU* case has a significant negative damping, similarly to the steady-state case, and significant out of phase component.
  - The *SAST* has a marginally negative damping, and minor out of phase component
  - The *ODIN* controller has a negative damping and significant out of phase component.
- At the Pitch natural frequency (R_Y NF, b)):
  - The *control frozen* case has a positive damping;
  - The *DTU* case has a small damping and important out of phase component. This out of phase component explains the change of the pitch natural frequency for this case.
  - The *SAST* and *ODIN* cases have very limited force fluctuations for varying input wind speed. They act as notch filter for the pitch natural frequency.

Comparisons between the DTU and the ODIN controllers have also been performed on LC2 ($U_w = 11.4\,m/s$) and LC3 ($U_w = 17.9\,m/s$) PSDs are depicted in Figure 104. The wave frequency bandwidths are not depicted as they are similar for both controllers.

The trends highlighted for the $U_w = 13.9\,m/s$ case are still valid for the $U_w = 11.4$ and $Uw = 17.9\,m/s$ cases. When we study the ODIN motions with respect to the DTU ones, we observe attenuations of the pitch R_Y NF motions and amplification of the surge motions at the surge natural frequency. We can notice that this surge amplification is less important for the LC2 and LC3 cases than for the LC1 case.

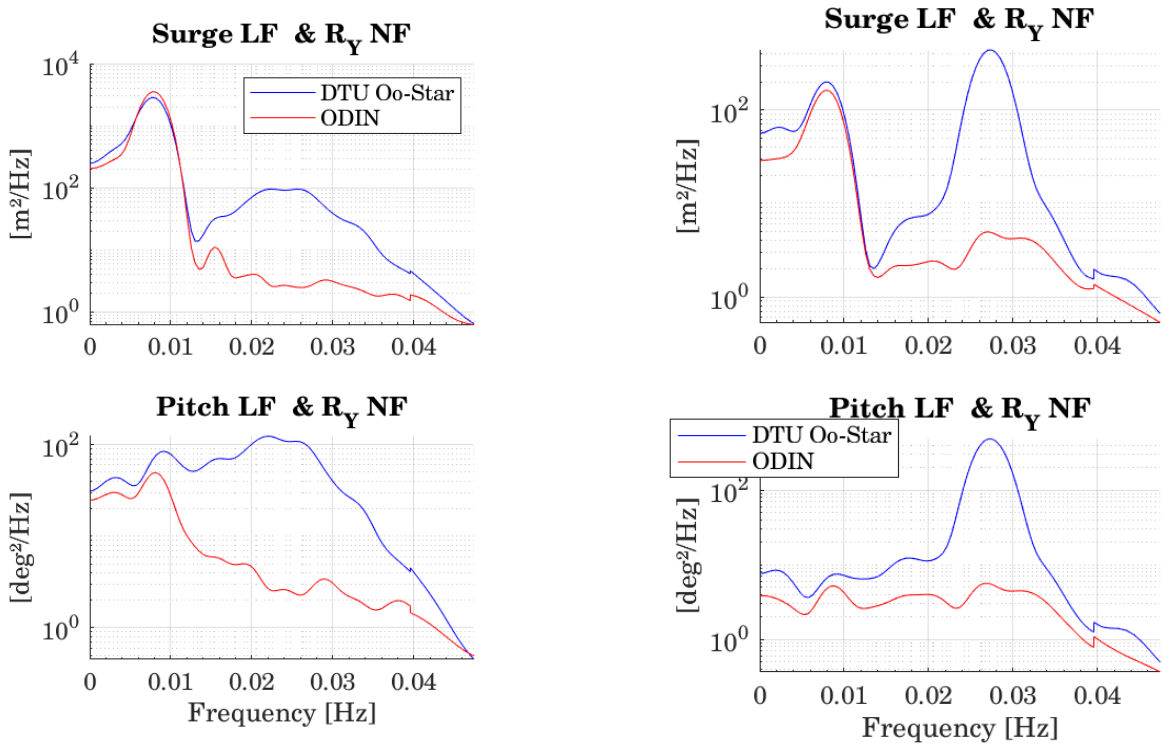

a) b)

Figure 104: Surge and pitch PSDs for LC2 (a) and LC3 (b).

To conclude, this campaign of various controllers in the wave tank shows that the different wind turbine control laws have a significant impact on the FWT motions. The SIL approach developed here is thus a crucial element to compare the effects of different control strategies on FWT motions. The impact is significant at the pitch natural frequency, and to some extent at the surge natural frequency.

Note that from the point of view of assessing the performances of the controller, other data need to be studied that are computed and provided as outputs in the SIL process. In that case, the wave tank SIL system constitutes a hardware-in-the-loop system with a higher fidelity concerning the loads acting on the floater and moorings than a numerical model. Moreover, it allows the correct control law execution on full scale hardware (PLC).

7.6 Conclusions

Several studies have been conducted during the SOFTWIND SPAR test campaign to investigate different key aspects of the SIL system characteristics. The main outcomes are about:

- The numerical model, thanks to comparison between state-of-the-art aerodynamic model real-time computations and simplified approaches:
  - The numerical model has a large impact at the surge and particularly at the pitch natural frequency;
  - Integration of the wind turbine controller is required to get the correct physics;
  - The differences depend on the operating points of the wind turbine;
  - Including the FWT motions in the numerical model computations is required to get the damping effects; the resulting change in the FWT motions is important for resonant frequencies.

- Actuators performances:
    - The actuators performances effects have not been evaluated at the tower natural frequency, but is expected to be very important;
    - At the platform pitch natural frequency, even if much smaller than the considered actuator cut-off frequency, the impact is not negligible.

8 Comparisons between experimental and numerical results

Contents

A numerical model of the wave tank experiments has been established. It includes the different subsystems of the floating wind turbine described in chapter 5 and in appendix D:

- Moorings,
- Floater,
- RNA,
- Tower,
- Wind turbine controller.

This numerical model has first been used before the experiments, during the set-up design phase, to anticipate the floating wind turbine behavior. The objectives are to:

- check the FWT behavior with the specified model scale characteristics;
- study the sensitivity of the FWT global motions to the system characteristics;
- tune the wind turbine controller.

Then, to complement the experiments, additional numerical simulations are performed with parameters tuned using the *as-built* system properties. The objectives are to:

- compare the experimental results with numerical results using a fully-coupled modeling. The experiments provide a reference in terms of hydrodynamics. This enables the evaluation of the different hydrodynamic modeling approaches.
- evaluate if the behavior and limitations of the SIL system are sufficiently characterized to interpret and exploit the results;
- prepare new experiments with the setup and explore new tests on the SOFTWIND SPAR 10MW FWT.

In this chapter, the numerical model under consideration is the *as-built* one, with the as-built FWT properties. In part 8.1, the numerical model framework is presented as well as the methodology to define and validate the model. In part 8.2, the most important validations of the numerical model are first presented and then the comparisons between experimental results and numerical results for irregular waves and turbulent wind.

8.1 Defining a numerical model of the experiments

This numerical model is established at full scale because of the full scale rotor and control law used in the experiments. Full scale numerical models of the tower, floater and moorings have been established, from model scale measurements (denoted *as-built*). The numerical framework is first introduced; then, the methodology to adjust and validate the model is detailed.

As stated in the general objectives of this chapter, a first investigation concern the effects of the hydrodynamic modeling assumptions on the FWT response. In that case, mimicking the SIL system actuation limitations is required. Indeed, the effect of the actuator performances on the FWT motions has been quantified in chapter 7. To mimic the actuator performances, two aspects should be taken into account:

- The single actuator reproducing only the F_x rotor load component;
- The SIL system delay and the actuator cut-off frequency (low-pass filtering effect).

A second investigation is about the effects of the SIL system limited actuation on the FWT response. To do this, comparisons are performed on the tuned numerical model with:

- a deteriorated actuation,

- a perfect rotor loads actuation (i.e. with the 6 rotor loads components transmitted to the FWT without any delay or low pass filtering effect).

8.1.1 Numerical framework

The selected aero-hydro-servo-elastic numerical framework is OpenFAST. The rotor modeling, including the wind turbine controller and the aerodynamics, is the same as in the SIL wave tank setup. Consequently, it does not introduce a source of discrepancies on the rotor loads side.

Additionally to the OpenFAST time-domain numerical model, a simplified frequency domain model of the FWT is also built. It includes the radiation and excitation forces, the hydrostatic stiffness, the FWT mass and inertias, and a linearized damping for the additional drag. Such model is useful for platform 6-DoF motion RAOs computations, drift force evaluation, and other frequency domain characteristics. It is based on the outputs of NEMOH (Babarit and Delhommeau, 2015), a Boundary Element Method (BEM) code for computing the radiation, diffraction and incident 1st order velocity potentials. The same *hydrodynamic database* (outputs of NEMOH) is used in the OpenFAST model.

A description of the main theories of each module is given in Table 38. The selected modeling is close to the state of the art offshore code implementations, such as the ones used in the OC3, OC4 and OC5 projects (Jonkman and Musial, 2010; Amy Robertson *et al.*, 2014; Robertson *et al.*, 2017).

Module	Main theories
Aerodynamics: AeroDyn v14	BEMT with semi-empirical corrections, same files as in the wave tank setup
Servo dynamics: ServoDyn	DTU baseline controller with OO-Star PI gains, same files as in the wave tank setup.
Moorings: MoorDyn	Elastic catenary equations and lumped-mass approach. Include the hydrodynamic loads on the mooring lines based on Morison's equation.
Hydrodynamics: HydroDyn	Hybrid modeling based on potential flow theories (1st and 2nd order, QTF- only from Newman approximation) and Morison drag component.
Structural and kinematics: ElastoDyn	Kinematics: • DoF activated: 6 platform DoF, 1st fore-aft and side-side modes of the tower • RK4 temporal scheme Tower modeling: modal approach Blades modeling: modal approach

Table 38: Main theories of the different key modules

One of the main interests of wave tank testing is the validation of hydrodynamic modeling. To define the suitable hydrodynamics theory, the most important dimensionless numbers characterizing the hydrodynamics are provided in Figure 105 at model and full scales. The oscillating Reynolds number $R_e = \frac{A^2\omega}{\nu}$ (Molin, 2002) is defined for the oscillating flow conditions with A the amplitude of the fluid particle velocities relatively to the structure, ω the pulsation and ν the kinetic viscosity of the water. The Keulegan-Carpenter number $KC = \frac{2\pi A}{D}$ is defined with D the representative dimension of the structure (SPAR diameter in our case), and A the amplitude of the fluid particle velocities. R_e and KC numbers are computed at the free surface, for the different frequency bandwidth of interest (WF, Pitch NF and Surge NF), at model scale (MS) and full scale (FS). The characteristic amplitude A value is computed as a rough approximation of the wave-induced kinematics minus a significant FWT horizontal motion per frequency bandwidth for the different load cases. For most of the load cases, $0.5 < KC < 3$;

the diffraction-radiation loads should be dominating at the wave frequencies. However, some drag forces due to vortex shedding and viscous effects should also be present for severe waves, as the KC number is not very small. For resonant motions at the surge and pitch natural frequencies, the diffraction and radiation loads become very small. This encourages a hybrid hydrodynamic model mixing potential flow diffraction/radiation and Morison drag components (e.g. for resonant motions, …). Concerning the range of R_e numbers, special care should be taken for scaling up the results. For smooth surfaces, a laminar-turbulent transition around $R_e = 3E + 5$ (Molin, 2002) is expected. At full scale, the flow conditions are therefore turbulent while at model scale the flow conditions are laminar. This is part of the scale effects concerning the hydrodynamics. Investigations concerning the hydrodynamic scale effects are considered out of scope of this work.

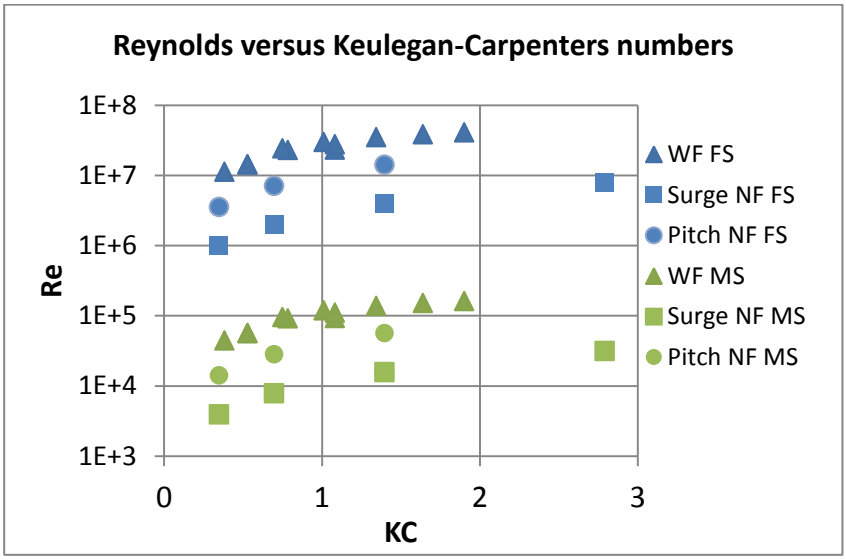

Figure 105: SOFTWIND SPAR flow conditions. Oscillating Reynolds number (Re) versus Keulegan-Carpenter number (KC)

Considering the hydrodynamic numerical framework and the differences in the flow conditions between full scale and model scale experiments, the different sources of hydrodynamic-related loads are listed in Table 39. The main underlying questions are how the model scale experiments and the numerical simulations represent those loads. The hydrodynamic-related loads are:

- Hydrostatic loads, including buoyancy and gravity. Both phenomena might be nonlinear e.g. (Lawson *et al.*, 2014);
- Diffraction: due to the diffracted wave field;
- Radiation: due to the radiated wave field. This is decomposed into added mass and damping;
- Froude-Krylov: due to the incident wave field;
- Vortex shedding and other non-potential flow phenomena.

Loading	Experimental representation	Numerical representation
Diffraction and Froude-Krylov	Respecting the Froude number ensures these loads are correctly scaled for the potential flow related part. However, the wave reflections make experimental conditions slightly different from target conditions. For the non-potential flow related part, it is not necessarily well represented as the oscillating Reynolds number analysis has shown.	• Linearized at the mean position of the free surface, • 1st order potential flow only.
Hydrostatics	Correctly scaled	Linear only for the buoyancy related part. Nonlinear for the gravity contribution.
Damping - radiation	Respecting the Froude number ensure these loads are correctly scaled for the potential flow related part.	For a SPAR platform without heave plates, it should be correctly represented by the NEMOH BEM code.
Damping – viscous flow	It is not necessarily well represented as the oscillating Reynolds number analysis has shown.	Modeled with the drag part of the Morison formula.
Nonlinear potential flow wave loadings – low frequency	It is partially correctly represented. The differences with the target wave-induced kinematics concern high-order low frequency free waves. This can excite the surge natural frequency.	Potential only 2nd order low frequency using the Newman approximation.
Nonlinear potential flow wave loadings – high frequency	It is partially correctly represented. The differences with the target wave-induced kinematics concern high-order high frequency free waves.	Not modeled. This should not have a large impact for this SPAR platform. This is important for TLP type platforms.

Table 39: Representation of different sources of hydrodynamic-related loadings. Qualitative analysis.

Concerning the low frequency nonlinear wave loadings, it is shown in appendix D that the 2nd-order low frequency waves that are present in the wave tank are negligible compared to the high frequency free waves or to the 1st harmonic. On the numerical side, the Newman approximation should represent approximately correctly the potential flow related excitation due to the low value of the surge natural frequency.

To conclude, the numerical framework has been presented. For the hydrodynamic part, different assumptions can explain possible differences between the experiments and the numerical simulations. However, it has been shown that the flow conditions at model scale are not the same as the full scale ones: extrapolation to the full scale should be done by quantifying the scale effects, especially the impact of the Reynolds number mismatch on the FWT response.

8.1.2 Methodology

Different methodologies could be used to define and tune the corresponding numerical model of the experimental setup. In all cases the starting points is to define the correct mass and geometry properties from the experimental measurements. Note that some of the identification tests have been used to validate the main inputs to the models. Indeed, due to the measurement uncertainties of e.g. the center of mass and floater inertia (cables, difficulties in handling the system on the CM measurement

apparatus), the steady-state properties (platform equilibrium position without any external loads applied, platform trim for different actuator thrusts) are used to gain more confidence in those inputs. Then, the main question is about the set of parameters that need to be identified from the experiments. Different methodologies have been identified to build the model:

- The "engineering limited experimental data" model, where most of the inputs, except mass and geometry, are based on numerical computations. This includes, among others, the different parameters in the Morison drag formula (hydrodynamics forcing on the mooring lines and on the floater), and the structural damping of the tower.
- The "engineering experimental data fit" model, where the identification tests such as the decay tests and the motions time series in irregular waves and turbulent wind are used to adjust the different numerical model parameters. This calibration of the parameters is for instance explained (Kvittem *et al.*, 2018), but there is no standard procedure to tune the parameters in the numerical models. Indeed, it completely depends on the implementations of the numerical models.

The "engineering limited experimental data" is not implemented in the present work but the drag coefficients are compared to commonly used values.

The definition and validation procedure is the following:

- Definition of the mass, stiffness and geometry inputs for the floater, tower and moorings. The hydrodynamic database of the floater (radiation and diffraction coefficients) is included. The damping is approximated at this stage. Each subsystem is validated independently when possible and then the FWT is validated:
  - Tower: validation of the tower mass, stiffness and natural frequency for a cantilevered condition.
  - Moorings: verification of the mooring stiffness at equilibrium position and of the surge-restoring force relation.
  - Floater: Equilibrium positions, validation of CM and dimensions with connections to the tower.
  - FWT: Verification of the natural frequencies.
- Tuning of the drag coefficients to match decay tests. Comparisons between quadratic and linear integrated damping and Morrison elements.
- Verifications of the motion RAOs in regular waves; Verification of wave drift forces.
- Verifications of the motion RAOs and time series for irregular waves; Investigations of differences.
- Irregular waves and turbulent wind; Investigations of differences.

One of the important adjustments is the definition of the drag properties of the FWT, different parameters are either obtained from the literature or tuned based on the different tests (decays, ..). The different identified methodologies are:

- As for the OC4 project (A. Robertson *et al.*, 2014), Morison drag coefficients are computed from existing drag coefficients for oscillating and steady flows;
- Then, different options to tune the drag from model scale flow conditions are used:
  - The linear and quadratic damping identified from the decay tests are used as inputs in the numerical model by means of 6 DoF matrices;
  - The Morison drag coefficients are tuned to match the decay tests with and without waves;

    - The drag coefficients are tuned to match the irregular waves and turbulent wind responses
- Between the different drag modeling approaches (6 DoF linear and quadratic damping matrices and discretized Morison drag coefficients), the Morison drag coefficients approach has been considered to be more representative.

The inputs provided to the numerical model are detailed in Appendix D.

8.1.3 Reproducing the actuator behavior

To take into account the actuation system limitation, the modifications detailed in chapter 3 are used. The differences with the experimental setup are:

- In the experimental setup, only the F_x rotor load is actuated. In OpenFAST, the F_x and M_x rotor load components are actuated as well as the gyroscopic M_z and M_y torques. The M_z gyroscopic torque is small compared to the aerodynamic M_z torque, but contributes to the yaw motion.
- In the experimental setup, there is a pure delay due to the motion observer, communication protocols, and actuator pure delay response. The total pure delay has been estimated to approximately 0.2s at full scale. In OpenFAST, the pure delay is not reproduced.

Note that for the *dynamic calibration* results, the low pass filtering effect is negligible (see chapter 6 for details).

8.2 Comparisons between measurements and simulations

8.2.1 Tuning and validation of the model

8.2.1.1 Decay tests

Heave, surge, and coupled surge-pitch decays are run with the numerical model, similarly to the decay tests performed in the wave tank. Decay tests are first performed in still water. The natural periods are validated and the hydrodynamic damping is tuned in still water conditions. Then, decays are performed in regular waves to investigate the consequent modification of the damping.

The Morison drag coefficients are tuned to get decay tests in the numerical model superposing with experimental decay tests. Details about the Morison elements implementations are provided in appendix D.

The drag coefficients that make the numerical surge, pitch and heave decays match the experimental decays are $C_{d\,ax} = 5$ and $C_{d\,n} = 0.3$. $C_{d\,ax}$ is the axial coefficient at the bottom of the SPAR, and $C_{d\,n}$ the normal (also called transverse) drag coefficient for the different sections of the SPAR. For fitting the pitch motions, a normal drag coefficient $C_{d\,n} = 0.5$ works better. Consequently, a quadratic damping term only for the pitch motions is added, $B_{drag\ quad}(5,5) = 1E + 10\frac{N.m}{[rad.s^{-1}]^2}$. It is assumed that the floater has an axisymmetric hydrodynamic behavior. Therefore, a roll quadratic damping is also assumed $B_{drag\ quad}(4,4) = 1E + 10\frac{N.m}{[rad.s^{-1}]^2}$. The yaw DoF is governed by the mooring system delta-connection that provides a large mooring stiffness and a large damping (due to the drag forces acting on it).

The natural periods extracted for the different DoFs are presented in Table 40. The numerical model natural periods match very well to the experimental results, which is a good indicator of the correct implementation of the system properties.

DoF	Expe. nat. period [s]	Num. nat. period [s]	Differences [%]
Surge	117.5	121	+3
Sway	116.5	122	+4.7
Heave	30.6	30.6	0
Roll	32.5	32.0	-1.5
Pitch	32.6	32.1	-1.5
Yaw	10.5	13	+23
Tower F-A 1st	2.61	2.82	+7.7

Table 40: Natural periods from decay tests in still water, experimental and numerical results

Decay tests with waves

In chapter 7, it has been highlighted the coupling between the wave frequency and the resonant motions at the natural frequencies, To investigate this in terms of damping, decay tests with waves are compared to decay tests without waves. This has been done for the surge DoF for the two following regular waves conditions:

- RW_1: $H = 1.9m$ and $T = 8.0s$,
- RW_2: $H = 3.4m$ and $T = 11.0s$

The numerical and experimental damping ratios (critical $\zeta[\%]$) as function of the oscillations amplitude are considered. An illustrative drawing is depicted in Figure 106. On this graph, a constant damping ratio with oscillation amplitude denotes a linear damping, while a linearly decreasing damping ratio (constant slope) with decrease of the oscillation amplitude denotes a quadratic damping. Basically, the linear damping is defined from the intercept and the quadratic damping from the slope.

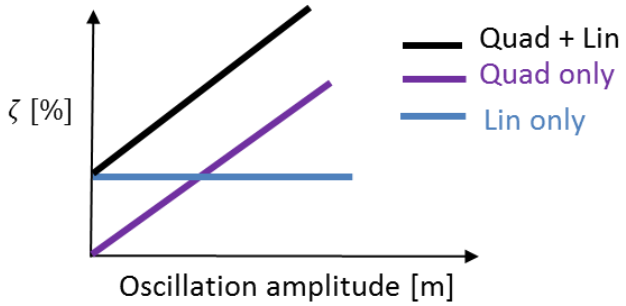

Figure 106: Damping ratio as function of oscillation amplitude

Results are presented in Figure 107. The regular waves condition significantly increases the level of linear damping. The larger the wave kinematics (increase of H and T), the larger the linear damping.

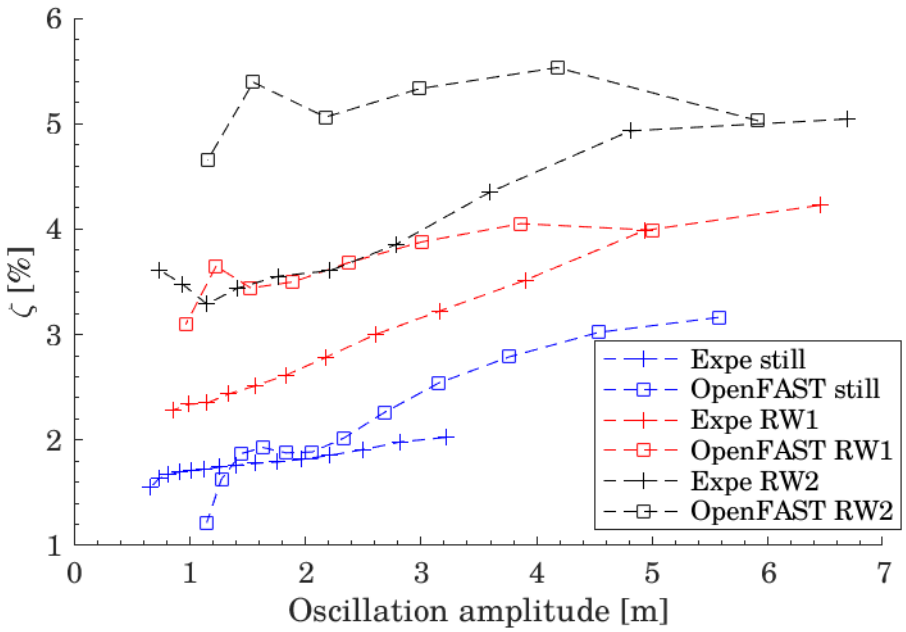

Figure 107: Evolution of damping ratio with amplitude of the oscillations. Numerical versus experimental, with and without regular waves

The reason why a linear damping of the low frequency motion appears in regular waves is well explained in, e.g. (Le Boulluec *et al.*, 1994; Molin, 2002). The main highlights are presented hereafter.

Consider a drag force acting on a portion of the SPAR or on the mooring lines, the widely used Morison relative flow formula is expressed in Eq. (7.1):

$$F_{drag} = \frac{1}{2}\rho C_D A\, U_{rel}|U_{rel}| \tag{8.1}$$

With:

- ρ the water density,
- C_D the drag coefficient. Normal flow is considered.
- A the normal area under consideration,
- U_{rel} the relative velocity of the fluid minus the wave-induced kinematics.

The Morison formula and typical values of drag coefficients have been obtained experimentally for steady flows and harmonic fluctuations of the flows. A problem appears when one uses this formula for multi-harmonic kinematics due to the wave-induced kinematics, to the wave frequency motions and to the low frequency motions. Two versions of the Morison formula, depending on how the flow behaves, have been defined (Molin, 2002):

- The *dependent flow* formula, using the total instantaneous fluid particle velocity on the body,
- The *independent flow* formula, splitting the low frequency (and eventually steady current) on one side and the wave frequency velocities on the other side.

The independent flow Morison formula consists in splitting the different frequencies. It is expressed in Eq. (8.2):

$$F_{drag} = \frac{1}{2}\rho C_{D\,WF} A \left(U_{wave} - \dot{X_{WF}}\right)\left|U_{wave} - \dot{X_{WF}}\right| + \frac{1}{2}\rho C_{D\,LF} A\, \dot{X_{LF}}\left|\dot{X_{LF}}\right| \tag{8.2}$$

With U_{wave} the wave-induced velocities, $\dot{X_{WF}}$ the wave frequency (WF) body motions, and $\dot{X_{LF}}$ the low frequency (LF) body motions. $C_{D\,WF}$ is a drag coefficient for the WF oscillating fluid particle

velocities and $C_{D\,LF}$ another drag coefficient, possibly different, for the LF oscillating fluid particle velocities.

The *independent flow* formula leads to a quadratic damping of the wave frequency motions and to a quadratic damping of the low frequency motions.

On the other side, the *dependent flow* formula applies directly the Morison formula without any considerations about the frequency of oscillations of the fluid particles velocities, as expressed in Eq. (8.3):

$$F_{drag} = \frac{1}{2}\rho C_D A \left(U_{wave} - \dot{X_{WF}} - \dot{X_{LF}}\right)\left|U_{wave} - \dot{X_{WF}} - \dot{X_{LF}}\right| \tag{8.3}$$

The *HydroDyn* module of OpenFAST implements this *dependent flow* formula. In large waves ($U_{wave} \gg \dot{X_{LF}}$), the dependent flow formula expression is approximated to Eq. (8.4):

$$F_{drag} \sim \frac{1}{2}\rho C_D A \left(\left(U_{wave} - \dot{X_{WF}}\right)\left|U_{wave} - \dot{X_{WF}}\right| + 2\left|U_{wave} - \dot{X_{WF}}\right|\dot{X_{LF}} + O\left(\dot{X_{LF}}^2\right)\right) \tag{8.4}$$

A term linearly proportional to the low frequency motion $\dot{X_{LF}}$ appears: this term is the additional linear damping of the LF motions due to the WF kinematics. The larger are the wave kinematics (term $\left|U_{wave} - \dot{X_{WF}}\right|$), the larger is the linear damping.

The *dependent flow* formula forces might be right for the mooring lines (high KC numbers), but is not necessarily valid for the floater. The validity depends on the dimensions and shape of the platform, and has been thoroughly investigated for Oil and Gas platforms that have typically smaller KC numbers than the considered SPAR. However, this Morison formula implementation is not available in the *HydroDyn* module of OpenFAST; it has not been tested in the present work.

Comparing the simulations with the experimental results, the linear damping component is more important in the numerical model. This might be due to:

- Over-estimation of the mooring line drag coefficients. However, when looking at the regular waves mooring lines tensions, the variations of the tensions are similar to the mooring lines tensions in the wave tank. Moreover, it has been observed in (Azcona *et al.*, 2017) the good consistency between full scale and model scale drag coefficients for mooring chains.
- Poor validity of the dependent flow formula for the floater.

This mismatch between calibrated damping coefficients for surge low frequency motions in decay tests and suitable damping coefficients in severe sea states has already been observed, e.g. in (Kvittem *et al.*, 2018). The conclusion is that using the Morison formula in a "*dependent flow*" formulation should be done carefully. For some configurations (wave conditions and floater type) using an independent flow formula may lead to better results. These conclusions are extracted from model testing. However, as presented in Figure 105, the flow conditions are more turbulent at full scale than at model scale: the appropriate formula at full scale is not necessarily an *independent flow* formula.

To conclude on the drag coefficients tuning in the numerical model, the following set of coefficients is used:

- $C_{d\,n\,floater} = 0.3$, the normal drag coefficient on the floater;
- $C_{d\,ax\,floater} = 5$, the axial drag coefficient at the bottom of the floater;
- $B_{drag\,quad}(5,5) = B_{drag\,quad}(4,4) = 1E+10\,\frac{N.m}{[rad.s^{-1}]^2}$, the additional quadratic damping for the pitch and roll motions;
- $C_{d\,n\,moorings} = 2.4$, the normal drag coefficient of the mooring lines.

The $C_{d\,n\,floater}$ value is smaller than the typical full scale values found in the literature for normal drag coefficient of circular cylinder (e.g. $C_{d\,n}$~0.6 in (Jonkman, 2010) from steady flow, $C_{d\,n} \in [0.5 - 1.5]$ from (Molin, 2002, chap. 4.3)). The outcome is that state-of-the-art engineering practices tend to underestimate the low frequency motions.

The consequence of the poor damping fit for decay tests in waves is that for small amplitudes of the low frequency motions and non-negligible wave frequency motions, the numerical model overestimates significantly the damping. For this SPAR, the surge low frequency motions in wave-only tests are expected to be underestimated by the numerical model. However, for turbulent wind and wave tests, the drag damping should be in the correct range.

8.2.1.2 Regular waves

Motion RAOs

The motion RAOs of the FWT have been computed from regular waves and irregular waves tests. In this subsection, the regular waves motion RAOs are considered. Note that the theoretical and practical background about RAO estimations from different kind of excitations is detailed in Appendix B.

Concerning the experimental results, the platform motion RAOs are computed for wave steepness $\epsilon = \frac{H}{\lambda}$ between 2% and 6%, with H the wave height (peak to trough) and λ the wavelength. These results are compared to the simplified frequency domain simulations (denoted *NEMOH FD*) and the time domain simulations (denoted *OpenFAST TD*). For the latter, the considered wave steepness is $\epsilon = 2\%$ with a maximal wave height of $H \leq 4m$.

The amplitude and the phase of the three DoFs excited by the incident waves (surge, heave and pitch) are depicted in Figure 108. It is clearly visible that the experimental platform motion RAOs are independent of the wave steepness. There are some small discrepancies for the phases of those RAOs, but the phase differences are significant when the motion amplitudes are very small. For those very small amplitudes, the phase is not well computed from a Fourier domain analysis. The two numerical models superimpose very well with the experimental results. The frequency domain model is even closer than the time domain results. There are some discrepancies for the phase plots, but a part of the discrepancies can be explained by an offset between the X-position of the reference wave gauge and the equilibrium position of the platform in the wave tank.

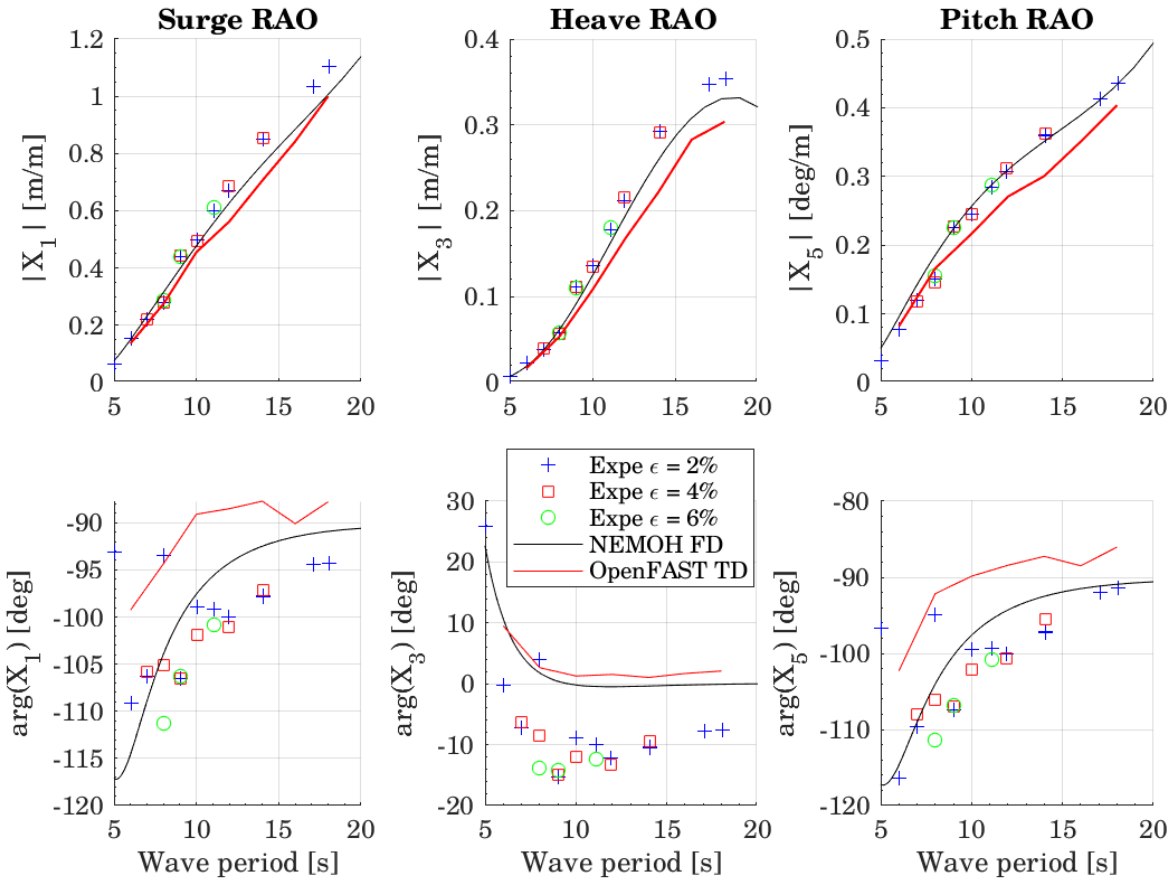

Figure 108: Experimental Surge, Heave and Pitch RAOs for different wave steepnesses and comparison with numerical computations

The influence of the aerodynamic loads is also investigated through regular waves and steady wind cases. A limited number of regular waves and steady wind conditions have been tested in the experimental setup using the SIL approach. Comparisons between numerical results and experimental results are depicted in Figure 109.

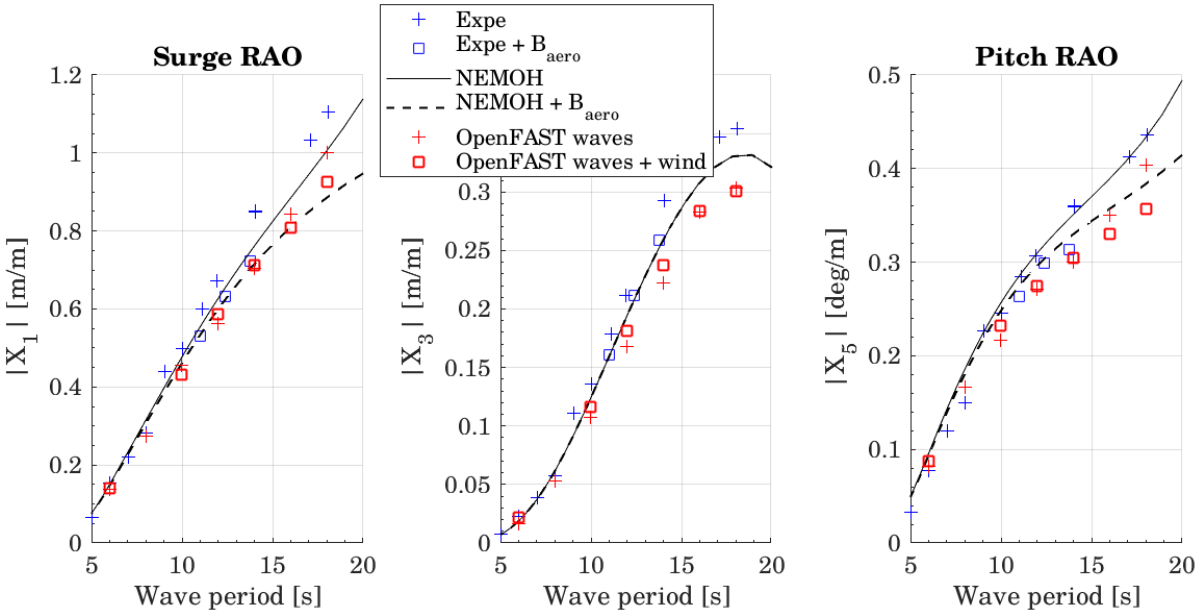

Figure 109: Surge, Heave and Pitch RAOs with and without steady wind

The aerodynamic damping has a minor influence on the platform surge and pitch RAOs for this setup (crosses (+) versus squares). The minor influence is predicted by the frequency domain model for wave periods above 12s and by the fully-coupled model for the wave periods of 16s and 18s. As for the experimental results, the main characteristic of this comparison is the larger is the wave period, the more important is the rotor load influence. This is due to the varying radiation damping with the frequency. The radiation and aerodynamic damping (estimated from the *drag disc* simplified model with a wind speed of $U_w = 12\,m.s^{-}1$) are depicted in Figure 110 for the (1, 1) (respectively (5, 5)) coefficients corresponding to the F_x force due to the surge velocity (respectively M_y moment due to the pitch velocity). The critical damping is estimated from the mass (respectively inertia I_{yy}), the 0-frequency added mass and the mooring stiffness (respectively the pitch hydrostatic stiffness). The radiation damping is maximum for wave period around 10s and then falls down to reach very small value beyond 20s. For the pitch damping ($B(5,5)$), the aerodynamic damping is significantly bigger than the radiation damping. However, the wave frequency motions are not resonant motions: their amplitudes are only marginally dependent to the damping levels. That is the reason why the rotor load influence seems small on the FWT motions.

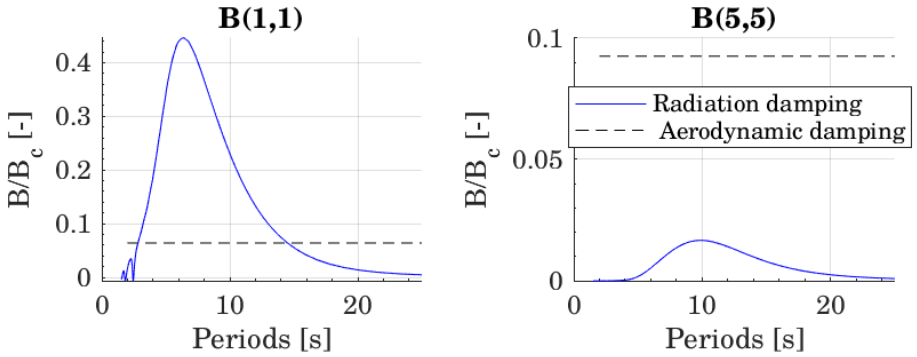

Figure 110: Radiation and aerodynamic damping ratios

To conclude, for regular waves, the FWT behaves linearly and could be well represented both by the simplified frequency domain model and by the fully-coupled time domain model. The rotor loads influence is marginal, and is captured for long wave periods both by the fully-coupled time domain and the simplified frequency domain models.

Wave drift forces RAOs

The low frequency responses, at the surge and pitch natural frequencies, are of interest in this work, as the rotor load influences occur especially within these frequency bandwidths. It has already been noted in chapter 7 the small influence of the wave excitation compared to the rotor load excitation at those frequencies. However, the potential related wave drift force scales with the square of the wave height. To check the numerical model inputs that will provide low frequency excitation and damping, the horizontal wave drift force is computed from the regular waves tests. The mean surge offset on the usable portion of the regular wave signal is computed, as presented in chapter 5. Then, from the surge - horizontal restoring force relation obtained from pull-out tests, the wave drift force is computed. As the wave drift forces are expected to be small for a SPAR, a threshold for detection is used (offset >2mm). For the numerical computation of the wave drift force, the Kochin functions of NEMOH are used for the "far-field" (momentum integration) computation of these forces. The two drift forces RAO are depicted in Figure 111 and superimpose very well. The corresponding wave drift force input file from NEMOH could be safely used in the FWT numerical model. Note that, for the wave periods of interest ($T > 9s$), the horizontal wave drift force is very small for this floater compared to the other source of

loads. Consequently, it is tempting to neglect this effect. However, the sea states considered have a small JONSWAP peak enhancement factor (incident wave energy spread on a large band of wave frequencies); moreover, a low frequency damping (wave drift damping) is also derived from this wave drift force. The best option is to integrate it into the numerical model.

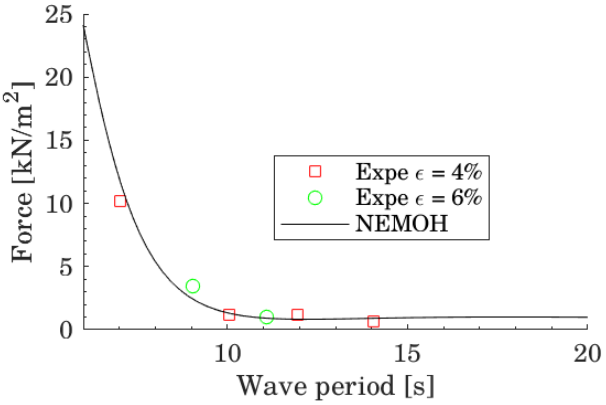

Figure 111: Experimental and numerical (NEMOH) horizontal wave drift force RAOs.

8.2.2 Irregular waves and turbulent wind

The OpenFAST model is now validated in irregular waves without and with turbulent wind. The validation is based on the superimposition of time-series and also PSDs. Note that, to get meaningful comparisons with the experimental tests, the same time history of waves and wind is considered. This deterministic reproduction (instead of stochastic only) has been done for several reasons:

- The tests are not long enough to get a statistically sufficient number of oscillations, especially for the low frequency motions,
- Only one *seed* of the pseudo-random generators has been tested per load case. Averaging over different seeds could not be performed.
- This provides more insights about temporal varying differences between the numerical model and the experimental tests.

The wave elevation is defined from a wave probe of reference, located close to the reference point of the numerical model (inertial frame origin) but not exactly at this point (offset of 2.8m at full scale is only 7cm at model scale). The set-up layout is described in chapter 5. The irregular wave elevation signal is then transported to the inertial frame origin, assuming linear wave theory for propagating the free surface elevation.

LC nb	$H_s[m]$	$T_p[s]$	$U_w[m.s^{-1}]$	$T_I[\%]$
LC1.1	5.8	10.9	/	/
LC1.2	5.8	10.9	18.0	17.0
LC2.1	7.7	12.4	11.4	15.1
LC2.2	7.7	12.4	11.4	15.1

Table 41: Wind and waves conditions considered for the SOFTWIND SPAR experimental and numerical comparisons

8.2.2.1 Wave-only

The PSDs of the surge and pitch DoF are depicted in Figure 112 for the LC1.1 (waves only). *Expe* is for the experimental results and *Num* for the numerical results.

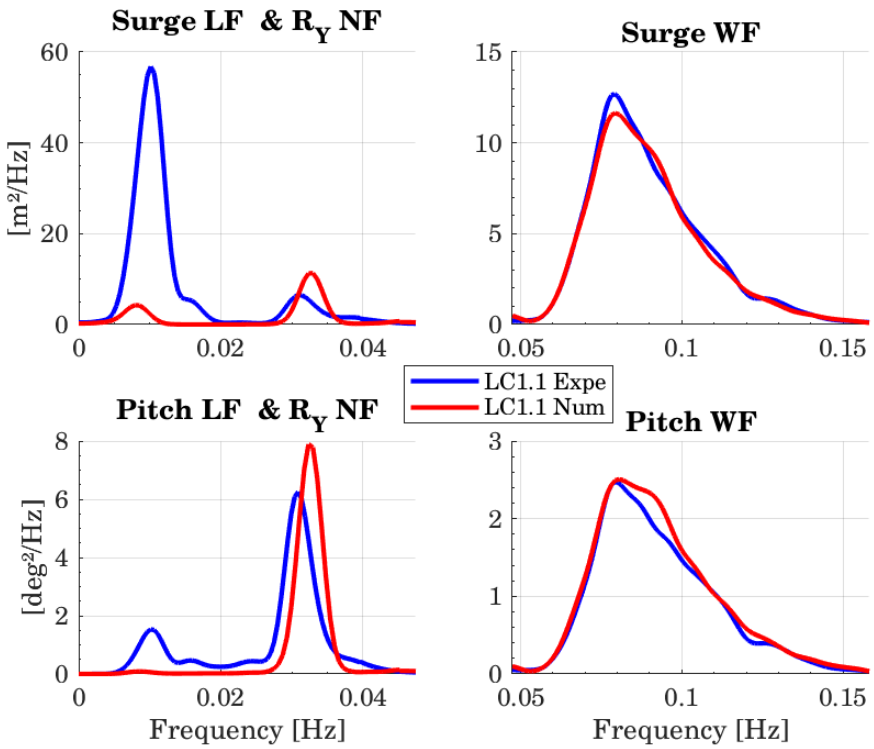

Figure 112: Surge and pitch PSDs for LC1.1

There are minor (negligible) differences at the wave frequency bandwidth. At the pitch natural frequency, the numerical motions are larger than the experimental motions, and the natural periods are marginally different. However, the pitch resonant motions are small compared to the wave frequency motions: differences on the resonant motions have no large impact on the total pitch motions.

At the surge natural frequency (0.008Hz), the discrepancies of the surge motion (figure top left) are substantial, the numerical model severely underestimating the motion (one order of magnitude on the PSD peak). This is due to:

- The overestimated damping for relative small low frequency oscillations, as seen in part 8.2.1.1.
- Under estimation of the low frequency wave excitation. The potential part is computed using the Newman approximation, but there is no viscous drift force in the splash zone for instance.
- Spurious long waves in the tank that could be:
    - second-order free waves generated by the wavemaker. The free wave content has been analytically computed and seems of low amplitude for that wave condition.
    - natural modes of the wave basin excited by the wave generation. The first three natural modes have full-scale frequencies of 0.012, 0.024 and 0.036 Hz for the wave basin of length 46 m and depth 5 m. Assessment of modes amplitude is required and could be done by placing wave probes at the nodes location.

Moreover, the experimental LF motions are not negligible compared to the WF motions. The differences are not negligible on the total surge motions.

This analysis has been applied to the LC2.1 with exactly the same conclusions.

8.2.2.2 Waves and wind

The PSDs of the surge and pitch DoF are depicted in Figure 113 for the LC1.2 and LC2.2. The wave frequency bandwidth is not represented as the numerical results superimpose very well with the experimental results.

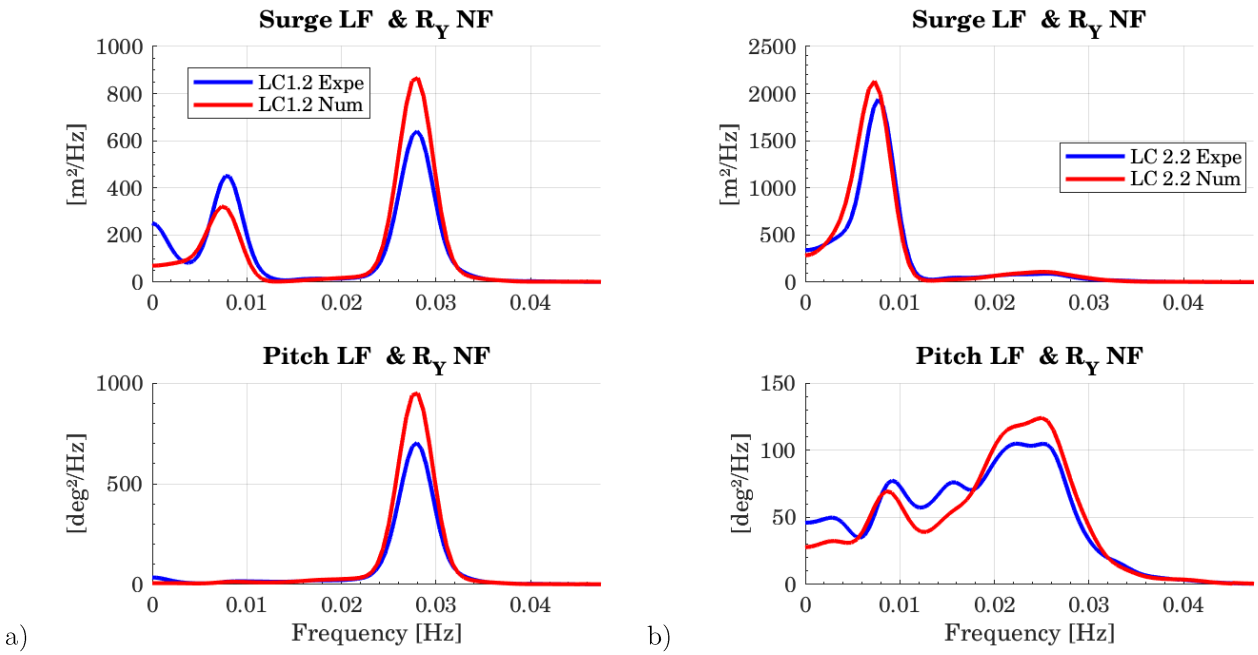

Figure 113: Surge and pitch PSDs for a) LC1.2 and b) LC2.2

Overall, the numerical results superimpose well with the experimental results. In both load cases, the change in the pitch natural frequency from waves only tests is captured. The pitch motions are a slightly overestimated by the numerical model while for the surge motions, the numerical results are much closer to the experimental results than in the wave-only cases. This is due to the fact that low frequency aerodynamic excitation is stronger than low frequency wave excitation. For LC1.2, the surge LF motion are a slightly underestimated while for the LC2.2, the surge motions are marginally overestimated. This difference in the behavior can still be explained with the decay tests background. Indeed, the surge LF oscillations are larger for LC2.2 than for LC1.2: the resulting damping is not overestimated for LC2.2 while it is still overestimated for LC1.2.

To conclude on the motions comparisons, the numerical results superimpose well with the experimental results. It has been seen than the pitch natural motions are slightly over estimated by the numerical model in wave-only and waves and wind load cases. For the surge natural frequency motions, results are consistent with observations made from decay tests with and without waves.

8.2.3 Effect of actuation system limitations

The actuation system limitations are here investigated by means of numerical simulations. The objectives are to address:

- the impact of the actuator cut-off frequency on the pitch motions. This is important to confirm the observations made in chapter 07.
- the differences between a fully actuated and a single actuated rotor load. This is similar to the study of chapter 3 but on the SOFTWIND SPAR setup, for which the hydrodynamic model is tuned to get the correct low frequency motions.

8.2.3.1 Actuator cut-off frequency

The load case LC1.2 defined in Table 35 is considered, which is similar to the LC1 of part 7.3. As in the experiments, three cases are compared:

- High cut-off frequency. This is the case presented in the previous part.
- Actuator cut-off frequency $f_{c\,1} = 0.16Hz$,
- Actuator cut-off frequency $f_{c\,2} = 0.08Hz$.

In Figure 114, the surge and pitch PSDs are compared between the experimental and the numerical results. Bypassing the difference of peak amplitudes between the two reference cases (high cut-off frequency), the attenuation is well reproduced at the pitch natural frequency in the numerical simulations. The small variation of the PSDs visible at the surge natural frequency for the numerical results is not visible for the experimental results. Due to the surge/pitch coupling, if the pitch decreases, the surge also decreases. Consequently, splitting the surge and pitch analyses is prone to errors and the modifications of the pitch might explain a part of the surge motions change with actuator cut-off frequency. Note that defining the surge motion at the center of rotation of the SPAR (between the center gravity and the center of buoyancy) can decrease the apparent coupling between the surge and pitch.

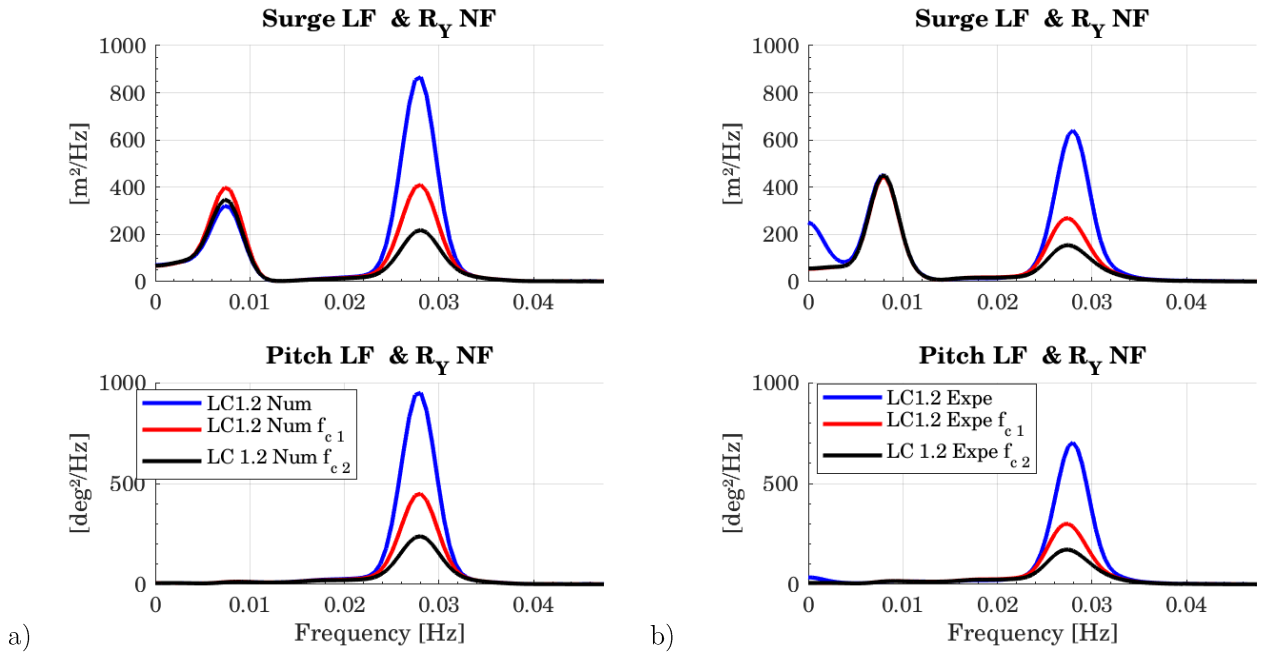

Figure 114: Surge and pitch PSDs for LC1.2 a) numerical and b) experimental results

To conclude, the attenuation observed in chapter 7 between different tests is confirmed to be linked to the cut-off frequency of the actuator. It is worth mentioning that the numerical simulations, when the model is correctly tuned (especially for the damping), can capture those effects.

8.2.3.2 Rotor load component addition

Similarly to the study done in part 3.3.2 comparisons are made between a fully actuated system and the F_x & M_x actuated configuration. The objective is to quantify, for this FWT with a model tuned on the experimental results, the differences in the motions. Two cases are compared:

- F_x & M_x actuation,
- *Fully-actuated*, with the 6-rotor load components being reproduced.

Note that although not presented here, tests have also been performed by removing one by one the load components in order to understand the effect of each DoF. In Figure 115, the surge and pitch PSDs are represented for the surge NF and R_Y NF frequency bandwidths. The fully-actuated case has a standard deviation of the pitch response 25% smaller than for the F_x & M_x actuated case. The platform pitch and surge attenuations are mainly due to the M_y rotor load component that contributes to pitch aerodynamic damping. At the surge natural frequency, the surge PSDs are the same for the single actuator and the fully actuated system which means that the single actuator is enough to correctly reproduce the surge natural motion.

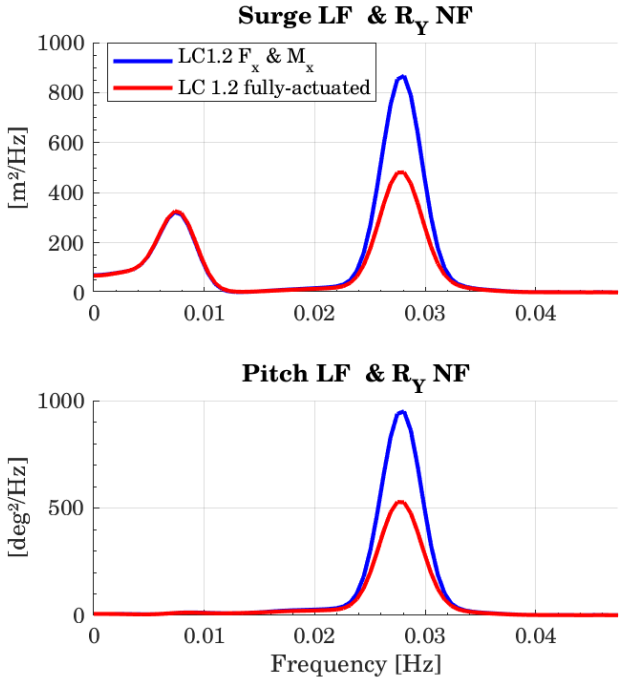

Figure 115: Surge and pitch PSDs for fully-actuated versus partially actuated LC1.2 numerical results

The six platform-DoF time series are depicted in Figure 116. The DoF excited by the waves and by the single actuator (in-plane, surge, heave and pitch) are on the left, and the out-of-plane DoF (sway, roll yaw) are on the right. The standard deviations of the DoF (all the frequency) for the two cases are listed in Table 42.

	$\sigma_{surge}[m]$	$\sigma_{sway}[m]$	$\sigma_{heave}[m]$	$\sigma_{roll}[deg]$	$\sigma_{pitch}[deg]$	$\sigma_{yaw}[deg]$
Fully-actuated	2.56	0.19	0.30	0.18	2.29	0.48
F_x & M_x actuation	2.20	0.62	0.32	0.52	1.80	1.33
Differences [%]	17	-69	-5	-64	27.3	-64

Table 42: Standard deviations of the motions DoF. fully-actuated versus partially actuated numerical results for LC 1.2

The in-plane DoFs have some differences, especially for the pitch motions, as mentioned above from the PSDs observations. Larger differences were expected for the platform heave, but due to the large wave kinematics ($H_s = 5.8m$) the F_z rotor load does not play a significant role. Moreover, the SPAR platform of chapter 3 was significantly lighter than this SPAR.

Note that the sway/roll and surge/pitch coupling are over-amplified by the selection of the center of rotation at the MSL and not at vertical position of the center of rotation. The 17% difference of the surge motion is entirely explained by the surge pitch coupling due to the center of rotation selection.

When selecting the center of rotation at the CoG position, the resulting difference on the "pure" surge motion is 2%.

All of the out-of-plane DoFs have very different behaviors between a fully actuated and a F_x & M_x actuation, with a standard deviation reduction between 60 and 80%. The sway and roll motions are governed by the F_y rotor load while the yaw motion is governed by the M_z rotor load. The M_x rotor load has a contribution of the mean roll but has a significantly smaller impact on the dynamic roll than the F_y rotor load component. This observation is done for an above-rated load case: for below-rated condition, the dynamic torque can also excite the roll motions of the FWT. Note that the standard deviations of the out-of-plane DoF are not negligible: modeling them with the actuation system is important for future studies.

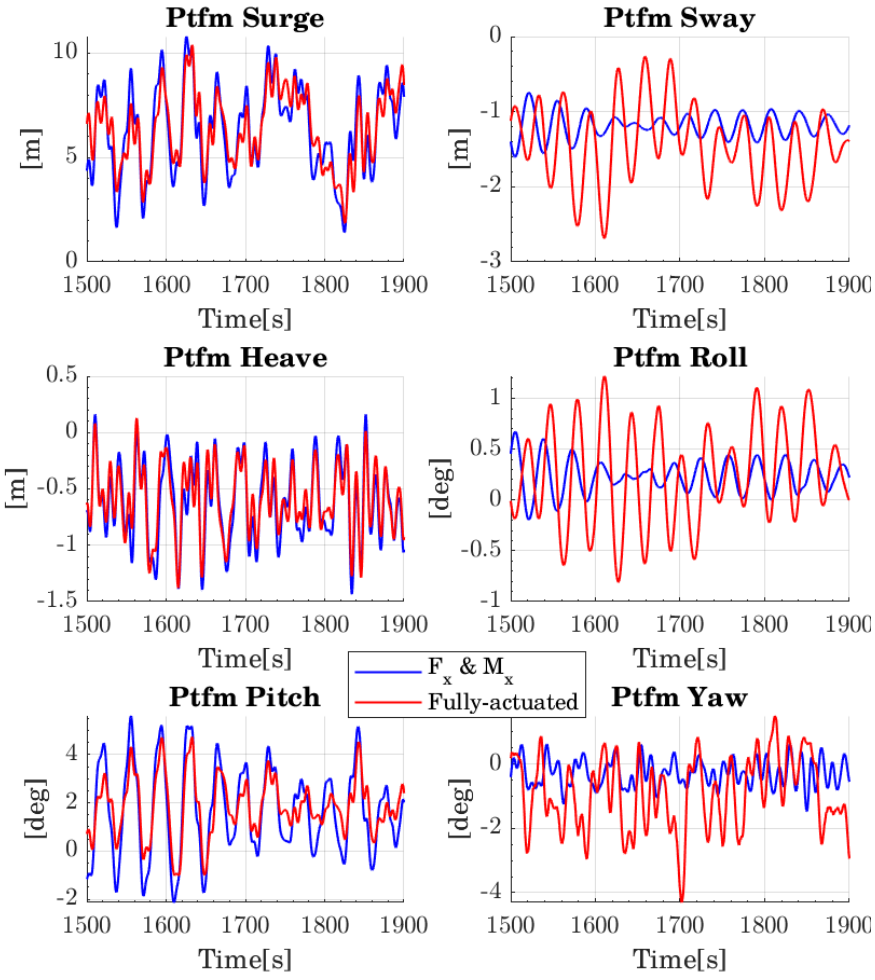

Figure 116: Platform 6-DoF for LC1.2, fully-actuated versus partially actuated numerical results

This numerical study on the actuation system limitation confirms the experimental observations in chapter 7 and the observations made in chapter 3 on other floaters. It also corroborates the need for a multi rotor-load components actuation. Finally, the multi-propeller system presented in chapter 5, which actuates F_x, M_y and M_z, can increase the fidelity of the SIL system if the cut-off frequency could be sufficiently high. To capture correctly the sway and roll motions, reproducing F_y and ideally M_x are required.

8.3 Conclusions

A methodology to define and validate a numerical model of the SOFTWIND SPAR experiments has been presented. A state of the art fully coupled numerical model has been established in the OpenFAST framework. A simplified frequency domain model has been established for wave frequency motions computations. Both superimpose well with regular waves tests, with and without wind. Then, the non-modeled physics of the fully coupled model (i.e. drag) has been tuned from decay tests. Some discrepancies between experimental and numerical results have been observed, especially in case of multi harmonics motions.

Then, the tests performed in the wave tank have been replayed in the numerical simulations. Even if, for irregular waves only tests, the overall agreement on the main quantities of interest is not satisfactory, the agreement is much better for irregular waves and turbulent wind. The main highlighted reason is about the modeling of the damping due to the hydrodynamic drag, which is not necessarily well captured by the Morison formula as implemented in the *HydroDyn* module of OpenFAST.

Eventually, the effects of the actuation system limitations have been partially reproduced numerically, as in chapter 3. The observations in chapter 7 on the actuator performance effects are recaptured in the numerical simulations. Additionally, the effect of a single actuator is also investigated. The load component removal (fully actuated versus single actuator) impacts the out-of-plane motions, i.e. sway, roll and yaw motions, which have negligible excitation (both hydrodynamics and rotor loads). It also impacts the platform pitch.

9 Conclusion and perspectives

Contents

This PhD thesis addresses the design and validation of an experimental apparatus to model rotor loads during FWT wave tank testing. It focuses on the architecture of a software-in-the-loop (SIL) system, the required developments of each sub-system and the performances characterizations as well as the performed identifications. The SIL system has been successfully designed and implemented in different test campaigns.

This last chapter presents the conclusions of this work with recommendations for the SIL system development and future works on this topic.

9.1 Conclusions

Several questions have been addressed in this PhD thesis. Partial conclusions have been summarized at the end of each chapter. In this section, the main conclusions are wrapped-up.

All the comparisons and characterizations performed in this work use indicators based on the most important FWT frequency bandwidths. For a physical system such as a FWT that is submitted to a large range of excitations, the frequency bandwidth analyses provide insights about different effects without decoupling the phenomena, i.e. studying one by one the different solicitations.

9.1.1 Rotor loads characterization

In chapters 2, 3 and 4, the rotor loads that have to be reproduced by the actuators in a SIL setup have been identified and characterized.

The characterization of the setpoint loads for the actuators was based on a review of driving physical phenomena and a parametrical study using aero-hydro-servo-elastic computations. The setpoint loads have been characterized in terms of statistical indicators (minimum, mean, maximum) but also in

terms of frequency content. The spectral content of different quantities of interest was presented. The original contributions of these studies are about the different load cases and floating wind turbines under consideration. Those specifications constitute an important input for the choice and the design of the actuation system.

The parametrical study was extended to mimic the experimental setup limitations (load component removal and low-pass filtering effect). Some guidelines have been provided in chapter 3, and this has been applied in chapter 8 to a FWT numerical model tuned on the SOFTWIND SPAR experiments.

9.1.2 SIL system design

The different subsystems of the SIL methodology have been presented with their specificities. The focus is on the design effort and the corresponding fidelity increase. The three main subsystems are:

- The *numerical model* for the rotor loads full scale simulation,
- The *actuators* that reproduce the setpoint load computed by the *numerical model*,
- The *real-time environment* that integrates the *numerical model*, masters the data acquisition (DAQ) and the corresponding *observers* and controls the *actuators*.

9.1.2.1 Numerical model

The suitable numerical models for the full-scale computations of the rotor loads have been identified and characterized. It has been shown all along this manuscript the reasons why this model must depend on the incident wind fields, the control strategy, and the real-time measured motions of the FWT.

In order to evaluate the motivations for the integration of the numerical model, comparison between simplified models (i.e. drag disk, steady-state thrust curve) and state-of-the-art models that run in real-time (i.e. BEMT) have been performed. The corresponding physical characteristics (damping, out-of-phase components) have been extracted. The main outcomes are that the discrepancies between the simplified models and OpenFAST depend on the characteristic frequency of the hub wind speed fluctuations. The integration of the wind turbine control law is mandatory to get the correct damping and out-of-phase components of the F_x rotor force.

9.1.2.2 Real-time environment

The architecture for the software-hardware integration is the first item to consider. This depends on the type of actuators (on-board or earth-fixed). Then, the motion and the force observers are presented, with their main characteristics.

Without feedback control, the performances of the force observer are not crucial to improve the bandwidth and delay of the actuators. However, these performances are crucial to have a successful identification of the actuator performances. Without this identification, it might be hard to reproduce numerically the exact conditions of the tests and then analyze the hydrodynamic-only related differences between the numerical model and the experimental tests.

The motion observer is crucial for the method as it contributes substantially to the coupling between the wave tank physical model and the numerical simulation. Many efforts have been deployed to get the finest results; Kalman filters have been implemented to use all the available sensors.

9.1.3 Actuators

On-board actuators have been selected for this work.

A large part of the work has been dedicated to the integration of a single actuator. Different important topics have been covered:

- A load analysis has been derived, with a simplified analytical model to get the main driving factors for the actuator performances;
- Identification of the performances on dedicated test benches;
- Use of these actuators during wave tank testing to study coupled phenomena.

This has also been extended for a multi-propeller set-up, with both numerical and experimental work:

- Derivation of the force allocation procedure;
- Numerical work to provide indicators and first insights about different layout possibilities;
- Experimental work, with a three-actuator system tested on a fixed test bench.

The main conclusions are:

- Moving from one to several actuators is not a barrier. Indeed, the characterization and calibration methodologies have been easily extended from a single actuator to several actuators and rotor load components modeled;
- The main barrier for fully-actuated system is the low saturation and poor performances of the actuator when they work at low regimes. An appropriate choice of actuator (motor and propeller) has to be done to avoid the low speed regime.

The major contribution of this work is about the evaluation of actuation performances and their dynamic identifications. This has been conducted by several means, using frequency domain and time domain indicators. The methodology is based on quasi-static and dynamic identifications, which is then used in the feedforward control strategy. The important outcomes are:

- The different frequency domain methods, based on linear system responses are consistent. It is also consistent when compared to realistic setpoints;
- The methodology has also been successfully applied to a single actuator and extended to a multi-actuator system;
- It is important to consider the variability of actuators performances with operating points. The model identification has to be conducted for several operating points. The higher the operating point, the faster actuators are;
- The dynamic compensation significantly improves the maximal frequency well captured by the actuator. It appears that the need for feedback control, to increase the frequency bandwidth and to reduce static errors due to, e.g., disturbances, does not seem important. The dynamic compensation works better when the dynamic of the actuator is not too far from the target dynamic (target cut-off frequency);
- Achievable bandwidths are compatible with the higher frequency of the aerodynamic loads. This is promising for wave basin experiments of FWT with flexible mast.

9.1.4 Floating wind turbine wave tank testing

Two wave tank test campaigns have been performed in this work to test the methodology. The SOFTWIND SPAR setup is the main set-up of this work. Different tests have been conducted to investigate key aspects of the SIL system. The main outcomes are about the relative contributions to the FWT motions of:

- The numerical model, thanks to comparison between state-of-the-art aerodynamic model real-time computations and simplified approaches,
- The actuator performance, with a parametrical study,
- The effects of different wind turbine control laws, with three different floating specific controllers tested.

9.2 Perspectives and future work

Developing a fully-functional hybrid system is not a trivial task. To improve the SIL system fidelity, provide more exhaustive guidelines and validate a fully-functional SIL system, different perspectives are presented in this section.

9.2.1 Parametrical study for rotor loads characterization

Different limitations of the parametrical study presented in chapter 3 have been identified. These limitations are briefly described.

Including TLP and larger rated power

Tension-Leg platforms (TLP) are not considered in the present work because neither 2nd nor 3rd order high frequency forces were freely available in the literature, though their influence could be predominant in severe sea states (Bachynski, 2014). TLP could provide more restrictive results in terms of delay and actuators dynamics because of their high natural frequencies (mostly in heave, pitch and roll).

Additionally, a semisubmersible with a 15MW Reference wind turbine has been recently made open-source as part of the IEA task 37. Including this new turbine might lead to slightly different ratios and sensitivities to the rotor loads.

Additional control laws

Additional control laws, using features such as the Individual Blade Pitch Control (Namik and Stol, 2010) would create increased moments on the rotor and then different specifications for the RNA loads. Also, nacelle yaw control, despite its low rate of change (in the order of 0.3 deg/s (Jonkman *et al.*, 2009)), could create asymmetric loading on the rotor, inducing increased gyroscopic effects and increased yaw aerodynamic moment. Consequently, the M_z and M_y components found in the parametrical study are expected to be underestimations of broader specifications.

Type of load cases

Different kinds of tests could increase the requirements for the actuators in terms of relative influence of global motions or maximum contributions. The main limitation of the selected approach is about the effect of limited actuation on the quantities of interest: it is not necessary the most severe conditions that will induce the maximum levels of errors when modeling actuator limitations. Some interesting tests could include:

- Decay tests in steady wind (Chabaud, 2016), for which the aerodynamic damping might have a significant role.
- Turbulent wind field with upstream rotor influence. This has recently been taken into account in the Design Load Case (DLC) of the certification bodies (see e.g. DLC 12.1 in DNV-ST-0437 (DNV GL, 2016)). We can also expect wake meandering (Larsen *et al.*, 2007) to have a large impact on the rotor loads (both due to the velocity deficit and the modified turbulence scales changing in space and time)(Wise and Bachynski, 2020).

Sensitivity to pure delay

The OpenFAST framework has been modified to take into account some of the actuators limitations (load component removal and actuator bandwidth). Adding a pure delay and exploring the induced effect need to be done. The theoretical background has been defined in chapter 3, and the effects of two pure delays have been obtained for the SOFTWIND SPAR setup in chapter 7. Indeed, especially for the tower deflection, anticipation of the impact of the SIL system delay on the FWT behavior is important. This should be done in parallel to the prediction part of the motion observer as described in section 9.2.3.

9.2.2 Six-component rotor loads modeling

From the conclusions listed in 9.1.3, two options could be pursued to get an accurate six-component rotor loads modeling:

- Moving to an over-actuated system, in order to have some flexibility in the force allocation;
- Try several actuator layouts, either fully-actuated or over-actuated, to get the most appropriate one.

These two options are detailed hereafter.

9.2.2.1 Moving to an over-actuated system

In chapter 4, it has been shown the interest of an over-actuated (eight-actuator) configuration compared to a fully-actuated (six-actuator) configuration. The challenges associated with the over-actuated layout are:

- The force allocation procedure (optimization) needs to run in real-time and to be implemented on the compactRIO PLC;
- The constraints and objectives of the optimization loop need to be adjusted to observations. It has been seen in chapter 4 that the most intuitive objective (error between setpoint load and the modeled actuated load) together with a common optimizer work well. However, this has not been applied to a realistic set-up.

For the next development steps and future works on the topic, the recommendations are:

- Use a standard frame for multicopters UAV and represent the F_x, M_y and M_z rotor loads components with four actuators. Based on the 8-actuator configuration presented in chapter4, two actuators should be generating along the positive x-direction and two actuators in the negative x-direction.
- Once the previous set-up is sufficiently identified, two additional actuators representing M_x and F_y could be implemented.
- Tune the actuator model used in the computation of the objective (error between setpoint load and the modeled actuated load) to match experimental identifications.

9.2.2.2 Multi-objective optimization of actuators layout

Instead of intuitive layouts such as the ones presented here above, moving to optimized actuators layout can improve the performances of the actuation system. This has been observed and implemented for parallel robot cables actuators applied to FWT SIL system (Chabaud *et al.*, 2018). A multi-objective optimization framework can been established to define the most adapted layout. The main objective is to deal with the non-negative thrust of each propeller and to improve actuated bandwidth. Ideally, the framework should work both with fully-actuated and over-actuated layouts.

The optimization variables, objectives and constraints are now defined.

Optimization variables

The three orientations and positions of each actuator, i.e. $n_{prop} * (3 + 3)$ variables. The selection of the most adapted actuators is another optimization loop on top of the frame definition loop.

Objectives

The same objective as for the over-actuated layouts could be used, i.e. the most intuitive objective. It is the error between the setpoint loads and the modeled actuated loads.

Constraints

- Aerodynamic interactions between the propellers. Minor work has been done on such topics. IHC multi-fan system lost up to 14.5% produced thrust due to near wake interaction of their propellers (Meseguer and Guanche, 2019).The most important problem is not the thrust loss leading to a decrease of the performances. The problem is about the non-deterministic behavior of such solutions, in particular looking at the dynamic performances. If the actuation system becomes non-deterministic, switching to feedback control will be mandatory;
- Solid interactions between the propellers, i.e. collisions. To avoid collisions between propellers, each propeller should have a certain distance with the other propellers;
- The mass and inertia budgets.

Once the optimization variables are identified, the objectives and the constraints are defined, the main inputs to the algorithms are:

- Model of the actuators, about their dynamics and saturations;
- Boundaries for each constraints;
- Penalty functions to transform as much as possible constraints into objectives;
- A list of suitable actuators.

This framework has been partially implemented during this work in the Platypus framework (Python) but it has not been fully validated and fulfilled due to lack of time.

9.2.3 Motion observer

Based on the characterizations performed, the recommendations concerning the motion observer for next test campaigns are:

- Definition of a methodology to get an accurate global frame orientation;
- Carefully characterize the MOCAP performances and recalibrate the working zone when required;
- Kalman filters are an interesting option, especially for angular velocities, but its implementation needs to be computationally less expensive and real-time mismatch treatment needs to be implemented in the state estimation.

Additionally, the prediction of FWT motions can significantly decrease the delay of the SIL system. The required short term horizon and the known import frequency at which motions occur make strategies such as cyclical and autoregressive models (Fusco and Ringwood, 2010) adapted. This has to fulfill the real-time execution constraints of the SIL methodology.

9.2.4 Numerical model

The different test campaigns have been performed with a coupled version of OpenFAST, either with AeroDyn v14 or with AeroDyn v15. The recommendations concerning the numerical model for next test campaigns are:

- Pursue sensitivity studies for the updated version of the AeroDyn module. The dynamic BEMT model has now been validated into OpenFAST; it improves the physics without impacting too much the CPU time. Investigations on the modifications of the damping and out-of-phase components of the rotor loads should be conducted;
- Adapt the blade discretization to get a sufficient margin between the RT loop time step and the OpenFAST computational time. The *OpenFAST RT mismatches* described in chapter 7 should be avoided as much as possible to improve the reproducibility.

In parallel, the simplified models such as the drag disk or the steady-state thrust curve did not lead to satisfactory results. However, the idea of a simplified approach should be pursued. An interesting alternative is to obtain a linear model of FWT *per frequency bandwidth*. Indeed, as seen in chapter 4 and 7, fitting of the rotor loads damping and equivalent stiffness / inertia should be done at different operating points and for different characteristic input frequencies of the hub velocity fluctuations. A linearization strategy *per frequency bandwidth* should be defined and applied with the wind turbine controller active.

9.2.5 Wave tank testing

The major limitation of the SOFTWIND SPAR test campaign lies in the numerical model bug. Testing with a corrected numerical model wrapper to get the correct tower deflections is important. The efforts to improve the actuators cut-off frequency and the overall SIL system delay will be fully realized when looking at this high resonant frequency of the FWT.

Then, reproducing additional rotor loads components is important to study different instabilities and out-of-plane FWT motions (see chapter 8). Testing first with the actuated F_x, M_y *and* M_z rotor load components can already improve the fidelity of the SIL setup. Moving to the full rotor loads tensor can then be done safely with the characterization and identification methodologies defined. Indeed, these methodologies have been found to be consistent between a large variety of identification setpoints and measurements during the tests.

9.2.6 Tuning of the numerical model

The numerical model has been tuned for wave-only and wave and turbulent wind cases. It has been seen that the drag modeling is a key factor to get similar responses between the experimental data and the numerical model. As shown in chapters 3 and 8, it is important to take into account the actuators limitations in the numerical simulations for meaningful comparisons between the experimental data and numerical ones. Consequently, the adaptation of the drag modeling could lead to better results. The following improvements could be envisaged:

- Increase of the pitch quadratic damping to fit irregular waves with and without wind;
- Change of the Morison drag coefficient depending on the KC and Re numbers. Alternatively, replacing a part of the quadratic damping due to the Morison formula with an additional linear damping can lead to better results.

Hydrodynamic scale effects, especially on the floater, need to be addressed. The model scale flow conditions have been used for the tuning despite the mismatch of Reynolds numbers.

Additionally, the tower deflections have not been compared to the experimental results due to a problem in the numerical tool. Investigations on this side might be important to assess the fidelity of the aero-hydro-servo-elastic calculations. The qualification of the modal approach for the coupled floater-tower modes needs to be addressed.

9.2.7 Future uses of the SIL system

The Centrale Nantes FWT wave tank testing facilities have been modernized thanks to the SOFTWIND project that funded this PhD work. Different EU-funded research projects are planning to use this system to investigate different aspects of the FWT physics. This system has shown its effectiveness to test and implement on a dedicated hardware wind turbine control laws.

References

Arnal, V. *et al.* (2019) 'Hybrid model testing of floating wind turbines: Test bench for system identification and performance assessment', in *Proceedings of the International Conference on Offshore Mechanics and Arctic Engineering - OMAE*. doi: 10.1115/OMAE2019-96374.

Asareh, M. A. and Prowell, I. (2012) *Seismic Loading for FAST: May 2011 - August 2011*. Golden, CO (United States). doi: 10.2172/1050131.

Azcona, José *et al.* (2014) 'Aerodynamic Thrust Modelling in Wave Tank Tests of Offshore Floating Wind Turbines Using a Ducted Fan', *Journal of Physics: Conference Series*, 524, p. 012089. doi: 10.1088/1742-6596/524/1/012089.

Azcona, J *et al.* (2014) *D 4.22: Methods for performing scale-tests for method and model validation of floating wind turbines*. INNWIND deliverables.

Azcona, J. *et al.* (2016) *D 4.24: Results of wave tank tests*. INNWIND Deliverables.

Azcona, J. *et al.* (2017) 'Experimental validation of a dynamic mooring lines code with tension and motion measurements of a submerged chain', *Ocean Engineering*. Elsevier, 129(February 2016), pp. 415–427. doi: 10.1016/j.oceaneng.2016.10.051.

Azcona, J., Bouchotrouch, F. and Vittori, F. (2019) 'Low-frequency dynamics of a floating wind turbine in wave tank–scaled experiments with SiL hybrid method', *Wind Energy*, 22(10), pp. 1402–1413. doi: 10.1002/we.2377.

Babarit, A. and Delhommeau, G. (2015) 'Theoretical and numerical aspects of the open source BEM solver NEMOH', in *Proceedings of the 11th European Wave and Tidal Energy Conference.*, pp. 1–12. doi: hal-01198800.

Bachynski, E. E. (2014) *Design and Dynamic Analysis of Tension Leg Platform Wind Turbines*. PhD Thesis, NTNU.

Bachynski, E. E., Chabaud, V. and Sauder, T. (2015) 'Real-time hybrid model testing of floating wind turbines: Sensitivity to limited actuation', *Energy Procedia*, 80(1876), pp. 2–12. doi: 10.1016/j.egypro.2015.11.400.

Bak, C. *et al.* (2013) *Description of the DTU 10 MW Reference Wind Turbine*, *DTU Wind Energy Report-I-0092*. doi: 10.1017/CBO9781107415324.004.

Battistella, T. *et al.* (2018) 'High fidelity simulation of multi-MW rotor aerodynamics by using a multifan', *Proceedings of the International Conference on Offshore Mechanics and Arctic Engineering - OMAE 2018*. doi: 10.1115/omae2018-77606.

Bayati, I. *et al.* (2016) 'Wind tunnel validation of AeroDyn within LIFES50+ project: Imposed Surge and Pitch tests', in *Journal of Physics: Conference Series*, p. 92001. doi: 10.1088/1742-6596/753/9/092001.

Bayati, I. *et al.* (2018) 'A wind tunnel/HIL setup for integrated tests of Floating Offshore Wind Turbines', *Journal of Physics: Conference Series*, 1037(5). doi: 10.1088/1742-6596/1037/5/052025.

Berthelsen, P. A. *et al.* (2016) 'Real-time hybrid model tests of a braceless semi-submersible wind turbine. Part III: calibration of a numerical model', in *OMAE 2016, Busan, South Korea*, pp. 1–13.

Bir, G. (2005) 'User's Guide to BModes (Software for Computing Rotating Beam Coupled Modes)', *Golden, CO: National Renewable Energy Laboratory*, (December), p. 21. Available at: https://www.osti.gov/biblio/861489 (Accessed: 19 June 2020).

Blondel, F. *et al.* (2016) 'Validation and comparison of aerodynamic modelling approaches for wind turbines', *Journal of Physics: Conference Series*, 753(2). doi: 10.1088/1742-6596/753/2/022029.

Bonnefoy, F. (2005) *Modélisation expérimentale et numérique des états de mer complexes*, *Ecole Centrale de Nantes*. PhD Thesis (in French), Ecole Centrale de Nantes.

Borg, M., Bredmose, H. and Hansen, A. M. (2017) 'Elastic deformations of floaters for offshore wind turbines: Dynamic modelling and sectional load calculations', in *Proceedings of the International Conference on Offshore Mechanics and Arctic Engineering - OMAE*. American Society of Mechanical Engineers (ASME). doi: 10.1115/OMAE2017-61446.

Borisade, F. *et al.* (2017) *Life50plus deliverable 7.4 : State-of-the-Art FOWT design practice and guidelines*.

Bortolotti, P. *et al.* (2019) 'Systems Engineering in Wind Energy - WP2.1 Reference Wind Turbines', *IEA Wind TCP Task 37*, (May). Available at: https://www.osti.gov/biblio/1529216-iea-wind-tcp-task-systems-engineering-wind-energy-wp2-reference-wind-turbines.

Bouabdallah, S. (2007) *Design and Control of Quadrotors With Application To Autonomous Flying*. École Polytechnique Fédérale De Lausanne, PhD Thesis. doi: 10.5075/epfl-thesis-3727.

Bouabdallah, S., Murrieri, P. and Siegwart, R. (2004) 'Design and control of an indoor micro quadrotor', (April), pp. 4393-4398 Vol.5. doi: 10.1109/robot.2004.1302409.

Le Boulluec, M. *et al.* (1994) 'Recent advances on the slow-drift damping of offshore structures', in *BOSS*.

Boulluec, M. Le *et al.* (2013) 'Tank testing of a new concept of floating offshore wind turbine', in *Proceedings of the International Conference on Offshore Mechanics and Arctic Engineering - OMAE*, pp. 1–8. doi: 10.1115/OMAE2013-11577.

Bredmose, H. *et al.* (2012) *MARINET deliverable D2.4: Collation of offshore windwave dynamics*.

Bredmose, H. *et al.* (2017) 'The Triple Spar campaign: Model tests of a 10MW floating wind turbine with waves, wind and pitch control', *Energy Procedia*, 137, pp. 58–76. doi: 10.1016/j.egypro.2017.10.334.

Brodtkorb, P. A. *et al.* (2000) 'WAFO - A Matlab toolbox for analysis of random waves and loads', in *Proceedings of the International Offshore and Polar Engineering Conference*, pp. 343–350.

Burton, T. *et al.* (2011) *Wind Energy Handbook, Second Edition*. doi: 10.1002/9781119992714.

Casiano, M. J. (2016) 'Extracting Damping Ratio From Dynamic Data and Numerical Solutions', *National Aeronautics and Space Administration (NASA)*, (NASA-TM-2016212218), pp. 1–29.

Chabaud, V. (2016) *Real-Time Hybrid model testing of Floating Wind Turbines*. PhD Thesis, NTNU.

Chabaud, V. *et al.* (2018) 'Multiple-degree-of-freedom actuation of rotor loads in model testing of floating wind turbines using cable-driven parallel robots', *Journal of Physics: Conference Series*, 1104(1). doi: 10.1088/1742-6596/1104/1/012021.

Chen, J. *et al.* (2018a) 'Comparisons of the dynamical characteristics of a semi-submersible floating offshore wind turbine based on two different blade concepts', *Ocean Engineering*. Elsevier Ltd, 153(2017), pp. 305–318. doi: 10.1016/j.oceaneng.2018.01.104.

Chen, J. *et al.* (2018b) 'Comparisons of the dynamical characteristics of a semi-submersible floating offshore wind turbine based on two different blade concepts', *Ocean Engineering*. Elsevier Ltd, 153(September 2017), pp. 305–318. doi: 10.1016/j.oceaneng.2018.01.104.

Courbois, A. (2013) *École Centrale de Nantes Étude expérimentale du comportement dynamique d ' une éolienne offshore flottante soumise à l'action conjuguée de la houle et du vent*. PhD Thesis (in French). Ecole Centrale de Nantes.

Cutler, M. and How, J. P. (2015) 'Analysis and control of a variable-pitch quadrotor for agile flight', *Journal of Dynamic Systems, Measurement and Control, Transactions of the ASME*, 137(10), pp. 1–14. doi: 10.1115/1.4030676.

Desmond, C. *et al.* (2016) 'Description of an 8 MW reference wind turbine', in *Journal of Physics: Conference Series*. doi: 10.1088/1742-6596/753/9/092013.

Desmond, C. J., Hinrichs, J. and Murphy, J. (2019) 'Uncertainty in the Physical Testing of Floating Wind Energy Platforms ' Accuracy versus Precision', pp. 1–14. doi: 10.3390/en12030435.

DNV GL (2016) *DNVGL-ST-0437 Loads and site conditions for wind turbines*.

DNV GL (2017) *DNVGL-RP-C205: Environmental Conditions and Environmental Loads*, *DNV GL Recommended Practice*.

DNVGL (2019) 'DNV-GL RP 0286 Coupled analysis of floating wind turbines', (May).

Duan, F. *et al.* (2016) 'Experimental comparisons of dynamic properties of floating wind turbine systems based on two different rotor concepts', *Applied Ocean Research*. Elsevier B.V., 58, pp. 266–280. doi: 10.1016/j.apor.2016.04.012.

Faltinsen, O. M. (1993) *Sea loads on ships and offshore structures*, *Cambridge University press*.

Farrugia, R., Sant, T. and Micallef, D. (2016) 'A study on the aerodynamics of a floating wind turbine rotor', *Renewable Energy*. Elsevier Ltd, 86, pp. 770–784. doi: 10.1016/j.renene.2015.08.063.

Fossen, T. I. (2011) *Handbook of Marine Craft Hydrodynamics and Motion Control*, *Handbook of Marine Craft Hydrodynamics and Motion Control*. doi: 10.1002/9781119994138.

Fusco, F. and Ringwood, J. V. (2010) 'Short-term wave forecasting for real-time control of wave energy converters', *IEEE Transactions on Sustainable Energy*, 1(2), pp. 99–106. doi: 10.1109/TSTE.2010.2047414.

Goodwin, G. C., Graebe, S. F. and Salgado, M. E. (2007) 'Control System Design', *IEEE Control Systems*, pp. 77–79. doi: 10.1109/MCS.2007.284513.

Goupee, A. *et al.* (2015) 'A Calibrated Blade-Element/Momentum Theory Aerodynamic Model of the MARIN Stock Wind Turbine', *Proceedings of International Society of Offshore and Polar Engineers Conference (ISOPE 2015)*, (April), pp. 584–592.

Goupee, A. J. *et al.* (2014) 'Additional wind/wave basin testing of the deepCwind semisubmersible with a performance-matched wind turbine', in *Proceedings of the International Conference on Offshore Mechanics and Arctic Engineering - OMAE*. doi: 10.1115/OMAE2014-24172.

Goupee, A. J., Kimball, R. W. and Dagher, H. J. (2017) 'Experimental observations of active blade pitch and generator control influence on floating wind turbine response', *Renewable Energy*. Elsevier Ltd, 104, pp. 9–19. doi: 10.1016/j.renene.2016.11.062.

Gueydon, S., Bayati, I. and de Ridder, E. J. (2020) 'Discussion of solutions for basin model tests of FOWTs in combined waves and wind', *Ocean Engineering*. Elsevier Ltd, 209(March), p. 107288. doi: 10.1016/j.oceaneng.2020.107288.

Gueydon, S. and Jonkman, J. (2016) 'Update on the Comparison of Second-Order Loads on a Tension Leg Platform for Wind Turbines', *Proceedings of the Twenty-sixth (2016) International Ocean and Polar Engineering Conference*, (August), pp. 323–332.

Hall, M. (2016) *Hybrid modelling of floating wind turbines*. PhD Thesis University of Maine.

Hall, M. and Goupee, A. (2015) 'Validation of a lumped-mass mooring line model with DeepCwind semisubmersible model test data', *Ocean Engineering*. Elsevier, 104, pp. 590–603. doi: 10.1016/j.oceaneng.2015.05.035.

Hall, M. and Goupee, A. J. (2018) 'Validation of a hybrid modeling approach to floating wind turbine basin testing', (December 2017), pp. 1–18. doi: 10.1002/we.2168.

Hall, M., Goupee, A. and Jonkman, J. (2017) 'Development of performance specifications for hybrid modeling of floating wind turbines in wave basin tests', *Journal of Ocean Engineering and Marine Energy*. Springer International Publishing, pp. 1–23. doi: 10.1007/s40722-017-0089-3.

Hansen, M. H. *et al.* (2005) 'Control design for a pitch-regulated, variable speed wind turbine', *Control*.

Haslum, H. (2000) *Simplified methods applied to nonlinear motion of spar platforms*. PhD thesis, NTNU.

Hasselmann, K. *et al.* (1973) 'Measurements of wind-wave growth and swell decay during the joint North Sea wave project (JONSWAP).'

Hegseth, J. M., Bachynski, E. E. and Martins, J. R. R. A. (2020) 'Integrated design optimization of spar floating wind turbines', *Marine Structures*. Elsevier Ltd, 72(April), p. 102771. doi: 10.1016/j.marstruc.2020.102771.

Hoffmann, G. M. *et al.* (2011) 'Precision flight control for a multi-vehicle quadrotor helicopter testbed', *Control Engineering Practice*. Elsevier, 19(9), pp. 1023–1036. doi: 10.1016/j.conengprac.2011.04.005.

IEC (2009) 'Wind Turbines - Part 3: Design requirements for offshore wind turbines', *European Committee for Electrotechnical Standardization*.

ITTC (2017) 'Model Tests for Offshore Wind Turbines', *ITTC Recommended Procedures and Guidelines*.

ITTC committee (2011) 'ITTC Recommended Procedures: Numerical Estimation of Roll Damping', *ITTC - Recommended Procedures*, pp. 1–33.

Joao Cruz, M. A. (2016) *Floating Offshore Wind Energy: The Next Generation of Wind Energy*. doi: DOI 10.1007/978-3-319-29398-1.

Jonkman, B. (2009) 'TurbSim user's guide: Version 1.50'. Available at: https://www.osti.gov/biblio/965520 (Accessed: 26 May 2020).

Jonkman, J. (2008) 'Influence of Control on the Pitch Damping of a Floating Wind Turbine', *46th AIAA Aerospace Sciences Meeting and Exhibit*. doi: 10.2514/6.2008-1306.

Jonkman, J. *et al.* (2009) *Definition of a 5-MW Reference Wind Turbine for Offshore System Development*. doi: 10.2172/947422.

Jonkman, J. (2010) *Definition of the Floating System for Phase IV of OC3*, *Contract*.

Jonkman, J. M. (2013) 'The new modularization framework for the FAST wind turbine CAE tool', in *51st AIAA Aerospace Sciences Meeting including the New Horizons Forum and Aerospace Exposition 2013*. doi: 10.2514/6.2013-202.

Jonkman, J. M. *et al.* (2015) *AeroDyn v15 User's Guide and Theory Manual*.

Jonkman, J. and Musial, W. (2010a) *Final Technical Report, IEA Wind task 23, Subtask 2, Offshore Code Comparison Collaboration (OC3)*. Available at: https://www.osti.gov/biblio/1004009 (Accessed: 2 July 2020).

Jonkman, J. and Musial, W. (2010b) 'Offshore code comparison collaboration (OC3) for IEA Wind Task 23 offshore wind technology and deployment'. Available at: https://www.osti.gov/biblio/1004009 (Accessed: 2 July 2020).

Kaimal, J. C. *et al.* (1972) 'Spectral characteristics of surface-layer turbulence', *Quarterly Journal of*

the Royal Meteorological Society, 98(417), pp. 563–589. doi: 10.1002/qj.49709841707.

Kanner, S. (no date) *Design, Analysis, Hybrid Testing and Orientation Control of a Floating Platform with Counter-Rotating Vertical-Axis Wind Turbines*. University of California Berkeley.

Kanner, S., Yeung, R. W. and Koukina, E. (2016) 'Hybrid testing of model-scale floating wind turbines using autonomous actuation and control', *OCEANS 2016 MTS/IEEE Monterey, OCE 2016*. doi: 10.1109/OCEANS.2016.7760997.

Koo, B. *et al.* (2012) 'Model tests for a floating windturbine on three different floaters', *Proceedings of the International Conference on Offshore Mechanics and Arctic Engineering - OMAE*, 7, pp. 455–466. doi: 10.1115/OMAE2012-83642.

Kvittem, M. I. *et al.* (2018) 'Calibration of hydrodynamic coefficients for a semi-submersible 10 MW wind turbine', in *Proceedings of the International Conference on Offshore Mechanics and Arctic Engineering - OMAE*, pp. 1–12. doi: 10.1115/OMAE2018-77826.

Kvittem, M. I. and Moan, T. (2014) 'Frequency Versus Time Domain Fatigue Analysis of a Semisubmersible Wind Turbine Tower', *Journal of Offshore Mechanics and Arctic Engineering*. doi: 10.1115/1.4028340.

Lagasco, F. *et al.* (2019) 'New engineering approach for the development and demonstration of a multi-purpose platform for the blue growth economy', in *Proceedings of the International Conference on Offshore Mechanics and Arctic Engineering - OMAE*. doi: 10.1115/OMAE2019-96104.

Larsen, G. C. *et al.* (2007) *Dynamic wake meandering modeling*.

Larsen, T. J. and Hanson, T. D. (2007) 'A method to avoid negative damped low frequent tower vibrations for a floating, pitch controlled wind turbine', *Journal of Physics: Conference Series*, 75(1). doi: 10.1088/1742-6596/75/1/012073.

Lawson, M. *et al.* (2014) 'Implementing nonlinear buoyancy and excitation forces in the WEC-SIM wave energy converter modeling tool', in *Proceedings of the International Conference on Offshore Mechanics and Arctic Engineering - OMAE*. doi: 10.1115/OMAE2014-24445.

Lemmer, F. *et al.* (2016) *Definition of the SWE-TripleSpar Floating Platform for the DTU 10MW Reference Wind Turbine*. Available at: http://www.ifb.uni-stuttgart.de/windenergie/downloads.

Leroy, V. *et al.* (2018) 'Impact of the aerodynamic model on the modelling of the behaviour of a Floating Vertical Axis Wind Turbine', *Journal of Physics: Conference Series*, 1104, p. 012001. doi: 10.1088/1742-6596/1104/1/012001.

Leroy, V. (2018) *Unsteady aerodynamic modelling for seakeeping analysis of Floating Offshore Wind Turbines*. PhD Thesis, Ecole Centrale de Nantes.

Li, L., Gao, Z. and Moan, T. (2015) 'Joint Environmental Data at Five European Offshore Sites for Design of Combined Wind and Wave Energy Devices', *Journal of Offshore Mechanics and Arctic Engineering*, 137(June), pp. 1–16. doi: 10.1115/OMAE2013-10156.

Lie, H. and Kaasen, K. E. (2008) 'Viscous drift forces on semis in irregular seas a frequency domain approach', in *Proceedings of the International Conference on Offshore Mechanics and Arctic Engineering - OMAE*. doi: 10.1115/OMAE2008-57313.

Lupton, R. C. and Langley, R. S. (2019a) 'Complex but negligible: Non-linearity of the inertial coupling between the platform and blades of floating wind turbines', *Renewable Energy*. Elsevier Ltd, 134, pp. 710–726. doi: 10.1016/j.renene.2018.11.036.

Lupton, R. C. and Langley, R. S. (2019b) 'Improved linearised models of wind turbine aerodynamics and control system dynamics using harmonic linearisation', *Renewable Energy*. Elsevier Ltd, 135, pp. 148–162. doi: 10.1016/j.renene.2018.11.067.

Manwell, J. F., McGowan, J. G. and Rogers, A. L. (2010) *Wind Energy Explained: Theory, Design and Application*, *Wind Energy Explained: Theory, Design and Application*. doi: 10.1002/9781119994367.

MARIN (2018) *Software-in-the-Loop provides valuable alternative to traditional offshore wind model testing*. Available at: https://www.marin.nl/software-in-the-loop-provides-valuable-alternative-to-traditional-offshore-wind-model-testing (Accessed: 7 May 2020).

Martin, H. R. *et al.* (2012) 'Methodology for Wind / Wave Basin Testing of Floating Offshore Wind Turbines', *ASME 2012 31st International Conference on Ocean, Offshore and Arctic Engineering*, pp. 1–10. doi: 10.1115/1.4025030.

Martinez-Alvarado, R. *et al.* (2014) 'Dynamic response of BLDC-thruster for small scale Quadrotors under aerodynamic load torque', *2014 IEEE International Autumn Meeting on Power, Electronics and Computing, ROPEC 2014*, (November). doi: 10.1109/ROPEC.2014.7036341.

Masciola, M., Jonkman, J. and Robertson, A. (2013) 'Implementation of a multisegmented, quasi-static cable model', in *Proceedings of the International Offshore and Polar Engineering Conference*, pp. 315–322.

Meseguer, A. and Guanche, R. (2019) 'Wind turbine aerodynamics scale-modeling for floating offshore wind platform testing', *Journal of Wind Engineering and Industrial Aerodynamics*, 186(November 2018), pp. 49–57. doi: 10.1016/j.jweia.2018.12.021.

Molin, B. (2002) *Hydrodynamique des structures offshores*. Technip Ed.

Müller, K., Lemmer, F. and Yu, W. (2018) *Life50plus Deliverable D4.2 Public Definition of the Two LIFES50+ 10MW Floater Concepts*. Life50plus deliverables.

Müller, K., Sandner, F. and Bredmose, H. (2014) 'Improved tank test procedures for scaled floating offshore wind turbines', in *International Wind Engineering Conference IWEC 2014*.

Muzar, D., Lanteigne, E. and McLeod, J. (2017) 'Dynamic characterization of brushless dc motors and propellers for flight applications', *Unmanned Systems*, 5(3), pp. 159–167. doi: 10.1142/S2301385017400027.

Namik, H. and Stol, K. (2010) 'Individual blade pitch control of floating offshore wind turbines', *Wind Energy*, 13, pp. 74–85. doi: 10.1002/we.

NREL (no date) *OpenFAST github deposit*. Available at: https://github.com/OpenFAST/openfast (Accessed: 8 October 2018).

Offshore wind in Europe – key trends and statistics 2019 | WindEurope (no date). Available at: https://windeurope.org/about-wind/statistics/offshore/european-offshore-wind-industry-key-trends-statistics-2019/ (Accessed: 29 May 2020).

Pao, L. and Johnson, K. (2009) 'A Tutorial on the Dynamics of Wind Turbines and Wind Farms', in *IEEE*, pp. 2076–2089.

Pegalajar-Jurado, A. ; *et al.* (2018) *Life50plus deliverable D4.8: Validation of advanced models and methods for cascading into simpler models*.

Pegalajar-Jurado, A. *et al.* (2018) *Life50plus deliverable D4.5: State-of-the-art models for the two LIFES50+ 10MW floater concepts*.

Pegalajar-Jurado, A., Borg, M. and Bredmose, H. (2018) 'An efficient frequency-domain model for quick load analysis of floating offshore wind turbines', *Wind Energy Science*, 3(2), pp. 693–712. doi: 10.5194/wes-3-693-2018.

Pérez-Collazo, C., Greaves, D. and Iglesias, G. (2015) 'A review of combined wave and offshore wind energy', *Renewable and Sustainable Energy Reviews*, 42, pp. 141–153. doi: 10.1016/j.rser.2014.09.032.

Philippe, M. (2012) *Couplages aéro-hydrodynamiques pour l'étude de la tenue à la mer des éoliennes offshore flottantes*. Phd Thesis (in French), Ecole Centrale de Nantes.

Pounds, P. E., Mahony, R. E. and Corke, P. I. (2008) 'Design of a Static Thruster for Microair Vehicle Rotorcraft', *Journal of Aerospace Engineering*, 22(1), pp. 85–94. doi: 10.1061/(asce)0893-1321(2009)22:1(85).

Pounds, P., Mahony, R. and Corke, P. (2010) 'Modelling and control of a large quadrotor robot', *Control Engineering Practice*. Elsevier, 18(7), pp. 691–699. doi: 10.1016/j.conengprac.2010.02.008.

Qualisys (2016) *Qualisys Track Manager User Manual*.

Roald, L. *et al.* (2013) 'The Effect of Second-Order Hydrodynamics on Floating Offshore Wind Turbines', in *DeepWind'2013*.

Robertson, A. *et al.* (2014) *Definition of the Semisubmersible Floating System for Phase II of OC4, NREL/TP-5000-60601*.

Robertson, Amy *et al.* (2014) 'Offshore code comparison collaboration continuation within IEA wind task 30: Phase II results regarding a floating semisubmersible wind system', *Proceedings of the International Conference on Offshore Mechanics and Arctic Engineering - OMAE*, 9B(March 2014). doi: 10.1115/OMAE2014-24040.

Robertson, A. *et al.* (2017) 'OC5 Project Phase II: Validation of Global Loads of the DeepCwind Floating Semisubmersible Wind Turbine', *Energy Procedia*. Elsevier B.V., 137, pp. 38–57. doi:

10.1016/j.egypro.2017.10.333.

Robertson, A. (2017) 'Uncertainty analysis of OC5-DeepCwind floating semisubmersible offshore wind test campaign', *Proceedings of the 27th International Ocean and Polar Engineering Conference*, (July), pp. 482–489.

Robertson, A. N. *et al.* (2018) 'Assessment of experimental uncertainty for a floating wind semisubmersible under hydrodynamic loading', in *Proceedings of the International Conference on Offshore Mechanics and Arctic Engineering - OMAE*. doi: 10.1115/OMAE2018-77703.

Roddier, D. *et al.* (2010) 'WindFloat: A floating foundation for offshore wind turbines', *Journal of Renewable and Sustainable Energy*, 2(3). doi: 10.1063/1.3435339.

Sauder, T. *et al.* (2016) 'Real-time hybrid model testing of a braceless semi-submersible wind turbine. Part I: the hybrid approach', in *Proc. of the 35th International Conference on Ocean, Offshore and Arctic Engineering, OMAE2016, June 19-24, 2016, Busan, Korea*.

Schepers, G. and Sieros, G. (2017) *Inventory of aerodynamic models*. AVATAR Deliverable 1.4.

Schepers, J. G. (2012) *Engineering models in wind energy aerodynamics*. PhD Thesis, TU Delft.

Sieros, G. (2017) *D1.6: Redesign of the AVATAR RWT rotor*. AVATAR Deliverables.

Six, D. (2018) *Conception et commande de robots parallèles volants*. PhD Thesis (in French), Ecole Centrale de Nantes.

Skaare, B. and Nielsen, F. G. (2014) 'Analysis of measurements and simulations from the Hywind Demo floating wind turbine', *Wind Energy*, 17(April 2013), pp. 657–669. doi: 10.1002/we.

Souza, C. E. S. and Bachynski, E. E. (2019) 'Changes in surge and pitch decay periods of floating wind turbines for varying wind speed', *Ocean Engineering*. Elsevier Ltd, 180(February), pp. 223–237. doi: 10.1016/j.oceaneng.2019.02.075.

Stansberg, C. T. *et al.* (2015) 'Challenges in Wave Force Modelling for Mooring Design in High Seas', in *Offshore Technology Conference*, pp. 4–7.

STATIONIS Consortium (2020) *STATIONIS internal project deliverables*.

Thys, M. *et al.* (2018) 'Real-time hybrid model testing of a semi-submersible 10MW floating wind turbine and advances in the test method', in *ASME 2018 1st International Offshore Wind Technical Conference, IOWTC 2018*, pp. 1–11. doi: 10.1115/IOWTC2018-1081.

Thys, M. *et al.* (2019) *Life50plus Deliverable 7.9 Guidance and Recommended Methods for Hybrid / HIL-based FOWT Experimental Testing*.

Uzunoglu, E. and Guedes Soares, C. (2019) 'Yaw motion of floating wind turbine platforms induced by pitch actuator fault in storm conditions', *Renewable Energy*. Elsevier Ltd, 134, pp. 1056–1070. doi: 10.1016/j.renene.2018.11.076.

Veers, P. *et al.* (2019) 'Grand challenges in the science of wind energy', *Science*, 366(6464). doi: 10.1126/science.aau2027.

Waals, O. J. (2009) 'On the application of advanced wave analysis in shallow water model testing (wave splitting)', in *Proceedings of the International Conference on Offshore Mechanics and Arctic Engineering - OMAE*. doi: 10.1115/OMAE2009-79413.

Welch, P. D. (1967) 'The Use of Fast Fourier Transform for the Estimation of Power Spectra: A Method Based on Time Averaging Over Short, Modified Periodograms', *IEEE Transactions on Audio and Electroacoustics*, 15(2), pp. 70–73. doi: 10.1109/TAU.1967.1161901.

Wise, A. S. and Bachynski, E. E. (2020) 'Wake meandering effects on floating wind turbines', *Wind Energy*. John Wiley and Sons Ltd, 23(5), pp. 1266–1285. doi: 10.1002/we.2485.

Yu, J. (2017) *Efficient rotor modelling for real-time hybrid testing*. MsC Thesis NTNU.

Zhang, C. *et al.* (2019) 'Adaptive super-twisting control of floating wind turbines with collective blade pitch control', in *IFAC-PapersOnLine*. doi: 10.1016/j.ifacol.2019.08.165.

Appendix A. Validation of the modified OpenFAST code

In this part, the modifications which have been brought to the OpenFAST code to make it possible to work in a SIL system are explained together with its validation process. Because simulations are run at full scale during experiment, data are given at full scale in this section.

The OpenFAST code is modular framework with a glue code to interface between the different modules. The integration in the real-time environment is recalled in Figure 117. To modify it to software-in-the-loop applications, the requirements were:

- the modifications should facilitate merging with updated version of the OpenFAST code;
- Different aerodynamic modules should be used;
- Similar input files as the original input files of the OpenFAST code;
- Motions are imposed through typical measurements in the wave tank.

The seismic module of FAST v7 (Asareh and Prowell, 2012) was originally intended to be used. However, it was initially developed for FAST v7 and consequently redevelopments were important to ensure portability to OpenFAST. Moreover, this seismic module was written to impose only the three platform translations, and not the rotations. Initially, to speed up the computational time, it was intended to replace the FAST glue code without using the ElastoDyn module, as many of its calculations are not used for the SIL application. However, the ElastoDyn module has been kept for different reasons:

- after some qualitative sensitivity studies for computational time profiling, it was clear that the aerodynamic module has more impact on the CPU time than the ElastoDyn computations.
- The ServoDyn inputs are based on ElastoDyn outputs. In order to facilitate the integration of external control laws, it has been considered as an important feature to keep compatibility with ServoDyn and its Bladed interface.
- To kinetics generation is done in the ElastoDyn module.

Finally, the only modifications to the FAST code concern the glue code, by imposing at the beginning of each time step the ElastoDyn platform and tower position and velocities states variables. These positions and velocities are transformed in the kinematic generator to the different modules. The main limitation of this approach is to impose the positions and velocities without imposing the corresponding accelerations and loads at the interfacing points. With this approach, the inertial loads in the shaft outputs of ElastoDyn don't contain the part due to the platform and tower deflections accelerations. Consequently, the ElastoDyn low-speed shaft outputs are considered for the tensor presented in part 2.1 with the only modification consisting in withdrawing the gravity contribution.

To make it work with LabView, a Fortran wrapper similar to the FAST_Library.f90 input file has been written, with the different inputs and outputs transformations and the call to the different steps of the OpenFAST calculations (initialization, initial solution, time stepping and closing/deallocation). Then, in the LabView programming interface, the call to the wrapper functions is done thanks to the Call_functions vi. To make it work on the compactRIO NI Linux real-time environment, different modifications to the original environmental variables are installed libraries

have been required. Additionally, to validate the modifications and run simulations with imposed motions, a Fortran test program similar to the OpenFAST program calls this wrapper. The validation test case is presented hereafter.

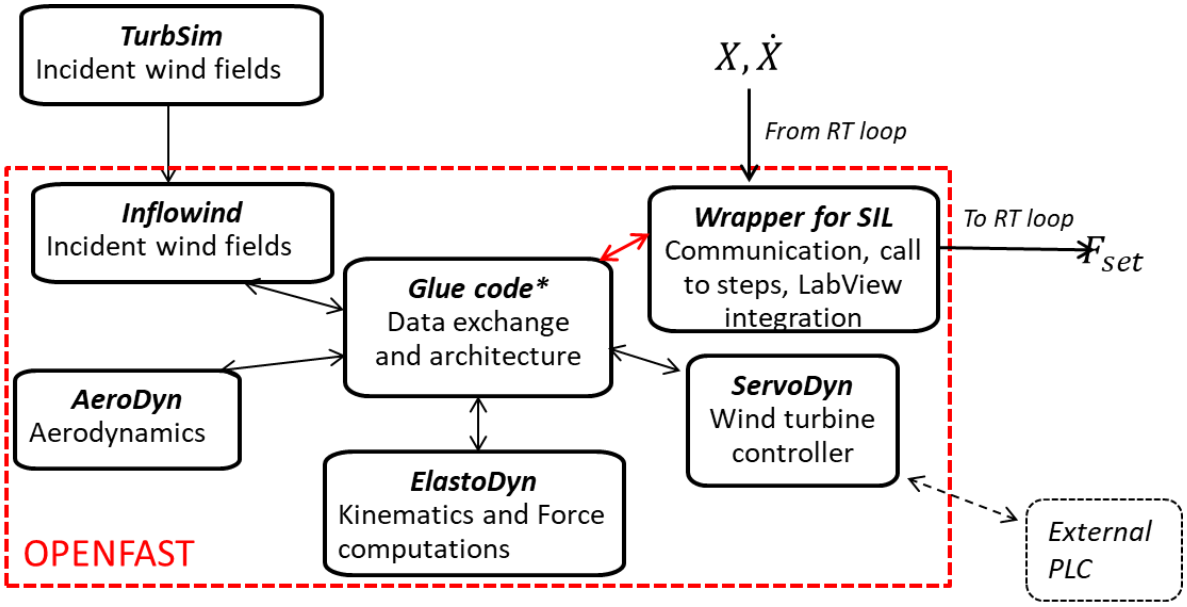

Figure 117: OpenFAST integration in the real-time environment.

Validation test case

The validation test case is extracted from the regression tests of OpenFAST (denoted 5MW_OC3Spar_DLL_WTurb_WavesIrr):

- FWT: OC3-Hywind SPAR (Jonkman, 2010),
- DoF activated: platform 6 DoF, generator, first fore-aft and side-side tower modes,
- Load case: $H_s = 6m; T_p = 10s; U_w = 12m.s^{-}1;$ NTM class B Kaimal turbulent wind fields.

A fully coupled simulation has first been performed. Then, another simulation has been performed imposing the platform and tower positions and velocities. The F_x aerodynamic forces are superposed in Figure 118. The bottom graph zooms on a smaller time window of the time series to show the differences for high frequency variations. Aerodynamic forces collapse for the different frequency bandwidths, from the slowly varying changes in the operating point to the high frequency. This means the different computations (aerodynamic, wind turbine control,…) works similarly in both cases, validating the wrapper for SIL wave tank testing. The validation has also been done for the six rotor load components including a part of the inertial loads as described in chapter 2.

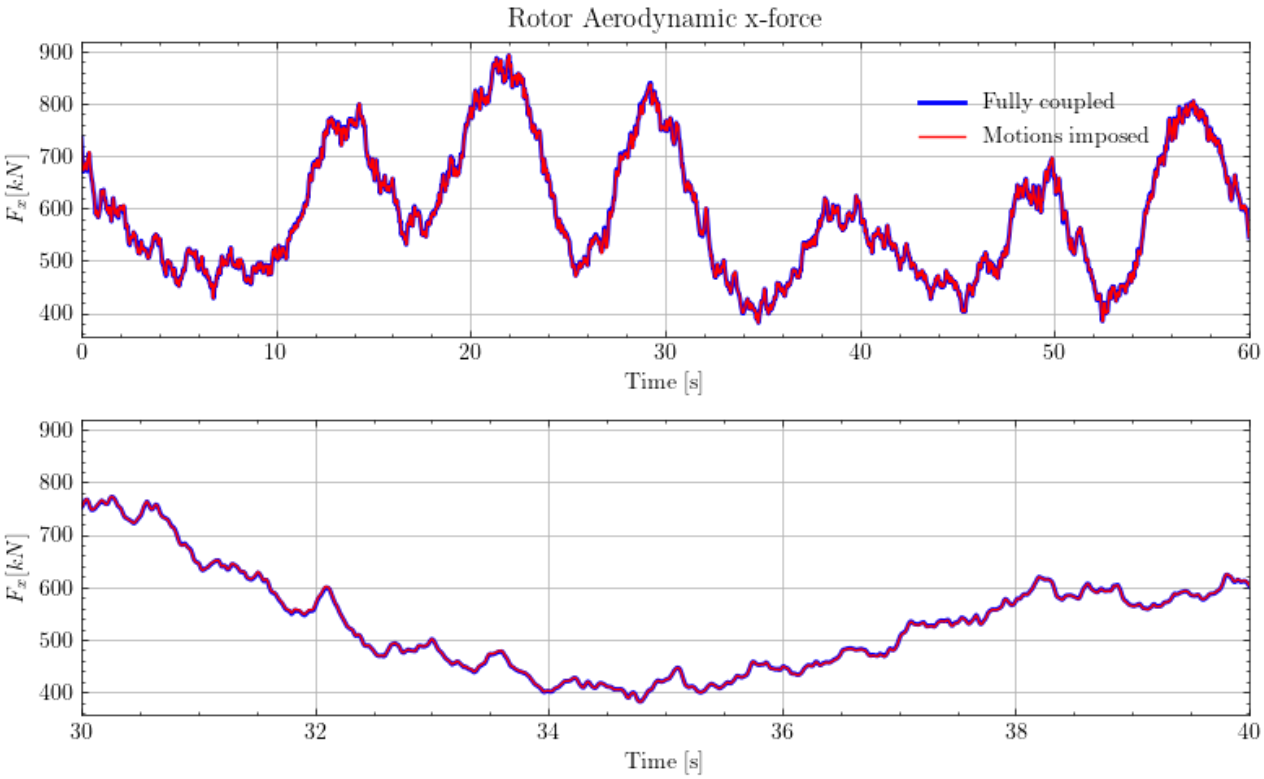

Figure 118: Comparison of the $\boldsymbol{F_x}$ component of the aerodynamic tensor for solved motions (fully coupled) and replayed imposed motions.

Appendix B. Identification of system characteristics

The theoretical and practical background about system characteristics identification (mass, damping, stiffness) is presented hereafter. It is based on ITTC recommendations and other identifications methodologies (Faltinsen, 1993; Molin, 2002; ITTC committee, 2011; Casiano, 2016).

Contents

B.1 Damping estimation

A mass-spring-damper system is decaying from an initial offset, without velocity, to zero. The logarithmic decrement $\delta(t)$ is defined as the natural logarithmic of the ratio of the amplitudes $x(t)$ of any two peaks separated by n oscillations. It is expressed in Eq. (1)

$$\delta(t) = \frac{1}{n}\ln\left(\frac{x(t)}{x(t+nT)}\right) \tag{1}$$

where $x(t)$ is the overshoot (amplitude - final value) at time t and $x(t + nT)$ is the overshoot of the peak n periods away, n an integer number of successive peaks. Note that in this work, the peak to trough amplitudes are used for the overshoot estimation to remove any offset of the mean value. the peaks and troughs detection is performed with WAFO v2.5 (Brodtkorb *et al.*, 2000).

The damping ratio is then found from the logarithmic decrement by Eq. (2). For small log decrement δ, the damping ratio simplifies to $\zeta(t) \sim \frac{\delta(t)}{2\pi}$.

$$\zeta(t) = \frac{1}{\sqrt{1+\left(\frac{2\pi}{\delta(t)}\right)^2}} \tag{2}$$

Once the damping ratio has been estimated at a given instant of the time series, different methodologies have been developed to deal with best fit of linear and quadratic damping coefficients. In this work, the methodologies used by…

B.2 Eigen values analysis

The period of the oscillations of a freely decaying mass-spring-damper system is linked to the natural period the system and to the damping ratio, by Eq. . The dependency to the damping ratio is often neglected for lightly damped system ($\zeta < o(1)$)

$$T_{resp}(t) = T_0\sqrt{1-\zeta^2(t)} \tag{3}$$

B.3 Transfer function (RAO) estimation

Transfer function estimation is extensively used ion this work, both for hydrodynamics response but also for the actuator performance identification. The transfer function between an input u and an output y is defined by :

$$H(s) = \frac{y(s)}{u(s)} \tag{4}$$

With s the Laplace domain variable; $s = j\omega$.

Motions transfer functions are defined by x/a where x is the complex amplitude of the considered DoF and a the complex amplitude of the free surface elevation. For translations, x is in meters, and in degrees for rotations. a is in meters. This definition of the RAO is dimensionless for translations but scales with $\sqrt{s}$ for the rotations. Using the steepness for the rotations RAO is a dimensionless alternative.

For regular waves, to get the complex amplitude of the free surface elevation and of the motions a Fourier domain analysis is performed with a specification of the 1st harmonic of the incident waves. Then, the RAO at a frequency f is defined as the ratio of the response's amplitude to the wave amplitude. Even if steep waves have non negligible higher order harmonics, the RAO is computed by looking only at the fundamental frequency f.

For irregular waves, different spectral variables are estimated:

- Wave spectrum $S_{cc}(f)$
- Force and motion spectra $S_{mm}(f)$where m means surge, sway, heave, roll, pitch and yaw.
- Cross-spectra $S_{mc}(f)$ between the wave elevation and the response signal under consideration.

This spectral estimates are based on Welch method.

The coherence $\mathrm{C(f)}$ between the 2 spectra is computed by Eq. (5)

$$\mathrm{C(f)} = \left(\frac{\mathrm{S_{mc}^2}}{\mathrm{S_{cc}\ S_{mm}}}\right)^{1/2} \tag{5}$$

When the coherence exceeds a threshold $\mathrm{C(f)} > [0.7 - 0.8]$, the transfer function H_{mc} could be safely evaluated by Eq.(6). Otherwise the linearity between the input and the output is not sufficient and a transfer function could not be estimated.

$$\mathrm{H_{mc}(f)} = \left(\frac{\mathrm{S_{mm}}}{\mathrm{S_{cc}}}\right)^{\frac{1}{2}} \exp(\mathrm{i}\arg \mathrm{S_{mc}}) \tag{6}$$

Appendix C. Electro-mechanical model of an aircraft propeller

Contents

C.1 Modeling of actuator thrust dynamics

An analytical model of the dynamics of the actuator thrust has been derived. This analytical model was used to :

- Predict actuator performances, in terms of bandwidth and maximal thrust variations.
- Highlight the main influencing parameters to help the choice between one {propeller + motor + ESC} configuration and another.

The main assumptions and limitations of this analytical development include:

- No blade flapping effects (blades are rigid) whereas it has already been demonstrated (e.g. (Hoffmann *et al.*, 2011)) the impact of blade flapping on the generated thrust of a drone.
- The aerodynamic modeling of the propeller:
  - Steady-state characteristics of the aerodynamic thrust generated. The typical characteristic time for unsteady aerodynamics has been estimated in the order of one rotor revolution (Pounds, Mahony and Corke, 2008). Classical rotational velocities of aircraft propeller are the range [3000-10000] RPM, this makes unsteady aerodynamics phenomena important for a time range of [6-20]ms;
  - The thrust and torque coefficient are assumed constant. The thrust of the propeller could be expressed by $T_{prop} = \overline{C_T}\omega_{prop}^2$ and $Q_{prop} = \overline{C_Q}\omega_{prop}^2$. The "integral" thrust and torque coefficients $\overline{C_T}$ and $\overline{C_Q}$ are related to the propeller geometry by $\overline{C_T} = \frac{1}{2}\rho_{air}C_T A_{prop}$ and $\overline{C_Q} = \frac{1}{2}\rho_{air}C_Q A_{prop}$, A_{prop} being the rotor swept area.
- Linearization around a working point defined by $(\omega_0, T_{prop\,0}, Q_{prop\,0})$;

- For typical brushless DC motors used for the quadcopters, the inductance L - associated to an electrical time constant - is usually assumed to have a negligible role (Bouabdallah, Murrieri and Siegwart, 2004; Bouabdallah, 2007) ;
- Regenerative and dissipation braking are neglected;
- Additional assumptions taking into account the specificity of aircraft propellers of multi-copters UAV are introduced when required.

Objective : we are looking for an Ordinary Differential Equation (ODE) of the thrust T depending on the input varying voltage percentage β. With suitable approximations, a transfer function between the two variables is obtained. Positive and negative saturations of the thrust and thrust derivative are also derived to complete the model.

C.2 ODE Thrust – Duty ratio

The electro-mechanical model of a BLDC motor with aircraft propeller could be summarized by the 2 equations in Eq.(7) (Bouabdallah, 2007; Martinez-Alvarado *et al.*, 2014; Muzar, Lanteigne and McLeod, 2017). The first line is the 2nd law of Newton applied to the {motor + propeller} assembly and the second line is the electrical balance for the motor.

$$\begin{cases} J_t \dot{\omega_m} = K_t(i - i_{idle}) - b_f \omega_m - \overline{C_Q}\omega_{prop}^2 \\ i = \dfrac{u - K_e \omega_m}{R_m} \end{cases} \quad (7)$$

With :

- J_t the total inertia of the shaft and propeller : $J_t = J_m + J_{prop} \times r^2$,
- K_e, K_t, R_m the motor constants introduced previously,
- b_f a linear friction coefficient, defined by $Q_{friction} = -b_f\, \omega_m$;
- i the current intensity and u the input voltage.

Combining the two equations in Eq. (7) leads to the electro-mechanical equation Eq. (8):

$$J_t \dot{\omega_m} + \left(b_f + \frac{K_t K_e}{R_m}\right)\omega_m + \overline{C_Q}\frac{\omega_m^2}{r^2} = \frac{K_t}{R_m} u \quad (8)$$

Additional set of relations are required to get the target ODE between the thrust T and the input duty ratio β. These relations are listed below without going into the details.

- Definition of the duty-ratio β : $u = \beta \times U_c$ with U_c the input stabilized voltage (battery or stabilized power units);
- No gearbox - typical assumption for multi-rotor setups - we have $\omega_{prop} = \omega_m \Leftrightarrow r = 1$;
- Due to the constant thrust coefficient $\overline{C_T}$, the thrust variation $\dot{T}$ could be approximated by $\dot{T} = 2\overline{C_T}\omega_m \dot{\omega_m}$;
- The propeller inertia is usually several order of magnitudes larger than the motor shaft inertia, $J_t \sim J_{prop}$;
- Relations between the motor constants, $K_t K_e = \frac{30}{\pi K_v^2}$,

The linearization is applied around an operating point, $\omega_m = \omega_0 + \delta_\omega$ with δ denoting a small variation for each quantity. We get $T = T_0 + \delta_T; \dot{T} = \dot{T_0} + \dot{\delta_T};\ \beta = \beta_0 + \delta_\beta$ and $i = i_0 + \delta_i$.

Applied to the thrust, this linearization leads to: $T_0 + \delta_T = \overline{C_T}(\omega_0 + \delta_\omega)^2 \sim \overline{C_T}\omega_0^2 + 2\overline{C_T}\omega_0\delta_\omega + o(\delta_\omega)$. This relation implies $\delta_T \sim 2C_T\omega_0\delta_\omega$.

For the thrust derivative, this leads to $\dot{T} = 2\overline{C_T}\omega_m\dot{\omega_m} \sim \dot{T}_0 + 2\overline{C_T}\omega_0\delta\dot{\omega_m}$. This relation implies $\dot{\delta_T} \sim 2\overline{C_T}\omega_0\delta\dot{\omega_m}$.

This first set of relations leads to Eq. (10):

$$\frac{J_{prop}\dot{\delta_T}}{2C_T\omega_0} + \left(b_f + \frac{K_tK_e}{R_m}\right)(\omega_0 + \delta_\omega) + (T_0 + \delta_T) * \frac{\overline{C_Q}}{\overline{C_T}} = \frac{K_t}{R_m}U_c\,(\beta_0 + \delta_\beta) \tag{9}$$

Simplification of this relation by removing the steady-state relations at the operating point ω_0 leads to Eq. (10):

$$\frac{J_{prop}\dot{\delta_T}}{2C_T\omega_0} + \left(b_f + \frac{K_tK_e}{R_m}\right)\delta_\omega + \delta_T * \frac{\overline{C_Q}}{\overline{C_T}} = \frac{K_t}{R_m}U_c\,\delta_\beta \tag{10}$$

Reorganizing the term leads to Eq. (11):

$$\dot{\delta_T}\left(\frac{J_{prop}}{2\overline{C_T}\omega_0}\right) + \delta_T\left(\frac{1}{2\overline{C_T}\omega_0}\left(b_f + \frac{30}{\pi\,K_v^2R_m}\right) + \frac{\overline{C_Q}}{\overline{C_T}}\right) = \frac{K_t}{R_m}U_c\,\delta_\beta \tag{11}$$

The expression of the δ_T coefficient is further simplified. The expression is called A and is detailed in Eq. (12):

$$A = \frac{1}{2\overline{C_T}\omega_0}\left(b_f + \frac{30}{\pi\,K_v^2R_m}\right) + \frac{\overline{C_Q}}{\overline{C_T}} \tag{12}$$

In the supplier documentation, the value of C_Q and C_T are rarely given. To express A with known variables, the steady-state relations are used again:

- $Q_{m\,|\,0} = \overline{C_Q}\omega_0^2 + b_f\omega_0$,
- Definition of the motor constant K_t : $Q_{m\,|\,0} = K_t(i_0 - i_{idle})$,
- Finally, we get $\overline{C_Q}\omega_0 \approx \frac{K_t(i_0 - i_{idle})}{\omega_0} - b_f$

The A coefficient is simplified in Eq. (13):

$$A = \frac{1}{2\overline{C_T}\omega_0} * \left(\frac{30}{\pi\,K_v^2R_m} + \frac{2K_t(i_0 - i_{idle})}{\omega_0} - b_f\right) \tag{13}$$

Finally, the characteristic ODE is re-expressed in a canonical form by Eq. (14)

$$\begin{cases} \tau\dot{T} + T = K \times \beta \\ \tau \cong \dfrac{J_{prop}}{\left(\dfrac{30}{\pi\,K_v^2R_m} + 2\dfrac{K_t(i_0 - i_{idle})}{\omega_0} - b_f\right)} \\ K \cong \dfrac{K_t \times U_c * \ 2\overline{C_T}\omega_0}{R_m * \left(\dfrac{30}{\pi\,K_v^2R_m} + 2 * \dfrac{K_t(i_0 - i_{idle})}{\omega_0} - b_f\right)} \end{cases} \tag{14}$$

This the characteristic equation of a 1st order low pass filter between the input duty-ratio β and the output thrust T.

C.3 Saturations of thrust variations

Different mechanisms might saturate the thrust variations. For positive variations of the thrust, the saturation comes from the maximal torque which could be produced by the motor. This maximal torque is defined from the maximal intensity sent to the motor. This maximal intensity might be related to the ESC settings to protect motor over-heating it could also be a limitation of the power supply. The batteries intensity limitation has been observed by Pounds et al. in (Pounds, Mahony and Corke, 2010) for UAV quadcopters applications. For negative variation of the thrust, the saturation is due to the constant sign of the torque - except when braking could be achieved and when motor reversing is used

Applying a torque balance to the {motor + propeller} assembly leads to Eq. (15):

$$J_t\dot{\omega_m} = -Q_{aero} + Q_m - Q_{friction} \tag{15}$$

Using the relations for each torque component leads to Eq.(16):

$$J_t\dot{\omega_m} = K_t(i - i_{idle}) + \overline{C_Q}\omega_m^2 - b_f\omega_m \tag{16}$$

The thrust time derivative could be expressed by $\dot{T} = 2\overline{C_T}\omega_m\dot{\omega}_m$. Eq.(16) is re-expressed in Eq. (17):

$$\frac{J_t}{2\overline{C_T}\omega_m} * \dot{T} = K_t(i - i_{idle}) + \overline{C_Q}\omega_m^2 - b_f\omega_m \tag{17}$$

The positive saturation $\left[\frac{\partial T}{\partial t}_{max}\right]^+$ comes from $i \leq i_{max}$ and the negative saturation $\left[\frac{\partial T}{\partial t}_{max}\right]^-$ comes from $i \geq 0$.

Positive saturation :

$$\left[\frac{\partial T}{\partial t}_{max}\right]^+ = \frac{2\overline{C_T}\omega_0}{J_t} * \left(K_t(i_{max} - i_{idle}) - \overline{C_Q}\omega_0^2 - b_f\omega_0\right)$$

Negative saturation:

$$\left[\frac{\partial T}{\partial t}_{max}\right]^- = -\left(\omega_0\left(\frac{2\overline{C_T}K_t i_{idle}}{J_t} + b_f\right) + \overline{C_Q}\omega_0^2\right)$$

C.4 Conclusion

The characteristic ODE expressed in a canonical form by Eq.(4.7). It is the characteristic equation of a 1st order low pass filter between the input duty-ratio β and the output thrust T with gain K and time characteristic τ. Two saturation mechanisms of the thrust variation $\frac{\partial T}{\partial t}$ have been taken into account to model positive saturation (maximal torque, characterized by i_{max}) and negative saturation (no braking). This modeling is valid around a working point defined by ω_0.

$$\begin{cases} \tau\dot{T} + T = Ku \\ \tau \sim \dfrac{J_{prop}}{\left(\dfrac{30}{\pi K_v^2 R_m} + 2\dfrac{K_t(i_0 - i_{idle})}{\omega_0} - b_f\right)} \\ K \sim \dfrac{K_t \times U_c * 2\overline{C_T}\omega_0}{R_m * \left(\dfrac{30}{\pi K_v^2 R_m} + 2 * \dfrac{K_t(i_0 - i_{idle})}{\omega_0} - b_f\right)} \\ \left[\dfrac{\partial T}{\partial t}_{max}\right]^+ = \dfrac{2T_0}{J_t\omega_0} * \left(K_t(i_{max} - i_{idle}) - \overline{C_Q}\omega_0^2 - b_f\omega_0\right) \\ \left[\dfrac{\partial T}{\partial t}_{max}\right]^- = -\left(\omega_0\left(\dfrac{2\overline{C_T}K_t i_{idle}}{J_t} + b_f\right) + \overline{C_Q}\omega_0^2\right) \end{cases} \tag{18}$$

In terms of application of this model, the different motor constants are usually accessible from the manufacturer specifications. J_{prop}, the propeller inertia around its axis of rotation, can be computed from mass properties and approximated geometry. $\overline{C_Q}$ and b_f can be estimated from tabulate steady-state characteristics of the motor + propeller assembly.

C.5 Perspectives

Modeling of braking

To decelerate the propeller, which has a lot of inertia, the motor can work as generator, sending the current back to the power supply. Regenerative braking corresponds to the switch to the generator mode of the motor, the power supply (batteries) receiving the current from the generator. Dynamic braking works similarly but the energy - the current - is dissipated into heat thanks to external resistors.

ESC dynamic

From discussions with manufacturers, the ESC limits the variations of the mechanical torque to prevent the de-synchronizing of electromechanical torque

C.6 Constitution of a database

To anticipate the single actuators performances and to apply the force allocation procedure to different set of actuators, different motors and propellers have been considered. The catalog of two manufacturers, KDE-Direct and T-motor have been considered. A pre-selection on the thrust and mass ranges highlight a couple of potentially suitable {motor + propeller} assembly.

Then, for each actuator, the cut-off frequency $f_{cut-off} = \frac{1}{2\pi\tau}$ has been estimated for different operating points as well as the thrust derivative saturations. With the model established here-above, the dependency of the cut-off frequency to the operating point is negligible. The motor, ESC, propeller diameter, mass of the motor and propeller, maximum thrust capacity and estimated cut-of frequency are presented in Table 43. The actuator names correspond to the motor names.

Motor	**ESC**	**Prop. diam. [mm]**	**Mass [g]**	**Thrust max [N]**	$f_{cut-off}$ **[Hz]**
KDE 4215XF-465	KDE XF-UAS55HVC	317	300	23	5.1
KDE 5215XF-220	KDE-UAS85UVC	395	410	47	6.9
T-motor MN501S	ALPHA 60A HV	356	190	39	5.0
T-motor P60	FLAME 70A LV	508	415	62	4.7

Table 43: Main actuators under consideration

The thrust derivatives saturations are represented for the four actuators in Figure 119. It illustrates that for low regimes, the freewheel of each actuator may have a strong impact on its dynamic.

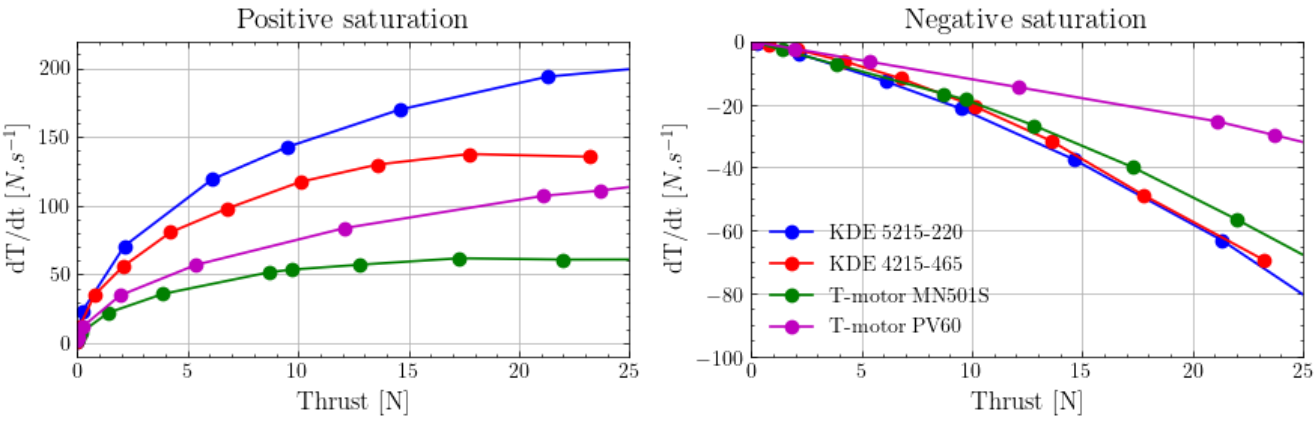

Figure 119: Positive (left) and negative (right) saturations of the four considered actuators

Appendix D. SOFTWIND SPAR tests characteristics

Contents

D.1 As-built FWT characteristics

An overview of the different parts is depicted in Figure 120. The flexible aluminum mast is surrounded by a white casing, which is not present on the left picture but partially visible on the right one. This casing is rigidly connected to the floater and its role is to hold the cables up to the RNA, avoiding long freely suspended cables between the nacelle and the floater. The cables linking the floater to the RNA are separated in four groups and each one is running along the casing from the floater to the top of the casing. At the top of the casing, each group is suspended in a short U-shape to the RNA. Each U-loop is only 80cm in order to minimize mass and stiffness influence on the RNA. In terms of mass budget, the casing mass is taken into account in the overall floater mass.

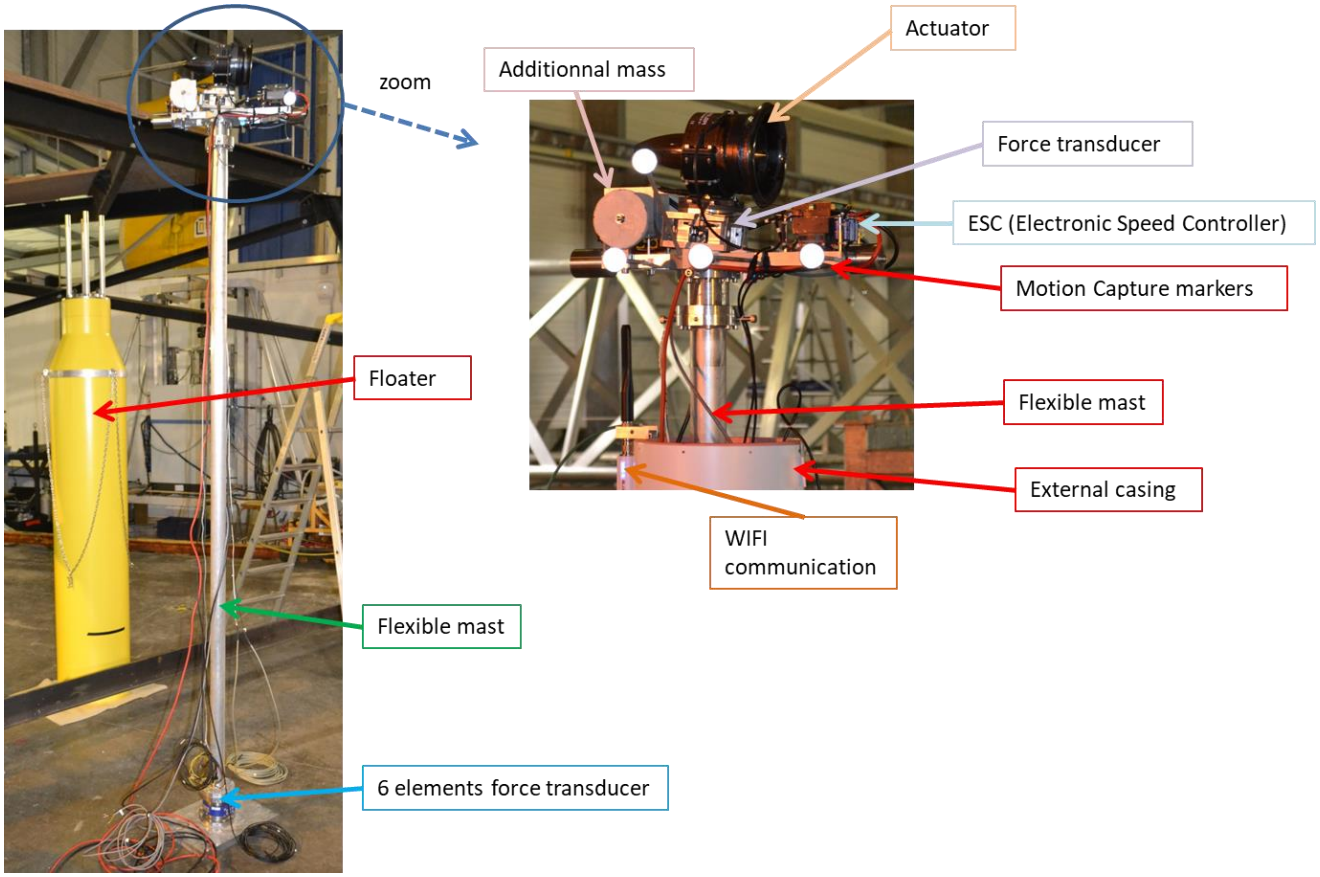

Figure 120: Description of the wind turbine experimental setup

D.1.1 Wind turbine

The as-built wind turbine is made of different sections to ensure the data acquisition (tower base 6-component force transducer) and the flexibility of the tower. These sections are, from top to bottom:

- The RNA, including the actuator, a 2-component force transducer, and additional mass to provide the correct RNA mass, CM and inertia, depicted in Figure 121. This RNA also includes 4 reflecting markers for the MOCAP system;
- The flexible mast, an aluminum beam with outer diameter 60mm and thickness 2mm,
- The mast is clamped to a tower base 6-component force transducer (HBM BG3).

To avoid any effects (weight and flexion forces and moments) due to the actuator and DAQ cables, an additional mast has been put in front of the wind turbine. This additional mast is replaced by a casing for the SOFTWIND SPAR setup.

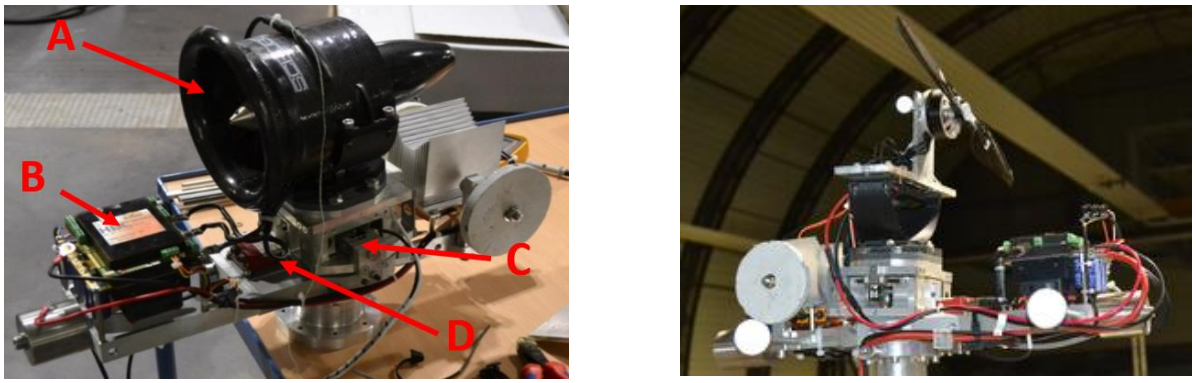

Figure 121: Model scale RNA. Left: initial RNA including A) actuator, B) motor drive, C) thrust sensor and D) accelerometer. Right: modified RNA including the KDE-Direct actuator for the BGF set-up

The main dimensions, mass and structural properties of the tower and RNA are detailed in Table 44. The tower is split in different parts, i.e. the BG3 assembly (BG3, screws and plates) and the flexible mast. The mass, stiffness and inertia of the flexible aluminum mast have been estimated from:

- The aluminum properties in the literature: $E_{Al} = 70\ GPa; \rho_{Al} = 2.7E+3\ kg; m^{-3}$.
- The specified properties concerning the external and internal diameters $\phi_{ext} = 60mm\ ; \phi_{int} = 56mm$. The external diameter has been checked using a caliper.

The associated uncertainties reflect these approximations. The RNA center of gravity (CoG) and inertias come from the CAD modeling as it was not possible to measure it. The impact due to these uncertainties on the RNA inertias are expected to be small.

	Scale 1:40		Scale 1:1	
	Values	Uncertainties	Values	Uncertainties
Overall properties				
Tower base height from MSL [m]	0.232	0.005	9.3	0.2
Tower top above MSL [m]	2.751	0.005	110.0	0.2
Hub height above MSL [m]	3.03	0.01	121.2	0.4
BG3 assembly				
Mass [kg]	10.98	0.05	7.03E+05	3.2E+03
Height [m]	0.15	0.001	5.88	0.04
Stiffness	Stiff			
Inertia	undetermined			
Mast / Tube 60 * 2mm				
Mass [kg]	2.50	0.03	1.6E+05	1.9E+03
Height [m]	2.519	0.002	100.76	0.08
Stiffness [N.m^2]	1.1E+04	5E+02	1.1E+12	5E+10
Lineic inertia [kg.m]	4.2E-04	1E-05	1.1E+03	3E+01
RNA				
Mass [kg]	12.45	0.1	8.0E+05	6.4E+03
CoG X above twr top [m]	-0.015	0.002	-0.59	0.08
CoG Y above twr top [m]	-0.001	0.002	-0.04	0.08
CoG Z above twr top [m]	0.142	0.005	5.7	0.2
Inertia xx around CoG RNA [kg.m^-2]	0.07	0.03	7.4E+06	3.1E+06
Inertia yy around CoG RNA [kg.m^-2]	0.27	0.05	2.7E+07	5.1E+06
Inertia zz around CoG RNA [kg.m^-2]	0.24	0.05	2.4E+07	5.1E+06

Table 44: Main characteristics of the as-built wind turbine

Cantilevered configuration

Different tests have been done for the identification of the tower. They include decay and hammer tests, and stiffness identification. These tests have been done by clamping the tower (including the 6-component tower base force transducer) to a rigid and flat surface. The nacelle displacements are recorded using 2 Qualisys cameras and 4 reflecting markers, with a proper calibration of the test zone.

Hammer test – identification of the natural frequencies:

Hammer tests are performed by impacting the tower at the nacelle height and also at the middle of the tower. The excitation at nacelle height provides a strong excitation of the odd tower modes, and the half nacelle height excitation excite mostly the even tower modes. The first 2 modes for the fore-aft and side-side directions are identified from the nacelle acceleration spectra. The natural frequencies identified by the hammer tests are given in Table 45.

Fore-aft 1st mode [Hz]	1.80
Side-side1st mode [Hz]	1.80
Fore-aft 2nd mode [Hz]	25.6
Side-side 2nd mode [Hz]	25.6

Table 45: Identified tower natural frequencies for a clamped configuration

Stiffness identification

The integrated stiffness identification was done by three means:

1. By calibrated masses, a pulley and a lightweight rope, pulling close to the Center of Thrust (CoT) of the actuator;
2. By steady-state thrust levels using the actuator,
3. By quasi-static linear ramp of thrust using the actuator.

This integrated tower stiffness represents the tower deflection [m] for a given horizontal force applied at the hub center [N]. The identified as-built stiffness and target stiffness are summarized in Table 46. The target tower stiffness for the DTU 10MW baseline has been obtained from linear fit of cantilevered full-scale wind turbine simulations and then scaled–down using Froude scaling factors. The as-built tower stiffness is slightly stiffer (+30%) than the target tower stiffness.

As-built tower stiffness $[N.m^{-1}]$	Target tower stiffness $[N.m^{-1}]$
1.6E+3	1.3E+3

Table 46: Identified tower integrated stiffness. Model scale as-built and target

Decay tests – damping identification

In this part, the damping is expressed as ratio of the damping with the critical damping for the 1st tower fore-aft mode. The critical damping identification includes the RNA assembly.

The structural damping is first investigated. Decay tests are performed without the SIL methodology. Two cases, one without any thrust generated by the turbine and then one with a steady thrust:

- Actuator is off, the same pulley and calibrated masses system are used as for the stiffness identification. The tower is released from a given deflected position. This gives the structural damping of the 1st tower fore-aft mode. The assumption is that the aerodynamic drag acting on the mast and the stopped turbine gives a negligible damping compared to the structural damping. $\zeta_{struct} = 0.6\ \%\ [\pm\ 0.1\%]$ has been identified.
- Actuator is on, the setpoint is a steady thrust. With the change in the actuator inflow condition due to the tower top velocities, this leads to an additional damping $\zeta_{act\ inflow}$. $\zeta_{act\ inflow} = 0.6\%\ [\pm 0.3\%]$ has been identified. This additional damping was poorly identified in this configuration and finer results have been obtained for the SOFTWIND SPAR campaign (c.f. hereafter).

The total "apparent" structural damping of the tower and the actuator is then given by Eq. (19):

$$\zeta_{struct\ apparent} = \zeta_{struct} + \zeta_{act\ inflow} \tag{19}$$

Then, the additional damping due to the SIL methodology is investigated. The actuator is activated and its setpoint is computed using the SIL methodology for a uniform steady wind case. The force computed by OpenFAST leads to an aerodynamic damping ζ_{aero}, which is the target load for the actuator. Then, as explained in details in part 3.4, the actuator aims at reproducing this setpoint thrust, and generates an actuated force with a certain delay and attenuation. This makes the actuated force differ to the aerodynamic damping, both due to the delay and to the attenuation. The resulting damping is called $\zeta_{aero\ resulting}$.

When clamped on a floating body, the tower mode is coupled to the platform mode; consequently, a hydrodynamic damping ζ_{hydro} could also damps the motions. The total damping acting for the tower fore-aft DoF is expressed in Eq. (20):

$$\zeta_{tot} = \zeta_{struct} + \zeta_{act\ inflow} + \zeta_{aero\ resulting} + \zeta_{hydro} \quad (20)$$

To compute ζ_{aero}, a numerical simulation is performed with OpenFAST. The represented tower is the full scale as-built tower. The correct mass and stiffness distributions, as explained in chapter 8, are used in the numerical model. Because the objective is to get an order of magnitude of the aerodynamic damping ratio, the uncertainties related to the experimental data inputs (mass and stiffness of the tower elements) are considered negligible. In Figure 122, the tower 1st fore-aft deflections are compared for a no wind case and a steady wind at 11.4 m/s case. These simulations are decay tests with an initial fore-aft deflection of 0.3m, plus the mean tower deflection (0.42m for a wind speed of 11.4 m/s), with only this DoF being enabled. The floater is not free to move, and for simplicity, the rotor speed and blade pitch angle are fixed to the steady-state values (respectively 9.6 RPM and 3.7 deg) for the $U_w = 11.4\,m/s$ case. A damping analysis run on this case leads to $\zeta_{aero} = 5\%$. However, in chapter 4 it has been shown that the aerodynamic damping depends on the operating point, and its value at $U_w = 18m/s$ is approximately a quarter of the rated wind speed value. This makes the aerodynamic damping in the range [1.25 - 5.0]%.

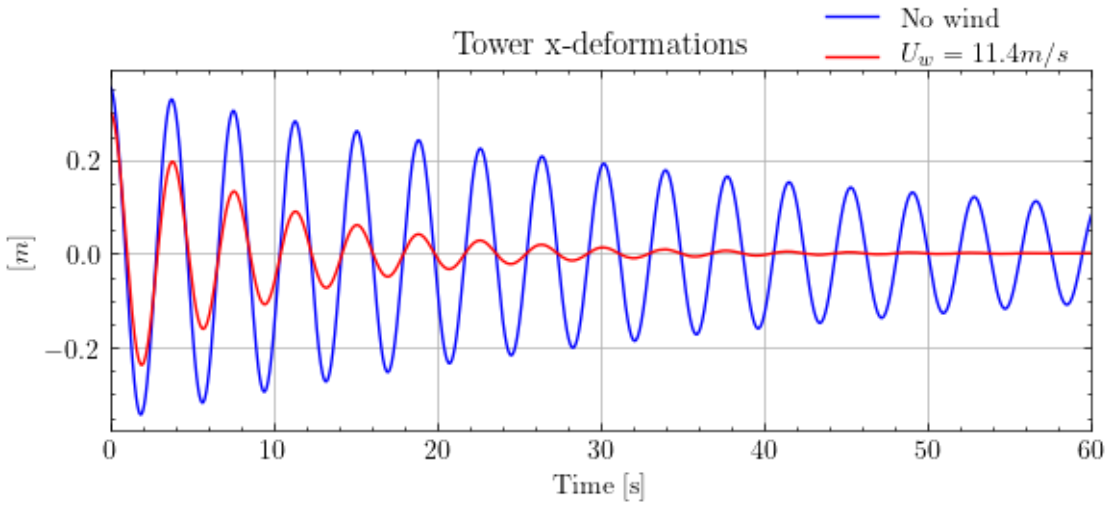

Figure 122: Tower deflection in the x-direction. Numerical simulations of full scale as-built clamped tower with and without wind.

In the DTU 10MW RWT documentation (Bak *et al.*, 2013), the considered damping ratio is 1% critical without the RNA mass. After a decay test in numerical simulations with the open source FAST model of the onshore DTU-10MW RWT, this leads to a damping ratio of 0.6% with the RNA mass. Consequently, this makes the estimated damping ratio of the clamped tower with the turbine on ($\zeta_{struct\ apparent} = 1.2\%\ [\pm 0.2\%]$) approximately 2 times bigger than the target structural damping. The identified 1st fore-aft mode natural frequency of the tower is 1.81Hz from the decay tests, very close to the 1.80 Hz identified with the hammer tests.

Due to problems in the tests performed with the SIL methodology activated, we are not able to quantify the value of $\zeta_{resulting}$ for the clamped configuration. Due to bugs in the numerical tool (see chapter 7 for details), this resulting damping has not been quantified.

	As-built	Target
ζ_{struct}[%]	0.6	0.6
$\zeta_{act\ inflow}$[%]	0.6	0.0
$\zeta_{aero\ resulting}$[%]	Non-identified	[1.25 - 5.0]

Table 47: Identified damping ratios for the clamped tower

Clamped on the SPAR configuration

The tests and analyses for a clamped configuration are performed again with the tower clamped on the floater, to check the differences in terms of damping, stiffness and natural frequencies. Indeed, what is expected from this new clamping condition is an overall decrease of the stiffness and increase of the natural frequency.

The tower natural frequencies, integrated stiffness and damping ratio are given in Table 48 for both configurations, cantilevered and clamped on the SPAR.

The additional damping due to the actuator inflow has been re-identified to $\zeta_{act\ inflow} = 0.15\%\ [\pm 0.1\%]$. The amplitude of this damping is approximately proportional to the amplitude of the oscillations, due to the square dependency between the actuator thrust and its exhaust speed. The actuator inflow damping ratio varies, for amplitudes of interest, in the range [0.05 – 0.25]%.

	Cantilevered	Clamped on the SPAR
Fore-aft 1st mode [Hz]	1.80	2.42
Side-side1st mode [Hz]	1.80	2.42
Fore-aft 2nd mode [Hz]	25.6	29.6
Side-side 2nd mode [Hz]	25.6	29.6
Stiffness [$N.m^{-1}$]	1.6E+3	1.1E+3
Structural damping ratio [%]	0.6	0.6

Table 48: Identified tower natural frequencies, integrated stiffness and damping ratio for the cantilevered and the clamped on the SPAR configurations

The damping reproduction by the SIL system, denoted $\zeta_{resulting}$ is expected to be a certain share of the aerodynamic damping ζ_{aero} of the numerical model. This portion is linked to the total SIL system delay as presented in part 3.3.

D.1.2 Floater

The floater is made of two parts: an aluminum shell that gives the external floater shape and the core of the buoy. For a full scale floater, the core of the buoy is mainly composed of different types of ballast (high density media, water, …). For the wave tank test purpose, the core of the buoy was made of different pieces:

- ballast made of lead masses,
- battery,
- power connections,
- compactRIO controller,
- Beckhoff controller for external control law,
- stabilized power units for the different sensors,
- Different suspended cables for a connection between the topside DAQ and the compactRIO

The core of the buoy is depicted in Figure 123. The installed floater in the wave tank is also depicted.

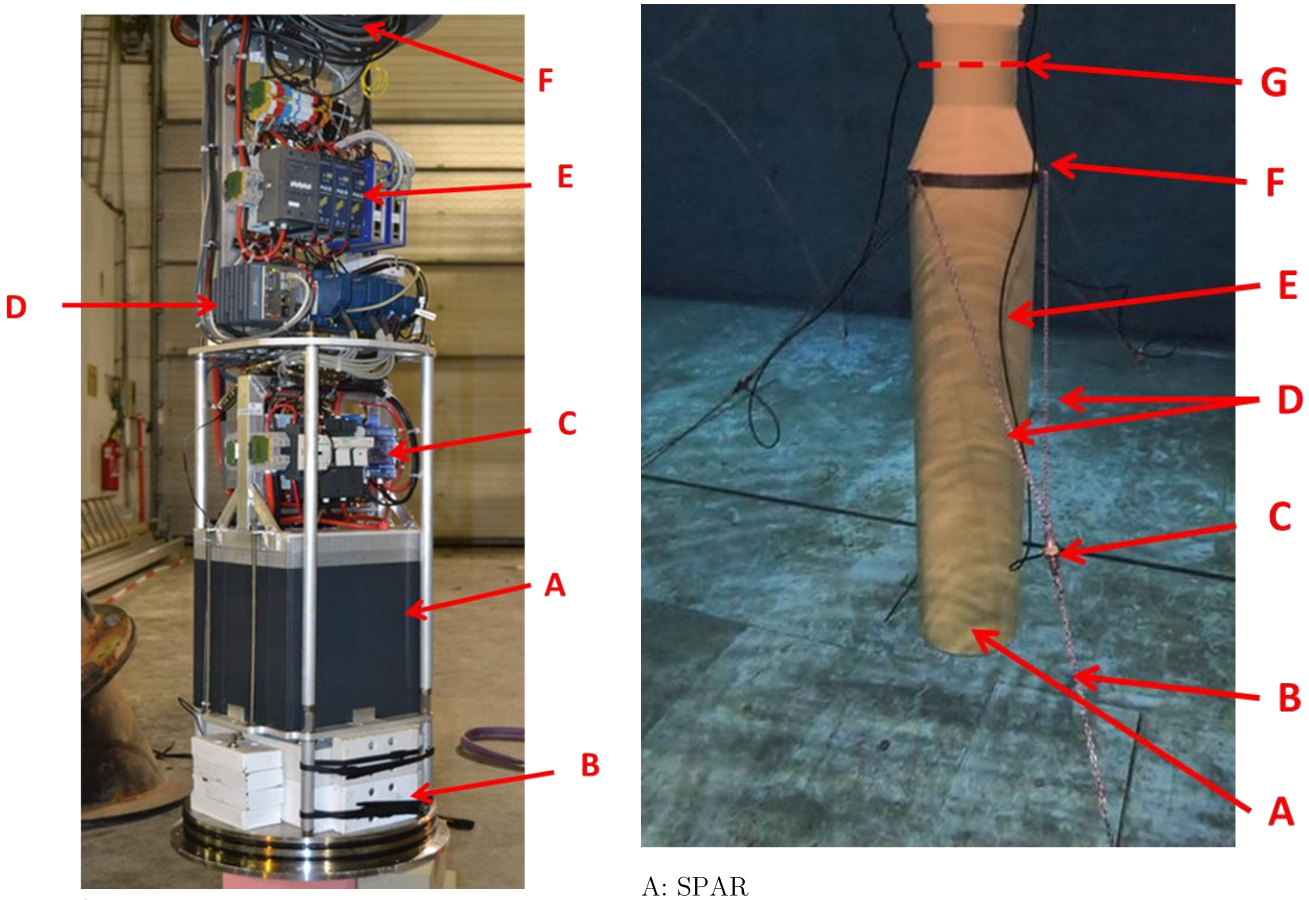

A: Battery
B: Ballast (Lead)
C: Power supply connections
D: CompactRIO controller
E: Power supply stabilized unit for DAQ
F: Suspended cables atop of the rigid ballast

A: SPAR
B: Bottom chain
C: Mooring tension sensor
D: Bridles
E: Mooring sensor cable
F: Fairlead
G: Free surface

Figure 123: Left) Inside the floater. Right) Underwater picture of the floater with its mooring system in the wave tank

The main dimensions and mass properties are summarized in Table 49 including the estimated uncertainties for each characteristic. Definitions of the different dimensions are illustrated in chapter 5.

	Values		Uncertainties	
	Scale 1:40	Scale 1:1	Scale 1:40	Scale 1:1
Floater				
Floater CoG X from centerline [m]	-0.004	-0.16	0.004	0.16
Floater CoG Y from centerline [m]	0.00	0.00	0.004	0.16
Floater CoG Z from MSL [m]	-1.789	-71.56	0.015	0.6
Floater Mass [kg]	303.8	1.94E+07	0.1	6.4E+03
Ixx [kg.m^2] around CoG FWT	190	1.95E+10	30	3E+09
Iyy [kg.m^2] around CoG FWT	190	1.95E+10	30	3E+09
Izz [kg.m^2] around CoG FWT	10	1.0E+09	5	5E+08
D_{MSL} [m]	0.280	11.2	0.001	0.04
D_{SPAR} [m]	0.450	18.0	0.001	0.04
Taper top from MSL [m]	-0.135	-5.40	0.005	0.2
Taper height [m]	0.100	4.00	0.002	0.08
CoB Z [m]	-1.023	-40.92	0.005	0.2
Draft [m]	2.285	91.4	0.003	0.12
Freeboard [m]	0.065	2.6	0.003	0.12
Wind turbine				
Hub height above MSL [m]	3.03	121.2	0.01	0.4
Tower height [m]	2.666	106.6	0.005	0.2
Tower mass [kg]	13.48	8.63E+05	0.05	3E+03
Tower CoG Z [m]	0.41	16.4	0.01	0.4
RNA mass [kg]	12.45	7.97E+05	0.15	9.6E+03
RNA CoG X [m]	-0.015	-0.6	0.01	0.4
RNA CoG Y [m]	0.000	0.0	0.005	0.2
RNA CoG Z [m]	0.142	5.7	0.01	0.4

Table 49: Main mass and dimensions properties of the as-built SOFTWIND SPAR FWT

D.1.3 Mooring system

The full-scale designed mooring system is made of 3 catenary mooring chains. In order to respect the mass properties and the geometry of the chains, studless stainless steel chains have been selected. Azcona et al. (Azcona *et al.*, 2017) studied the behavior of model scale mooring chains in wave tank experiments. They concluded that the hydrodynamic coefficients recommended in the standards, which have been fit to full scale moorings properties, apply well to a scale of 1/40. In Table 50, the as-built model and full scale moorings properties are presented with the associated uncertainties.

	Values		Uncertainties	
	Scale 1:40	Scale 1:1	Scale 1:40	Scale 1:1
Anchor 1 positions (X,Y) [m]	(15.96, -0.03)	(15.96, -0.03)	0.015	0.6
Anchor 2 positions (X,Y) [m]	(-7.97, 13.85)	(-7.97, 13.85)	0.015	0.6
Anchor 3 positions (X,Y) [m]	(-8.01, -13.86)	(-8.01, -13.86)	0.015	0.6
Anchors depth [m]	5.00	200	0.010	0.4
Bottom chain 1 length [m]	15.69	627.6	0.01	0.4
Bottom chain 2 length [m]	15.74	629.6	0.01	0.4
Bottom chain 3 length [m]	15.72	628.8	0.01	0.4
Diameter chain [mm]	3.7	148	0.05	2
Mass chain in water [kg/m]	0.237	379	0.001	1.6
Mass chain in air [kg/m]	0.275	440	0.001	1.6
Mass load cell in water [kg]	0.43	2.75E+04	0.02	1280
Length load cell [m]	0.235	9.4	0.005	0.2
Bridle chain length [m]	1.20	48.0	0.01	0.4
Fairleads depth [m]	-0.335	-13.4	0.005	0.2
Fairleads radius [m]	0.261	10.4	0.005	0.2

Table 50:As-built model scale and full scale mooring properties

The different elements constituting the mooring chain are depicted in Figure 124. The underwater unidirectional load cells constitute the connections between the bottom chains and to the bridles. The mass in air and mass in water of the different chains has a minor variability (<0.1%). The measurement of the mass per unit length in water is depicted in Figure 124.b. Note that the mass per unit length in air and in water of the model scale chain fits perfectly to the formulas fitted on full scale offshore mooring chains. This is due to the very similar shape of these model scale chain links compared to full scale studless mooring chain links.

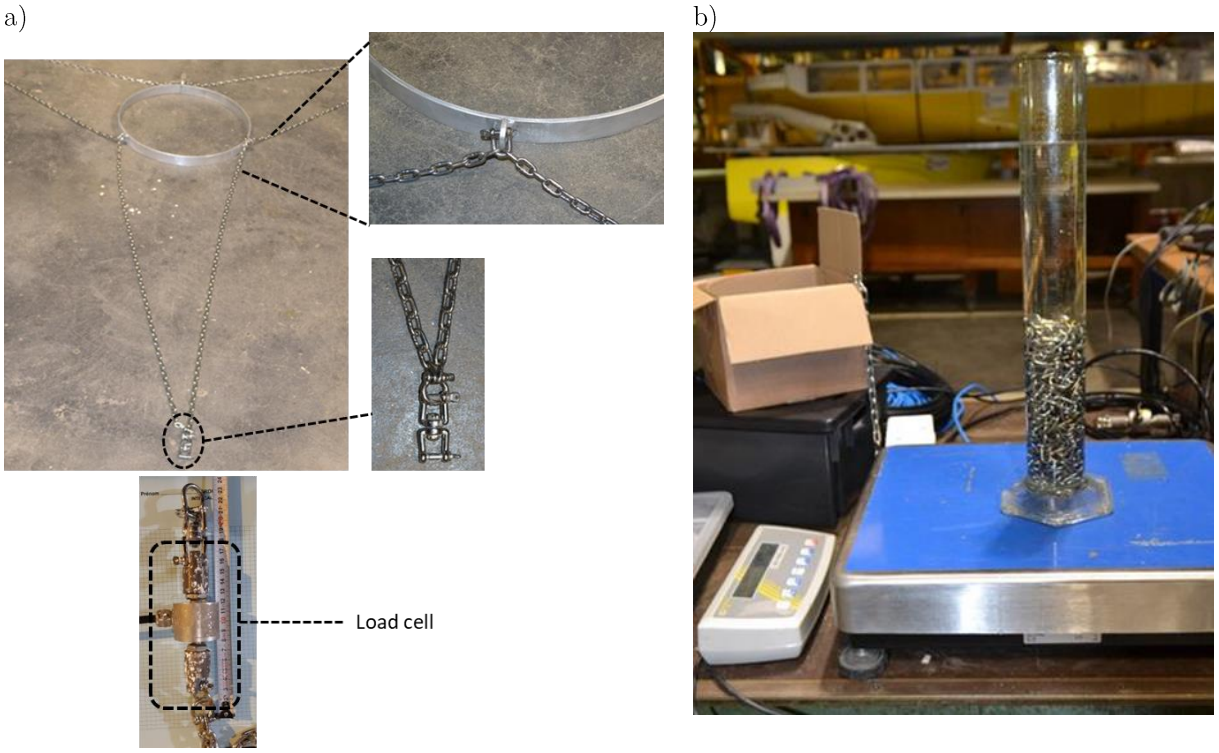

Figure 124: Moorings details. a) the different elements constituting a mooring line. b) evaluation of the mass per unit length of the mooring line in water.

D.1.4 Floating wind turbine characterization

Different identification steps have been performed on the model. They include:

- Hydrostatic stiffness characterization, especially for the platform pitch DoF, with linear ramp of the actuator thrust,
- Mooring horizontal restoring forces characterization with pull-out test,
- Eigen period analysis with decay tests in still water,
- Damping analysis with decay tests in still water and in waves,
- Regular waves tests to compute the FWT global motions RAO and the wave drift forces.

Different pull-out tests have been performed to characterize the horizontal mooring stiffness for the platform surge DoF. One of the pull-out test is presented in Figure 125. The estimated horizontal mooring stiffness is $K_{moor\,11} = 75\,N.m^{-1}$ from the slope of the Force/Surge relation. Note that this mooring restoring force seems well approximated by a linear force, which is surprising for catenary systems. The reason is that the single line force/displacement characteristics should not be confused with the total restoring force. For this specific mooring layout (two lines upward and one line backward with a 120° orientation), the total restoring horizontal force is linear. For the semisubmersible model in the DeepCWind test campaign (Koo *et al.*, 2012) and the corresponding OC4 numerical model (Robertson *et al.*, 2014), the total restoring force tends to be nonlinear for higher offset values.

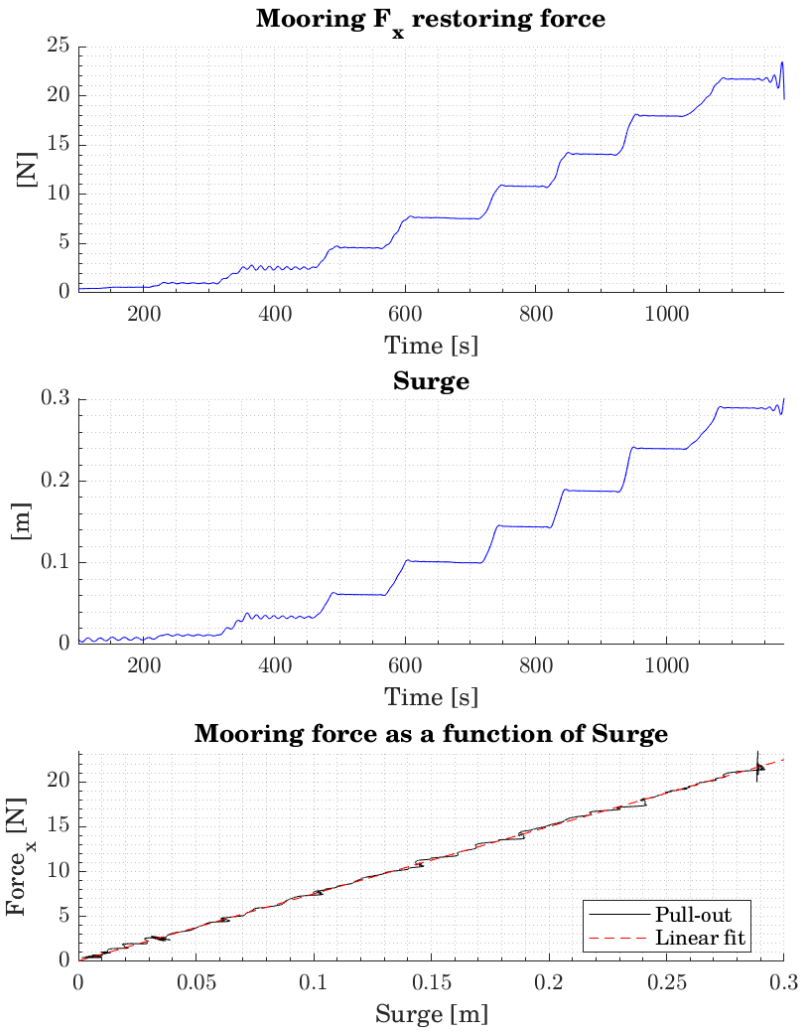

Figure 125: Pull-out test in X direction. External force sensor in the x-direction versus platform surge

Decay tests in different conditions have been performed several times. Those decay tests have mostly been done in still water, but decay tests in regular waves and in Software-in-the-loop mode have also been performed. Getting a proper decay test is not a trivial task especially for the rotational DoF. Basically, the objective is to impose an offset for only one DoF, get a zero velocity, and then release it suddenly. To get a pure rotation (e.g. platform Pitch) without any translation (e.g. platform Surge), two pulling points are required. Instead of having a small rope hanging in the water column, for the pitch decay tests, the actuator has been used to provide a steady force and then stop it suddenly. It is assumed that, compared to the natural periods, the actuator force decreases very quickly to zero. The objectives of those decay tests is to get a damping ratio estimation as well as the natural frequencies. Moving from still water tests to regular waves help to understand the added damping due to the waves-induced fluid particles velocities. For coupled DoF and decay tests in regular waves, the signals are band-pass filtered around the natural frequency of the DoF. This is required to do a proper estimation of the peaks and troughs.

Heave decay test and associated damping estimation is presented in Figure 126. As explained in Appendix B, the linear and quadratic damping could be assessed from the intercept and slope of the lower plot. An averaged linear fit on the different oscillations is also provided to get an order of magnitude of the equivalent damping for each DoF. This is represented by the *envelope eq. lin.* on the top plot.

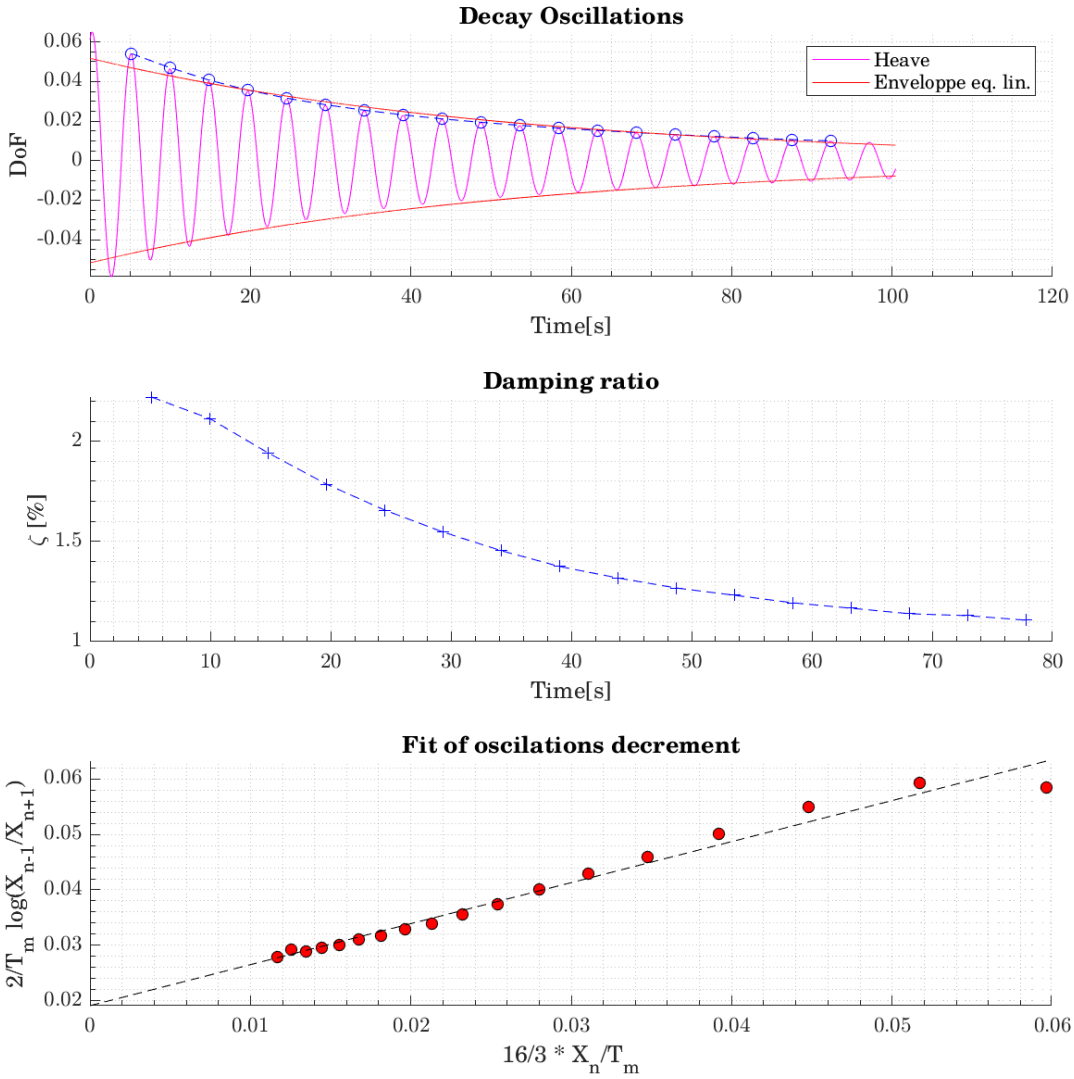

Figure 126: Heave decay test and damping fit. Top: considered signal and fitted envelope. Middle: damping ratio evolution. Bottom: quadratic and linear damping fit.

D.2 Fitting experimental system characteristics for the numerical model

The as-built experimental system characteristics have been presented in chapter 5. In this part, the important quantities for the numerical model implementation are presented.

D.2.1 Floater

It was intended to define the floater and tower properties from the perimeters define in chapter 5. However, as a linear interpolation of the inputs are done in the ElastoDyn module of OpenFAST, it was not convenient to define small elements (in particular the tower base force transducer) in the numerical tower, with its very large lineic mass compared to the flexible aluminum tube. Consequently, the numerical tower model contains only the flexible part (aluminum tube) and the other parts (considered rigid) belong either to the RNA or to the floater. The mass and inertia inputs of the floater are defined in Table 51.

Quantity	Value	Uncertainty
Mass [kg]	2.012E+07	1.3E+04
ZCOG [m] from MSL	-68.8	0.4
Inertia xx around COG Floater [kg.m^2]	2.37E+10	2E+09
Inertia yy around COG Floater [kg.m^2]	2.37E+10	2E+09
Inertia zz around COG Floater [kg.m^2]	6.2E+08	1E+07
XCOG from centerline [m]	-0.1	0.1
Draft at equilibrium [m]	-91.4	0.1
Displacement [m^3]	2.176E+04	1E+01

Table 51: Floater properties for the numerical model

Now the hydrodynamic modeling of the floater is adressed. As presented in chapter 8, the hydrodynamic model of the floater is based on a HDB and Morison drag only elements. The two parts are described hereafter.

The HDB is computed at the equilibrium position of the floater, i.e. including the added draft due to the vertical pretension of the mooring lines. After mesh convergence studies, it has been found that a mesh with 800 panels is sufficient to get converged added mass, excitation, radiation damping and horizontal drift force.

For the Morison modeling, the floater is discretized in Morison elements of 10m each at the bottom and with smaller heights closer to the free surface. The reference dimension is the diameter of each section. The same drag coefficients values are used along the SPAR even if the local Keulegan-Carpenters numbers are different. This choice has been done because the overall drag coefficients are different at model scale for the KC and Re numbers of interest than the literature values for oscillatory or steady flows.

D.2.2 Tower

The ElastoDyn inputs are the dimensions (height), mass and inertia properties of the nacelle, tower and rotor. The nacelle properties are described in the next subsection, the rotor properties are the same as the full scale DTU 10MW RWT, and the tower properties have already presented in Table 44. Additionnaly, the tower and blade modes shapes should be described as polynomial decompositions.

For the blade modes, this has not been changed from the DTU 10MW RWT FAST model description (v1.0).

For the tower mode polynomial decompositions, a least square fit to a 6^{th} order polynom is performed. The cantilevered beam boundary condition impose a zero deflection derivative and zero deflection at the tower base. In Figure 127 the first fore-aft mode shape from BModes FEA (Bir, 2005). The baseline DTU 10 MW tower fit and the modified tower for the Olav Olsen Oo-Star 10 MW FWT (Müller, Lemmer and Yu, 2018) are also represented.

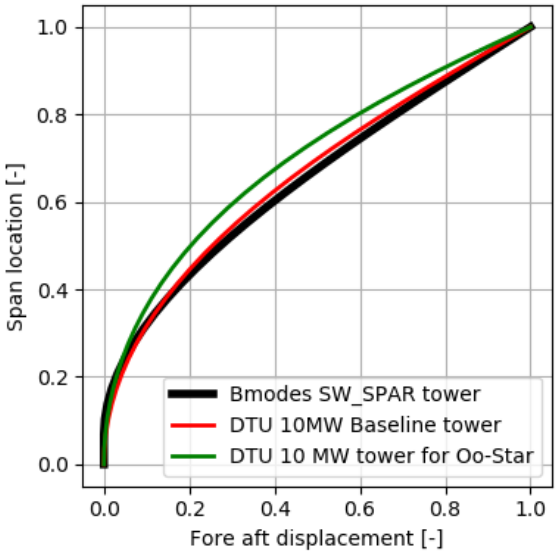

Figure 127: Shape of the 1st fore-aft mode of the SW SPAR tower and of the Baseline DTU 10MW tower

The values of the mode shape polynomial decomposition is presented in Table 52.

Coefficient	SOFTWIND SPAR	Baseline DTU 10MW	Oo-Star 10MW
x^2	-0.151	0.9689	0.6867
x^3	6.393	0.09762	0.2239
x^4	-11.847	-0.0108	-0.161
x^5	9.582	0.06656	0.6315
x^6	-2.977	-0.1222	-0.381

Table 52: Mode shape polynomial coefficients for the different DTU 10MW Tower

D.2.3 RNA

The same RNA as the physical one is included in the numerical model of the nacelle. However, the blades are in the numerical model while they are not present in the physical setup. Consequently, from the overall RNA values listed in Table 44, the nacelle mass and CoG are adapted to get the correct RNA ones. The nacelle properties are listed in Table 53.

Quantity	Value	Uncertainty
Mass and CoG		
Mass Nacelle above twr Top [kg]	6.38E+05	6.40E+03
CoG X Nacelle above twr top [m]	1.02	0.08
CoG Y Nacelle above twr top [m]	0.0	0.08
CoG Z Nacelle above twr top [m]	4.3	0.2
Dimensions		
Tower Base height from MSL [m]	9.3	0.1
Tower height (twr base to twr top)[m]	100.8	0.1
Tower top above MSL [m]	110.0	0.2
Tower top to Hub thrust application [m]	10.6	0.2
Hub height above MSL [m]	121.2	0.4

Table 53: Nacelle and hub APEX properties for the numerical model

D.2.4 Mooring system

The mooring system with its delta-connection is a multi-segmented catenary mooring system. This is modeled in the MoorDyn OpenFAST module, based on analytical elastic catenary solvers and lumped-mass approaches. It has been found that the robustness of the model depends of different factors:

- Internal damping of the mooring line, to avoid non-physical longitudinal and lateral oscillations,
- Soil modeling, especially damping, to avoid non-physical oscillations due to the mooring line impact (touchdown point) on the soil,
- Elastic stiffness,
- Mooring line segments discretization.

Different observations and modifications have been performed to improve the robustness

- The upscaled stiffness value was too large compared to classical value for the same chain diameter. This stiffness has been decreased to a value which ensure robustness without impacting too much (less than 1%) the tension levels.
- Even if the wave tank floor can be considered rigid, a large soil damping value has been considered. Additionally, a friction coefficient has been kept to avoid non-realistic lateral motions of the bottom chain.
- The computations were unstable for small discretization of the mooring lines segments. A trade-off between segment length and robustness has been obtained for segment length of approximately 8m.

D.3 Frequency domain modeling

D.3.1 Background

A simplified frequency domain model is established from the NEMOH Boundary Element Method diffraction-radiation. NEMOH outputs the frequency dependent excitation force RAO $F_e(\omega)$, added mass $A(\omega)$ and radiation damping $B_{rad}(\omega)$. Using the geometry and mass characteristics of the FWT, the hydrostatic stiffness K_H can be computed. The main source of loads are hydrodynamics. We also

consider a linear aerodynamic damping B_{aero}. Writing the 2nd law of Newton for the FWT, it comes Eq. (21):

$$X(\omega) = \frac{F_e(\omega)}{\big(M + A(\omega)\big)\omega^2 - i\omega\big(B_{rad}(\omega) + B_{aero} + B_{drag\ lin}\big) + (K_H + K_{Moor})} \quad (21)$$

With:

- $X(\omega)$ the motion RAOs of the system. In our case, it is the platform 6 DoF.
- M the mass matrix expressed in the reference frame,
- K_{Moor} the linearized mooring stiffness,
- $B_{drag\ lin}$ a linearized drag damping.

In this model, the linearized mooring stiffness and the linearized drag damping are neglected. The aerodynamic damping is computed from the *drag disc* formula presented in chapter 4. Note that more advanced frequency domain models exist, including the tower deflection DoF (e.g. (Pegalajar-Jurado, Borg and Bredmose, 2018)).The drift force are then computed based on the motion RAOs.

D.3.2 Inputs

The inputs to this frequency domain concern the entire FWT. Inputs for the overall FWT are described in Table 54. z_{COG} is the vertical position of the Center of Gravity, and z_{COB} the vertical position of the Center of Buoyancy. Note that in this model the SPAR has axisymmetric properties. The motions of interest are the surge, heave and pitch.

Parameter	Mass [kg]	z_{COG} $[m]$ from MSL	I_{yy}[kg.m^2] around CoG FWT	$z_{CoB}[m]$
Value	2.11E+7	-60.8	5.1E+10	-48.5

Table 54: Main inputs to the frequency domain model

The mass matrix M_{R_I} expressed in the inertial frame (centered on (0,0,0), i.e. at the MSL) is:

$$M_{R_I} = \begin{bmatrix} 2.11E+7 & 0 & 0 & 0 & -1.3E+9 & 0 \\ 0 & 2.11E+7 & 0 & 1.3E+9 & 0 & 0 \\ 0 & 0 & 2.11E+7 & 0 & 0 & 0 \\ 0 & 1.3E+9 & 0 & 1.3E+11 & 0 & 0 \\ -1.3E+9 & 0 & 0 & 0 & 1.3E+11 & 0 \\ 0 & 0 & 0 & 0 & 0 & 2E+9 \end{bmatrix}$$

The hydrostatic stiffness including gravity, buoyancy and waterplane area effect is:

$$K_H = \begin{bmatrix} 0 & 0 & 0 & 0 & 0 & 0 \\ 0 & 0 & 0 & 0 & 0 & 0 \\ 0 & 0 & 9.7E+5 & 0 & 0 & 0 \\ 0 & 0 & 0 & 2.6E+9 & 0 & 0 \\ 0 & 0 & 0 & 0 & 2.6E+9 & 0 \\ 0 & 0 & 0 & 0 & 0 & 0 \end{bmatrix}$$

D.4 Bugs in the experiments

Corrupted tests and bugs in the numerical model have been detected after the SOFTWIND SPAR and Blue Growth Farm campaigns. Details are presented in this appendix.

D.4.1 Corrupted tests

It has been identified after the experimental test campaign a non-achievement of the real-time (RT) cadency for the main RT loop running on the compactRIO in the LabView programming interface. This non-achievement of the RT (denoted *RT mismatch*), mostly in the range [0-6] iterations has reached up to [15-50] iterations for a 10 min long test (1.2E+5 iterations). This sounds negligible but problems arose since the implementation was not designed for such RT mismatch. The consequence was an increasing delay in the motion observer from this RT mismatch. Basically, as the RT loop runs as 200 Hz, each missing iteration increases the overall cumulative delay of 5ms. It is not problematic for most of the frequencies of interest (Surge and Pitch natural frequency, wave frequency) but is problematic for the tower natural frequency, as 5 RT mismatch iterations represent already a phase of $\phi = \frac{\pi}{8}$ at this frequency. Consequently, for comparison of tower deflection, a maximal RT mismatch of 3 iterations is allowed. This RT mismatch and its effect on the motion observer is intended to be corrected for latter development of this hybrid system. The detection of RT mismatch could be easily implemented on the compactRIO thanks to high precision clock signals, which can be compared to the reference iteration duration. Moreover, the use of Kalman filters, being time-consuming, contributes to this RT mismatch. As presented in chapter 5, their foreseen added value is not as expected and then, could be removed.

For future campaigns, keeping only the IMU angular velocity measurements and eventually low pass filtering the motions at a high frequency (~20Hz) are recommended.

Non-achievement of the RT cadency of the OpenFAST real-time loop running on the compactRIO has also been observed. This is denoted *OpenFAST RT mismatch.* The two RT loops run on two separated cores of the Linux real-time operating system. The latest information produced by the loop is kept for the other loop. A very high priority is affected to the OpenFAST RT loop, and both the numerical model options (blade discretization,…) and the numerical model cadency are selected to keep a certain margin between the numerical model RT loop time step (10ms for the floating setups) and the duration required to compute one iteration of the numerical simulation (approximately 5.5ms for the floating setups). For tests performed with an external PLC (see part 7.5), the average time due to the UDP communication (2-ways) is approximately 1ms. However, jitter has been observed regarding this single iteration computational duration. For tests without an external PLC, memory leaks are suspected to contribute to this jitter. When an external PLC is used, the communication duration itself varies and has reached sometimes more than 2ms. This non-achievement of the real-time introduces a delay in the numerical simulation, which is a concern for the input wind fields. However, if there is no RT mismatch of the main RT loop, the motions are correctly updated.

Finally, an *OpenFAST RT mismatch* is not problematic for the motion-induced fluctuations of the rotor loads forces. However, when comparing two tests performed with the same numerical configuration (wind field, control law, …) *OpenFAST RT mismatches* imply increasing delay in the input wind fields. This impacts mostly the low frequency motions (both LF and $R_Y\,NF$) and also the excitation at 3P rotor frequency. A threshold of 30 *OpenFAST RT mismatches* has been considered acceptable for comparison of low frequency motions between two tests. For future campaigns, different options are envisaged to limit the number of mismatches:

- Thoroughly investigate memory leaks;
- Increase the margin between the OpenFAST 1-iteration duration and the OpenFAST RT loop time step;
- Use an external real-time operating system of a high performance computer, on the dry side of the wave tank. The same Ethernet cable that is used for emergency stop might be used to

make the communication between the compactRIO and the external computer dedicated to the numerical simulation. This has the advantage to facilitate the compiling and development of the numerical tool as a non-deteriorated development environment could be used.

D.4.2 Bugs in the numerical model

As explained in chapter 4, the OpenFAST framework has been selected for the numerical tool. The validation described in appendix A was originally performed with the Hexapod setup, with the following characteristics:

- Using AeroDyn15 module for the setpoint load, neglecting the other sources of loads that have to be included in the setpoint load;
- For a rigid tower, with only the 6 platform DoF considered.

To keep the original DTU 10MW RWT input files and to include the part of the inertial loads that need to be included in the rotor loads setpoints , the simulation was then performed using AeroDyn14 and ElastoDyn.

However, as the tower for the floating setups was flexible, the required modifications have been done in the OpenFAST glue code and SIL wrapper (see appendix A for details). Two bugs have been involuntarily introduced:

- Tower DoF numbering was not correctly respected. The measured tower deflection in the y-direction was input to OpenFAST as the amplitude of the 2nd fore-aft mode instead of the 1st side-side mode. An inconsistency problem arises because the tower x-deflection and y-deflection are not in phase, the resulting F_x load differs from pure aerodynamic damping in phase with the hub x-velocity;
- The tower top trim angle was not removed from the gravity contribution present in the ElastoDyn outputs. This error implies a gravity contribution (proportional to the positions) included in the setpoint, and not in phase with hub x-velocity.

To illustrate the impact of the gravity contribution bug on the overall SIL system delay, the setpoint force for a tower decay test performed in the SOFTWIND SPAR campaign is analyzed. For such tests, the side-side motions of the tower is negligible. The wind speed is $U_w = 13.9\, m.s^{-1}$. In Figure 128, the hub x-velocity and the x-force are superimposed for the tower decay (starting at t ~300s). The represented forces are:

- "wrapper bug", the OpenFAST force produced with the SIL wrapper as used in the campaign,
- "wrapper corrected", the OpenFAST force produced with the debugged wrapper,
- "theoretical", the damping component of the aerodynamic force, computed from the simplified expression of the aerodynamic damping component.

The simplified expression of the aerodynamic damping component $F_{aero\ damping}$ is recalled in Eq. (22):

$$F_{aero\ damping} = -\frac{2 * F(U_0)}{U_0}\, \dot{X}_{hub\ |x} \tag{22}$$

For clarity, the setpoint force output by OpenFAST and the hub velocity are bandpass filtered around the tower natural frequency (0.38Hz).

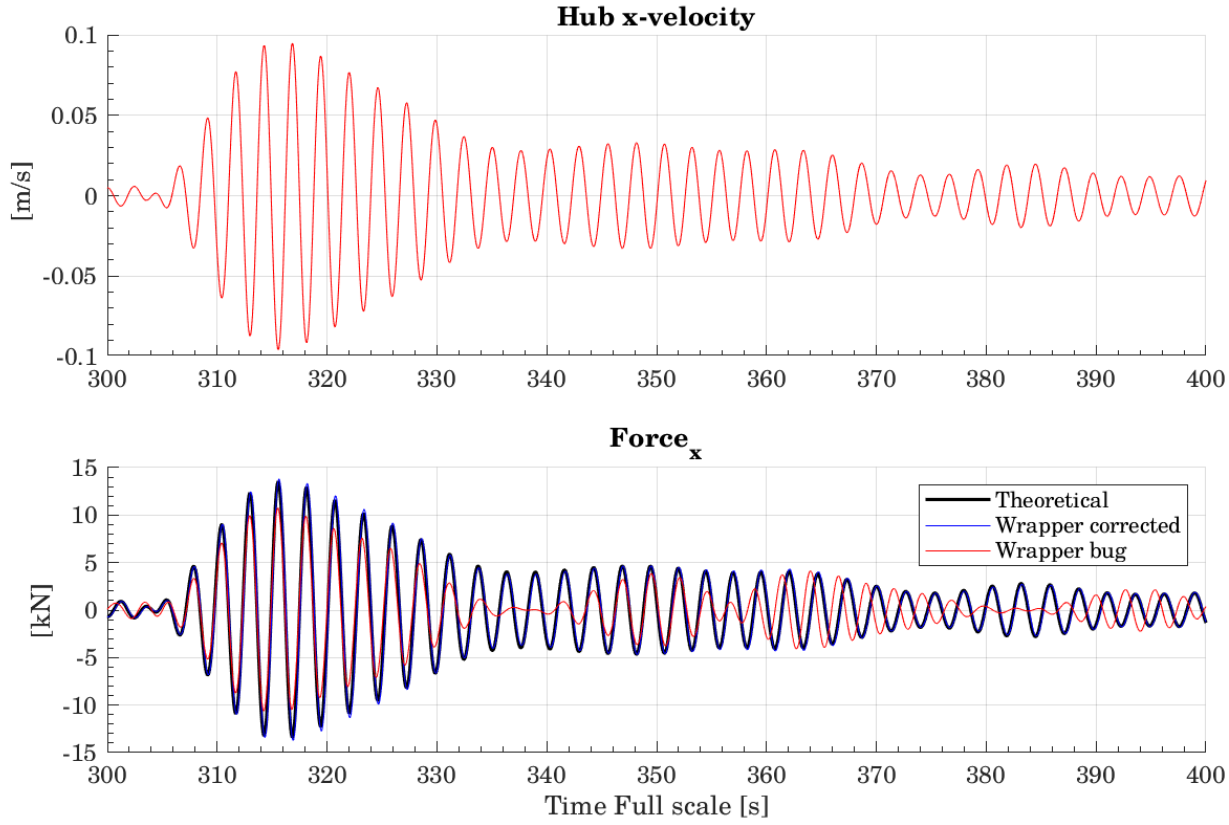

Figure 128: Illustration of the wrapper bug effect on the setpoint force

The theoretical and the wrapper corrected results superimposed very well, which means the setpoint force should be in phase with $-\dot{X}_{hub\,|x}$. However, the force obtained with the *wrapper bug* has a varying phase and attenuation compared to the corrected wrapper. On the range t = [310 - 350]s, the signals are in-phase. Then, on the range t = [360 - 400]s, the signals are nearly out of phase of π. Note that the impact of this bug on the tower motion is clearly visible: at the beginning of the test, the damping reproduced is positive, and the hub x-velocity decreases. Then (t~335s), the damping reproduced is nearly 0 and the hub x-velocity stops to decrease. On the last part, the hub x-velocity is not decreasing to zero, due to this phase shift between the correct force and the real-time computed force.

To conclude, the problem is, in the perspective of a SIL system analysis, an equivalent delay and attenuation of the force that could not be highlighted due to the bugs in the numerical model. The consequence is about the tower motions for the floating setups analyzed in this work, which are not correctly reproduced for all the cases with the SIL method active.

D.5 Wave reproduction

The wave quality is an important contributor to the total uncertainties. This has been studied in details in the literature, and its detailed investigation is out of scope of the present work. The important phenomena include (see e.g. (Molin, 2002; Bonnefoy, 2005)):

- 2nd-order free waves and evanescent modes due to the non-adapted geometry of the wavemakers (hinged-flap wavemaker),
- Influence of the wave ramp on the transient excitation of the platform. This ramp is applied to the target wave amplitude,
- Reflected wave field due to the partial energy absorption of the absorbing beach,

- Side-wall reflections due to the gaps between the different flaps and also due to the diffracted and radiated wave fields(due to the interaction of the incident wave field with the FWT). The consequence is that some crosswise natural modes of the wave tanks may be excited during the test.
- Specific wave tank instabilities, such as Benjamin-Feir.

Among those phenomena, three aspects are briefly investigated:

- The influence of the wave ramp on the low frequency motions,
- The estimation of the incident / reflected wave field,
- The 2nd-order free waves

D.5.1 Ramp duration on low frequency motions

The ramp duration influences how the wave energy is transferred to the FWT. A short ramp duration leads to a pronounced transient response of the system at its natural frequencies. As a rule of thumb, a ramp duration twice the longest natural period of the system is expected to lead to acceptable transient response. However, for the SOFTWIND SPAR setup, the maximal natural period was 18.6s for the surge motion, and so the acceptable ramp duration should be approximately 37s. But, to avoid a very long ramp duration, this duration was limited to 10s . For the analyses, the consequence is that the first part of the test (40s) is skipped to avoid an overestimation of the low frequency (transient) response.

The wave elevation, platform surge and pitch motions are illustrated in Figure 129 for a regular wave test with $A = 0.035m \; and \; T = 1.11s$. The arrival of the wave field is represented by the green line, and the established wave front (after the ramp duration) with green lines. The 2nd green and red lines are the reflected waves. The useful part of the test for the regular waves analysis is between the 1st red line and the 2nd green line (only established incident waves without reflected waves). The incident wave field provides excitation at the wave period and at the 0th harmonic (drift force), this is why the steady value of the platform surge is above zero on the useful part of the signal. Because the energy is transmitted over a small duration, the FWT oscillates at its natural frequency (two oscillations at $T_{surge} \sim 18.6s$ could be seen). As a consequence, the regular wave analysis is performed using Fourier transform to get the FWT response only at the 1st harmonic of the incident wave.

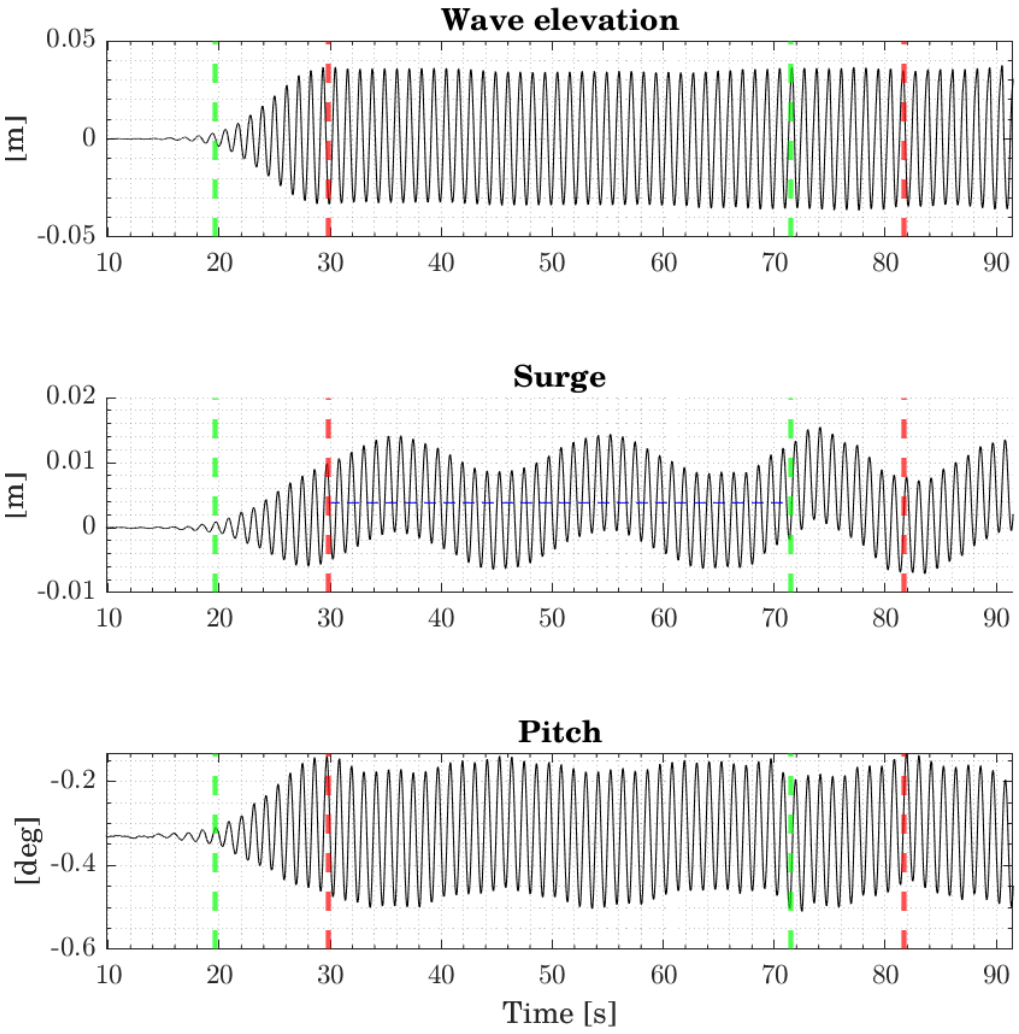

Figure 129: Wave ramp effect on Surge and Pitch motions. Incident and reflected wave front are represented with dashed vertical lines. The mean surge is represented with dashed blue line.

D.5.2 Wave reflection

The present wave probes layout was not sufficient in terms of numbers and spatial distribution to conduct a proper separation between incident and reflected waves. To get an order of magnitude about the importance of the reflected waves at the fundamental frequency of the waves, the reflection coefficient for a steepness $\frac{H}{\lambda} = 3\%$ determined by Bonnefoy for Centrale Nantes internal studies has been used. In Figure 130, the reflection coefficient is computed for different regular waves conditions using a wave probe array near the absorbing beach. Overall, the reflection coefficient at the 1st harmonic is between 5 and 10 % for regular waves. For irregular waves, the computation is more complex and depends also on the frequency distribution of the incident wave field (peak enhancement factor for the JONSWAP spectra).

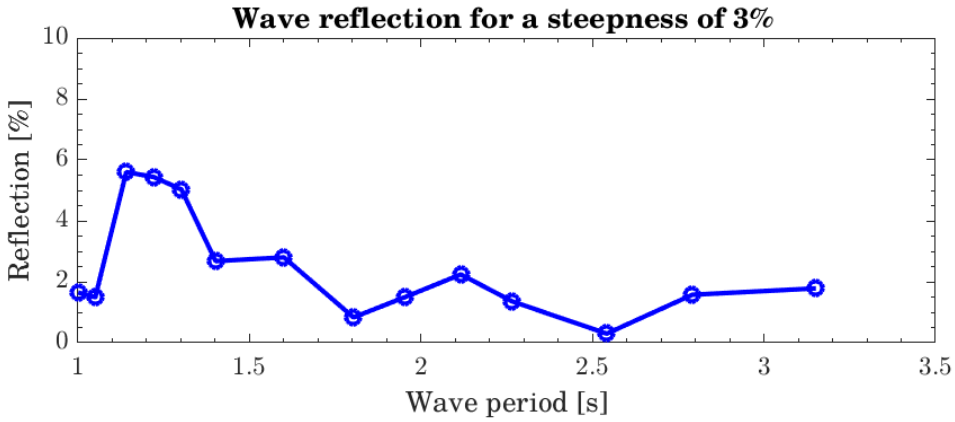

Figure 130: Reflection coefficient in the Ecole Centrale de Nantes wave tank.

D.5.3 Second-order free waves

The wave reflection influences mostly the 1st harmonic of the wave, i.e. what is called the wave frequencies. However, other wave reproduction phenomena present in the wave tank make it differ from the full scale wave kinematics. Two types of spurious waves need to be considered:

- Evanescent modes. These modes are stationary, they don't propagate and they stay close to the wavemakers. A common engineering practice is to consider them non-significant for distances above two times the water depth (i.e. 10m in our case). Due to the mean position of the SPAR platform (17m from the wavemakers) they can be safely neglected.
- High-order free waves. These modes are not stationary, they propagate at their own velocity. High-order bound waves propagate at the 1st harmonic phase velocity while free waves respect the wave dispersion relation at their frequency.

It has already been shown for large floating platform wave tank experiments the influence of the second-order low frequency free waves on the surge motion at its natural period (e.g. (Waals, 2009)). In order to investigate possible source of differences between the experimental and the numerical results, the second-order free waves are analyzed for the SOFTWIND SPAR experiments. This has been performed by F. Bonnefoy by means of the analytical wave elevation solutions. Second-order free waves have two components for each couple of ω_i & ω_j of the incident wave spectrum:

- A sum-frequency mode, producing a high frequency wave component at $\omega_i + \omega_j$,
- A difference-frequency mode, producing a low frequency wave component at $\omega_i - \omega_j$.

The sum-frequency mode component is not of interest to explain the low frequency surge motions. The difference-frequency mode are considered. For all the sea states considered, the amplitude of the difference-frequency components are negligible compared to the sum-frequency and to the 1st harmonic components. This is due to the type of wavemakers that have been used for the SOFTWIND SPAR experiments. Indeed, the waves are generated with hinged-flap wavemakers, that impose a vertical profile of the kinematics, but is not necessarily the target wave-induced kinematics. When computing the dimensionless kh number, i.e. the wave number times the depth, deep water waves can be considered ($kh >$) for all the wave conditions. For this reason, hinged-flap wavemakers are better suited than piston-type wavemakers, which impose a uniform horizontal velocity whatever the vertical position.

Appendix E. Existing hybrid systems

Actuators illustrations

While not being exhaustive, a summary of the different recent initiatives is given in Table 55 with the research institutes involved, some publications and the main actuators technologies with illustrative pictures.

Institute	Actuator technology	Illustrative picture
CENER	1 on-board ducted fan (J Azcona *et al.*, 2014; José Azcona *et al.*, 2014; Azcona, Bouchotrouch and Vittori, 2019)	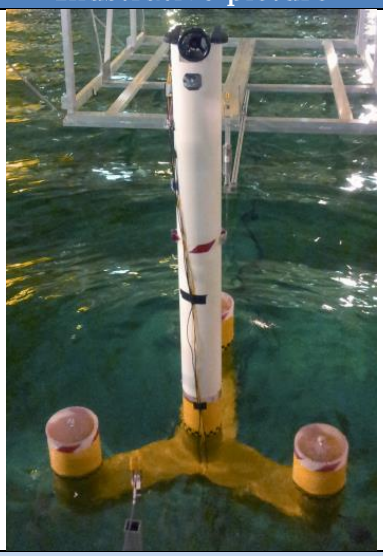
NTNU and SINTEF Ocean	6 force-controlled wires with winch units (Bachynski, Chabaud and Sauder, 2015; Berthelsen *et al.*, 2016; Chabaud, 2016; Sauder *et al.*, 2016; Kvittem *et al.*, 2018; Thys *et al.*, 2018, 2019)	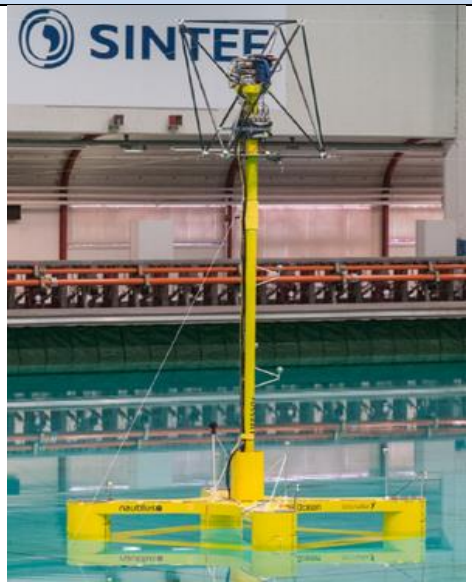 © SINTEF

University College of Cork	2 on-board ducted fans (Desmond, Hinrichs and Murphy, 2019)	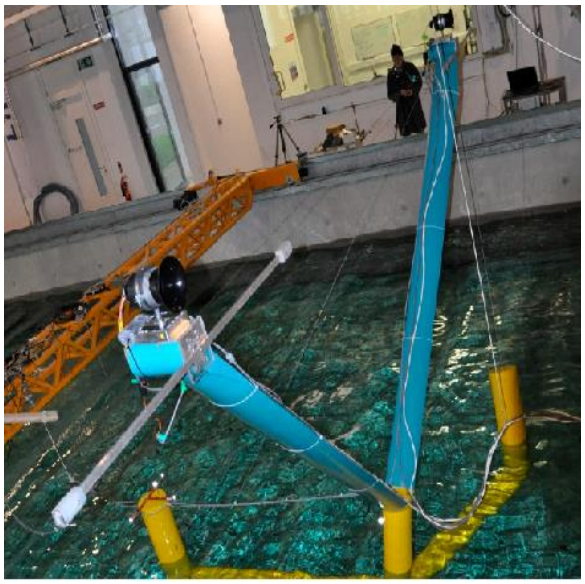 © UCC
MARIN	6 force-controlled wires with winch units (MARIN, 2018). Recently, the multi-fan system of IH Cantabria (Gueydon, Bayati and de Ridder, 2020)	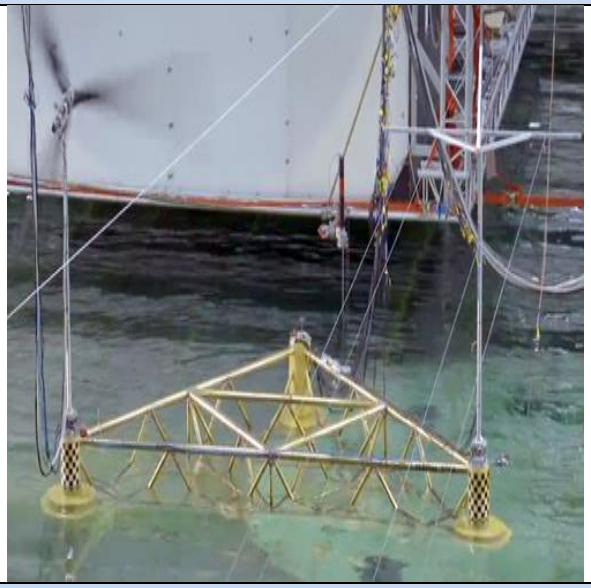
IH Cantabria	6 on-board fans (Battistella *et al.*, 2018; Meseguer and Guanche, 2019)	 

University of maine	2 force-controlled wires with winch units (Hall, 2016; Hall, Goupee and Jonkman, 2017; Hall and Goupee, 2018)	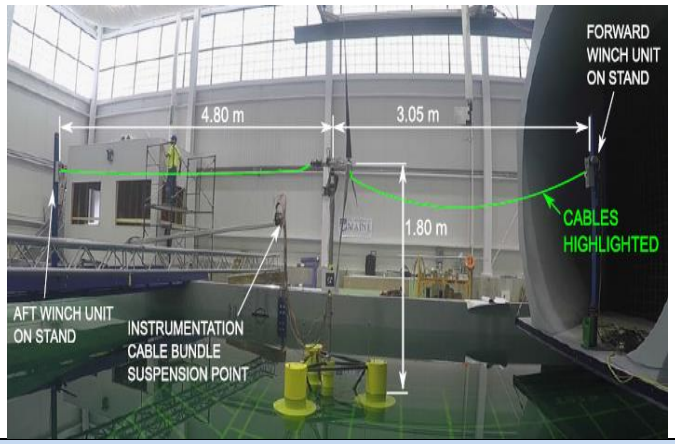
UC Berkeley	2 fans on rotating masts (Kanner, no date)	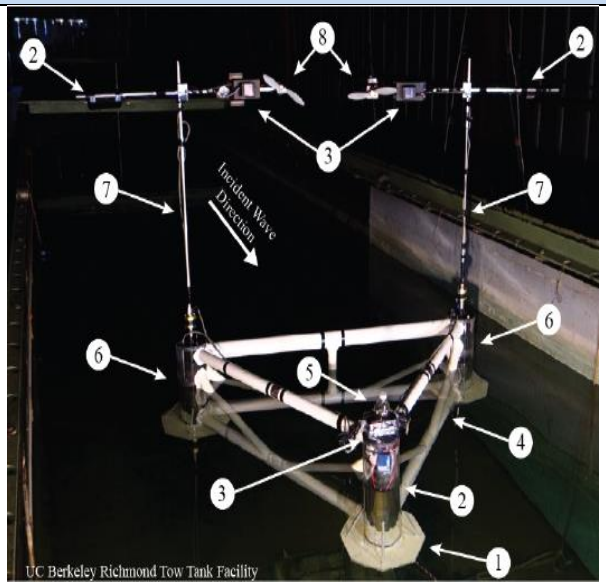

Table 55: Some recent hybrid experimental systems for wave tank model testing of FWT

Titre : Modélisation expérimentale d'une éolienne flottante par une approche « software-in-the-loop »

Mots clés : Eolien flottant, modélisation, numérique, expérimental, approche hybride temps-réel, aérodynamique du rotor.

Résumé : Les outils de calcul actuels pour la modélisation numérique multi-physique (vent, vagues, courant, etc.) d'une éolienne flottante ont besoin de validations par des campagnes expérimentales. L'objectif de ce travail est le développement et la validation d'un dispositif expérimental dédié aux essais en bassin à houle d'une éolienne flottante, en se concentrant sur la représentation des efforts du vent. Pour cela, une approche hybride combinant modélisations physique et numérique est développée, appelée "software-in-the-loop" (SIL). Le développement des différentes briques composant un système SIL inclut (i) la sélection et le développement du modèle numérique (ii) le dimensionnement du système de reproduction des efforts (actionneurs) et (iii) la définition de l'environnement temps-réel pour l'intégration du modèle numérique, le contrôle des actionneurs, et l'acquisition des grandeurs mesurables.
Pour caractériser et identifier les performances du système SIL, des méthodologies dédiées sont développées. Des bancs d'essais spécifiques sont construits, et des essais en bassin d'une éolienne flottante sont réalisés. Ces essais en bassins sont ensuite comparés à des simulations couplées aéro-hydro-servo-structure pour investiguer les hypothèses du modèle d'efforts hydrodynamiques.

Title : Experimental modelling of a floating wind turbine using a « software-in-the-loop » approach

Keywords : Floating wind turbine, modelling, numerical, experimental, real-time hybrid method, rotor aerodynamics.

Abstract : Actual calculation tools for the multi-physical numerical modeling (wind, waves, current, etc.) of a floating wind turbine need validation through experimental campaigns. The objective of this work is the development and validation of an experimental apparatus dedicated to floating wind turbines wave tank testing, focusing on the representation of wind turbine forces. A hybrid approach combining physical and numerical modeling is developed, called "software-in-the-loop" (SIL). The development of the different subsystems of an SIL system includes (i) the selection and development of the numerical model (ii) the design of the force reproduction system (actuators) and (iii) the definition of the real-time environment for the integration of the numerical model, the control of actuators, and the data acquisition.
To characterize and identify the performances of the SIL system, dedicated methodologies are developed. Specific test benches are built, and wave tank tests of a floating wind turbine are carried out. These wave tank tests are then compared to coupled aero-hydro-servo-structure simulations to investigate the hypotheses of the hydrodynamic force model.